

The Structure and Interaction History of Moderate Luminosity Mergers



Dissertation

zur
Erlangung des Grades
„Doktor der Naturwissenschaften“
der Fakultät für Physik und Astronomie
an der Ruhr-Universität Bochum

von
Eva Manthey
aus
Essen

Bochum 2006

1. Gutachter: Priv. Doz. Dr. Susanne Hüttemeister

2. Gutachter: Dozent Dr. Susanne Aalto

Datum der Disputation: 4.7.2006

We do not ask for what purpose the birds do sing, for their song is pleasure since they were created for singing. Similarly, we ought not ask why the human mind troubles to fathom the secrets of the heavens. The diversity of the phenomena of Nature is so great, and the treasures hidden in the heavens so rich, precisely in order that the human mind shall never be lacking in fresh nourishment.

Johannes Kepler

Contents

| | | |
|----------|---|------------|
| 1 | Motivation | 11 |
| 1.1 | The importance of mergers in galaxy evolution | 11 |
| 1.2 | The different types of mergers | 13 |
| 1.3 | Recent S+E merger models | 16 |
| 1.4 | Outline of the thesis | 23 |
| 2 | Physical Properties of Galaxies | 27 |
| 2.1 | Optical/NIR | 27 |
| 2.2 | The Star Formation Rate | 29 |
| 2.3 | Molecular gas | 32 |
| 2.4 | Atomic gas | 33 |
| 2.5 | ISM | 34 |
| 2.5.1 | Optical Emission Lines | 34 |
| 2.5.2 | Molecular lines | 36 |
| 3 | Optical and NIR properties | 43 |
| 3.1 | Introduction | 43 |
| 3.2 | The sample | 44 |
| 3.3 | Observations | 46 |
| 3.3.1 | Optical imaging | 46 |
| 3.3.2 | NIR imaging | 47 |
| 3.3.3 | Optical spectroscopy | 48 |
| 3.4 | Data reduction | 49 |
| 3.4.1 | Optical and NIR images | 49 |
| 3.4.2 | Spectroscopy | 52 |
| 3.5 | Results and Discussion | 52 |
| 3.5.1 | The Morphology and Colours of the Sample | 53 |
| 3.5.2 | Optical spectroscopy | 93 |
| 3.6 | Summary | 96 |
| 4 | Gas content of NGC 4441 | 101 |
| 4.1 | Introduction | 101 |
| 4.2 | Observations | 102 |
| 4.2.1 | WSRT | 102 |
| 4.2.2 | Onsala Space Observatory 20 m | 103 |
| 4.2.3 | IRAM 30 m | 103 |
| 4.2.4 | Optical imaging | 104 |
| 4.3 | Data Reduction | 104 |
| 4.3.1 | HI interferometry | 104 |
| 4.3.2 | CO single-dish observations | 105 |
| 4.4 | Results | 105 |
| 4.4.1 | Neutral hydrogen | 105 |
| 4.4.2 | 20 cm Continuum | 109 |
| 4.4.3 | Molecular gas | 111 |
| 4.5 | Discussion | 112 |

| | | |
|----------|---|------------|
| 4.5.1 | Size of the star forming region | 112 |
| 4.5.2 | Star formation efficiency | 114 |
| 4.5.3 | Kinematics of the gas | 115 |
| 4.5.4 | Molecular gas properties | 117 |
| 4.6 | Summary and Conclusions | 120 |
| 5 | HI in the Medusa | 123 |
| 5.1 | Introduction | 123 |
| 5.2 | Observations & Data Reduction | 124 |
| 5.2.1 | HI observations | 124 |
| 5.2.2 | Optical imaging | 125 |
| 5.3 | Results | 125 |
| 5.3.1 | Continuum | 125 |
| 5.3.2 | Neutral hydrogen | 125 |
| 5.4 | Discussion | 132 |
| 5.4.1 | Star Formation Rate | 132 |
| 5.4.2 | The merger remnant | 133 |
| 5.5 | Conclusions | 134 |
| 6 | HI and CO properties | 137 |
| 6.1 | Introduction | 137 |
| 6.2 | Observations | 137 |
| 6.2.1 | HI and 20 cm continuum observations | 138 |
| 6.2.2 | CO observations | 140 |
| 6.3 | Data Reduction | 141 |
| 6.4 | Results | 142 |
| 6.4.1 | Neutral hydrogen | 142 |
| 6.4.2 | Continuum | 155 |
| 6.4.3 | Molecular gas | 160 |
| 6.5 | Discussion | 161 |
| 6.5.1 | Stellar versus gaseous morphology | 161 |
| 6.5.2 | The star forming regions | 163 |
| 6.5.3 | Star Formation Efficiency | 163 |
| 6.5.4 | Possible merger scenarios for the sample galaxies | 164 |
| 6.6 | Conclusions | 166 |
| 7 | Summary | 169 |
| | Acknowledgements | 175 |
| | Curriculum vitae | 177 |

List of Figures

| | | |
|----|--|-----|
| 1 | Toomre–Sequence | 14 |
| 2 | Stellar component simulated by Weil & Hernquist (1993) | 19 |
| 3 | Stellar component simulated by Kojima & Noguchi (1997) | 20 |
| 4 | Gas component simulated by Weil & Hernquist (1993) | 21 |
| 5 | Gas component simulated by Kojima & Noguchi (1997) | 22 |
| 6 | Emission line spectrum | 36 |
| 7 | NGC 4441: optical and NIR data | 61 |
| 8 | NGC 4441: optical and NIR colour maps | 62 |
| 9 | NGC 4441: optical and NIR profiles | 63 |
| 10 | NGC 4194: optical and NIR data | 64 |
| 11 | NGC 4194: optical and NIR colours | 65 |
| 12 | NGC 4194: optical and NIR profiles | 66 |
| 13 | NGC 4004: optical and NIR data | 67 |
| 14 | NGC 4004: optical and NIR colours | 68 |
| 15 | NGC 4004: optical and NIR profiles | 69 |
| 16 | NGC 5607: optical and NIR data | 70 |
| 17 | NGC 5607: optical and NIR colours | 71 |
| 18 | NGC 5607: optical and NIR profiles | 72 |
| 19 | UGC 8264: optical and NIR data | 73 |
| 20 | UGC 8264: optical and NIR colours | 74 |
| 21 | UGC 8264: optical and NIR profiles | 75 |
| 22 | Arp 161: optical and NIR data | 76 |
| 23 | Arp 161: NIR colours | 77 |
| 24 | Arp 164: optical and NIR data | 78 |
| 25 | Arp 164: optical colours | 79 |
| 26 | ESO 156-18: optical data | 80 |
| 27 | ESO 156-18: optical colours | 81 |
| 28 | ESO 159-03: optical data | 82 |
| 29 | ESO 159-03: optical colours | 83 |
| 30 | ESO 416-09: optical data | 84 |
| 31 | ESO 416-09: optical colours | 85 |
| 32 | NGC 2996: optical data | 86 |
| 33 | NGC 2996: optical colours | 87 |
| 34 | ESO 341-04: NIR data | 88 |
| 35 | ESO 341-04: NIR colours | 89 |
| 36 | ESO 511-35: NIR data | 90 |
| 37 | ESO 511-35: NIR colours | 90 |
| 38 | IC 5065: NIR data | 91 |
| 39 | IC 5065: optical colours | 92 |
| 40 | ESO 295-02: optical data | 92 |
| 41 | Optical spectra | 94 |
| 42 | NGC 4441: HI data | 107 |
| 43 | NGC 4441: HI channel maps | 108 |
| 44 | NGC 4441: HI distribution in the center | 109 |
| 45 | 20 cm continuum flux image of NGC 4441 | 110 |

| | | |
|----|--|-----|
| 46 | NGC 4441: OSO ^{12}CO spectrum | 111 |
| 47 | NGC 4441: Inner $6'' \times 6''$ maps in $^{12}\text{CO}(1-0)$ and $^{12}\text{CO}(2-1)$ | 114 |
| 48 | NGC 4441: Large $^{12}\text{CO}(1-0)$ map | 115 |
| 49 | NGC 4441: Large $^{12}\text{CO}(2-1)$ map | 116 |
| 50 | NGC 4441: ^{13}CO spectra | 116 |
| 51 | NGC 4441: Position-velocity diagrams | 117 |
| 52 | HI spectra of NGC 4441 | 117 |
| 53 | LVG vs. RADEX | 119 |
| 54 | NGC 4441: LVG and RADEX results | 119 |
| 55 | 20 cm continuum flux of NGC 4194 | 126 |
| 56 | NGC 4194: Surroundings in HI | 127 |
| 57 | NGC 4194: HI spectra | 128 |
| 58 | NGC 4194: HI data | 129 |
| 59 | NGC 4194: HI channel maps | 130 |
| 60 | NGC 4194: HI absorption spectrum | 131 |
| 61 | NGC 4194: HI map of the main body | 132 |
| 62 | NGC 4004: HI data | 144 |
| 63 | NGC 4004: HI channel maps | 145 |
| 64 | NGC 4016/17: HI data | 146 |
| 65 | NGC 5607: HI data | 148 |
| 66 | NGC 5607: HI channel maps | 149 |
| 67 | UGC 8264: HI data | 150 |
| 68 | UGC 8264: HI channel maps | 151 |
| 69 | UGC 8264: The surroundings in HI | 152 |
| 70 | Arp 161: HI data | 153 |
| 71 | Arp 161: HI channel maps | 154 |
| 72 | HI spectra | 155 |
| 73 | Arp 164: companion in HI | 156 |
| 74 | ESO 156-18: HI non-detection | 156 |
| 75 | ESO 159-03: companion in HI | 157 |
| 76 | 20 cm continuum maps of the sample | 159 |
| 77 | CO spectra of the sample | 161 |

List of Tables

| | | |
|----|---|-----|
| 1 | CO lines | 33 |
| 2 | Most important emission lines | 37 |
| 3 | Basic properties of the sample | 45 |
| 4 | Obtained optical observations | 47 |
| 5 | Obtained NIR observations | 48 |
| 6 | Obtained optical spectroscopy | 48 |
| 7 | Optical photometric calibration | 50 |
| 8 | NIR photometric calibration | 50 |
| 9 | Star formation rate based on the H α line | 95 |
| 10 | Abundance of the ISM | 97 |
| 11 | Basic properties of NGC 4441 | 102 |
| 12 | WSRT HI observations of NGC 4441 | 103 |
| 13 | IRAM 30 m and OSO CO observations of NGC 4441 | 104 |
| 14 | HI properties of NGC 4441 | 105 |
| 15 | 20 cm continuum flux properties of NGC 4441 | 110 |
| 16 | NGC 4441: CO properties of the IRAM 30 m map | 113 |
| 17 | NGC 4441: ^{12}CO and ^{13}CO at the center | 113 |
| 18 | NGC 4441: Molecular line ratios | 113 |
| 19 | Basic properties of NGC 4194 | 124 |
| 20 | WSRT HI observations of NGC 4194 | 125 |
| 21 | HI properties of NGC 4194 | 126 |
| 22 | 20 cm continuum flux results of NGC 4194 | 133 |
| 23 | Basic properties of galaxies observed in HI and CO | 138 |
| 24 | ATCA HI observations | 139 |
| 25 | WSRT HI observations | 139 |
| 26 | VLA HI observations | 140 |
| 27 | CO observations | 141 |
| 28 | HI properties of the sample | 143 |
| 29 | 20 cm continuum results of the sample | 158 |
| 30 | CO results of the sample | 160 |
| 31 | SFE of the sample | 164 |
| 32 | Summary of the properties | 172 |

1 Motivation

Abstract

The collision of galaxies as a major factor in galaxy evolution has been considered for 30 years now. In the beginning, the most important part of studies of merging effects was of course optical observations, with the drawback that it is only possible to observe a snapshot of an evolution process lasting more than 100 million years. In the last years, with the development of decent and evergrowing computer power, numerical simulations become more and more important to study the whole merger process. Still, it is inevitable to obtain diverse observations to compare them with the models, because only the observations show the reality.

When we consider the various kinds of galaxies, it is clear that there are also a lot of possibilities for different merger events. One of the key questions then becomes: What happens during a merger and are all mergers essentially the same? Although this topic is still under discussion, it seems to be clear at least, that we do find a variety of mergers, but until now we are far from obtaining a comprehensive picture of merger processes and their influence on the galaxy remnants.

1.1 The importance of mergers in galaxy evolution

One of the major topics in extra-galactic astronomy is how galaxies are evolving. Nowadays, it is widely accepted, that mergers play an important role, and it is suggested that every large galaxy has undergone at least one and probably several of different merger events in its lifetime. In the most successful and widely accepted model for structure formation in the universe, the hierarchical clustering, the formation of large galaxies is only possible by successive merging and gas accretion (e.g., White & Frenk (1991), Steinmetz (2003)). The most commonly used model to simulate the structure formation is the so-called Λ CDM model (i.e., cold dark matter (CDM) is the dominating matter in the universe, and the the cosmological constant Λ is not zero to restore the flat geometry of space and account for an accelerated expansion of the universe). The Λ CDM model is consistent with many cosmological observations, like the estimation of the age of the universe, the primordial abundance of light elements and the fluctuations in the microwave background as measured with COBE (Bunn & Sugiyama (1995), Kofman et al. (1993)) or WMAP (Spergel et al. (2006)). In the picture of hierarchical clustering, first small disk galaxies were formed by gas infall into a dark matter halo. The accreted gas settles in a rotating disk and is partly transformed into stars. When these proto-galaxies merge, the disk is disrupted and relaxes into a spheroidal object. By the accretion of gas from the intergalactic medium, a new, larger disk with a central spheroidal component, the bulge, develops. Such an object is similar to bright spiral galaxies like the Milky Way. Internal structure, like the formation of a central bar, can be influenced by the ongoing accretion of small companions or other forms of interaction. If two of these large spiral galaxies merge, a new, large spheroidal galaxy, i.e., a large elliptical, is created according to many models.

If merging is therefore seen as the dominant process of structure formation and evolution in galaxies throughout the history of the universe, it is obviously essential to gain a deep understanding of all types of merger processes. This does not only include large disk-disk mergers, but also collisions between galaxies of unequal mass and gas content. This is all the more important, because the model of disk-disk merging as the obvious way leading to Ellipticals has been challenged, e.g., by the observations of very long time scales of purely passive evolution in large Ellipticals. Therefore, the entire spectrum of possible merger types

needs to be investigated. In detail, this can only be done in the *local* universe, because the fine structure revealing how the merging proceeded and what the progenitor galaxies were like can only be studied with sufficient resolution, if the galaxies are not too distant. This thesis embarks on such a study of a newly defined class of mergers of moderate far-infrared luminosity.

The study of galaxy–galaxy interaction began with the ‘simulations’ by Holmberg (1941). Due to the lack of available computers, he studied the tidal effects during encounters by replacing gravity by light. As ‘test particles’, 37 candles for each galaxy were used, mounted on two platforms, which allowed rotation and could approach each other. The power of each candle is proportional to the mass it represents. A photocell was used to measure the total light along the x and y direction. Despite the simplicity of this experiment, the results were inspiring, showing for the first time tidal arms as a result of a galaxy–galaxy encounter.

Detailed observations in the following years revealed a large number of peculiar galaxies, which could not be classified within the classical Hubble sequence. but show disturbances when compared to regular galaxies. A systematic investigation led to two major compilations, the *Atlas and catalog of interacting galaxies* (Vorontsov-Velyaminov (1959)) and the *Atlas of Peculiar Galaxies* (Arp (1966)), both showing a large variety of disturbed galaxies resembling both of classical Ellipticals and Spirals. These catalogs made clear, that the Hubble sequence is not the end of the story, and galaxies cannot be treated as isolated objects, undergoing pure passive evolution, dominated by the ageing of the stellar population.

The importance of galaxy interactions was not clear until the first modern, computational models came up in the 70’s. For the first time, restricted N–body simulations, in which massless test particles move in the gravitational field of two galactic potentials, were used by Toomre & Toomre (1972) to investigate the effects of gravitational interaction. In their seminal work, they related the occurrence of *tidal* tails and bridges to different kinds of encounters. Depending of the mass ratio between the interacting galaxies, either bridges or tails are favoured. Furthermore, they found the resulting tidal features to be dependent on the geometry of the passage.

To relate the simulations to real galaxies, an observational analogy was composed by Toomre (1977). In his famous merger sequence (Fig. 1), he selected 11 peculiar galaxies from the New General Catalog (NGC), which had a similar optical morphology as the modelled galaxies at different time steps, and proposed them being candidates for showing the progress of a galaxy–galaxy merger at different stages. Furthermore, he estimated the number of past galaxy mergers within the last 500 Myr in the NGC as ~ 500 , considering a calculated time of $\sim 5 \cdot 10^8 \text{ yr}$ for the tidal features being visible. From the fact, that this number is similar to the total number of elliptical galaxies found in the NGC, and that the end product of typical merger simulations appear strikingly similar to an elliptical, he formed the hypothesis, that Ellipticals originate from mergers between two disk galaxies. This theory is not disproved until today, although some observational facts like the generally old, for several Gyr passively evolved stellar populations in Ellipticals are difficult to explain in this scenario.

This merger theory was corroborated by the discovery of faint shells and ripples around a large fraction of elliptical galaxies (e.g., Malin & Carter (1983)).

A further step in understanding mergers was done by Larson & Tinsley (1978), who connected the gravitational influences to the stellar population properties of the galaxies involved. They conducted an investigation of a sample of peculiar galaxies, which appear to cover a large range of optical colours. In combination with first theoretical stellar population models, they

concluded that these galaxies must have undergone a starburst phase in the near past. Thus, the interaction/merging has not only an effect on the morphology of a galaxy, but also on its star forming behaviour and therefore its stellar content!

With the launch of the IRAS infrared satellite, a new class of objects, which are extremely bright in this wavelength range, the so-called ULIRGs (ultra-luminous infrared galaxies) was found. It turned out, that these objects all show signs of strong interaction/merging in the optical. The extreme brightness in the far-infrared could be related to an enormous increase of star formation induced by the interaction, which is only possible when a large amount of gas is available. Therefore, ULIRGs are suggested to be ongoing disk-disk mergers, undergoing an extreme starburst (Sanders & Mirabel (1996)). In fact, the far-infrared brightness can be used to identify and classify mergers (see below).

After an extensive investigation of peculiarities of elliptical galaxies, Schweizer et al. (1990) defined the so-called fine structure index Σ to characterise the different features found, e.g., shells, plumes, and tails. Furthermore, they correlated the fine structure with the age of the dominating stellar population. Younger systems typically show a higher Σ value, indicating the connection between the morphological features and the enhanced star formation.

Recent more sophisticated simulations of merging galaxies were able to prove this connection. It could be shown, that in particular in a disk-disk merger, the gas becomes concentrated in less than a kpc in the nuclear region, leading to a super-starburst, while parts of the outer stellar and gaseous disk form large tidal features like tails (e.g., Barnes & Hernquist (1991), Barnes (1994)). The remnant of these mergers has a spheroidal distribution like a large Elliptical galaxy (e.g. Hernquist (1993)). The influence of the interaction on the star formation is reviewed by Kennicutt (1998). Further extensive investigations of disk-disk mergers are in particular done by Hibbard & Mihos (1995), Hibbard & van Gorkom (1996), Hibbard & Yun (1999a), Hibbard & Yun (1999b), Hibbard et al. (2000) and Hibbard & Sansom (2003), studying both the stellar and gaseous component of these mergers from the early stage to the merger remnants. Thanks to these works, mergers between two large disk galaxies are fairly well understood today. One has to keep in mind, however, that these galaxies represent only a small fraction of all galaxies in the Universe, thus the importance for the overall galaxy evolution might not be as dominant as their spectacular appearance suggests. The (until now unanswered) question therefore arises, what happens during mergers between galaxies, that are at least as common as large Disks?!

Furthermore, despite the general success of the hierarchical clustering models, recent simulations by Naab & Burkert (2000), Naab & Burkert (2001) and Khochfar & Burkert (2003) revealed, that the formation of Ellipticals is more complex than just the merger of two large spirals. They found, that a large fraction ($\sim 50\%$) of bright Ellipticals are formed by a merger of a spheroidal and a disk galaxy. A useful tool to discriminate the different merger scenarios seems to be the analysis of the kinematics and the shape of the isophotes of Ellipticals (Burkert & Naab (2003)). However, as mentioned by Khochfar & Burkert (2003), these aspects are poorly studied until now despite their importance, and more simulations of S+E and E+E mergers have to be done as well as detailed observational investigations to better understand the processes in those mergers.

1.2 The different types of mergers

Since there are different kind of galaxies in the Universe (Spirals, Ellipticals, Dwarfs), one can easily imagine that there may be different kind of merger scenarios, depending on which



Figure 1: The so-called *Toomre-Sequence* (adopted from Toomre (1977)) as an example for a classical merger sequence based on the optical morphology of galaxies. In the left column the NGC numbers of the galaxies are given.

galaxies are involved in the collision. The absolute and relative properties of the progenitors determine the evolution of the remnant. As an example, the total amount of gas present in both progenitors is decisive for whether a starburst will be induced by the merger and how strong this will be. The occurrence of a starburst and tidal features is also dependent on the mass ratio between both progenitors. Furthermore, the geometry of the merger plays a role, i.e., under what angle do the galaxies merge and how do they rotate. The rotation direction, e.g., has influence on the merger time and the formation of tidal tails.

In the following, the different possibilities for mergers are summarised, depending on the galaxy types involved.

- **ULIRGs:** Mergers between two large gas-rich disk galaxies are most probably the cause of Ultra-Luminous Infrared Galaxies, so-called ULIRGs. This kind of merger is often called *major merger*. These objects are among the most prominent sources found within the IRAS survey (Sanders & Mirabel (1996)) and were not known so far. Optical follow-up observations revealed host spiral galaxies clearly interacting. The gas of the two galaxies involved is being concentrated during the merger process and thus might lead to an enormous starburst in the central few hundreds of parsec. The UV photons of the young hot stars are absorbed by dust, which therefore is heated and becomes a very strong radiator in the far-infrared (FIR). Typical FIR luminosities are larger than $10^{12} L_{\odot}$. However, since two large disk galaxies are needed as progenitors, ULIRGs are rather rare in the local Universe. Prominent examples for disk–disk mergers resulting in a ULIRG are Arp 220, Arp 299 and Mrk 231.
- **Minor Mergers** There is not a clear definition of minor mergers, as in the case for major mergers. In the literature, mostly this term is used for a merger with one partner being a dwarf galaxy. Most large galaxies are believed to have undergone a minor merger event at least once in the past. Our own galaxy is currently absorbing the Sagittarius Dwarf Spheroidal (first reported by Ibata et al. (1994)). This, however, does not seem to influence the Milky Way seriously. Minor merger events are believed to be a common phenomenon, which does not change the large merging partner globally, but might have local consequences like enhanced star formation in parts of the disk, triggering a warp or other asymmetries commonly found in (spiral) galaxies. Furthermore, the disk can be heated by the infall of a small satellite, which can lead to the often observed thickening of the disk (Benson et al. (2004)).
- **S+E mergers** Mergers between an Elliptical and a Spiral are only poorly studied so far. In fact, Ellipticals are not implemented in most simulations, because it is difficult to simulate a three-dimensional spheroidal object consisting of particles with a random movement. Because Ellipticals typically host only little cold gas, it is very likely that an enormous starburst, as in the case of ULIRGs, does not occur in S+E mergers. In fact, it is unclear, if a starburst is induced by the merger at all. The few existing theoretical models make different predictions, which are later discussed in more detail (see Ch. 1.3). Because of the large fraction of (small) Spirals and Ellipticals, this class of mergers is potentially important for galaxy evolution in the local universe.
- **E+E mergers** Mergers between two elliptical galaxies are rarely a topic of interest in the literature. The most obvious reason is the same as for the S+E mergers, that they are not expected to be interesting, because only little gas is involved, thus no

starburst can be expected which will change the appearance, the stellar populations and the chemical composition of the ISM significantly. However, recent simulations by Naab et al. (2006) show, that some photometric and kinematic properties of massive Ellipticals can be more easily explained by E+E mergers than by mergers between two spirals, which are commonly accepted as the origin of Ellipticals.

It is believed that elliptical galaxies, esp. large ones, are the result of ULIRGs, and maybe also of S+E (and E+E) mergers. Often, faint shells are found around Ellipticals, which might be the last witnesses of the past collision (e.g., Malin & Carter (1983)). Furthermore, simulations predict a spheroidal stellar distribution, once the stellar motions are thermalised. However, in this picture it is difficult to explain why Ellipticals are typically red, i.e., they consist of old stars, whereas mergers are found at all redshifts, which implies a smooth age distribution of Ellipticals as the potential merger remnant. Another interesting point is the fact, that most of the Ellipticals are poor of cold gas, maybe because all gas was used for star formation in the past, but there also exist Ellipticals which show a complex gas distribution (e.g, NGC 5128, Charmandaris et al. (2000)). Possibly, several processes result in elliptical galaxies.

1.3 Recent S+E merger models

Despite their potential importance, S+E mergers are lacking a detailed systematic study. Two main models exist in the literature, which describe the merger event between an Elliptical and a Spiral (Weil & Hernquist (1993) and Kojima & Noguchi (1997)). In Fig. 2 and Fig. 3 the simulations for one merger scenario considered by both groups are shown for the stellar distribution. The models are in good agreement, both predicting the formation of tidal features like one tail and shells on the opposite side, in particular for a radial encounter. This morphology is in fact very typical for S+E mergers and might be used to identify them, even if the merger is too advanced to classify the progenitor galaxies any more (which would be of course the most convincing way to identify an S+E merger). Interestingly, the models make however contradictory predictions concerning the occurrence of a starburst. The differences between these models come from the way the gaseous component is simulated. In principle, there are two approaches:

1. *Smoothed particle hydrodynamics (SPH)*: SPH is used by Weil & Hernquist (1993) to simulate the behaviour of the gas in S+E mergers. The advantage of SPH lies in the easy realisation in three dimensions while still being computationally efficient. The basic idea is, that the fluid is represented by a large number of particles, which, however, move freely under self-gravitation and pressure forces (Monaghan (1992), Rasio (2000)). Thus, no grids or meshes are needed. Instead, spatial derivations are calculated from the particle positions by the determination of a pressure gradient. Using a Lagrangian formulation, the equation of motion of the particles can be expressed with the Euler equation

$$\frac{d\vec{v}}{dt} = \frac{\partial\vec{v}}{\partial t} + (\vec{v} \cdot \nabla)\vec{v} = -\frac{\nabla p}{\rho} \quad (1)$$

which describes the conservation of momentum as a differential equation. Furthermore, it holds

$$\frac{d\vec{r}}{dt} = \vec{v} \quad (2)$$

Here, \vec{r} and \vec{v} are the position and the velocity of each particle, ρ the density of the gas and p the pressure. The Lagrangian function, written in a discrete representation because of accounting for a finite number of particles, can be written as

$$L = \sum_{i=1}^N m_i \left[\frac{1}{2} \cdot v_i^2 - \frac{p}{(\gamma - 1) \cdot \rho} \right] \quad (3)$$

with γ being the adiabatic exponent. To solve the equation with SPH, a differentiable interpolant of the density has to be defined. This is done with the help of a differentiable smoothing kernel $W(\vec{r}, h)$ of the width $\sim h$:

$$\rho(\vec{r}) = \sum_i m_i \cdot W(\vec{r} - \vec{r}_i, h) \quad (4)$$

The interpolating kernel must have the properties that it integrates to unity (i.e., the integral over the density gives the total mass) and for the limit of $h \rightarrow 0$, W becomes the Dirac delta function $\delta(\vec{r})$. Typically, for a physical interpretation, a Gaussian is used (written here for the one-dimensional case):

$$W(r, h) = \frac{1}{h \cdot \sqrt{\pi}} \cdot e^{-(r^2/h^2)} \quad (5)$$

In a full implementation of SPH, an additional term for artificial viscosity is introduced to allow for the presence of shock waves. Self-gravity is taken into account with the combination of the classical SPH and new algorithms for N-body simulations like the hierarchical tree method, which also works without gridding. This approach is realised e.g. by Hernquist & Katz (1989) in TREESPH.

2. *Sticky Particle Method*: The sticky particle method is used by Kojima & Noguchi (1997). In this approach, the gas is treated as individual gas clouds, which move on ballistic orbits around the center of a galaxy, independent of any intercloud medium. In the models first described by Roberts & Hausman (1984), the gravitational potential $U(r, \theta, t)$ of a two-dimensional perturbed disk (following Roberts et al. (1979)) is:

$$U(r, \theta, t) = U_0(r) \cdot (1 + \zeta(r) \cdot \cos[2 \cdot \theta - 2 \cdot \Omega_p \cdot t + \Phi(r)]) \quad (6)$$

Here, Ω_p is the constant pattern speed of the perturbations, θ and r the coordinates of the two-dimensional disk. $U_0(r)$ is the so-called Toomre-disk (defined by Toomre (1963)), describing an unperturbed axisymmetric disk potential (with a and B constant parameters):

$$U_0(r) = - \frac{B^2 \cdot a^2}{\sqrt{a^2 + r^2}} \quad (7)$$

The amplitude of a (spiral) perturbation $\zeta(r)$ is defined by Roberts & Hausman (1984) as the following (with A a constant parameter):

$$\zeta(r) = \frac{A \cdot a^2 \cdot r^2}{5 \cdot (a^2 + r^2)^2} \quad (8)$$

The phase of maximum perturbation is determined by

$$\Phi(r) = \frac{2 \cdot \ln[1 + (r/r_0)^j]}{j \cdot \tan i_0} \quad (9)$$

This formula describes a pattern which is bar-like for $r < r_0$ and spiral-like at larger distances, with a pitch angle i_0 . The sharpness of the transition from the bar-like to the spiral-like feature is determined by the power j .

To account for the dissipative nature of the interstellar medium, gas cloud collisions are treated inelastically, changing the mutual radial velocity component while the tangential component is not affected. Beside collisions, the velocity of an individual cloud can be changed by the interaction with an expanding supernova remnant, which in the models give an extra randomising effect on the cloud velocity.

There are three main advantages over the fluid description of the ISM, as argued by Roberts & Hausman (1984). First, in the fluid description, it is assumed that in all volume elements there exists a sufficient large number of particles, but in reality star formation mainly takes place in giant molecular clouds, which are not very frequent. Thus, small number statistics effects may appear locally, and those are implemented in the models of Roberts & Hausman (1984). Second, in the fluid approach cooling and heating are typically treated locally. But due to the long time scales between star formation and supernovae explosions as well as the long free path, non-local energy transport in the ISM can occur in the sticky particle models. And finally, in contrast to the fluid models, the sticky particle approach can account for self-propagating star formation. This is done by converting cloud particles with a given probability into stellar particles, simulating an association of protostars. After a delay-time, the association produces a supernova event, which might affect other clouds (see above), changing the other clouds' properties and thus possibly inducing a new star formation event.

The differences in the simulation of the gas have severe consequences on the behaviour of the gas, in particular the development of the distribution with time. This can be seen in Fig. 4 and Fig. 5, which show the results of the simulations for the gas component in a radial merger. Weil & Hernquist (1993) find a quick segregation between gas and stars, i.e., the distributions of gas and stars are quickly different. In contrast to the stars, which form extended tidal features like a tidal tail and shells (see Fig. 2), the gas becomes concentrated in the new nuclear region, where a starburst might occur due to the high gas density. Their results are thus similar to what is found in ULIRGs, in which the gas is concentrated on some few 100 pc and which therefore undergo an extreme starburst phase. Of course one has to keep in mind that in the case of ULIRGs two large gas-rich Spirals are involved, whereas in an S+E merger at least one partner (the Elliptical) might contribute only little gas. Thus, even if the distribution of the gas is similar in both merger kinds, the strength of the burst can be different because of the different absolute amount of gas involved.

In contrast to these predictions, the simulations run by Kojima & Noguchi (1997) show a different picture. The cloud particles develop a similar morphology as the stellar component, showing a multiple shell system for more than a Gyr. The reason for this behaviour lies in the reduction of gas cloud collisions after the galaxy encounter. The gas disk of the Spiral is basically destroyed and its material scattered by the center of the Elliptical and dispersed into a large volume. Thus, the gas clouds behave similar to the stars after the encounter, therefore forming the same structures. The gas scattering has another consequence which is in disagreement with the predictions of Weil & Hernquist (1993). No period of enhanced star formation is possible, because the gas density always remains too low. Kojima & Noguchi (1997) argue, that the star formation is damped several 10^8 yr before shells develop, thus maybe mimicking a 'poststarburst' nucleus, which is found in some shell galaxies (Carter

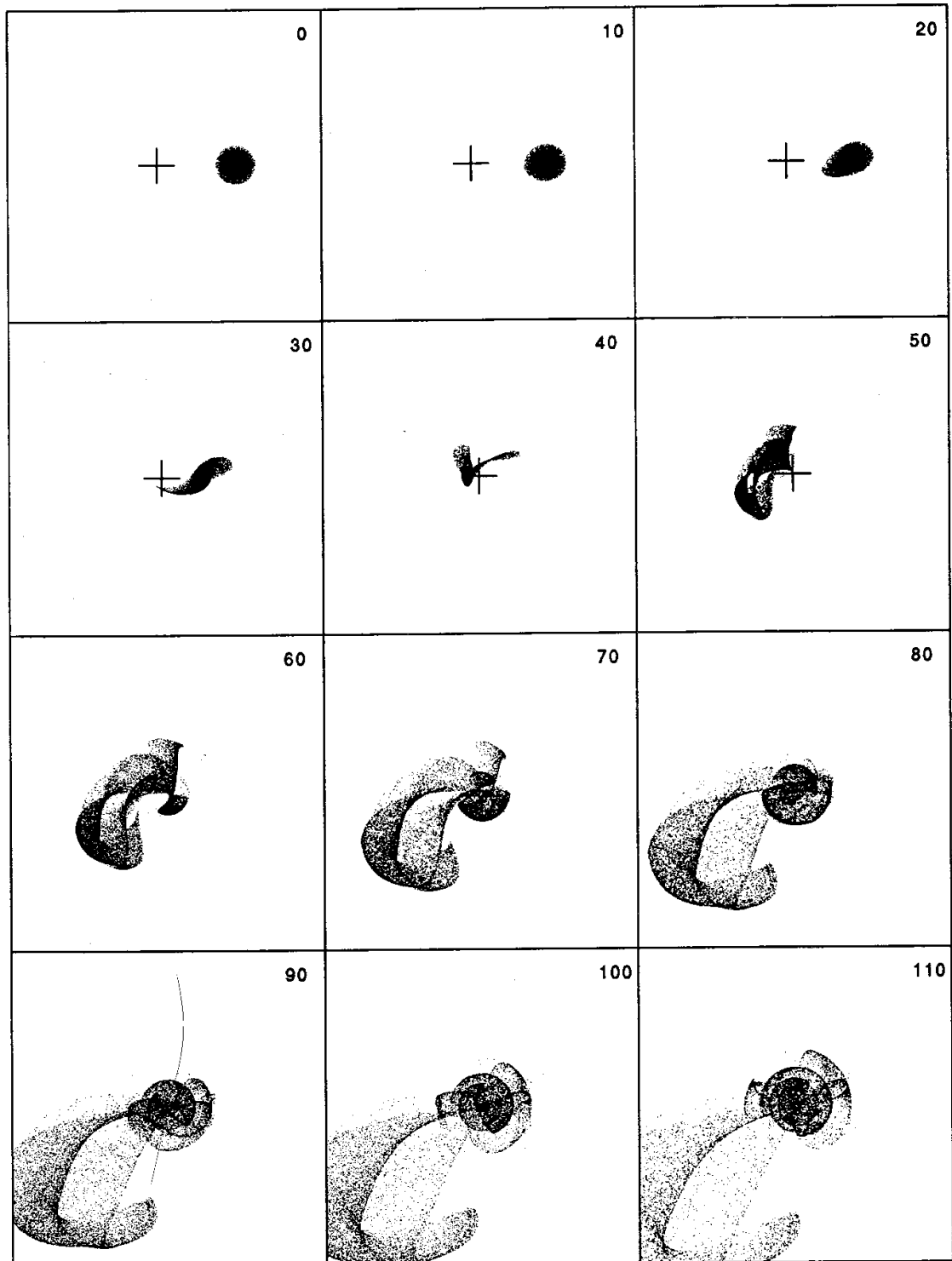


Figure 2: Simulations of the stellar component distribution during a radial S+E merger event by Hernquist & Weil (1992). The stellar mass ratio of the Elliptical and the companion disk galaxy is 10:1. One time unit corresponds to $\sim 4 \cdot 10^6$ yr.

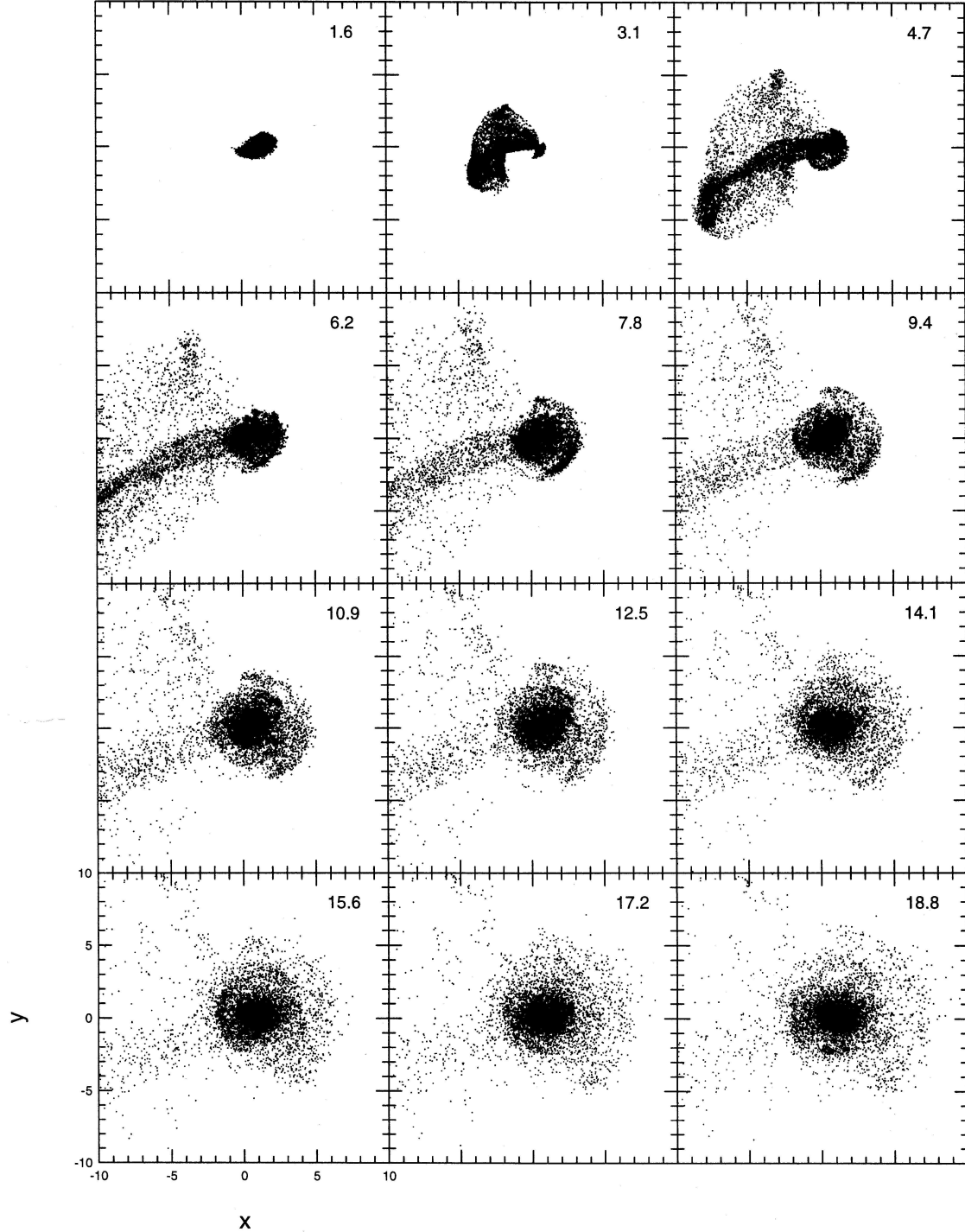


Figure 3: Simulations of the stellar component distribution during a radial S+E merger event by Kojima & Noguchi (1997). The stellar mass ratio of the Elliptical and the companion disk galaxy is 10:1. One time unit corresponds to $\sim 10^8$ yr.

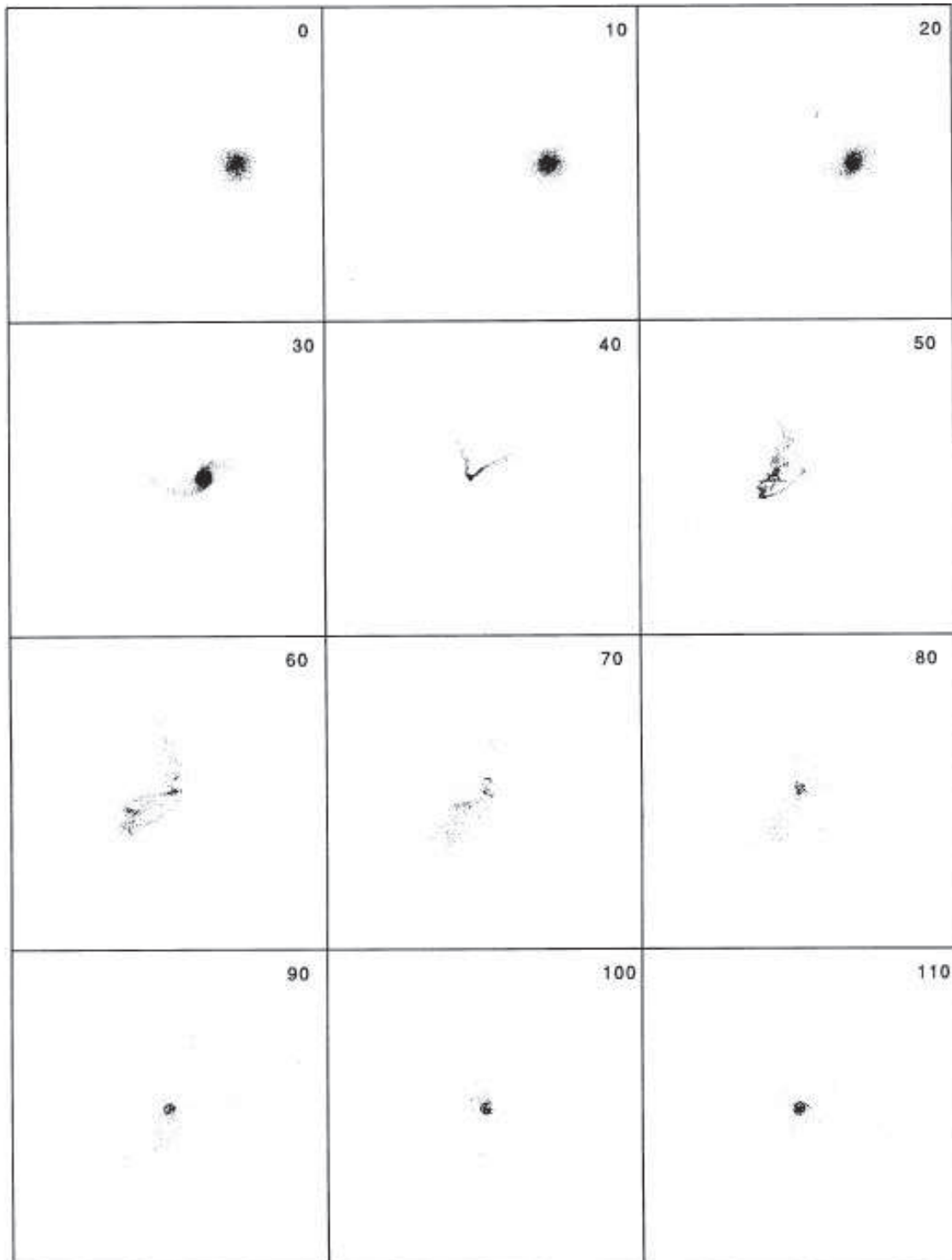


Figure 4: Simulations of the gaseous component distribution during a radial S+E merger event by Weil & Hernquist (1993). The properties of the merger are the same as in Fig. 2. The gas mass of the disk galaxy is 1/10 of the stellar mass. One time unit corresponds to $\sim 4 \cdot 10^6$ yr.

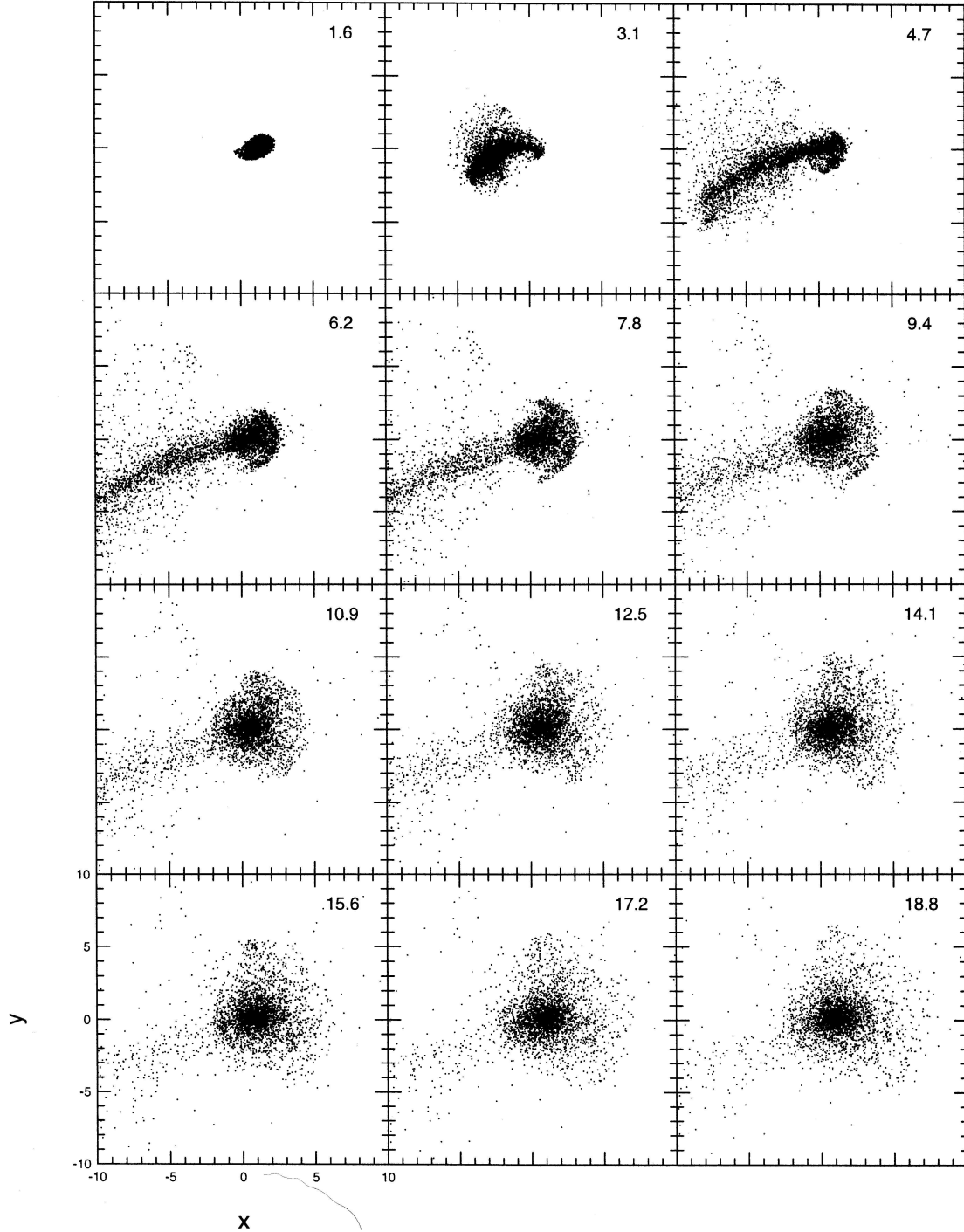


Figure 5: Simulations of the gaseous component distribution during a radial S+E merger event by Kojima & Noguchi (1997). The properties of the merger are the same as in Fig. 3. The gas mass of the disk galaxy is 1/10 of the stellar mass. One time unit corresponds to $\sim 10^8$ yr.

et al. (1988)).

As mentioned by Kojima & Noguchi (1997), it is not clear until now, which approach for the gas simulation is a more realistic description. Considering the enormous differences in the predictions and the consequences for the evolution of (not only) S+E mergers, it is worth to investigate in particular the interstellar medium and the star formation behaviour of those galaxies to better understand the processes during the mergers and apply what is learned to the numerical simulations.

Observations of the prototypical S+E merger candidate NGC 4194 reveal a complex situation in this mergers, neither properly described by the models of Weil & Hernquist (1993) nor Kojima & Noguchi (1997). In this galaxy, a starburst is found along with extended molecular gas and a clear shell structure (Weistrop et al. (2004), Aalto & Hüttemeister (2000)). Obviously, a more detailed study of a sample of S+E merger candidates is necessary to bring light into the nature of those mergers.

1.4 Outline of the thesis

This thesis concentrates on mergers with a moderate FIR luminosity ($< 10^{11} L_{\odot}$, i.e. no ULIRGs) which are possible candidates for S+E mergers. In this work, a multiwavelength investigation of a sample of moderate luminosity mergers was obtained to analyse both the stellar and gaseous component. This approach allowed to study the morphology and distribution of the stars, also with respect to different stellar populations, the estimation of the star formation rate (thus to answer the question: does a starburst occur in such mergers?), to search for molecular gas which can fuel a burst, and to analyse the atomic gas which reflects best the interaction history. The distribution of the gas is of particular interest in the context of the different predictions of the numerical simulations. Observations of a sample might therefore be used to narrow the parameter space for the simulations to improve the predictions. A description of how to study the physical properties by the observations presented here is given in Ch. 2.

The data and the results are presented in the following four chapters.

Ch. 3 gives an introduction to the sample, how it is selected and what the galaxies look like in the optical and near-infrared. Optical and near-infrared imaging as well as optical spectroscopic data are presented in this chapter. By multicolour imaging it is possible to give a detailed compilation of the present tidal features, to trace the distribution of the stellar populations and the dust. Radial profiles were extracted to analyse the general stellar distribution (e.g., searching for a rather disk-like distribution versus a distribution typical for Ellipticals, under consideration of disturbances due to the tidal features). Optical spectra were used to derive the ongoing star formation rate.

The gas content of the two most prominent examples of the sample is furthermore analysed in detail. These two chapters will be submitted in similar form to A&A.

In Ch. 4 the HI and CO results of NGC 4441, which is an excellent example of a strong S+E merger candidate, are shown. In addition to the CO(1–0) observations obtained for the other galaxies of the sample, also the transition (2–1) was observed in this galaxy, as well as the isotope ^{13}CO (in both the (1–0) and (2–1) transitions). With these data, it is possible to get hints of the temperature and density of the molecular ISM, which is then discussed with respect to the question of ongoing star formation and merger state. HI data of the prototypical S+E merger candidate, NGC 4194, are presented in Ch. 5. This work was done in collaboration with S. Aalto and C. Horellou from the Onsala Space Observatory, Sweden.

The results of the study of the gas content of the remaining galaxies are given in Ch. 6. Interferometric HI data as well as single-dish CO data are presented here. The CO observations allow the estimation of the total amount of molecular gas, which forms the reservoir for star formation. The HI data are very well suited to study the distribution and kinematic of the atomic gas, which is most sensitive to interaction. Most of the observed galaxies show a complex and extended HI structure with a variety of tidal features. However, they cover a broad range of HI mass.

Finally, in Ch. 7 all results are discussed comprehensively to get a rounded view of moderate luminosity mergers. The observed variety of different properties is summarised, with special emphasis on the occurrence of a starburst.

References

- Aalto, S. & Hüttemeister, S. 2000, *A&A*, 362, 42
- Arp, H. 1966, *ApJS*, 14, 1
- Barnes, J. E. 1994, in *The Formation and Evolution of Galaxies*, 399
- Barnes, J. E. & Hernquist, L. E. 1991, *ApJ*, 370, L65
- Benson, A. J., Lacey, C. G., Frenk, C. S., Baugh, C. M., & Cole, S. 2004, *MNRAS*, 351, 1215
- Bunn, E. F. & Sugiyama, N. 1995, *ApJ*, 446, 49
- Burkert, A. & Naab, T. 2003, *LNP Vol. 626: Galaxies and Chaos*, 626, 327
- Carter, D., Prieur, J. L., Wilkinson, A., Sparks, W. B., & Malin, D. F. 1988, *MNRAS*, 235, 813
- Charmandaris, V., Combes, F., & van der Hulst, J. M. 2000, *A&A*, 356, L1
- Hernquist, L. 1993, in *ASSL Vol. 188: The Environment and Evolution of Galaxies*, ed. J. M. Shull & H. A. Thronson, 327
- Hernquist, L. & Katz, N. 1989, *ApJS*, 70, 419
- Hernquist, L. & Weil, M. L. 1992, *Nature*, 358, 734
- Hibbard, J. E. & Mihos, J. C. 1995, *AJ*, 110, 140
- Hibbard, J. E. & Sansom, A. E. 2003, *AJ*, 125, 667
- Hibbard, J. E., Vacca, W. D., & Yun, M. S. 2000, *AJ*, 119, 1130
- Hibbard, J. E. & van Gorkom, J. H. 1996, *AJ*, 111, 655
- Hibbard, J. E. & Yun, M. S. 1999a, *AJ*, 118, 162
- . 1999b, *ApJ*, 522, L93
- Holmberg, E. 1941, *ApJ*, 94, 385

- Ibata, R. A., Gilmore, G., & Irwin, M. J. 1994, *Nature*, 370, 194
- Kennicutt, R. C. 1998, in *Saas-Fee Advanced Course 26: Galaxies: Interactions and Induced Star Formation*, 1
- Khochfar, S. & Burkert, A. 2003, *ApJ*, 597, L117
- Kofman, L. A., Gnedin, N. Y., & Bahcall, N. A. 1993, *ApJ*, 413, 1
- Kojima, M. & Noguchi, M. 1997, *ApJ*, 481, 132
- Larson, R. B. & Tinsley, B. M. 1978, *ApJ*, 219, 46
- Malin, D. F. & Carter, D. 1983, *ApJ*, 274, 534
- Monaghan, J. J. 1992, *ARA&A*, 30, 543
- Naab, T. & Burkert, A. 2000, in *ASP Conf. Ser. 197: Dynamics of Galaxies: from the Early Universe to the Present*, ed. F. Combes, G. A. Mamon, & V. Charmandaris, 267
- Naab, T. & Burkert, A. 2001, in *ASP Conf. Ser. 230: Galaxy Disks and Disk Galaxies*, ed. J. G. Funes & E. M. Corsini, 453–454
- Naab, T., Khochfar, S., & Burkert, A. 2006, *ApJ*, 636, L81
- Rasio, F. A. 2000, *Progress of Theoretical Physics Supplement*, 138, 609
- Roberts, W. W. & Hausman, M. A. 1984, *ApJ*, 277, 744
- Roberts, W. W., Huntley, J. M., & van Albada, G. D. 1979, *ApJ*, 233, 67
- Sanders, D. B. & Mirabel, I. F. 1996, *ARA&A*, 34, 749
- Schweizer, F., Seitzer, P., Faber, S. M., Burstein, D., Dalle Ore, C. M., & Gonzalez, J. J. 1990, *ApJ*, 364, L33
- Spergel, D. N., Bean, R., Dore, O., Nolta, M. R., Bennett, C. L., Hinshaw, G., Jarosik, N., Komatsu, E., Page, L., Peiris, H. V., Verde, L., Barnes, C., Halpern, M., Hill, R. S., Kogut, A., Limon, M., Meyer, S. S., Odegard, N., Tucker, G. S., Weiland, J. L., Wollack, E., & Wright, E. L. 2006, *ArXiv Astrophysics e-prints*
- Steinmetz, M. 2003, *Ap&SS*, 284, 325
- Toomre, A. 1963, *ApJ*, 138, 385
- Toomre, A. 1977, in *Evolution of Galaxies and Stellar Populations*, 401
- Toomre, A. & Toomre, J. 1972, *ApJ*, 178, 623
- Vorontsov-Velyaminov, B. A. 1959, in *Atlas and catalog of interacting galaxies (1959)*, 0
- Weil, M. L. & Hernquist, L. 1993, *ApJ*, 405, 142
- Weistrop, D., Eggers, D., Hancock, M., Nelson, C. H., Bachilla, R., & Kaiser, M. E. 2004, *AJ*, 127, 1360
- White, S. D. M. & Frenk, C. S. 1991, *ApJ*, 379, 52

2 Studying the Physical Properties of Galaxies

Abstract

The individual components of galaxies, e.g., the stellar populations, the interstellar gas and the dust, can be studied using different wavelength windows. In the following, some analysis techniques are introduced, which are used in this thesis. Included are methods to investigate the morphology and stellar population distribution, the estimation of the star formation rate, the study of the interstellar medium and the analysis of HI imaging as a tracer of the merger history.

To understand a galaxy as a whole, it is necessary to study all components, with special emphasis on the interplay between them. For example, the analysis of a star forming galaxy cannot be restricted to the investigation of the ongoing star formation, but one has to consider as well the gas reservoir to form new stars, in particular the gas density influenced by the merger. In the following subsections, a short description is given about the methods used in this work to study the interstellar medium and the stars of the moderate luminosity merger sample. This covers techniques to investigate the morphology and distribution of different kind of stars, in particular star forming regions like HII regions, the star formation history based on optical spectra, the molecular gas content, the atomic gas distribution and the properties of the ISM.

2.1 The Distribution of Stars – Insights from the Optical and NIR

The global distribution of stars can be studied by investigating optical and near-infrared images. In principle, optical emission, particularly in the U and B band, is sensitive to hot, young stars, whereas redder filter bands, in particular the near-infrared bands show the distribution of the old underlying population. Thus, one can expect to find differences in the morphology of a galaxy when looking at different filters. These differences are of particular interest in this thesis, because they might reflect the merger history (from the point of view of the stellar components). The morphology of galaxies can be studied in several ways. A common way to describe the stellar distribution is to create radial surface brightness profiles visualising the surface brightness dependence on the radial distance from the center. With the resulting profiles one can give a morphological classification of the galaxy type, at least for undisturbed galaxies. The surface brightness $\mu(R)$ in disk galaxies typically follows an exponential decrease (Freeman (1970)):

$$\mu(R) = \mu(0) \cdot \exp(-R/h_R) \quad (10)$$

Here, h_R is the so-called scale length. The inner part has to be excluded from this expression due to a surface brightness bump coming from the bulge component. In contrast, Ellipticals follow the so-called de Vaucouleur law ($r^{1/4}$ law) (de Vaucouleurs (1948)):

$$\mu(R) = \mu(R_e) \cdot \exp[(R/R_e)^{1/4}], \quad (11)$$

with R_e the effective radius which includes half of the light of the galaxy. In general, radial profiles can be described by the so-called Sersic-profile (Sersic (1968)):

$$\mu(R) = \mu(0) \cdot \exp[-(R/R_0)^{1/n}] \quad (12)$$

If the exponent has a value of $n = 1$, then the expression is equal to the exponential decrease of a pure galactic disk. If $n = 4$, then the Sersic-law is identical with the de Vaucouleur

law. Especially in merger systems, it is unlikely that the stellar distribution follows either a pure disk or pure elliptical distribution. Thus, the Sersic profile is best suited to account for symmetric deviations from the classical profiles.

Furthermore, it is valuable to account for asymmetric features when deriving radial profiles. In the following, two methods used in this work for radial profile extraction are summarised.

1. *Ellipse fitting:* If the morphology of a galaxy is roughly elliptical, an easy way to derive radial profiles is by fitting ellipses to the surface brightness distribution with a fixed stepsize. This is a commonly used method implemented in the established imaging reduction softwares like IRAF and MIDAS. Typical outputs are, besides the integrated intensity, the major and minor axes (A and B) and the position angle of the fitted ellipses. It is reasonable to calculate an equivalent photometric radius $R = \sqrt{A \cdot B}$. Irregularities in the morphology as well as fore- and background sources can lead to large uncertainties. Thus, this method can only be used with caution for merging galaxies, which show a highly disturbed and peculiar appearance.
2. *Pixel summation:* This method accounts better for morphological irregularities and is described in Papaderos et al. (1996) and Noeske (1999). In this approach, all pixels within a given surface brightness limit are counted, and the intensity threshold is decreased with a given stepsize. The equivalent photometric radius is calculated as $R = \sqrt{\#pixels \cdot pixscale^2 / \pi}$. It can be appropriate to smooth the image with a Gaussian before pixel summation to account for small scale variations in the morphology due to noise.

It is instructive to build a model galaxy with the help of the fitted ellipses and subtract this model from the real image. Deviations from the model give a hint of additional structures which might be formed during the merger.

In the case of merger studies, deviations from the symmetric star distributions (disks or spheroidals) are of special interest. In a qualitative way, this can be done by examining peculiar morphological features like tails, shells and plumes. Often, these features are faint and found in the outskirts of galaxies, thus, deep images are inevitable for morphological investigations. An alternative to visualise differences depending on the position angle is the conversion of cartesian images to polar coordinates. In these images the x axis represents the distance from the center, the y axis the position angle. Asymmetries with respect to the radial distance can be immediately seen when looking at each column in those images. A second useful tool to highlight in particular faint features is enhancing the contrast of the image, e.g., using the *unsharp masking* technique (e.g., Gonzalez & Woods (1992) and realised by Aronica (2006)). In this method, small structures are emphasised using a highpass filter (which amplifies high frequency variations like morphological structures). This is accomplished by subtracting a smoothed, i.e., blurred, image from the original one.

Morphological differences between two filters originate in first order from differences in the age of the mean population. Discrepancies can be visualised efficiently by creating colour-maps, i.e. either divide intensity images or subtract magnitude images of different filter bands, e.g. B–R. Bright blue regions are typically regions with hot young stars, whereas redder parts represent older stars. However, this basic view can be extremely influenced by dust, which reddens the stellar light due to extinction. Near-infrared images are in this case especially useful because they are not sensitive to dust due to the longer wavelengths and allow to look through dust clouds, at least in case of moderate density. However, there is a second aspect

which leads to an intrinsic reddening of the stellar light apart from dust. Metallicity differences are also reflected in different colours (for the same spectral type). This phenomenon is known as *age-metallicity degeneracy*. This means, that it is very difficult to distinguish differences in age from differences in metal abundances using colours (and optical spectra!). In a merger, colour differences can either point to two different populations from the progenitors which have different metallicities or, in addition to the old stars from the progenitors (assuming they have similar metal abundances), they point to a second, younger stellar component formed during the merger process. It is worth to mention that there exists also a *age-burst strength degeneracy*, which makes it difficult to distinguish between recent weak and older strong starbursts. This degeneracy further complicates the analysis of the star formation history of merger systems (e.g., Kennicutt (1998a)).

2.2 The Star Formation Rate

To determine the star formation rate (SFR), ideally one would study the stars individually, e.g. by measuring magnitudes and fitting isochrones to the resulting colour-magnitude-diagrams. This is, however, only possible in the case of nearby galaxies, where individual stars can be resolved. In most cases, as in this work, it is only possible to measure integrated colours and spectra, which show the dominating population within the covered region.

To get a spectrum, the most commonly used method is to obtain longslit spectroscopy to get a spectrum of the region of interest, e.g., the nucleus. This can be very efficient, depending on the brightness of the source. However, in the case of the sample presented here, the objects are extended over several arcminutes on the sky plane. In this case, a single observation covers only a small part of the galaxy. Therefore, one cannot study the populations within the whole galactic body, but only local populations with one spectrum. Taking several longslit spectra along the galaxy is possible in principle, but is very time-consuming, in particular for a larger sample.

A second sophisticated method is the so-called driftscan spectroscopy, invented by Kennicutt (1992). Here, the slit is moved over the region of interest, e.g., the galaxy body, in several cycles while the light is integrated. This leads to a single spectrum of the whole galaxy. The resulting spectrum shows a mix of all stellar populations present and is not affected by local variations as in the case of the longslit spectrum. Information about the spatial distribution of different populations, however, cannot be gathered this method (which, in contrast, could be achieved when using several longslit spectra). In this work, we obtained both driftscan spectra and long-slit spectra of the nuclei to find differences between the populations in the centers of the galaxies (where a starburst might occur) and the overall dominating populations.

The SFR can be estimated by several tracers found over a broad wavelength range. Three possibilities, which are all used in this work, are listed in the following:

1. *optical recombination lines*: It is possible to use nebular lines, e.g., the $H\alpha$ line, as an estimator of the ongoing star formation in a galaxy, because this emission comes from gas which is ionised by hot young stars. Typically, only stars with masses $> 10 M_{\odot}$ (lifetime < 10 Myr) contribute significantly to the ionising flux. The conversion factor between, e.g., the $H\alpha$ flux and the star formation rate is usually derived by the usage of population synthesis codes. Obviously, the factor is dependent on the metal abundance and initial mass function used in those codes. A commonly used relation between the detected $H\alpha$ flux and the current star formation rate, assuming solar abundance and Salpeter IMF

($0.1 - 100 M_{\odot}$), is given by Kennicutt (1998b):

$$\text{SFR}_{\text{H}\alpha} (M_{\odot}/\text{yr}) = 7.9 \times 10^{-42} L_{\text{H}\alpha} (\text{erg/s}) \quad (13)$$

Of course, it is necessary to correct for extinction by dust which might dim the optical light. This can be done by using the Balmer decrement $c(\text{H}\beta)$, which is the logarithmic ratio of $\text{H}\alpha$ and $\text{H}\beta$ (see Osterbrock (1989), p.202ff):

$$c(\text{H}\beta) = \frac{-1}{-0.37} \cdot [\log(\frac{I(\text{H}\alpha)}{I(\text{H}\beta)}) - \log(2.76)] \quad (14)$$

Here, $I(\text{H}\alpha)$ and $I(\text{H}\beta)$ are the measured line intensities in the observed spectrum. With the Balmer decrement it is possible to determine the visual extinction (using extinction curves) and finally deredden the observed spectrum. This can be done, e.g., with the IRAF task *deredden*. The dereddened spectrum can then be used to estimate the star formation rate by measuring the extinction corrected $\text{H}\alpha$ intensity $I(\text{H}\alpha, 0)$. The $\text{H}\alpha$ luminosity $L_{\text{H}\alpha}$ is defined as:

$$L_{\text{H}\alpha} (\text{erg/s}) = 4 \cdot \pi \cdot D (\text{cm})^2 \cdot I(\text{H}\alpha, 0) (\text{erg/s/cm}^2) \quad (15)$$

Note, that the distance of the object D has to be given in cm for unit consistency; 1 pc corresponds to $3.086 \cdot 10^{18}$ cm.

2. *Far infrared:* As already mentioned, interstellar dust absorbs a large fraction of the stellar light. Its absorption cross section is largest in the ultraviolet, i.e., for the light from hot, young stars. The dust re-emits the radiation in the far infrared. Thus, the infrared emission of galaxies is correlated with the amount of newly formed stars and can be used as a tracer of star formation. A correlation between the SFR and the FIR flux is again dependent on the synthesis models used, the assumed IMF and other parameters like the star formation time scale. An often used relation is given by Kennicutt (1998c):

$$\text{SFR}_{\text{FIR}} (M_{\odot}/\text{yr}) = 0.17 \cdot 10^9 L_{\text{FIR}} (L_{\odot}) \quad (16)$$

In the literature, the definition of L_{FIR} is not always fixed. In most cases, as it is done in this thesis, the following relation is used:

$$L_{\text{FIR}} (L_{\odot}) = 1.26 \cdot 10^{-14} [2.58 \cdot f_{60} (\text{Jy}) + f_{100} (\text{Jy})] \cdot 4 \cdot \pi \cdot D (\text{cm})^2 / 3.85 \cdot 10^{26} \quad (17)$$

Here, f_{60} and f_{100} are the IRAS fluxes at $60 \mu\text{m}$ and $100 \mu\text{m}$, respectively, and D denotes again the distance of the object. One has to be somewhat careful with this method, because in general the thermal emission in the FIR has its origin in three major processes. First, as mentioned, the emission comes from dust which is heated by the young stars, e.g., OB stars (Devereux & Young (1990), Devereux & Hameed (1997)). This is the most important fraction in luminous IR starbursts, where the SFR estimated from the FIR flux is nicely correlated with the SFR based on $\text{H}\alpha$. A second part comes from circumstellar envelopes of red giants and other evolved stars which undergo a phase of enormous mass loss (Knapp et al. (1992), Mazzei & de Zotti (1994)). Finally, so-called diffuse "cirrus" emission is found in galaxies, which comes from dust within the optically thin ISM and is heated by the stellar radiation field. To use the FIR flux as an indicator of the ongoing star formation, often the assumption is

made that only the first described process plays a significant role, i.e., the young hot stars dominate the radiation field, and that the dust opacity is infinite throughout the galaxy. Unfortunately, until now it is not clear how good these assumptions are for all types of galaxies. For (dusty) starbursts this correlation works nicely, however when going from late-type to early-type galaxies, the other two processes become more and more important and the dust opacity may decrease as well.

3. *Radio continuum*: It is possible to estimate the SFR from radio emission, e.g., the 20 cm continuum flux density. The relation between star formation and the flux density is, following Condon (1992) and Haarsma et al. (2000):

$$\text{SFR}_{20\text{ cm}}(\text{M}_{\odot}/\text{yr}) = 0.14 \cdot D(\text{Mpc})^2 \cdot F_{20\text{ cm}} \quad (18)$$

$F_{20\text{ cm}}$ is the flux density at 20 cm, D the distance of the object. This correlation is derived under the assumption, that the 20 cm continuum emission mainly comes from supernovae remnants (synchrotron emission) and thermal emission from HII regions. Both components are proportional to the high-mass star formation rate ($M > 5 \text{M}_{\odot}$). The advantage of this method compared with an optical star formation tracer is, as in the case of the far infrared method, the independence of dust extinction. Furthermore, when using the far infrared emission, in particular in major mergers it is also difficult to distinguish star formation from active galactic nuclei (AGN) as the original energy source. In principle, this problem can be solved when using several radio continuum frequencies and by inspecting the morphology at high resolution and the spectral index of the source.

It is important to note, that these indicators do not agree very well, because the emission at the different wavelengths has a different origin and may thus not be produced at the same time. But since they trace the same phenomenon in principle, they are correlated, even if the derived absolute values for the SFR differ. Until now, the relations between the tracers are not understood in detail.

For completeness, it has to be mentioned that there exist further more sophisticated stellar population analysis techniques. Depending on the expected complexity of the stellar population mix, one can analyse the data by comparing line ratios, e.g., Lick indices (Worthey et al. (1994), Trager et al. (1998)), or by comparing with model spectra as calculated with stellar synthesis models. In principle, with the latter method it is possible to reconstruct the full star formation history. However, it is necessary to keep in mind that those solutions are often ambiguous and depend on how complete our understanding of the stellar physics is and how to solve for various degeneracies. If a broad range of colours is available, it is also possible to compare them with modeled colours, but of course the results are less precise than those based on spectra.

The basic idea of Lick indices is to break the age–metallicity degeneracy by using ratios of emission lines of which one is age-sensitive and the other metallicity-sensitive, e.g. $\text{H}\beta$ and MgFe . However, Lick indices are not very useful for the analysis of mergers, since they are valid for single stellar populations only, which is most probably not realised in interacting galaxies due to induced enhanced star formation on top of an underlying older population. But, they could be used for age-determination of young globular clusters and tidal dwarf galaxies, which both can be formed during a merger event.

Various stellar synthesis codes exist in the literature, optimised for different wavelength

ranges, specific scenarios like starbursts, wavelength resolution and so on. Among those, the most commonly used codes are GALAXEV (Bruzual & Charlot (1993), Bruzual & Charlot (2003)), Starburst99 (Leitherer et al. (1999)) and PÉGASE (Fioc & Rocca-Volmerange (1997)).

2.3 Fuel of the Burst – the Molecular Gas

To form new stars, of course raw material, i.e., molecular gas, is needed. Star forming regions are embedded in molecular gas clouds, and stars in the making are usually found in the cores of initially cold and dense gas condensations. In starbursts triggered by a merger event, it is crucial to concentrate the molecular gas of the progenitors at least to a critical surface density $\Sigma_c = \alpha \cdot (\kappa \cdot \sigma) / (\pi \cdot G)$ (Kennicutt (1989), for a thin isothermal gas disk) to form instabilities and thus activate the star formation. In this equation, κ is the epicyclic frequency expressing the gyration of a particle with respect to the galaxy center. σ is the velocity dispersion of the gas, $\alpha \leq 1$ a dimensionless constant. If the gas becomes too dispersed, the gas density is too low to collapse and build star forming regions. In case the progenitors are gas-poor, there might not be enough gas even after concentration to induce enhanced star formation. Thus, the determination of the total amount of molecular gas is essential to investigate the potential for star formation, and, in combination with mapping, the spatial extent of a possible starburst. Furthermore, if the star formation history of a galaxy can be studied (e.g., by optical spectra), one gets hints about the gas content of the progenitors. For example, E+E mergers are intrinsically gas-poor and should not show any signs of enhanced star formation activity, whereas faded ULIRGs might host a moderate amount of gas, but show an extreme starburst in their recent history.

Due to the structural complexity of molecules (compared to atoms) several kinds of transitions have to be considered for observations. Electronic transitions with energies of a few eV can be observed in the ultraviolet and the optical. Vibrational transitions with typical energies of 0.01 – 0.1 eV lie in the infrared range, and rotational transitions with energies of a few 10^{-3} eV fall in the mm- and cm-regime. The transition is typically named according to the quantum numbers of angular momentum J of the transition involved, e.g., $J = 1 \rightarrow J = 0$ becomes the (1-0) transition, which is the lowest one. For dipole emission, the possible transitions are $\Delta J = -1$.

The by far most common molecule is molecular hydrogen H_2 . However, this molecule is difficult to detect, since it has no permanent electric dipole moment due to its symmetry. It is possible to observe H_2 directly in the ultraviolet and infrared (vibrational and rotational transitions), but the lines are often very weak, because they are excited only at high temperatures, and the observations are only possible using satellites.

An easier and more common way to investigate molecular hydrogen is to use other molecules as a tracer. Typically, ^{12}CO is used, since it is the second common molecule, however 10^{-4} times less frequent. The easiest way to study the CO lies in the observation of rotational transitions in the mm-range.

Although the $^{12}CO(1-0)$ line is typically optical thick, it is a good estimator for the total molecular mass. It is convenient to determine the column density of H_2 first, using the relation

$$N(H_2) = X_{CO} \cdot \int T_{MB} dv \cong X_{CO} \cdot T_{MB} \cdot \Delta v \text{ cm}^{-2} \quad (19)$$

with the main beam brightness temperature T_{MB} as the measured antenna temperature T_{A}^* corrected for the beam efficiency η . Δv is the line width. T_{MB} is a line temperature which includes beam dilution within the main beam. Thus, the column density is a value which is averaged over the entire main beam. In an extragalactic context and single-dish observations, the beam filling factor is usually quite small. The conversion factor $X_{\text{CO}} = I_{\text{CO}}/N(\text{H}_2)$ is still under discussion and one of the major uncertainties in molecular mass estimations. Several techniques are commonly used to estimate the conversion factor for both the Milky Way and nearby external galaxies, e.g., the correlation of CO with the optical extinction, the analysis of the $^{13}\text{CO}/^{12}\text{CO}$ line ratios, virial mass estimation of ^{13}CO and ^{12}CO clouds and comparison with γ -ray emission (Young & Scoville (1991)). For the calculations in this work the standard factor of $2.3 \cdot 10^{20}$ was used (Strong et al. (1988)). This is appropriate for disk galaxies with metallicities close to that of the Milky Way. In starbursts, X_{CO} tends to be smaller, while it is higher, at least globally, in metal poor dwarf galaxies (Arimoto et al. (1996)). The dependence on metallicity is, however, not entirely straightforward, since the real dependence is on τ , and selective photodissociation plays a major role. The area covered with the beamsize θ and with a given distance D (in cm) to the galaxy is $A \cong (\tan(\theta/2) \cdot D)^2 \cdot \pi$. Thus, the gas mass within the covered region and the estimated column density is

$$M_{\text{H}_2} = m(\text{H}_2) \cdot A \cdot N(\text{H}_2) M_{\odot} \quad (20)$$

where $m(\text{H}_2) = 1.68 \cdot 10^{-57} M_{\odot}$ is the mass of one H_2 molecule.

Other tracer molecules are used for a more detailed analysis of the molecular ISM. For example, HCN can be used as a tracer of dense gas, HNC is found in cold clouds but also in planetary nebulae and CN is possibly a good indicator of photon-dominated regions (PDRs).

Table 1: The CO lines and frequencies used in this work (Rohlfs & Wilson (2004)).

| line | rest frequency (GHz) |
|-----------------------|----------------------|
| $^{12}\text{CO}(1-0)$ | 115.271203 |
| $^{12}\text{CO}(2-1)$ | 230.538001 |
| $^{13}\text{CO}(1-0)$ | 110.201370 |
| $^{13}\text{CO}(2-1)$ | 220.398714 |

2.4 HI – Witness of the Interaction

The atomic gas is an ideal tracer to study interactions and/or merging, in particular when observed with interferometers. Typically, HI is distributed in a disk which is much more extended than the stellar component. Thus, especially the outskirts of the HI disk can be more easily gravitationally affected. Furthermore, line observations of HI do not only give information about the distribution, but also provide kinematical information. Often, gravitational influences in pairs and groups are seen in HI (e.g., tails, bridges), whereas in the stellar body no effects are visible, neither in morphology nor in enhancement of star formation.

Various studies of the HI distribution in galaxy groups and pairs exist in the literature (e.g., Smith et al. (1997), Koribalski et al. (2003), Gordon et al. (2003), Koribalski & Dickey (2004), Koribalski & Manthey (2005)). These examples show the formation of gaseous bridges as a consequence of a close encounter, which can contain a significant fraction of the HI present

in the encountering galaxies. In some cases, faint optical counterparts of the HI bridges are found. The analysis of the gaseous, and, if present, stellar material, which is stripped out during the encounter, gives clues to the interaction history. The most important parameters are, e.g., the timescales, the geometry and the impact parameter, i.e., the closest distance of the galaxies during the encounter. The formation of both kinds of bridges (with and without stellar component) are successfully modelled in the literature (e.g., Barnes & Hernquist (1991), Mihos & Hernquist (1996), Struck (1997)).

HI studies of infrared luminous galaxies by Hibbard & van Gorkom (1996) and Hibbard et al. (2000) reveal a diversity of gaseous and stellar tidal features. Along a possible merger sequence, the amount of assembled HI increases in the outskirts during the active phase of the merger. Furthermore, they found differences in the distribution of gas and stars within tidal tails, plumes and haloes. In particular, they found anticorrelations of the two components, both HI tails without any optical counterpart as well as large stellar tidal features with only little, if any, associated gas. Again, the formation of these features highly depends on the merger history and the influence on the star formation. Thus, HI maps (particularly in combination with optical images) are ideal to study the diverse consequences of a merger event.

Tidal HI tails which are formed in a merger are favoured hosts for the formation of a new generation of galaxies, the so-called *tidal dwarf galaxies*. Usually, a large fraction of HI, which is stripped out during the merger, assembles in the galactic halo or even disperses into the intergalactic medium. At least parts of this tidal debris might fall back and recondense, forming compact, self-gravitating and star forming objects. Tidal dwarf galaxies are typically found at the tip of tidal tails of mergers between at least one gas-rich galaxy (Duc & Mirabel (1999), Duc et al. (2000)). However, not all mergers with tidal tails form tidal dwarf galaxies, and not all star forming clumps in tails will survive and end as a separate entity. The conditions under which tidal dwarf galaxies are formed (the properties of the merging galaxy, the merger history, the environment etc.) are still under ongoing investigation.

To get an impression of the variety of the effects of gravitational influences on HI, the reader might refer to the comprehensive collection in the HI Rogues Gallery (Hibbard et al. (2001)). A useful characteristic parameter to describe the proportion of gaseous and luminous material is the HI mass-to-light ratio $M_{\text{HI}}/L_{\text{B}}$ (M_{\odot}/L_{\odot}). Following Rohlfs & Wilson (2004), the HI mass can be calculated as

$$M_{\text{HI}}(M_{\odot}) = 2.3354 \cdot 10^5 \cdot F_{\text{HI}} \cdot D^2 \quad (21)$$

with F_{HI} the integrated HI flux density (in Jy km/s) and D the distance of the object in Mpc.

2.5 The Properties of the ISM

2.5.1 Optical Emission Lines

If hot stars are present to ionise the interstellar medium, as it is the case in starforming regions, the properties of the ISM can be derived using emission lines as tracers for the metallicity, the temperature and the electron density. The radiation processes in the ISM are different from those under terrestrial conditions: After photoionisation, low-energy levels with small transition probabilities can be excited by collisions between thermal electrons and ions. Due to low densities in the ISM ($\leq 10^4 \text{ cm}^{-3}$), collisional de-excitation is not very likely. Thus, most excitations lead to emission, also in forbidden lines (Osterbrock (1989)), labeled with

squared brackets. In Tab. 2 the most important optical emission lines are listed, which can be also seen in Fig. 6.

Commonly the abundance of a given element is determined using the ratio of strong emission lines, e.g., $R_{23} = ([\text{OII}]\lambda 3727 + [\text{OIII}]\lambda\lambda 4959, 5007)/\text{H}\beta$ (Pagel et al. (1979)). In this equation, the total cooling due to oxygen is estimated. Because oxygen is one of the most important coolants, the estimation is sensitive to the oxygen abundance. The problem with this abundance indicator is that it strongly depends on the ionisation parameter $q = S_{\text{H}0}/n$, with $S_{\text{H}0}$ the ionising photon flux through a unit area and n the local number density of hydrogen atoms. Another definition is the dimensionless value $U = q/c$, with c the speed of light. Typical ionisation parameter diagnostics like $[\text{OIII}]\lambda 5007/[\text{OII}]\lambda\lambda 3726, 3729$ in turn depend on the abundance (Kewley & Dopita (2002)). A second problem with the R_{23} and other line ratios used for abundance estimation is, that they are double-valued, because at high abundances the electron temperature becomes too low to excite forbidden lines by collisions (leading to a decrease of emission). Therefore, the same line ratio appears for both high and low abundances.

Kewley & Dopita (2002) give a good overview of new calibrations of the most important abundance diagnostics and their reliability. They also give a metallicity-dependent optimised abundance determination method which exploits the advantages of different methods. Note, that the abundance is typically given as the ratio between oxygen and hydrogen: $\log(\text{O}/\text{H}) + 12$. In principle, Kewley & Dopita (2002) distinguish three abundance intervals for which different methods are best suitable:

- $\log \frac{\text{O}}{\text{H}} + 12 \geq 8.6$: To start with the abundance estimation and for abundances larger than 8.6 the ratio $[\text{NII}]\lambda 6584/[\text{OII}]\lambda 3727$ is the best means. The relationship between $[\text{NII}]/[\text{OII}]$ and the abundance is fitted as:

$$\log(\text{O}/\text{H}) + 12 = \log[1.54020 + 1.26602 \cdot R + 0.167977 \cdot R^2] \quad (22)$$

with $R = \log([\text{NII}]/[\text{OII}])$.

If the abundance is less than 8.6, the methods below have to be applied. The ionisation parameter can be determined using a third-order polynomial fit to the $\log([\text{OIII}]/[\text{OII}])$ ratios depending on the metallicity. Fitting parameters are given in Kewley & Dopita (2002).

- $8.6 > \log \frac{\text{O}}{\text{H}} + 12 \geq 8.5$: As a second step, the average of the R_{23} calibrations from McGaugh (1991) and its parameterisation in Kobulnicky et al. (1999) and Zaritsky et al. (1994) can be used to estimate the abundance. Zaritsky et al. (1994) give the relation:

$$\log(\text{O}/\text{H}) + 12 = 9.265 - 0.33 \cdot R_{23} - 0.202 \cdot R_{23}^2 - 0.207 \cdot R_{23}^3 - 0.333 \cdot R_{23}^4 \quad (23)$$

The relation determined by McGaugh (1991) is as follows:

$$\log(\text{O}/\text{H}) + 12 = 12.0 - 4.944 + 0.767 \cdot R_{23} + 0.602 \cdot R_{23}^2 - y \cdot (0.29 + 0.332 \cdot R_{23} - 0.331 \cdot R_{23}^2) \quad (24)$$

Here, $y = \log\left[\frac{[\text{OIII}]\lambda\lambda 4959, 5007}{[\text{OII}]\lambda 3727}\right]$. The result of the average of these two methods is appropriate down to a value of $\log(\text{O}/\text{H}) + 12 = 8.5$.

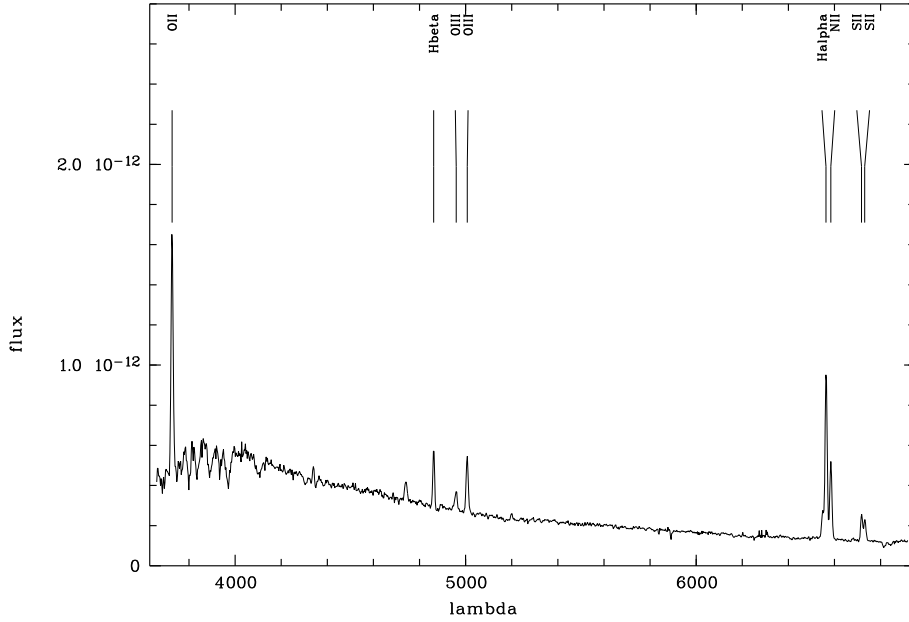


Figure 6: Optical spectrum of NGC 4194 showing the most important emission lines.

- $\log \frac{O}{H} + 12 \leq 8.5$: For abundances below 8.5, the R_{23} as calibrated in Kewley & Dopita (2002) can be used. Kewley & Dopita (2002) recommend to estimate the abundance first using the calibration of Charlot & Longhetti (2001):

$$\log(O/H) + 12 = \log \left(5.09 \cdot 10^{-4} \left[\left(\frac{[OII]/[OIII]}{1.5} \right)^{1.5} \right] \cdot \left[\left(\frac{[NII]/[SII]}{0.85} \right)^{1.17} \right] \right) + 12 \quad (25)$$

With this initial guess the ionisation parameter q can be estimated using the ratio $R = \log([OIII]/[OII])$. Kewley & Dopita (2002) give the fitting parameters for the exponential fit equation for q . The derived q value can then be used for the abundance determination according to the R_{23} method:

$$\log(O/H) + 12 = \frac{-k_1 + \sqrt{k_1^2 - 4 \cdot k_2 \cdot (k_0 - R_{23})}}{2 \cdot k_2} \quad (26)$$

Here, k_0, k_1, k_2 are constants depending on q . In principle, the ionisation parameter can now be re-calculated and after that iteratively the abundance. Kewley & Dopita (2002) mention that in almost 90% of all fits convergence is reached after the first iteration. To minimise errors one can take the average of the abundance determined with R_{23} and the method of Charlot & Longhetti (2001).

It is also possible to estimate the abundance in case that fewer emission lines are available. Of course, one has to deal with a lower accuracy then. Ways to do so are also given by Kewley & Dopita (2002).

2.5.2 Molecular lines

The properties of the molecular interstellar medium can be studied by observations of different molecules, isotopomers and transitions. To interpret molecular line ratios, one has to

Table 2: The most important emission lines used to study the ISM (Osterbrock (1989)).

| name | wavelength (\AA) | transition |
|------------|-----------------------------|--|
| [OII] | 3727 | $^4S_{3/2} - ^2D_{3/2}$ and/or $^4S_{3/2} - ^2D_{5/2}$ |
| [OIII] | 4959 | $^3P_1 - ^1D_2$ |
| [OIII] | 5007 | $^3P_2 - ^1D_2$ |
| [SII] | 6717 | $^4S_{3/2} - ^2D_{5/2}$ |
| [SII] | 6731 | $^4S_{3/2} - ^2D_{3/2}$ |
| [NII] | 6584 | $^3P_2 - ^1D_2$ |
| H α | 6563 | Balmer (3 - 2) |
| H β | 4861 | Balmer (4 - 2) |

understand the radiative transfer within the molecular clouds. Usually, radiative transfer is expressed in terms of intensity as follows (Boehm-Vitense (1989), van Langevelde & van der Tak (2004), Rohlfs & Wilson (2004)):

$$\frac{dI_\nu}{ds} = -\kappa_\nu(\vec{r}) \cdot I_\nu + \epsilon_\nu(\vec{r}) \quad (27)$$

I_ν is the intensity at a given frequency, defined as $I_\nu = \frac{dE}{d\nu \cdot dA \cdot dt \cdot d\Omega \cdot \cos\theta}$, with Ω the solid angle of the source, A the collecting area of the detector and θ the angle between dA and the source. Note, that I_ν is constant with distance but depends on the true size of the source. In the equation above, $\kappa_\nu(\vec{r})$ is the absorption coefficient (in cm^{-1}), $\epsilon_\nu(\vec{r})$ the emission coefficient. Introducing the optical depth $\tau_{\nu(s)} = \int_0^s \kappa(s') ds'$ of a layer with the thickness s , one can express the radiative transfer as

$$\frac{dI_\nu}{d\tau} = -I_\nu + S_\nu(\vec{r}) \quad (28)$$

Here, $S_\nu(\vec{r}) = \epsilon_\nu(\vec{r})/\kappa_\nu(\vec{r})$ is the so-called *source function*. In case of thermal equilibrium, i.e., equilibrium of the radiation with the surrounding medium, the intensity is equal to the Planck function and only dependent on the temperature: $I_\nu = B_\nu(T)$. This is also known as the Kirchhoff law: $B_\nu(T) = \epsilon_\nu/\kappa_\nu$.

In reality, in most cases this relation not valid for the entire astronomical object. Instead, often the approach of local thermodynamical equilibrium (LTE) is used. It means, that the emission is equal to a black body radiation, even if it is possible that absorption can take place in one or a few spectral lines.

Integrating Equ. 28 leads to

$$I_\nu = I_\nu(0) \cdot e^{-\tau_\nu} + \int_0^{\tau_\nu} e^{-(\tau_\nu - \tau'_\nu)} \cdot S_\nu(\tau'_\nu) d\tau'_\nu \quad (29)$$

Often, κ and ϵ are expressed in terms of the *Einstein coefficients*, which are used to describe absorption and emission in atomic physics. Spontaneous emission can be expressed as

$$\epsilon_\nu = \frac{h \cdot \nu}{4 \cdot \pi} \cdot n_2 \cdot A_{21} \cdot \phi(\nu) \quad (30)$$

In this equation, $\phi(\nu)$ accounts for the line shape, often assumed to be rectangular for simplicity. A_{21} is the Einstein coefficient, n_2 the number of atoms in the higher excitation state.

Furthermore, it is assumed that the emission is isotropic. The absorption coefficient can be expressed in a similar way, considering the absorption B_{12} and induced emission B_{21} :

$$\kappa_\nu = \frac{h \cdot \nu}{4 \cdot \pi} \cdot (n_1 \cdot B_{12} - n_2 \cdot B_{21}) \cdot \phi(\nu) \quad (31)$$

If $\kappa = \epsilon$, that leads to

$$\frac{n_2}{n_1} = \frac{B_{12}}{A_{21} + B_{21}} \quad (32)$$

In thermodynamical equilibrium, the level populations are distributed following the *Boltzmann distribution*

$$\frac{n_2}{n_1} = \frac{g_2}{g_1} \cdot e^{-\frac{h \cdot \nu}{k \cdot T}} \quad (33)$$

with k the Boltzmann constant, g_1 and g_2 the statistical weights. Thus, we can derive the Einstein relations

$$g_1 \cdot B_{12} = g_2 \cdot B_{21} \quad (34)$$

and

$$A_{21} = \frac{2 \cdot h \cdot \nu^3}{c^2} \cdot B_{21} \quad (35)$$

For a homogeneous isothermal medium ($T(\tau) = T = \text{const}$) this can be explicitly solved as

$$I_\nu(s) = B_\nu(T) \cdot (1 - e^{-\tau_\nu(s)}) + I_\nu(0) \cdot e^{-\tau_\nu(s)} \quad (36)$$

In radio astronomy, the Planck law can be approximated by the *Rayleigh-Jeans* approximation, for which holds: $h \cdot \nu \ll k \cdot T$. The black body radiation can then be written as

$$B_{\text{RJ},\nu}(T) = \frac{2 \cdot \nu^3}{c^2} \cdot k \cdot T \quad (37)$$

This relation means, that the brightness and the thermodynamic temperature of the black body emitting the radiation are simply proportional. Thus, it is useful to define the *brightness temperature* T_b which is the temperature equivalent to the given brightness in the Rayleigh-Jeans case: $T_b = \frac{c^2}{2 \cdot k \cdot \nu^2} \cdot B_\nu$. In the Rayleigh-Jeans case and for B_ν emitted by a perfect black body, T_b is independent of the frequency and equal to the thermodynamic temperature. Even if these assumptions are not valid, as it is often the case in (sub)mm observations, the brightness temperature is still a useful quantity. One has, however, to keep in mind that the brightness temperature is then different from the thermodynamic temperature. Applying the Rayleigh-Jeans approximation to the radiative transfer equation Equ. 28, one obtains

$$\frac{dT_b(s)}{d\tau_\nu} = T_b(s) - T(s) \quad (38)$$

Here, $T(s)$ is the thermodynamic temperature of the medium. T_b is the temperature which excites the transition between the levels 2 and 1, which are distributed following Equ. 33. For an isothermal medium, the solution then is:

$$T_b(s) = T_b(0) \cdot e^{-\tau_\nu(s)} + T(1 - e^{-\tau_\nu(s)}) \quad (39)$$

For $T_b(0) = 0$ and $\tau \ll 1$ (the optically thin case), it follows $T_b = \tau_\nu \cdot T$, for the optically thick case ($\tau \gg 1$) $T_b = T$ is obtained.

To solve the equation of radiative transfer, it is essential to know some values of n_i . They depend on the collision rates C_{ij} which in turn depend on the density of the collision partner, mostly H_2 , and the collision cross sections (integrated over all velocities). In thermodynamic equilibrium, it holds $n_1 \cdot C_{12} = n_2 \cdot C_{21}$. Applying this to the Boltzmann distribution, this results in

$$C_{12} = \frac{g_2}{g_1} \cdot C_{21} \cdot e^{-\frac{\Delta E}{kT}} \quad (40)$$

The change of the level population in statistical equilibrium for e.g., the upper level, can then be expressed as follows (for the lower level the right side is negative)

$$\frac{dn_2}{dt} = n_1 \cdot (B_{12} \cdot J + C_{12}) - n_2 \cdot (A_{21} + B_{21} \cdot J + C_{21}) \quad (41)$$

Here, J is the average intensity over the whole sphere and integrated over $\phi(\nu)$. For this solution, one has to estimate the radiation field. A common method is the introduction of the *escape probability* β of a photon from the cloud. If the cloud is completely opaque, $\beta = 0$ and J is equal to the source function. Otherwise, it holds: $J = S \cdot (1 - \beta)$. β can be expressed without referring to the radiation field. Equ. 41 then becomes

$$\frac{dn_2}{dt} = n_1 \cdot C_{12} - n_2 \cdot C_{21} - \beta \cdot n_2 \cdot A_{21} \quad (42)$$

Thus, the level population and radiation field are decoupled and can be solved separately. To estimate the escape probability, one has to consider the geometry of the source and the optical depth. A simple approximation is

$$\beta = \langle e^{-\tau} \rangle = \frac{1}{\tau} \int_0^\tau e^{-\tau'} d\tau' = \frac{1 - e^{-\tau}}{\tau} \quad (43)$$

for the one-dimensional case.

In this thesis, two different codes were used to solve the radiative transfer problem. These two programs use different approaches, thus, the comparison of the results is a good indicator of the reliability of the outputs. The codes are shortly introduced in the following:

- *RADEX*: This code is valid in the non-LTE case and uses the escape probability approximation. It is written by J. Black (Schöier et al. (2005)) and is available online¹. Geometry and velocity fields are not considered. It is only assumed that the medium is homogeneous. In an iterative process, the relative level populations are estimated for the optical thin case (when the radiation in the lines does not affect the level population). From this the optical depth is calculated and thus a new solution for the excitation can be derived. This process is repeated until a consistent solution for the level population and the radiation is found.
- *LVG*: The *large velocity gradient* (LVG) approximation was first introduced by Sobolev (1960) to solve the radiative transfer equation. It is assumed, that the major mechanism for line broadening comes from a large scale velocity gradient $\frac{dv}{dr}$ in the observed gas cloud, whereas the thermal broadening plays a minor role. Therefore, if a photon is emitted, it can only be re-absorbed by nearby molecules, otherwise it can leave the cloud. This approach reduces the global radiative transport problem to a local one. The LVG

¹<http://www.strw.leidenuniv.nl/~moldata/radex.html>

assumption also allows the definition of $\beta = \frac{1-e^{-\tau}}{\tau}$, showing that the two approaches are consistent. The code used for this thesis is originally written by Ch. Henkel (Henkel (1980)) and improved by S. Hüttemeister and others (Hüttemeister (1993), Dahmen (1995)).

The outputs of both approaches are the level populations, the optical depth and the line brightness temperature, from which the line ratios can be calculated. Line ratios should be used when comparing to observational results, since (hopefully) the unknown beam filling factors are identical in the transitions compared and thus cancel.

From the above derivation of the radiative transfer problem, it is obvious that at least two transitions of e.g., ^{12}CO need to be measured for an estimation of the cloud parameters (i.e., temperature and density). However, since the line ratios are also dependent on the density, the results from different transitions of one molecular species alone are not definite enough for a proper determination of the cloud properties. A given line ratio defines a curve in T–n–space, not a unique solution. Therefore, by observing transitions of other isotopomers like ^{13}CO , it is possible to get a more unique solution by finding intersections of curves corresponding to different ratios.

References

- Arimoto, N., Sofue, Y., & Tsujimoto, T. 1996, PASJ, 48, 275
- Aronica, G. 2006, (PhD thesis)
- Barnes, J. E. & Hernquist, L. E. 1991, ApJ, 370, L65
- Boehm-Vitense, E. 1989, Introduction to stellar astrophysics. Volume 2 - Stellar atmospheres (Cambridge and New York, Cambridge University Press, 1989, 251 p.)
- Bruzual, G. & Charlot, S. 1993, ApJ, 405, 538
- . 2003, MNRAS, 344, 1000
- Charlot, S. & Longhetti, M. 2001, MNRAS, 323, 887
- Condon, J. J. 1992, ARA&A, 30, 575
- Dahmen, G. 1995, The Large Scale Distribution of Molecular Gas in the Galactic Center Region from C^{18}O and the Nitrogen Isotope Abundance in the Galaxy (PhD thesis)
- de Vaucouleurs, G. 1948, Annales d’Astrophysique, 11, 247
- Devereux, N. A. & Hameed, S. 1997, AJ, 113, 599
- Devereux, N. A. & Young, J. S. 1990, ApJ, 350, L25
- Duc, P.-A., Brinks, E., Springel, V., Pichardo, B., Weilbacher, P., & Mirabel, I. F. 2000, AJ, 120, 1238
- Duc, P.-A. & Mirabel, I. F. 1999, in IAU Symp. 186: Galaxy Interactions at Low and High Redshift, 61

- Fioc, M. & Rocca-Volmerange, B. 1997, *A&A*, 326, 950
- Freeman, K. C. 1970, *ApJ*, 160, 811
- Gonzalez, R. C. & Woods, R. E. 1992, *Digital Image Processing* (Addison–Wesley Company, 1992)
- Gordon, S., Koribalski, B., & Jones, K. 2003, *MNRAS*, 342, 939
- Haarsma, D. B., Partridge, R. B., Windhorst, R. A., & Richards, E. A. 2000, *ApJ*, 544, 641
- Henkel, C. 1980, (PhD thesis)
- Hibbard, J. E., Vacca, W. D., & Yun, M. S. 2000, *AJ*, 119, 1130
- Hibbard, J. E. & van Gorkom, J. H. 1996, *AJ*, 111, 655
- Hibbard, J. E., van Gorkom, J. H., Rupen, M. P., & Schiminovich, D. 2001, in *ASP Conf. Ser. 240: Gas and Galaxy Evolution*, 657
- Hüttemeister, S. 1993, *Molecular Clouds in the Galactic Center and Selected External Galaxies* (PhD thesis)
- Kennicutt, R. C. 1989, *ApJ*, 344, 685
- . 1992, *ApJS*, 79, 255
- Kennicutt, R. C. 1998a, in *Saas-Fee Advanced Course 26: Galaxies: Interactions and Induced Star Formation*, 1
- . 1998b, *ARA&A*, 36, 189
- . 1998c, *ApJ*, 498, 541
- Kewley, L. J. & Dopita, M. A. 2002, *ApJS*, 142, 35
- Knapp, G. R., Gunn, J. E., & Wynn-Williams, C. G. 1992, *ApJ*, 399, 76
- Kobulnicky, H. A., Kennicutt, R. C., & Pizagno, J. L. 1999, *ApJ*, 514, 544
- Koribalski, B. & Dickey, J. M. 2004, *MNRAS*, 348, 1255
- Koribalski, B., Gordon, S., & Jones, K. 2003, *MNRAS*, 339, 1203
- Koribalski, B. & Manthey, E. 2005, *MNRAS*, 358, 202
- Leitherer, C., Schaerer, D., Goldader, J. D., Delgado, R. M. G., Robert, C., Kune, D. F., de Mello, D. F., Devost, D., & Heckman, T. M. 1999, *ApJS*, 123, 3
- Mazzei, P. & de Zotti, G. 1994, *ApJ*, 426, 97
- McGaugh, S. S. 1991, *ApJ*, 380, 140
- Mihos, J. C. & Hernquist, L. 1996, *ApJ*, 464, 641

- Noeske, K. 1999, Mehrfarben-Flächenphotometrie und Strukturuntersuchungen an Blauen Kompakten Zwerggalaxien (Diploma thesis)
- Osterbrock, D. E. 1989, Astrophysics of gaseous nebulae and active galactic nuclei (Research supported by the University of California, John Simon Guggenheim Memorial Foundation, University of Minnesota, et al. Mill Valley, CA, University Science Books, 1989, 422 p.)
- Pagel, B. E. J., Edmunds, M. G., Blackwell, D. E., Chun, M. S., & Smith, G. 1979, MNRAS, 189, 95
- Papaderos, P., Loose, H.-H., Thuan, T. X., & Fricke, K. J. 1996, A&AS, 120, 207
- Rohlfs, K. & Wilson, T. L. 2004, Tools of radio astronomy (Tools of radio astronomy, 4th rev. and enl. ed., by K. Rohlfs and T.L. Wilson. Berlin: Springer, 2004)
- Schöier, F. L., van der Tak, F. F. S., van Dishoeck, E. F., & Black, J. H. 2005, A&A, 432, 369
- Sersic, J. L. 1968, Atlas de galaxias australes (Cordoba, Argentina: Observatorio Astronomico, 1968)
- Smith, B. J., Struck, C., & Pogge, R. W. 1997, ApJ, 483, 754
- Sobolev, V. V. 1960, Moving envelopes of stars (Cambridge: Harvard University Press, 1960)
- Strong, A. W., Bloemen, J. B. G. M., Dame, T. M., Grenier, I. A., Hermsen, W., Lebrun, F., Nyman, L.-A., Pollock, A. M. T., & Thaddeus, P. 1988, A&A, 207, 1
- Struck, C. 1997, ApJS, 113, 269
- Trager, S. C., Worthey, G., Faber, S. M., Burstein, D., & Gonzalez, J. J. 1998, ApJS, 116, 1
- van Langevelde, H. J. & van der Tak, F. 2004, RADEX Manual
- Worthey, G., Faber, S. M., Gonzalez, J. J., & Burstein, D. 1994, ApJS, 94, 687
- Young, J. S. & Scoville, N. Z. 1991, ARA&A, 29, 581
- Zaritsky, D., Kennicutt, R. C., & Huchra, J. P. 1994, ApJ, 420, 87

3 Optical and NIR Properties of Moderate Luminosity Mergers

Abstract

Until now, mergers between different galactic types, e.g., between a Spiral and an Elliptical (so-called S+E mergers) are poorly studied. Here, we introduce a galaxy sample of candidates for S+E mergers. They all show the typical tidal features like tails and shells, which are predicted by numerical models for this kind of merger. Optical and near-infrared images are presented, which show a variety of morphological disturbances, but an overall disk-like light distribution. Furthermore, optical spectroscopy was obtained, which revealed a broad range of ongoing star formation activity within the sample galaxies.

3.1 Introduction

The importance of mergers for galaxy evolution is discussed now since more than 30 years. In the seminal work of Toomre & Toomre (1972) the effects of gravitational tidal forces on the appearance of galaxies were investigated by simulations, which could reproduce observed peculiarities very nicely. Since then, numerous studies of interacting and merging galaxies showed the connection between the interaction and the properties of the galaxies, in particular the star formation rate and thus the stellar populations (among those, Larson & Tinsley (1978), Sanders & Mirabel (1996), Kennicutt (1998a), Barnes & Hernquist (1991), Barnes (1994)).

But galaxy mergers are not only of interest for the evolution of individual galaxies. With the definition of a possible merger sequence of two disk galaxies by Toomre (1977), the hypothesis was stated, that these mergers might be the origin for all (large) Ellipticals. Thus, mergers play also a role in cosmological questions like how galaxies are formed.

A milestone in the studies of merging galaxies was the discovery of objects ultra-luminous in the far infrared ($L_{\text{FIR}} > 10^{12} L_{\odot}$), so-called ULIRGs. These objects turned out to be major mergers between two large disk galaxies undergoing an extreme phase of star formation, which causes the high infrared luminosity (Sanders & Mirabel (1996)). Since then, a lot of work has been done to understand the processes in these disk-disk mergers (e.g., Hibbard & Mihos (1995), Hibbard & van Gorkom (1996), Hibbard et al. (2000), Barnes & Hernquist (1991), Sanders & Mirabel (1996), Schweizer (2005) and references therein). However, ULIRGs are rare objects in the local Universe with a space density comparable to quasars (e.g., Sanders et al. (2003)). Instead, smaller or less gas-rich (elliptical) galaxies dominate the galaxy population. Therefore, mergers between galaxies of unequal masses and/or Spirals and Ellipticals (S+E mergers) are expected to be considerably more frequent than major mergers leading to ULIRGs and may be overall more important for galaxy evolution.

Despite their importance, such 'moderate luminosity mergers' are still poorly studied and not well understood. One of the most essential questions connected to these objects is the nature of the starburst induced (if any). There is a very significant disagreement between numerical simulations. A ULIRG is characterised by a very compact central gas distribution extended only a few 100 pc. Weil & Hernquist (1993) suggest a similarly strong central concentration, accompanied with a starburst, too. In contrast, calculations by Kojima & Noguchi (1997) indicate a scattering of gas on large scales, possibly not resulting in a starburst at all, because the gas will become too dispersed in the collision.

Observations of Aalto & Hüttemeister (2000) of a young and clearly starbursting prototypical S+E merger candidate, NGC 4194, show a molecular gas distribution with a size of 5 kpc,

which lies just between the two different theoretical predictions. Aalto et al. (2001) detected molecular gas in the tidal tail of NGC 4194, arguing that this material was thrown out in the collision, similar to the stellar component. These observations tend to corroborate the theory of Kojima & Noguchi (1997), but their models clearly need modifications to allow for starburst activity, which may, however, be much more extended than in a ULIRG. Possibly, this activity may also continue over a longer period of time or proceed more sequentially than in a ULIRG, where all the gas is likely to be consumed on short timescales.

Clearly, the questions how a S+E merger proceeds, what the star formation activity induced by this merger is, how long it lasts and how far into the outskirts of the galaxy it extends can only be approached by the systematic multiwavelength dissection of both the stellar and gaseous content of a sample of moderate luminosity mergers. We have embarked on such a detailed study of a sample of S+E merger candidates, including NGC 4194.

In most (major) merger studies galaxies in different stages of the merger sequence are observed. But how unique is this classification and the placement on the different stages? In our project, we go the opposite way and analyse a sample of galaxies which shall occupy the same advanced stage in the sequence, based on the optical appearance. This will show how significant such a classification really is. We obtained multiwavelength observations to study the stellar morphology, the star formation history, with special emphasis on a starburst period, the large scale HI distribution and the molecular gas reservoir to feed a burst.

Here we will introduce our sample and will present first results from our optical and near-infrared (NIR) observations, both imaging and (optical) spectroscopy. HI and CO observations will be shown in a second chapter (Ch. 6).

This chapter is structured as follows: We describe the selection of our sample in Section 2. In Section 3 and 4 we give information about the observations presented here and the reduction of the data. Finally, we discuss the results in Section 5 and summarise the project in Section 6.

3.2 The sample

In our study, we are interested in the impacts of the merger on the remaining object, in particular the possibility of an induced starburst. Thus, it is necessary to investigate galaxies which are completely merged to make sure, that a starburst phase is ongoing or has passed, if at all. Therefore, a selection criterion for our sample was, that only one nucleus was left, at least on Digitised Sky Survey (DSS) resolution. Of course, this does not exclude the existence of two separate nuclei that could be seen at higher resolution, but it ensures an advanced stage of merging. The drawback of this constraint is, that obviously the progenitors are not clear, because the merger is too advanced and the merged galaxies already lost their individuality. To sort out this difficulty, we selected galaxies which have an optical morphology similar to those predicted by simulations. Although, as mentioned above, the models have to be taken with care when looking at the gas and the star formation rate, the models agree very nicely in the evolution of the stellar component.

To get a sufficient spatial resolution in our images and to be able to detect HI and CO in the targets, we selected only galaxies with a velocity < 15000 km/s from the RC3 catalog (de Vaucouleurs et al. (1995)). Furthermore, galaxies from all types which are classified as peculiar were chosen. We excluded peculiar Spirals, because they were most probably disk-disk mergers. To exclude ULIRGs, the far infrared (FIR) luminosities were calculated and only galaxies with a FIR luminosity of $< 10^{11} L_{\odot}$ remained in the catalog.

Table 3: The sample galaxies and some basic parameters adopted from the Upsala General Catalog (UGC) and the NASA/IPAC Extragalactic Database (NED)³. The distance is calculated assuming an $H_0 = 72$ km/s/Mpc. Based on the terminology of the RC3 (de Vaucouleurs et al. (1995)), the galaxy classification is as follows: ?: doubtful, '?': uncertain, pec: peculiar, SAB0: mixed lenticular (in terms of having a bar), IBm: barred irregular of the magellanic type, SAB(s)0: mixed, s-shaped spiral, S0+: late lenticular, SB(s)0: barred, s-shaped lenticular. Special classifications are labeled as: NELG: narrow emission line galaxy, BCG: blue compact galaxy, HII: galactic spectrum dominated by HII-region features, LINER: low-ionisation nuclear emission-line region.

| Galaxy | RA (^h ^m ^s) | DEC ([°] ' ") | type | velocity (km/s) | distance (Mpc) | diameter (arcmin) | B mag mag | L _{FIR} (10 ⁹ L _⊙) |
|------------|--|----------------------------|-------------------|--------------------|-------------------|----------------------|--------------|---|
| Arp 164 | 01 15 57.6 | +05 10 43 | S? | 5269 | 73 | 2.7 | 13.55 | – |
| Arp 161 | 11 42 12.4 | +00 20 03 | Sb pec; Sbrst HII | 5564 | 77 | 0.4 | 13.7 | 32 |
| NGC 4004 | 11 58 05.2 | +27 52 44 | Pec, NELG | 3377 | 47 | 2.0 | 14.0 | 12 |
| NGC 4441 | 12 27 20.3 | +64 48 05 | SAB0+ pec | 2674 | 39 | 4.5 | 13.5 | 5.4 |
| NGC 4194 | 12 14 09.5 | +54 31 37 | IBm pec;BCG, HII | 2442 | 36 | 2.3 | 13.0 | 85 |
| NGC 5607 | 14 19 26.7 | +71 35 18 | Pec | 7595 | 105 | 0.9 | 13.9 | 73 |
| UGC 8264 | 13 08 29.4 | +84 37 50 | Pec | 4641 | 59 | 1.7 | 14.03 | 17 |
| ESO 156-18 | 03 52 13.6 | -54 53 15 | SAB(s)0: pec | 13315 | 175 | 2.1 | 14.5 | 5.1 |
| ESO 159-03 | 05 16 09.1 | -54 06 17 | SB0: pec | 3994 | 49 | 2.1 | 14.01 | – |
| IC 5065 | 20 51 45.8 | -29 50 50 | SB pec | 9800 | 131 | 1.1 | 14.58 | – |
| ESO 416-09 | 02 42 22.6 | -30 19 20 | S0? pec | 6506 | 86 | 1.1 | 14.16 | – |
| ESO 295-02 | 00 43 25.4 | -38 45 26 | SAB(s)0 pec | 11895 | 158 | 0.98 | 15.25 | 14 |
| NGC 2996 | 09 46 30.2s | -21 34 18 | S0+ pec: | 8775 | 114 | 1.5 | 13.54 | – |
| ESO 511-35 | 14 22 06.6 | -26 51 27 | SB(s)0? pec | 6709 | 88 | 1.9 | 14.21 | – |
| ESO 341-04 | 20 41 13.9 | -38 11 36 | S0+: pec; LINER? | 6057 | 80 | 1.9 | 13.38 | 13 |

In a next step, all galaxies were checked in NED⁴ for any obvious close interacting partner which might induce a starburst and affect the HI distribution. Also galaxies with AGN signature were excluded, because the spectral emission features of the AGN would dominate the spectrum and thus make an interpretation of the stellar populations and the ongoing star formation rate difficult. Still, our sample galaxies may host a weak AGN. Finally, we looked on DSS images of all remaining galaxies to select those galaxies which have similar morphologies as those predicted by models of S+E mergers, i.e., they have tails and shell-like structures. In total, 15 galaxies were left, 7 in the northern and 8 in the southern hemisphere (including NGC 4194). Most of the galaxies have not been studied in detail so far. In particular about the southern galaxies only little is known. Tab. 3 lists all sample galaxies with the basic properties.

3.3 Observations

3.3.1 Optical imaging

Optical broad-band imaging was obtained during various observing runs at the Nordic Optical Telescope (NOT, 2.5 m) on La Palma, the Calar Alto 2.2 m telescope (CAHA) and the Advanced Technology Telescope (ATT, 2.3 m) at Siding Spring (SSO). The NOT is an alt-azimuthal mounted telescope with a rotating building and a focal ratio of $f/11$. The instruments are mounted in the Ritchey–Chretien focus. The optical instrument ALFOSC is a 2048×2048 pixel CCD with a read-out-noise of $3.2 e/\text{pix}$. The Calar Alto 2.2 m telescope as well uses the Ritchey–Chretien system. The optical instrument CAFOS is a focal reducer, which changes the focal ratio to $f/4.4$. The detector is equipped with a blue sensitive 2048×2048 pixel SITE chip with a read-out-noise less than $7 e/\text{pix}$. The field diameter is $16'$, which is given in Tab. 4. The ATT got its name, because it is the first telescope, which combines an unusual thin mirror, an altazimuthal mounting and a rotating building. The focal ratio of this telescope is $f/2.05$. For our observations, the optical Imager was equipped with a E2V 1024×1024 chip with a read-out-noise of $7 e/\text{pix}$, which recently has changed. Tab. 4 summarises the observing runs. The seeing conditions were generally moderate, with a typical seeing between $1''$ and $2''$.

Biases and twilight flats were taken before and after each observing night. For every filter we obtained at least three images and for every integration the telescope was shifted slightly to remove more easily cosmics and bad pixel. In Tab. 4 the total integration time is given in brackets after the filter designation. For photometric calibration, standard stars were observed three times each night, typically in the evening, in the middle of the night and in the morning. The fields were chosen from the Landolt catalog (Landolt (1992)): PG 0231+051, PG 1047+003, PG 1323-085 (NOT), RU 149, PG 0918+029, PG 1323-085, PG 0231+051 (SSO) and PG 0918+029, RU 149, PG 1525-071, PG 1528+062, PG 1633+099 (CAHA). At least two standard fields with different elevations were observed each time to estimate atmospheric extinction. In general, the observations were carried out in dark time to detect also faint tidal features, but often the weather conditions were moderate.

Due to weather and observing time constraints, not all galaxies could be observed.

⁴<http://nedwww.ipac.caltech.edu/index.html>

Table 4: Summary of the optical imaging campaigns. The data of Arp 164 are taken by courtesy of E. Wehner.

| Galaxy | telescope (see text) | Filters (Int.time (min)) | FOV (') | pixelscale ("/pix) | date |
|------------|-------------------------|-------------------------------|------------|-----------------------|----------|
| Arp 164 | WIYN 0.9 m | B (15) V (10) R (10) | 20.48 | 0.6 | Sep 2005 |
| NGC 4004 | CAHA 2.2 m | B (30) R (15) | 18.09 | 0.53 | Apr 2004 |
| | NOT | U (20) R (40) | 6.4 | 0.19 | Feb 2003 |
| NGC 4194 | NOT | B (120) V (10) | 6.4 | 0.19 | Feb 2003 |
| NGC 4441 | CAHA 2.2 m | B (120) R (60) | 18.09 | 0.53 | Apr 2004 |
| NGC 5607 | CAHA 2.2 m | B (90) R (45) | 18.09 | 0.53 | Apr 2004 |
| UGC 8264 | CAHA 2.2 m | B (120) R (60) | 18.09 | 0.53 | Apr 2004 |
| ESO 156-18 | SSO 2.3 m | U (20) B (90) V (10) R (60) | 6.62 | 0.59 | Jan 2004 |
| ESO 159-03 | SSO 2.3 m | U (20) B (105) R (60) | 6.62 | 0.59 | Jan 2004 |
| ESO 416-09 | SSO 2.3 m | U (20) B (120) V (10) R (45) | 6.62 | 0.59 | Jan 2004 |
| NGC 2996 | SSO 2.3 m | U (20) B (110) V (10) R (300) | 6.62 | 0.59 | Jan 2004 |

3.3.2 NIR imaging

NIR imaging was obtained at the Telescopio Carlos Sanchez (TCS, 1.5 m) on Tenerife, the NOT, the Calar Alto 3.5 m (CAHA) and the New Technology Telescope (NTT, 3.5 m) on La Silla. The TCS is an equatorial mounted Cassegrain telescope optimised for near-infrared observations. The focal ratio is $f/13.8$. The used instrument CAIN is equipped with a 256×256 HgCdTe array. At the NOT, the observations were done with NOTCam, a 1024×1024 Rockwell Hawaii HgCdTe array. Near-infrared observations at the Calar Alto were obtained at the 3.5 m Ritchey–Chretien telescope. We used the Omega Prime instrument, which is mounted in the prime focus of the telescope, with a focal ratio $f/2.6$. The detector of this instrument is a Rockwell 1024×1024 HgCdTe array with a read-out-noise of $8.4 e/\text{pix}$. The NTT is a alt-azimuth Ritchey–Chretien telescope with a rotating building. It is the first telescope which work with active optics to correct deformations of the mirror. The instruments are mounted in two Nasmyth–foci. The near-infrared instrument SOFI is equipped with a 1024×1024 Hawaii HgCdTe array with a read-out-noise of 2.1. In Tab. 5 we summarise the observations. The seeing was typically between $1.0''$ and $2.0''$.

Twilight flats were taken before and after the observations at the TCS and NOT, at the NTT and CAHA 3.5 m domeflats were done. Dark frames were obtained for each integration mode to measure the dark current. We observed standard stars chosen from Hunt et al. (1998), Elias et al. (1982) and Carter & Meadows (1995) during all nights. However, the final images were calibrated using 2MASS⁵ stars within the observed field. This method is less sensitive to background variation caused by the atmosphere. The standard stars were used to check this calibration method. Since the galaxies of our sample are fairly extended, we could not use dithering techniques for sky subtraction. Instead, we observed additional skyframes in the mode ON–OFF–ON–OFF and so on. To remove stars in the skyframes, we observed different positions around the target galaxies.

Again, not all galaxies could be observed due to observing time constraints.

⁵Two Micron All Sky Survey, <http://www.ipac.caltech.edu/2mass/>

Table 5: Summary of the NIR imaging campaigns.

| Galaxy | telescope (see text) | Filters (Int.time (min)) | FOV (') | pixelscale ("/pix) | date |
|------------|-------------------------|--------------------------|------------|-----------------------|----------|
| Arp 161 | TCS | J(40) H(60) K(60) | 4.3 | 1.0 | Feb 2003 |
| NGC 4004 | TCS | J(40) H(60) K(60) | 4.3 | 1.0 | Feb 2003 |
| | NOT | J(10) H(10) | 3.9 | 0.23 | Jan 2003 |
| NGC 4441 | TCS | J(40) H(60) K(60) | 4.3 | 1.0 | Feb 2003 |
| NGC 4194 | TCS | J(40) H(60) K(60) | 4.3 | 1.0 | Feb 2003 |
| | NOT | H(10) | 3.9 | 0.23 | Jan 2003 |
| NGC 5607 | CAHA 3.5 m | J(25) H(25) K(30) | 6.8 | 0.4 | Feb 4004 |
| UGC 8264 | CAHA 3.5 m | J(25) H(25) K(20) | 6.8 | 0.4 | Feb 2004 |
| IC 5065 | NTT | K(35) | 4.9 | 0.29 | Jul 2004 |
| ESO 341-04 | NTT | J(30) H(40) K(45) | 4.9 | 0.29 | Jul 2004 |
| ESO 511-35 | NTT | H(35) (45)K | 4.9 | 0.29 | Jul 2004 |

3.3.3 Optical spectroscopy

To study the star formation history in more detail, we obtained long-slit spectra with the Boller & Chivens spectrograph mounted at the Bok telescope at Kitt Peak. The Ritchey–Chretien type Bok telescope has a mirror diameter of 2.3 m and a focal ratio of $f/9$ for spectroscopic observations. The detector of the spectrograph has a size of 1200×800 pixel and a read-out-noise of 5.5 e/pix. For our observations, we used a 1×2 binned read-out mode and gained a spectral resolution of $2.75 \text{ \AA}/\text{pix}$.

We obtained so-called integrated driftscan spectra, introduced by Kennicutt (1992). In this method, the slit is moved across the area of interest, here, the galactic main body. The advantage of this approach over longslit spectroscopy is the independence of the positioning of the slit. The resulting spectrum reflects all population within the covered region. In addition, we obtained classical longslit spectra from the nuclear regions. For this, the slit was aligned to cover the brightest region of each galaxy. In Tab. 6 the observations are summarised.

Table 6: Summary of the optical spectroscopy observing campaign with the Bok telescope at Kitt Peak. The observations were done with a $2.5''$ slit. Given is the total integration time. Note, that the meaningful integration time of the driftscan spectra is the effective time, calculated as $T_{\text{int,eff}} = t_{\text{int,total}} \cdot \text{slitwidth}/\text{driftlength}$.

| Galaxy | Int.time (s) | $t_{\text{int,total}}$ (s) | integration area (") |
|----------|--------------|----------------------------|----------------------|
| | driftscan | longslit | driftscan |
| NGC 4004 | 1800 | 1800 | 50×90 |
| NGC 4441 | 1800 | 300 | 50×90 |
| NGC 5607 | 1800 | 300 | 50×60 |
| UGC 8264 | 1800 | 300 | 50×40 |
| NGC 4194 | 1800 | 300 | 50×96 |
| Arp 161 | 1800 | 300 | 30×60 |

The observations were done in collaboration with R. Kennicutt, J. Moustakas and Ch. Tremonti. In the beginning of each night, bias frames, dome flats and sky flats were ob-

served. Both kinds of flats were taken to benefit of the particular advantages. Dome flats are basically free of lines and well illuminated, however is the dome plane nearby and the intensity at the edges might be lower than in the center of the image. In contrast, the sky flats are 'polluted' with solar and sky lines, but the illumination over the frame is more constant than in dome flats. Both flats are finally multiplied to gain an illumination pattern. For the wavelength calibration, Helium-Argon spectra of arc lamps were taken after each observation. Spectroscopic standards stars (Feige 34, Feige 66, BD +332642, Hz 44, G 191B2B, taken from the catalog of Oke (1990)) were observed during the nights to subtract sky lines. The standard stars were observed with a slitwidth of 2.5" and 4.5".

3.4 Data reduction

3.4.1 Optical and NIR images

The standard reduction of the optical data was done using the IRAF⁶ software. Bias frame subtraction and overscan correction were applied to each image, then the object frames were divided by a flatfield image. Finally, the individual frames of each filter were summed up to a final image.

The correction for atmospheric extinction was achieved using photometric standard stars observed during the nights at different airmasses. This allows for fitting the atmospheric extinction curves for the individual nights. The standard stars were taken from the Landolt catalog (Landolt (1992)). Because most observations were not done under truly photometric conditions, only a constant zero point and the airmass were taken into account:

$$\text{mag}_{\text{obs}} = \text{mag}_{\text{Landolt}} + C_0 + C_1 \cdot X \quad (44)$$

X is the airmass, C_0 and C_1 are the fitting parameters, $\text{mag}_{\text{Landolt}}$ the literature magnitudes of the observed standard stars from the literature and mag_{obs} the observed magnitudes. Fit values for colour terms lied within the errors of C_0 and C_1 and thus were not included. Tab. 7 gives the derived fit values of the optical calibration. Note, that the data from the second night of the Calar Alto observation and the last night of the Siding Spring observation could not properly calibrated due to the lack of useful standard star observations. Therefore, we used the derived calibrations of the other nights instead.

The NIR images of the NTT, Calar Alto 3.5 m and NOT were reduced using the MIDAS⁷ software. We wrote our own routines for the standard reduction, including dark subtraction, flatfield division, sky subtraction and summation of the individual images. The skyframes which were subtracted were created by averaging typically four skyframes observed at different positions on the sky. The actual number of averaged frames depend on the weather conditions, which means on the variability of the sky.

The data taken with the TCS were reduced with IRAF routines written by M. Pohlen. These routines are comparable to our MIDAS routines, however modified for the special way of data storage at the TCS.

Photometric calibration of the NIR data was done using the 2MASS near-infrared survey and catalog. Magnitudes of stars in our frames were compared with magnitudes in the 2MASS catalog. Due to the larger photometric uncertainties compared to optical imaging caused

⁶Image Reduction and Analysis Facility

⁷Munich Image Data Analysis System, developed and maintained by ESO

Table 7: Derived optical photometric calibration values for the different observing campaigns.

| Observation | Filter | C_0 | C_1 |
|-------------|--------|------------------|-----------------|
| NOT 28 Jan | U | 23.93 ± 0.13 | 0.57 ± 0.10 |
| | B | 25.76 ± 0.04 | 0.25 ± 0.03 |
| | V | 25.59 ± 0.05 | 0.11 ± 0.04 |
| | R | 25.48 ± 0.06 | 0.08 ± 0.04 |
| CAHA 26 Apr | B | 23.56 ± 0.07 | 0.31 ± 0.04 |
| | R | 23.88 ± 0.03 | 0.11 ± 0.02 |
| SSO 23 Jan | B | 24.75 ± 0.04 | 0.31 ± 0.03 |
| SSO 24 Jan | B | 24.79 ± 0.09 | 0.36 ± 0.06 |
| SSO 24 Jan | R | 24.89 ± 0.05 | 0.15 ± 0.04 |
| SSO 25 Jan | U | 22.37 ± 0.05 | 0.51 ± 0.03 |
| SSO 25 Jan | V | 25.09 ± 0.02 | 0.18 ± 0.01 |
| SSO 25 Jan | R | 24.86 ± 0.03 | 0.1 ± 0.02 |

Table 8: Derived NIR photometric calibration values for the different observing campaigns. For the ESO observations, the values for the second night are given in brackets.

| Observation | Filter | C_0 |
|---|--------|------------------------|
| TCS (excl. NGC 4194) (NGC 4194 only) | J | 24.3 ± 0.12 |
| | J | 23.6 ± 0.14 |
| | H | 23.3 ± 0.11 |
| | K | 21.9 ± 0.15 |
| NOT | J | 22.1 ± 0.11 |
| | H | 22.4 ± 0.13 |
| CAHA (NGC 5607) | J | 25.6 ± 0.15 |
| | H | 25.5 ± 0.14 |
| | K | 26.1 ± 0.15 |
| (UGC 8264) | J | 24.4 ± 0.15 |
| | H | 24.3 ± 0.16 |
| | K | 26.0 ± 0.15 |
| ESO | J | 22.7 ± 0.13 |
| | H | $22.6 (22.8) \pm 0.12$ |
| | K | $22.1 (22.0) \pm 0.12$ |

by the atmospheric variability, higher background radiation contamination and a non-linear dependency on the airmass, we did not correct for airmass, but derived constants only for calibration. These constants were stable during the observing runs, thus, we calculated mean values, which are given in Tab. 8

Note, that the photometric constant derived for the J filter for NGC 4194 (TCS observations) differs from the values derived for the other galaxies. Thus, we excluded NGC 4194 J from calculating the mean constant in the J band and give two values instead, one derived for NGC 4194 and one for the others. The difference can be explained by different weather conditions in the night, when NGC 4194 was observed in the J-band.

Further analysis of both the optical and NIR images was done with MIDAS.

First, the sky background was subtracted from all images using the MIDAS command *fit/flatsky*. Here, the sky is approximated by a two-dimensional polynomial using manually selected areas from the given image. When selecting the areas, from which the sky background is calculated, care has to be taken that no stars are included. A polynomial of the first order was in all cases sufficient for a proper background fitting.

As a last step, astrometric calibration was done using the KARMA task *COORDS*. DSS2 images were used as reference frames. At least five pairs of stars were used to calculate the coordinates in our science frames, leading to an accuracy less than 0.3 pixels on average.

We further show images converted to polar coordinates to visualise asymmetries in the two-dimensional radial distribution. In these images, the radial distance from the center and the position angle are the new coordinates. The conversion was done using the KARMA task *kpolar*. Note, that the flux is conserved in this conversion.

To highlight the tidal features, we additionally show images processed with the unsharp masking technique (e.g., Gonzalez & Woods (1992), Aronica (2006)). In this technique, the image is blurred by a median-filter and subtracted from the original one. Depending on the size of the filter area, either small-scale or large-scale features are emphasised. To get the best results for the individual galaxies, several images were created with different areas considered for the filtering. The circular aperture of the filter was varied in radius from 3 to 45 pixels. Here, we present those images which show best the tidal features. The filter width is given in the captions.

Radial profiles

For each observed filter the radial profile was derived by ellipse fitting using the MIDAS command *fit/ell3* within the *surfphot* package. In advance, all bright stars were removed with the MIDAS command *mod/area*, because otherwise they would contribute to the galactic profiles. In a few cases, however, there were extremely bright, saturated stars near the galaxies, which could not properly be removed. This has been taken into account when deriving the radial profiles (see below).

Because our sample consists of peculiar and disturbed galaxies, ellipse fitting is only of limited use. To consider the irregular morphology of the objects, we also used a pixel summation method introduced by Papaderos et al. (1996). In this approach, all pixels within a given intensity interval are counted. An equivalent photometric radius is then defined as $R = \sqrt{\#pixels \cdot pixelscale^2 / \pi}$. In this method, the real morphology of a galaxy does not play a role, in contrast to ellipse fitting. The removal of stars within the area which is taken into account for this analysis is, however, more critical than using ellipse fitting. If stars cannot be properly removed, their light often accounts for the highest intensity ranges. Thus, in particular the highest intensity intervals, which normally represent the nucleus and/or a bulge, have to be taken with care.

Colour profiles were calculated by subtraction of two derived profiles in different filters from each other. To account for data points taken at different radii in different filters, a spline function for each profile was derived. With these functions, colour differences between two filters could be calculated in a given stepsize.

Colour maps

To study the twodimensional colour distribution in galaxies, colour maps are an appropriate tool. Optical filters alone are affected by dust, which means that redder colours do not necessarily mean an older stellar population, but can simply be redded by a higher dust concentration. NIR colours are much less sensitive to dust and show the old population almost unambiguously. Thus, we created B–R, J–K and, where available, B–K colour maps to trace the distribution of different populations, especially ongoing star forming regions and the dust.

The differences in the point spread functions (PSF) were taken into account by smoothing the images with a smaller PSF with a Gaussian to the larger PSF. Since the optical images have in general a higher resolution, they had to be regridded to the pixel scale of the NIR images. Finally, the relevant images were shifted to the same coordinate system and subtracted, after converting the scale to surface brightnesses considering the photometric calibration.

3.4.2 Spectroscopy

The longslit spectra were reduced with *ispec*, a software package written in IDL⁸ by J. Moustakas (Moustakas & Kennicutt (2005)). Special emphasis is put on the error estimates, including skyline subtraction and bad pixel masks, which are available within the resulting three-dimensional fits file of the reduced spectrum. Thus, it is easily possible to examine the quality of particular regions or pixels of the spectrum even after the reduction.

The reduction includes the standard steps trimming, bias subtraction and flat fielding and illumination calibration, cosmic ray rejection, wavelength calibration using reference arc lamp spectra, flux calibration using spectrophotometric standard stars, sky subtraction and extracting a one-dimensional spectrum out of a two-dimensional spectrum. In the last step, all emission within the two-dimensional spectrum coming from the galaxy was added together to increase the signal-to-noise ratio, with the drawback of loosing spatial resolution information. Furthermore, the Galactic extinction was corrected for using the extinction curves provided by Schlegel et al. (1998). The final spectrum is a datacube with the reduced spectrum in the first layer, the error spectrum, the bad pixel spectrum and the sky spectrum in the following ones.

3.5 Results and Discussion

In the following, we present our sample galaxies in detail. For most of the galaxies, we show deep R– and K–band images of the whole galaxy and a close-up of the center in the R – band. R–band images enhanced in contrast with the unsharp masking method are presented to highlight the irregularities within the galaxies due to the merger. R–band images in polar coordinates are shown to demonstrate the asymmetries with respect to the distance from the galactic nucleus. (B–R), (J–K) and (if possible) (B–K) colour maps, and radial surface brightness and colour profiles of the observed optical and near-infrared filters are also given. As described above, we used two different methods to derive the radial profiles. The radial distribution based on ellipse fitting is given on the left part. Error bars of the photometry are additionally given. These profiles are used to assess the type of the galaxy. For comparison, the results from the second method are shown on the right side of the images. No errors can

⁸Interactive Data Language

be given here, because the profiles are derived from pure pixel counting. In most cases, the profiles do not differ much. This is a hint that despite their peculiarities in morphology the ellipse fitting method works quite well.

For those galaxies, of which no optical images were observed by us so far, we show the DSS-2-red images for completeness.

In addition, for six galaxies optical spectra of the nuclei and driftscan spectra are presented here.

3.5.1 The Morphology and Colours of the Sample

The optical images of the sample galaxies reveal a variety of optical features, from long tails to more diffuse disturbances on smaller scales.

It is remarkable, that the overall structure, represented by the radial profiles, is little affected by the tidal disturbances. Instead, most of the galaxies show a clear and smooth distribution of a stellar disk, mostly in combination with an inner spheroidal distribution, either a bulge or the elliptical remnant. The disk character of the outer parts of the galaxies is a hint that the merger is advanced but not very old. Otherwise, one would expect to find a distribution following the $r^{1/4}$ -law due to relaxation, as it is found in old advanced mergers, e.g., Hibbard & van Gorkom (1996). They found such a brightness distribution even in merges which still show tidal features in the outskirts, arguing that the light profiles in the merger remnants are assembled long before the tidal features disperses or fall back.

The colours of the tidal features like the shells are found to be mostly bluer than the main galaxies, indicating younger stars either formed during the merger or thrown out from the smaller companion during the encounter (first simulated by Dupraz & Combes (1985), observationally confirmed by Fort et al. (1986)). This is in agreement with bluish shell colours found in other, more evolved shell galaxies (e.g., Carter et al. (1982), Fort et al. (1986), McGaugh & Bothun (1990), Turnbull et al. (1999)). Dupraz & Combes (1985) found in their simulations, that sharp-edged shells are formed by the accretion of either a small, cold disk galaxy or a small, rather hot elliptical (see also Hernquist & Quinn (1988)). The colours of the shells therefore can span a broad range in case they exist of stars from the accreted galaxy. This explains that in some examples in the literature no colour difference between the main body of the remnant and the shells are found (e.g., Carter et al. (1982), Fort et al. (1986), Pence (1986)), and even in a few cases the shells seem to appear redder than the main galaxy (e.g., McGaugh & Bothun (1990)).

In our sample, e.g., ESO 156-18 and ESO 159-3 show no significant colour differences between the shells and the main body. This might be due to merged galaxies with similar colours and thus the thrown out material does not vary much as well. Or, as discussed by McGaugh & Bothun (1990), it is possible that shells are biased towards high mass stars and thus evolve faster than the stellar population in the main body. Therefore, after a while the blue shells develop redder colours more similar to those of the main body.

In the following, the individual galaxies are described in detail.

NGC 4441

One of the most beautiful examples in the sample is NGC 4441 with its northern tail and two distinct southern shells. Therefore, the morphology of this galaxy is very similar to the prediction of S+E mergers (Weil & Hernquist (1993), Kojima & Noguchi (1997)). Furthermore,

NGC 4441 closely resembles the Medusa, our prototypical S+E merger candidate. However, in a closer comparison to the Medusa, NGC 4441 seems to be more evolved with clearer developed shells. The distance from the center to the outer shell is $\sim 1.76'$, corresponding to 18 kpc. The tail has a length of $1.85'$, i.e., 19 kpc, measured from the center. The main body itself has a diameter of $\sim 1.76'$ equals 18 kpc in its major axis.

The main body, although regular in the inner parts, is embedded in a chaotic fainter stellar distribution (Fig. 7). The unsharp masking image highlights in particular these disturbances, which appear similar to fragments of shells. In the inner center, a thin dust lane perpendicular to the major axis of the main body is visible when increasing the contrast (Fig. 7, b)).

The tidal features are barely visible in the near-infrared, in particular when looking at longer wavelengths (H- and K-band). This is a hint that the tail and the shell do not consist of old, red stars from the progenitor galaxies but rather might be formed during the merger and therefore host younger stars. This is also corroborated by the optical and near-infrared colour maps (Fig. 8), in which the tidal features appear slightly bluer than the main galaxy. The nucleus is redder compared to the galaxy, possibly due to dust extinction, which often is the case in the centers of galaxies. Apart from this, the colours do not change much with distance from the center, as also can be seen in the colour profiles (Fig. 9).

The radial profiles in BRJHK derived with the two different methods are similar, both showing a steep decrease of luminosity in the center and than an almost straight, flatter decline, which is typical for a spheroidal (bulge?) distribution in the center embedded in a disk. Fits of a Sersic-profile excluding the inner parts confirm a disk-like relation (the Sersic index n varies slightly between 1.0 and 1.8, depending on the filter).

There are two spiral galaxies south-east of NGC 4441, but they are probably background galaxies. In addition, our deep optical images show a galaxy cluster underlying. In the inner shell, there are three bright knots with an unclear nature. Two of them are point-like and might be foreground stars, but the leftmost one is slightly extended and diffuse. Thus, it might be connected to NGC 4441, but it is also possible that this is also a background object. Our results are in good agreement with the investigation of Bergvall (1981). Based on his spectral analysis, he claimed that NGC 4441 is an advanced merger, in which the star formation phase is going down, and the dominating spectral features are those of A–F stars. He stated that there is a faint bridge to one of the small Spirals south-east of NGC 4441. In our images, there is no indication for this, however. Furthermore, we think that these objects are rather background galaxies than companion galaxies.

NGC 4194

NGC 4194, the Medusa, is the prototypical S+E merger candidate due to its morphology. As predicted by simulations (Weil & Hernquist (1993), Kojima & Noguchi (1997)), this galaxy has a tail in one direction and shells on the opposite side. In our deep images, we detected two shells, a bright one attached to the galactic body at a distance of $32''$ (6.1 kpc) and a much fainter one further out ($1.06'$ or 12 kpc). The shells are connected via a faint stellar stream (Fig. 10). In contrast to the shells, the brightness distribution of which is smooth, the tail hosts several bright knots, which are probably HII regions. In the optical colour images (Fig 11), this idea is supported since the knots and their surroundings appear bluer than the main body. Furthermore, Aalto et al. (2001) found molecular gas in the tidal tail which might fuel the star forming regions.

Besides the remarkable tidal features, there is a prominent dust lane which contributes to the

characteristic appearance of the Medusa. Aalto & Hüttemeister (2000) found a large amount of molecular gas associated with the dust lane. In the near-infrared images, the morphology of the main body is not affected by dust extinction and thus appears symmetric. The inner shell is visible in the near-infrared, however fainter relative to the galactic body than in the optical. The outer shell is not seen, the tail is very weak and diffuse. In particular, the bright knots visible in the optical can only barely be detected, which is a strong indication that they do not consist of old stars. This is in agreement with the colour maps, in which the shells appear bluish. The dust lane emerges in the colour maps as a broad, red area.

Although the main galactic body appears to be symmetric at a first glance, the unsharp masking image reveals disturbances, in particular at the beginning of the tidal tail.

When zooming into the center, the shell-like structure proceeds also in the inner region. Bright, distinct clumps are found, which could be identified as regions of ongoing star formation using HST images (Weistrop et al. (2004)). These clumps have blue colours as seen in the colour maps, which is typical for star forming regions. The innermost center, however, is red, both in optical and near-infrared colour maps. This is probably due to a large amount of dust.

The radial profiles can be fitted with a Sersic-index close to one, which corresponds to an exponential disk. In the inner region, the decline is steep, typical for a bulge. The overall colours do not change much with distance

North-east of the tidal tail, there is a small, extended object of unknown nature. It is not yet clear, if it belongs to the system (either formed during the merger or surviving it) or if it is a background object.

NGC 4004

The absence of a distinct galactic main body is the most remarkable feature of NGC 4004. Instead, this galaxy consists of a long chain of bright knots, which is twisted in the region in which the galaxy is brightest and thus is called the main region here (Fig. 13). North of the turned-around chain there are also a few knots embedded in a diffuse, three-peaked stellar distribution. The chain of knots ends up in a tail 1.48' long (19.4 kpc). South-east of the tip of the tail, there is faint fuzzy stellar object at a distance of 1.85' (24.2 kpc) from the main region, probably torn out during the merger. Also north of the galaxy, there are a few faint patches of what appears to be stellar debris. In total, the north-south extension of NGC 4004 is 2.85' (37.3 kpc).

In the near-infrared, only the main region is visible, but only faint hints of the tail. The knots in the tail might be younger than in the main region and thus not host a significant fraction of red stars, which would be detectable in the near-infrared bands. The diffuse northern part is visible in the long wavelengths. Thus, the stellar populations in this region are probably older than in the tail.

Although this galaxy does not consist of a distinct main body, neither disk-like or ellipsoid, the radial profiles derived with both presented methods show a rather smooth run, comparable to a light distribution of a disk galaxy (Fig. 14). The colours vary with distance, as can be seen in the colour maps. The bright knots in the tail are bluer than the main region, indicating ongoing star formation. The inner part of the center is extremely red, and the outskirts of the northern distribution are bluer than the central galaxy part. For this galaxy, the two different methods give different results in the radial light distribution, in particular in the

distribution of the colours. This is not surprising, because NGC 4004 differs extremely from a typical galaxy with a defined bright center. Here, the bright knots even in the outer part of the tail contribute additionally to the light that becomes part of the 'inner part' of the artificial radius.

NGC 4004 has a companion elliptical galaxy at a distance of $3.11'$ (40.6 kpc). This galaxy shows no signs of interaction and thus probably is not the only or even the main cause of the extremely disturbed appearance of NGC 4004.

NGC 5067

NGC 5607 shows a disturbed and irregular but generally spiral-like structure on our deep optical images (Fig. 16). The unsharp masking images highlights this structure particularly. When looking at the inner part, an asymmetry is visible to the western direction, where a large arc, maybe a distorted spiral arm is visible. An inspection of the whole galaxy additionally reveals a fainter, larger 'hook' to the east, with an extension out to $57''$, corresponding to 30 kpc. This feature is patchy and hosts some brighter regions at the largest distance from the center. In addition, a faint spur to the south is visible in the deep images with no obvious relation to either the western or the eastern loop. It extends out to a distance of $1.51'$ (44.1 kpc) from the center.

Neither the spur nor the eastern loop are seen in the near-infrared regime. Only the closer, western arm is clearly visible in J and faintly seen in H and K.

In particular in the B-R and B-K colour maps (Fig. 17), radial variations are seen within the disk. The 'inter-arm' regions appear redder than the 'arms', because this is where new stars are formed, and this galaxy has an enhanced star formation activity (see below). The radial light distribution is typical for a disk galaxy with a steep decrease in the inner part (bulge) and a flat one in the outer part (Fig. 18), corresponding to a disk, which is corroborated by the derived Sersic index of ~ 1 .

UGC 8264

The very compact galaxy UGC 8264 has a very diffuse and patchy tidal tail emanating to the east, which turns around almost 180 degrees northwards (Fig. 19). The tip of the tail consists of four bright knots in a row, which might be a tidal dwarf galaxy in the making. These clumps have a total diameter of $20''$, equal to 6 kpc. The distance from the galactic center is $1.19'$ (21.5 kpc), the total length of the tail in projection is $\sim 2.18'$, corresponding to 39.5 kpc. A further tidal feature found in the deep optical images is a faint spur to the south, similar to what is observed in NGC 5607. In the western direction a bright clump is $12.3''$ (3.7 kpc) separated from the main galaxy. This clump might either be tidal debris or the remnant nucleus of one of the merged galaxies. The main body of UGC 8264 has only a diameter of $22'$ (6.7 kpc), excluding the western clump.

In the near-infrared, only the main body is visible, and the separation between the galactic body and the western clump is even more apparent than in the optical. Neither the tail nor the knots at the tip are seen in the long wavelengths. This is a strong indication that the knots consist of newly formed stars only, which is in good agreement with the tidal dwarf galaxy hypothesis.

The colours of UGC 8264 (Fig. 20) furthermore support the assumption that these knots are star forming, because they appear bluer than the main galaxy. The center of the main body

is also bluer than the surrounding region, which fits the star forming nature of this galaxy (see below). This region is elongated in the east–west direction. The structure of the different colours is also reflected in the colours profiles (Fig. 21) and is particularly seen in the (B–R) and (J–K) profiles, which show the short scale colour variations within the galactic body. The radial surface brightness profiles are difficult to interpret due to the small extension of the galaxy. In the near-infrared, the profiles are fitted by a Sersic index equivalent to a disk distribution, but in the optical, the situation is more complex, indicating two components with a different degree of brightness decline.

Arp 161

Arp 161 is a compact HII galaxy (Kewley et al. (2001)) with a faint optical fan to the south-west with a length of $\sim 45''$ (16.2 kpc) (Fig. 22). The main body of the galaxy has only a diameter of $24''$, corresponding to 8.6 kpc. Only near-infrared images from our observing runs are available here, therefore a DSS2 image is shown. In the near-infrared, the beginning of the fan is visible.

Dopita et al. (2000) observed this galaxy in the optical and $H\alpha$ and found significant differences in the $H\alpha$ morphology. Only the beginning of the fan is visible in $H\alpha$, but more remarkably are star forming knots west of the galactic body and a region of diffuse emission north of the main body, which have no counterpart in the continuum images. The star-forming character of Arp 161 is also analysed by Raimann et al. (2000), who obtained stellar population synthesis and found a young, dominating population and an old underlying population.

The near-infrared colours (Fig. 23) show a red nucleus, which is elongated in east–west direction in accordance to the major axis.

The radial surface brightness distribution can be described by a pure disk without any central spheroid, characterised by a Sersic index of ~ 1 .

Arp 164

Not much can be found in the literature about Arp 164. This object is a peculiar galaxy with a short spike to the north and two loops, a brighter inner and a fainter outer one, to the south-east (Fig. 24, particularly c)). The structure in the center is regular, smooth and featureless. The colour distribution is also smooth and does not change much over the disk, not even in the tidal features (Fig. 25). The radial profiles are typical for disk galaxies with a bulge in the center.

ESO 156-18

This galaxy is mentioned in the catalog of galaxies with shells by Malin & Carter (1983). As can be seen in Fig. 26, the main body has a boxy shape embedded in a diffuse light distribution and a pair of shells on both sides parallel to the minor axis. The inner shells are brighter and more compact, the outer are fainter and more diffuse. The inner shells are very symmetric with respect to the galactic center with a distance to the center of $22''$ (18.7 kpc) (north-east) and $23''$ (19.5 kpc) (south-west), respectively. The outer shells, in contrast, have different distances: $49''$ (41.6 kpc) (north-east) in comparison to $34''$ (28.8 kpc) (south-east). The optical colour (Fig. 26) of this galaxy varies slightly over the disk. The center is reddish,

probably due to dust, the inner shells are slightly bluer than the main body. This is in agreement with what was found in the other galaxies with shells in this sample.

The radial profiles derived using the ellipse fitting method show a broad ellipsoidal brightness distribution forming the main body. Still, the outer parts can be fitted with a typical exponential disk. The differences between the ellipse fitting results and those from the pixel summation method, which shows a steep decline in the 'center', can be explained by the presence of an extremely bright star nearby, which could not be properly removed from the images because of artefacts due to overexposing. Thus, additional light from this star is counted in the pixel summation method, pretending a brighter 'nucleus'.

ESO 159-03

Also ESO 159-03 is found in the catalog of shell galaxies (Malin & Carter (1983)). In the optical images (Fig. 28) several shells and fragments are visible. As in the case of ESO 156-18, the shells are roughly orientated in the direction of the major axis of the galactic body, but not as strict as in ESO 156-18. To the south-west, a faint tail is furthermore visible, connecting two shells with the main body of the galaxy. In particular these southern shells are remarkably sharp and distinct. Overall, this galaxy is one that rather closely resembles the Medusa and NGC 4441. The inner shell has a distance of 1.13' (16.2 kpc) from the center, the fainter outer one a distance of $\sim 1.7'$ (24.3 kpc). The center of this galaxy does not show any internal substructure, in contrast to what is found, e.g., in the Medusa. However, the unsharp masking image shows, that the main body is far from having a symmetric and regular distribution. Also to the north there is a faint shell-like feature, with a distance of 1.52' (21.7 kpc) from the center.

When looking at the optical colour image (Fig. 29), the most remarkable feature is the reddish 'bar' along the major axis, whereas the remainder of the galaxy is bluer. The colour varies slightly with distance, as can be seen in the colour profile. The radial brightness distribution can be described with a broad central spheroid (a possible bulge) and a disk in the outer parts. Here, the Sersic profile fitting does not provide a distinct classification into disk or spheroidal light distribution. This might be the result of the advanced, evolved merger with a more relaxed stellar distribution. Thus, this object warrants further investigation, because it may take an 'evolutionary sequence' starting with the Medusa and including NGC 4441 one step further.

ESO 416-09

This galaxy has two tails, a shorter one with a length of 1.02' (25.5 kpc) measured from the center to the east and a longer one (length from the center 2.32', i.e., 58 kpc) on the opposite side to the West (Fig. 30). This galaxy is suggested to have a weakly active nucleus of the LINER (Low Ionisation nuclear emission line region) (Maia et al. (1987)) type, showing gaseous emission from the nucleus which cannot be explained by star formation alone. However, the authors of this paper could not provide equivalent widths of the investigated [OIII] and H α lines, which makes this classification doubtful.

The compact main body of the galaxy seems to consist of several components or complete shells. This is also seen in the radial profiles (Fig. 31), which shows a 'double-bulge' run, i.e., after a steep decline typical for a bulge, there is a bump, which again is steeper than the remaining light profile of the tidal features. We do not show a B-R colour map here, because

the R–band image was observed under much worse seeing conditions compared to the B–band image (full width of half maximum was 8 pixels compared to 2.5 pixels). Thus, it was not possible to properly correct for the seeing. Smoothing the image by such a large factor and subtracting the images led to artefacts which made the interpretation difficult. For the same reason, no B–R colour profile is shown.

NGC 2996

Another galaxy from the shell galaxy catalog (Malin & Carter (1983)) is NGC 2996. Among the few references in the literature concerning this galaxy, there is the study of Forbes et al. (1994) investigating shell galaxies with respect to a second nucleus. In agreement with our observations, they did not find any signs of a second nucleus, arguing that the short phase where both the remnant nuclei and shells are visible is already over. As seen in our images (Fig. 32), the shells are clearly developed. The largest shell structure is found to the west at a distance of $1.17'$ (38.8 kpc) from the center, with a sharp and distinct edge. On the opposite side, there is a long, thin spike (length measured from the center: $1.8'$ (59.8 kpc)). Further shell fragments are found all around the galactic body, in particular to the north-east, north of the spike, at a distance of $40''$ (22.1 kpc) and on the other side of the spike, to the south-east, at a slightly larger distance of $55''$ (30.4 kpc). The unsharp masking image reveals further shell fragments even closer to the nucleus.

Unfortunately, there is a very bright star close to the spike, which could not properly removed from the images due to artefacts by overexposing. This affects the radial profiles (Fig. 33) derived by the pixel summation method. Nevertheless, the radial profiles achieved by ellipse fitting show a typical distribution of an inner bulge and an outer disk.

The colour map shows a red nucleus. The spike and the outer parts of the main body, in which the shell structure is already present, are in contrast bluer than the galactic body, in agreement with what we found in other galaxies.

ESO 341-04

This peculiar galaxy was a target of a few studies of interacting galaxies. Johansson (1988) obtained multicolour optical and near-infrared imaging as well as optical spectroscopy. He found signs of an old underlying population, in particular in the near-infrared images, as well as the presence of a young stellar population. He argues, that this galaxy is probably the merger with at least one disk galaxy among the progenitors. In the spectrum, he detected only H α emission, indicating a moderate present star formation rate. The dominating features in the spectrum are those of main sequence A stars with the characteristic absorption lines on top of a red continuum. A further detailed study is done by Bergvall et al. (1989). They found an optical light distribution following the $r^{1/4}$ -law valid for Ellipticals out to $\sim 60''$ (23.3 kpc) and a young stellar population formed in a burst ~ 0.8 Gyr ago. Thus, they claim this galaxy to be a juvenile Elliptical produced by a merger. Because the derived mass of the young stellar component is similar to the largest gas masses found in disk galaxies, they argue that a merger between two disk galaxies is more likely than a merger with an Elliptical involved in order to provide the gas mass necessary for the formed stars. They also cite as an evidence for the disk–disk merger the appearance of a faint tail to the East and interpret the loop to the south-west as a possible second tail seen in projection, which are formed during the encounter of two disk galaxies. But this could not be proved observationally.

The disturbed morphology of ESO 341-04 is clearly seen in the DSS2 image in Fig. 34. A bright loop to the south-west with a largest extension of 48'' (18.7 kpc) measured from the center is even visible in our near-infrared images, including the longest wavelength in the K-band. On the opposite side, there is a fainter, patchy plume only seen in the optical. The outermost feature traced in the DSS2 images is 1.6' (37.3 kpc) away from the center to the east.

In the near-infrared colour image, the nucleus appears reddish compared with the main body and the tidal loop. The colour profile shows a slight variation with respect to the distance to the center.

The light distribution is nicely represented by a bulge component in the central part and a disk in the outer galactic body. This is in disagreement with what Bergvall et al. (1989) found in the optical, where the light follows $r^{1/4}$ -law even into the outskirts.

ESO 511-35

Not much information can be found about this distorted galaxy in the literature. We show here a DSS2 image, because we only have near-infrared images available (Fig. 36) for our own survey. In the optical, a spur to the north-east with a length of 50'' (21.4 kpc) and on the opposite side to the south-west a second spur with a length of 32'' (13.7 kpc) are visible. In addition, to the west there is a faint diffuse fan with a length of 53'' (22.6 kpc) measured from the center. In the near-infrared images, these tidal features are not distinctive, but diffuse emission is detected at least in the direction of the south-west spur. The radial profiles in the H- and K-band can be fitted with an inner spheroidal and an outer disk component (Fig. 37).

IC 5065

IC 5065 was observed in the near-infrared only, thus, we show in Fig. 38 also a DSS2 image. This galaxy has a faint fuzzy plume to the North-West and a shell fragment to the South-East. It is therefore also found in the shell galaxy catalog of Malin & Carter (1983). In the near-infrared K-band, only the main galactic body is seen, with no internal structure, but a smooth distribution. The brightness distribution in the K-band is well described by a bulge in the inner part and a disk component further out (Fig. 39).

ESO 295-02

For completeness, a DSS2 image and the representation in polar coordinates are shown here for ESO 295-02. This galaxy is poorly studied so far, thus, not much is found in the literature. It is part of our sample, but due to observation constraints and its position on the sky, we could not observe it until now.

On the DSS image (Fig. 40), a plume is seen in the south-east of the main body, turning to the north-west. A diffuse fan is additionally emanating from the main disk to the north-west.

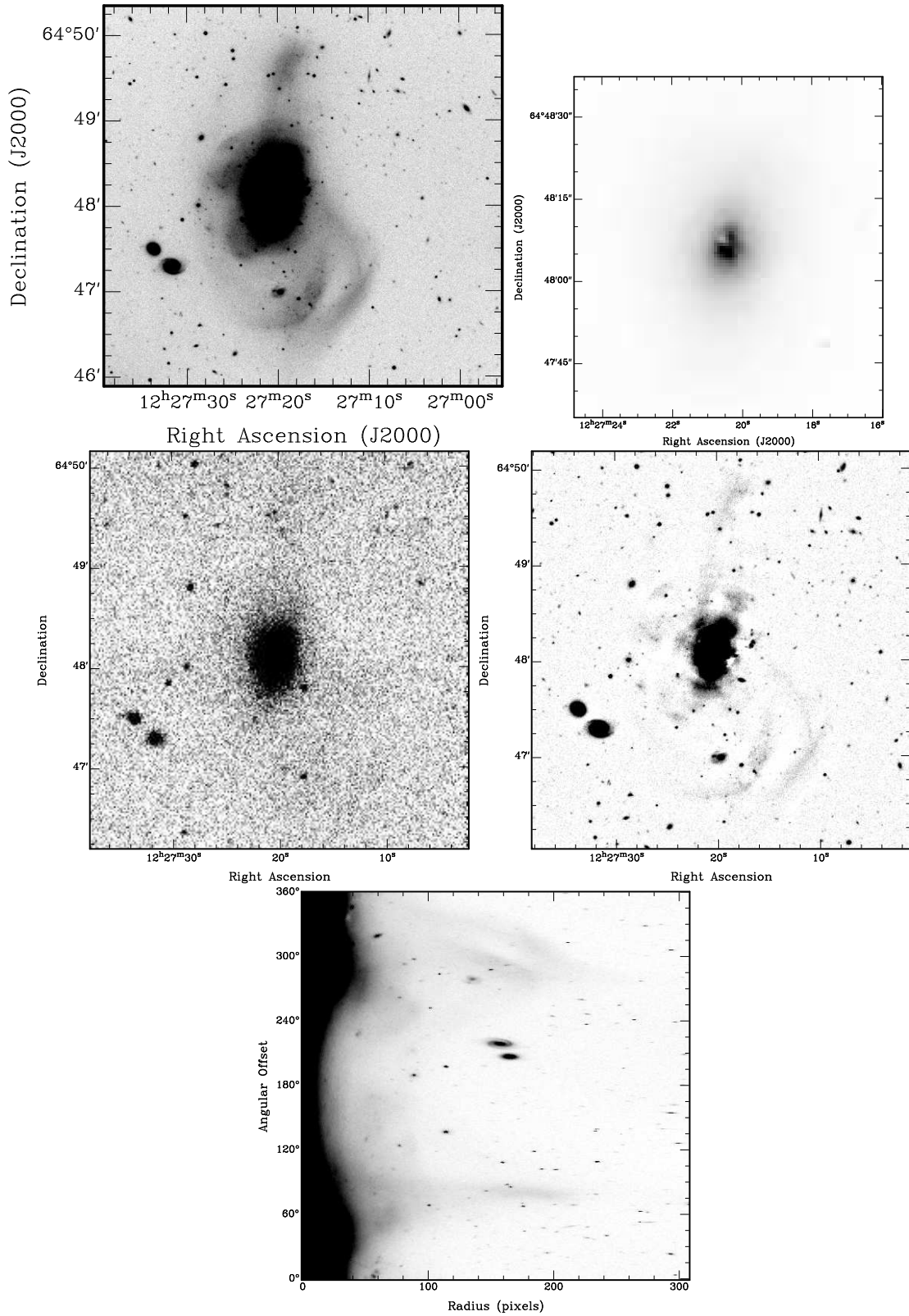


Figure 7: **NGC 4441**: (top left) R-band image, (top right) R-band image of the center, (middle left) K-band image, (middle right) R-band unsharp masking image ($r=23$ pix), (bottom) R-band image in polar coordinates.

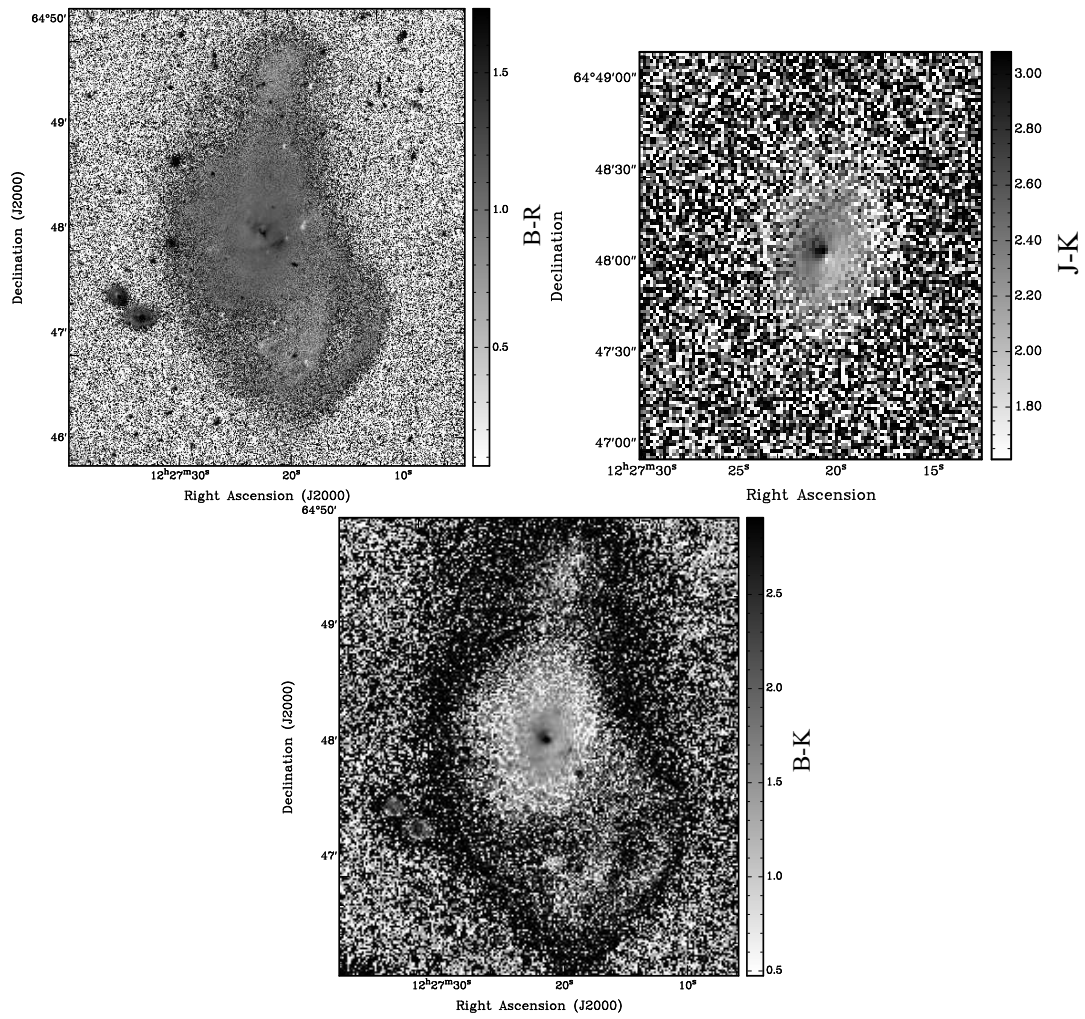


Figure 8: **NGC 4441**: (top left) B-R colour map, (top right) J-K colour map, (bottom) B-K colour map.

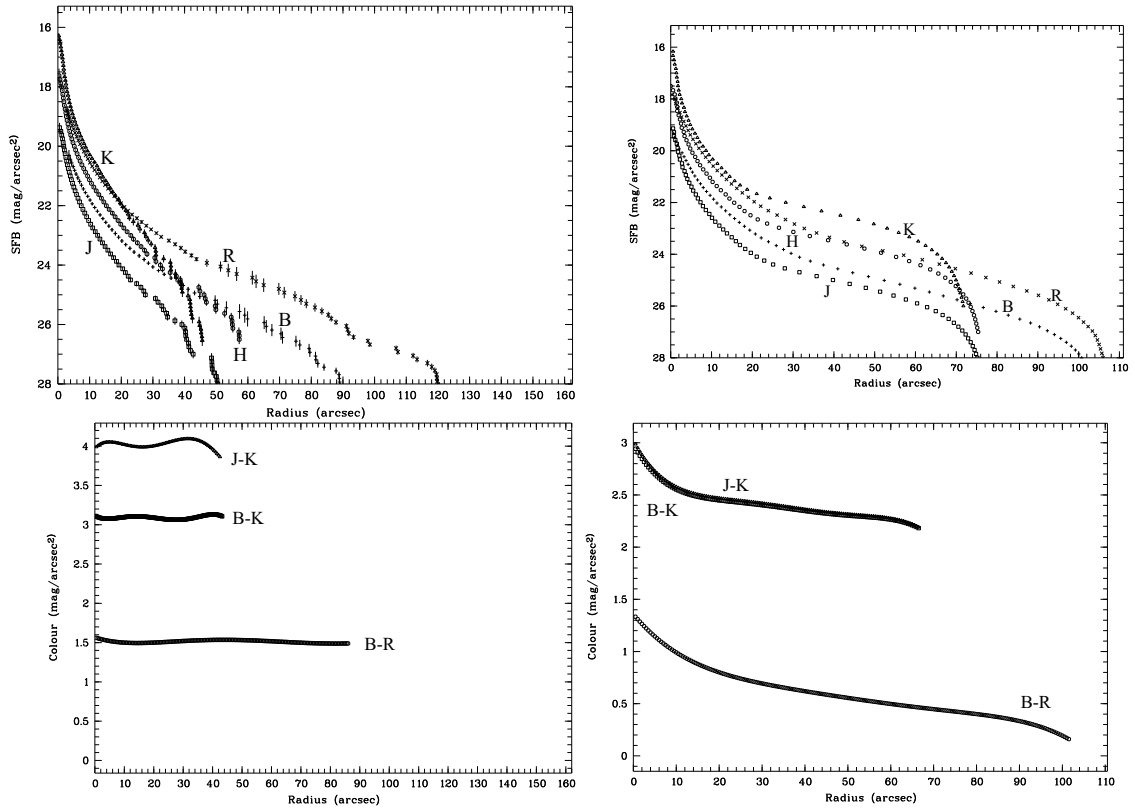


Figure 9: **NGC 4441**: (top left) radial profiles derived by ellipse fitting, (top right) radial profiles derived by pixel summation, (bottom left) colour profiles from the ellipse fitting, (bottom right) colour profiles from the pixel summation.

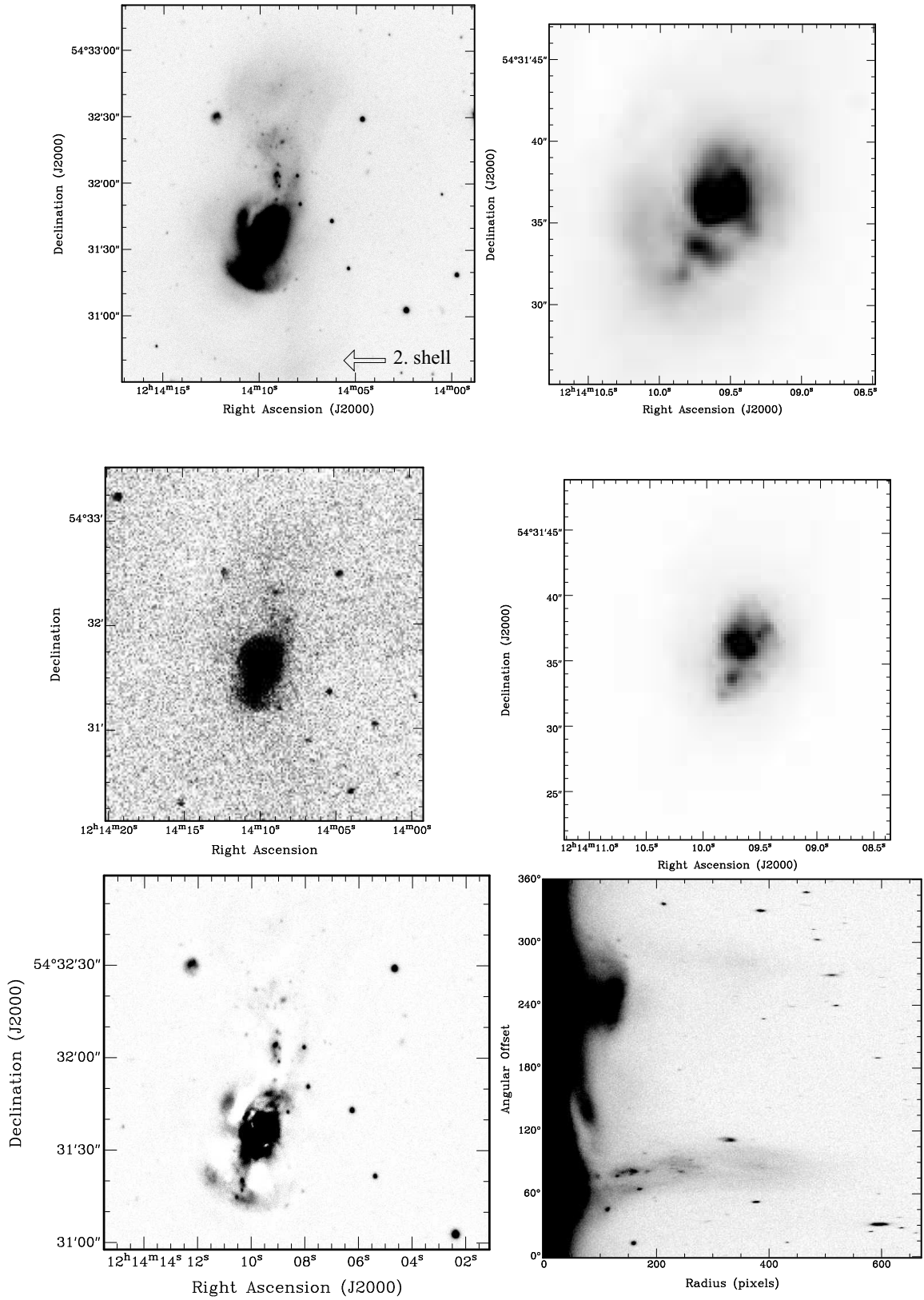


Figure 10: **NGC 4194**: (top left) V-band image, (top right) V-band image of the center, (middle left) K-band image, (middle right) K-band image of the center, (bottom left) V-band unsharp masking image ($r=38$ pix), (bottom right) V-band image in polar coordinates.

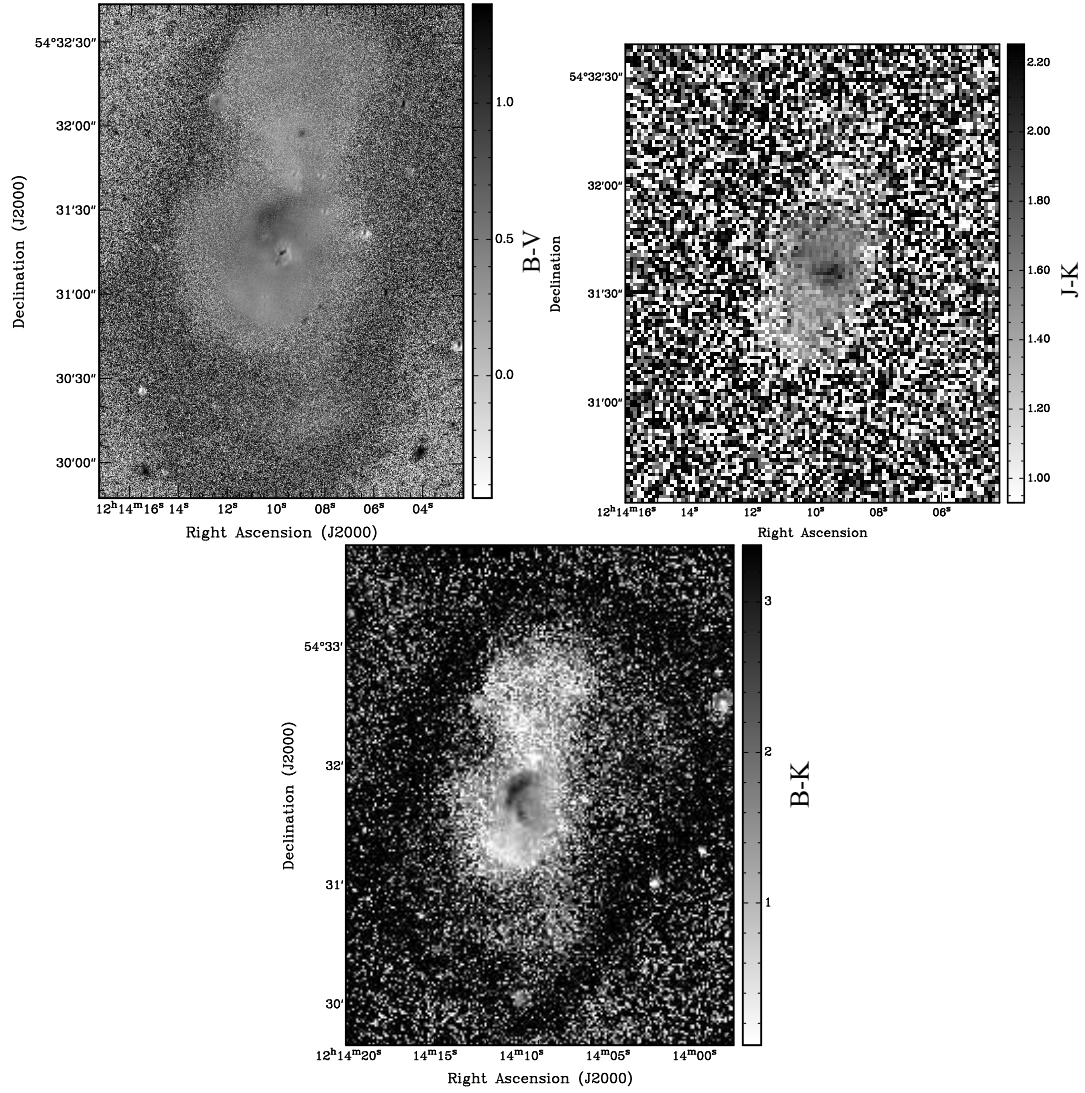


Figure 11: **NGC 4194:** (top left) B-V colour map, (top right) J-K colour map, (bottom) B-K colour map.

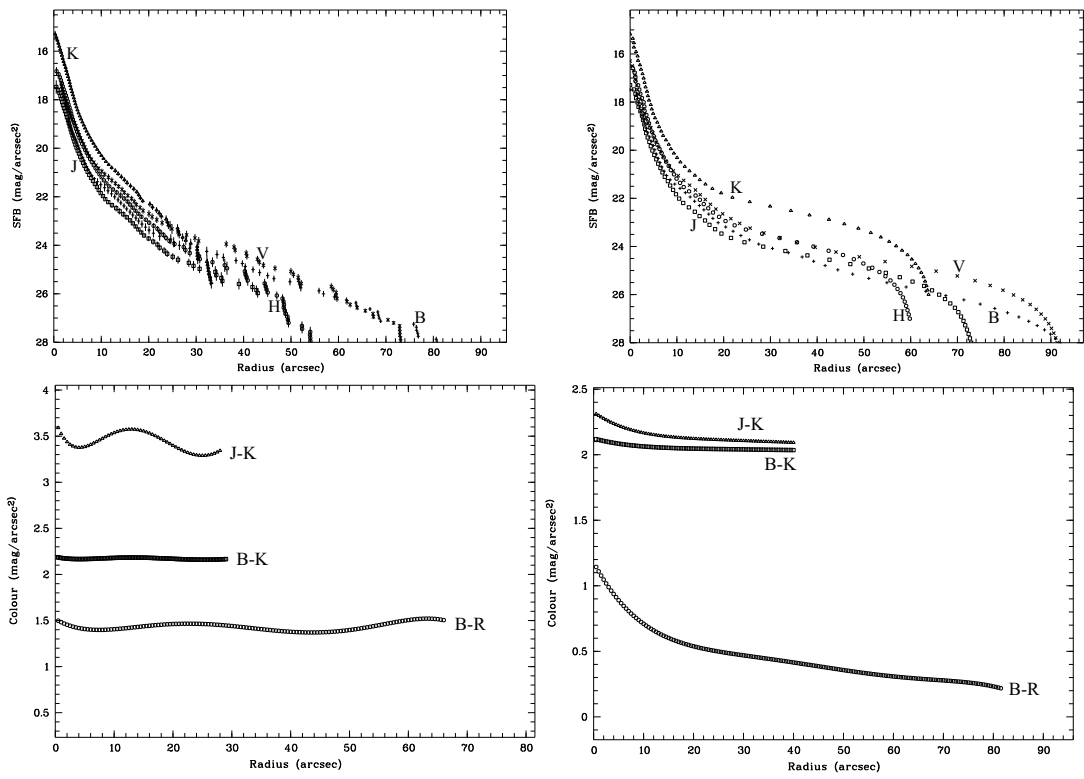


Figure 12: **NGC 4194**: (top left) radial profiles derived by ellipse fitting , (top right) radial profiles derived by pixel summation, (bottom left) colour profiles from the ellipse fitting, (bottom right) colour profiles from the pixel summation.

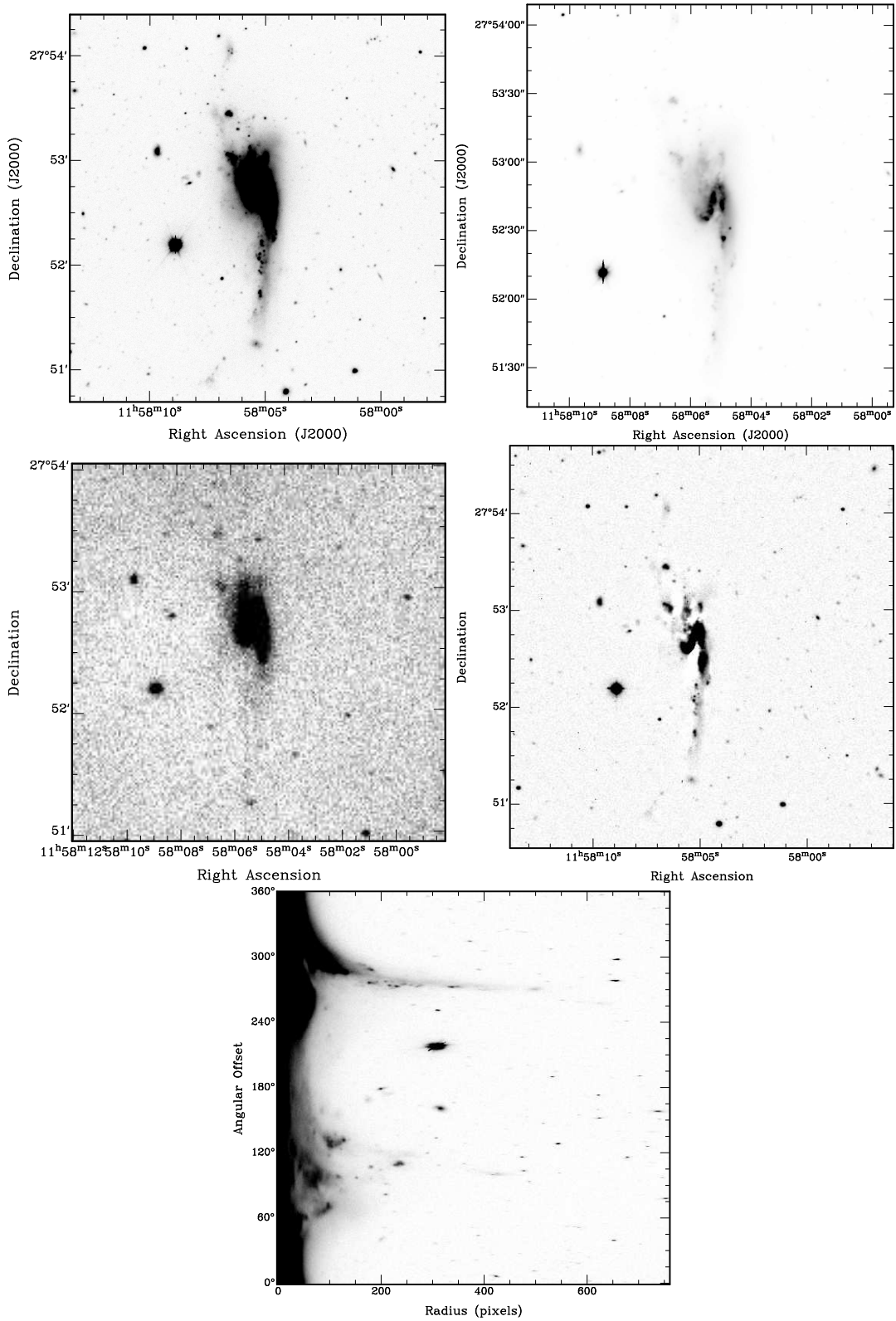


Figure 13: **NGC 4004**: (top left) R-band image, (top right) R-band image of the center, (middle left) K-band image (TCS), (middle right) R-band unsharp masking image ($r=18$ pix), (bottom) R-band image in polar coordinates.

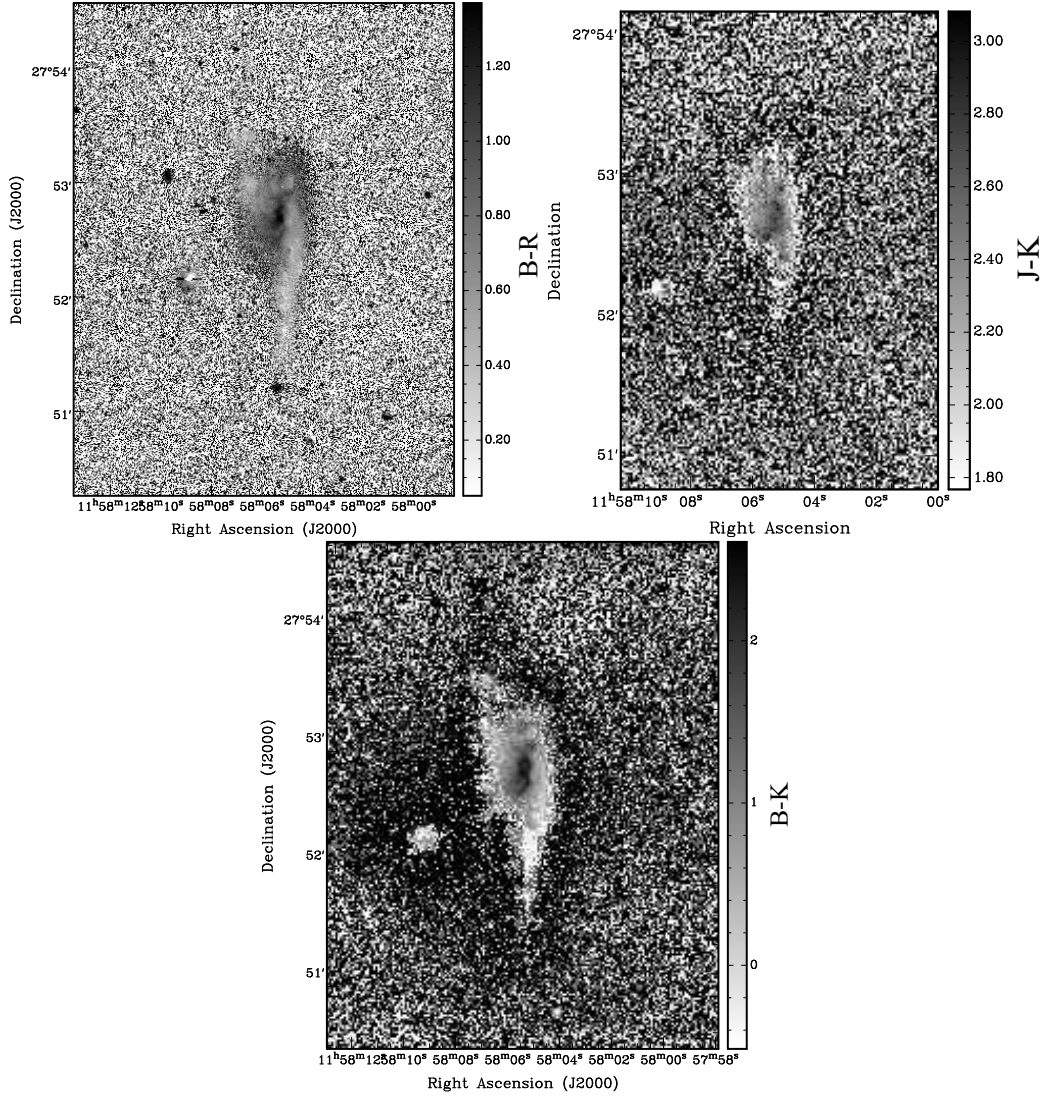


Figure 14: **NGC 4004:** (top left) B-R colour map, (top right) J-K colour map, (bottom) B-K colour map

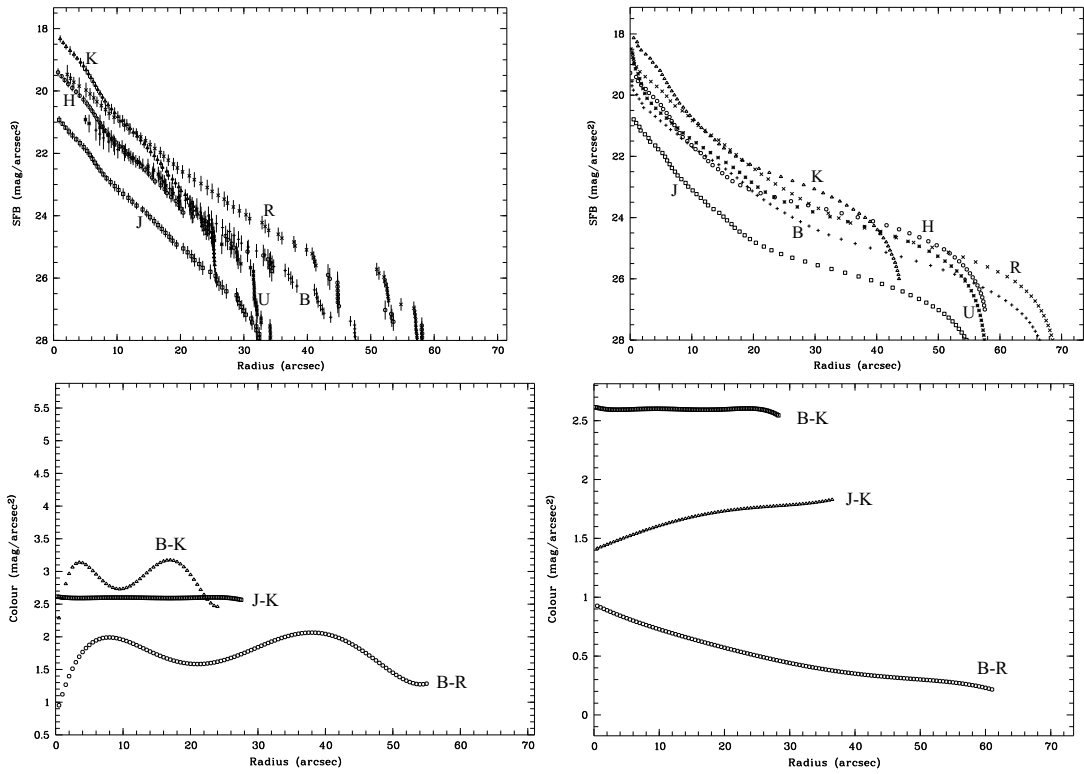


Figure 15: **NGC 4004:** (top left) radial profiles derived by ellipse fitting , (top right) radial profiles derived by pixel summation, (bottom left) colour profiles from the ellipse fitting, (bottom right) colour profiles from the pixel summation.

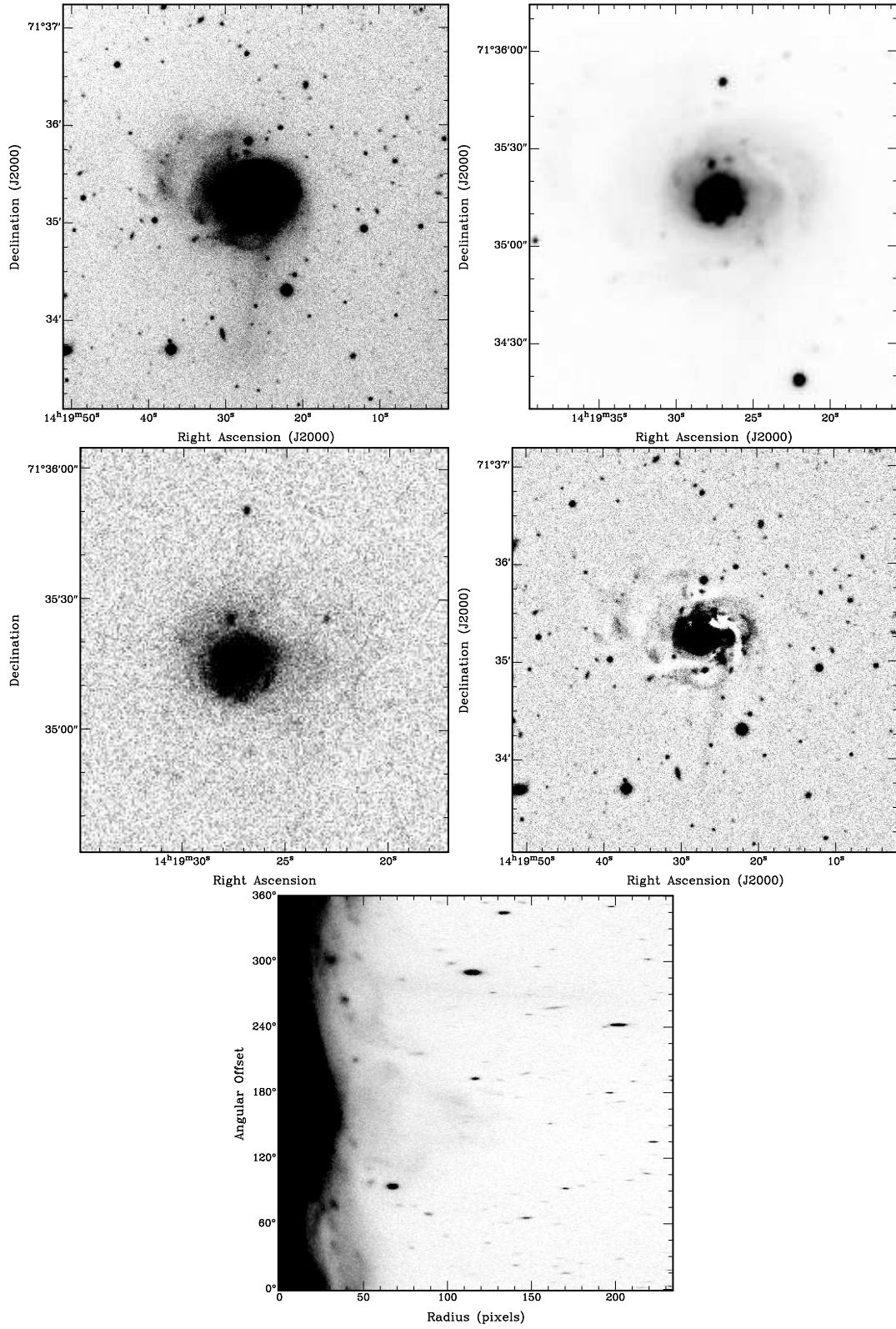


Figure 16: **NGC 5607**: (top left) R-band image, (top right) R-band image of the center, (middle left) K-band image, (middle right) R-band unsharp masking image ($r=23$ pix), (bottom) R-band image in polar coordinates.

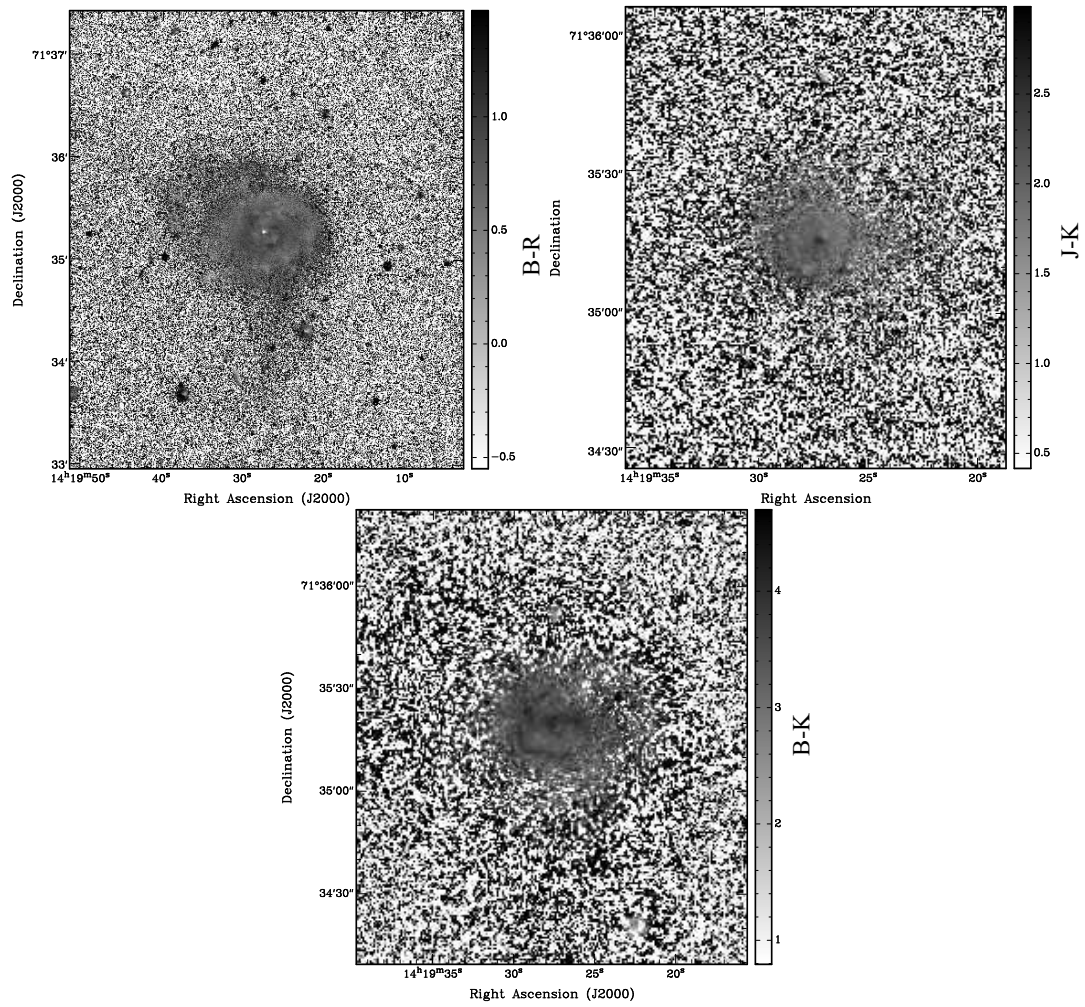


Figure 17: **NGC 5607**: (top left) B-R colour map, (top right) J-K colour map, (bottom) B-K colour map.

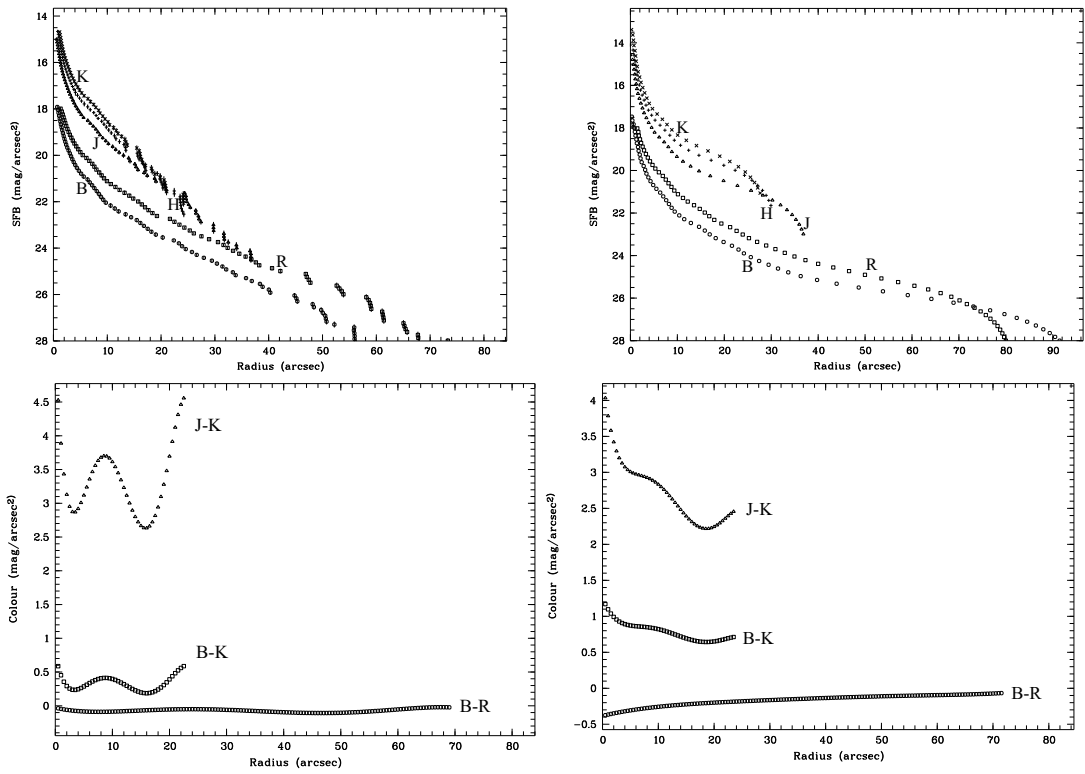


Figure 18: **NGC 5607**: (top left) radial profiles derived by ellipse fitting, (top right) radial profiles derived by pixel summation, (bottom left) colour profiles from the ellipse fitting, (bottom right) colour profiles from the pixel summation.

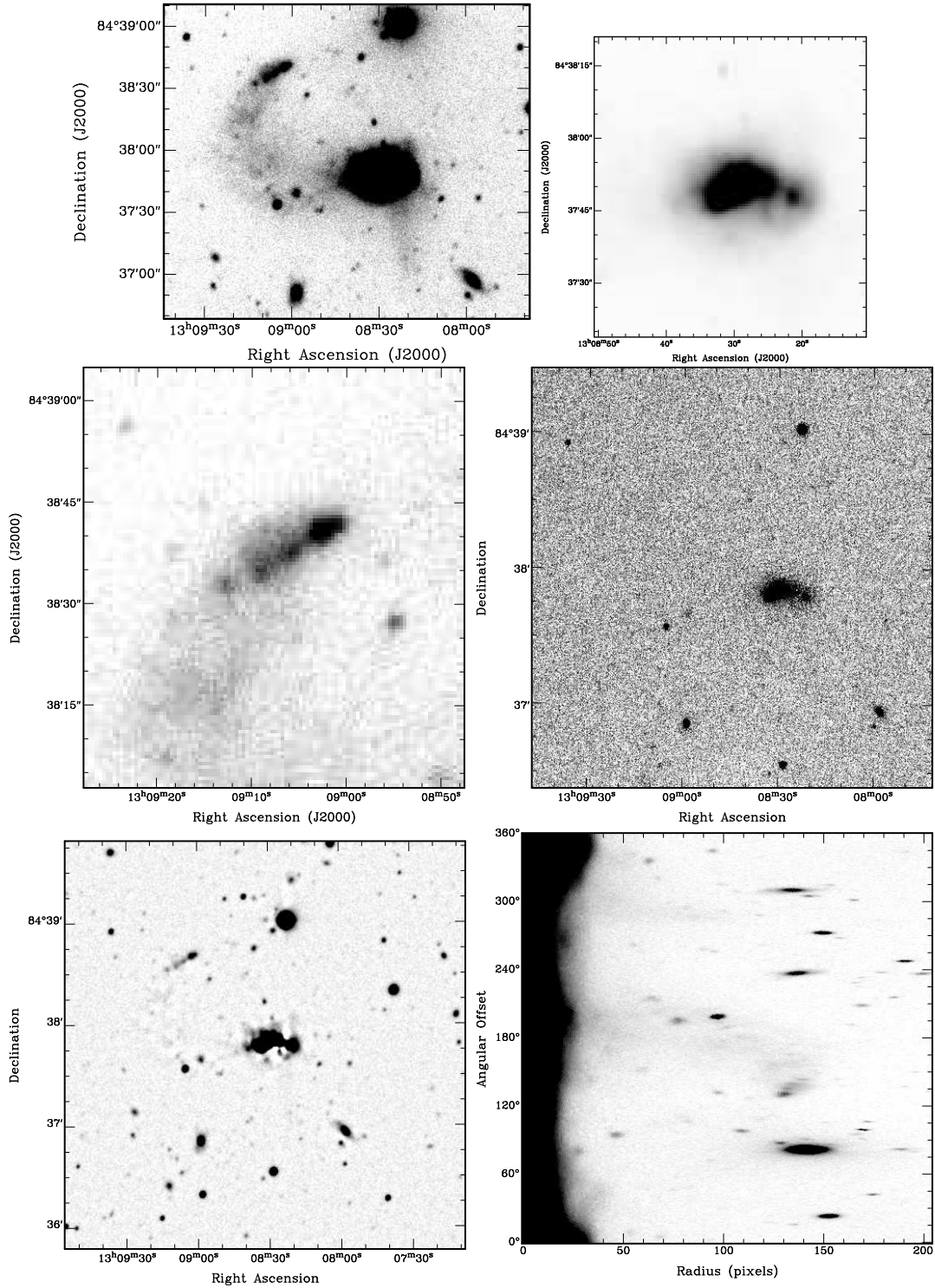


Figure 19: **UGC 8264**: (top left) R-band image, (top right) R-band image of the center, (middle left) R-band image of the tidal dwarf galaxy candidate, (middle right) K-band image, (top left) R-band unsharp masking image ($r=13$ pix), (top right) R-band image in polar coordinates.

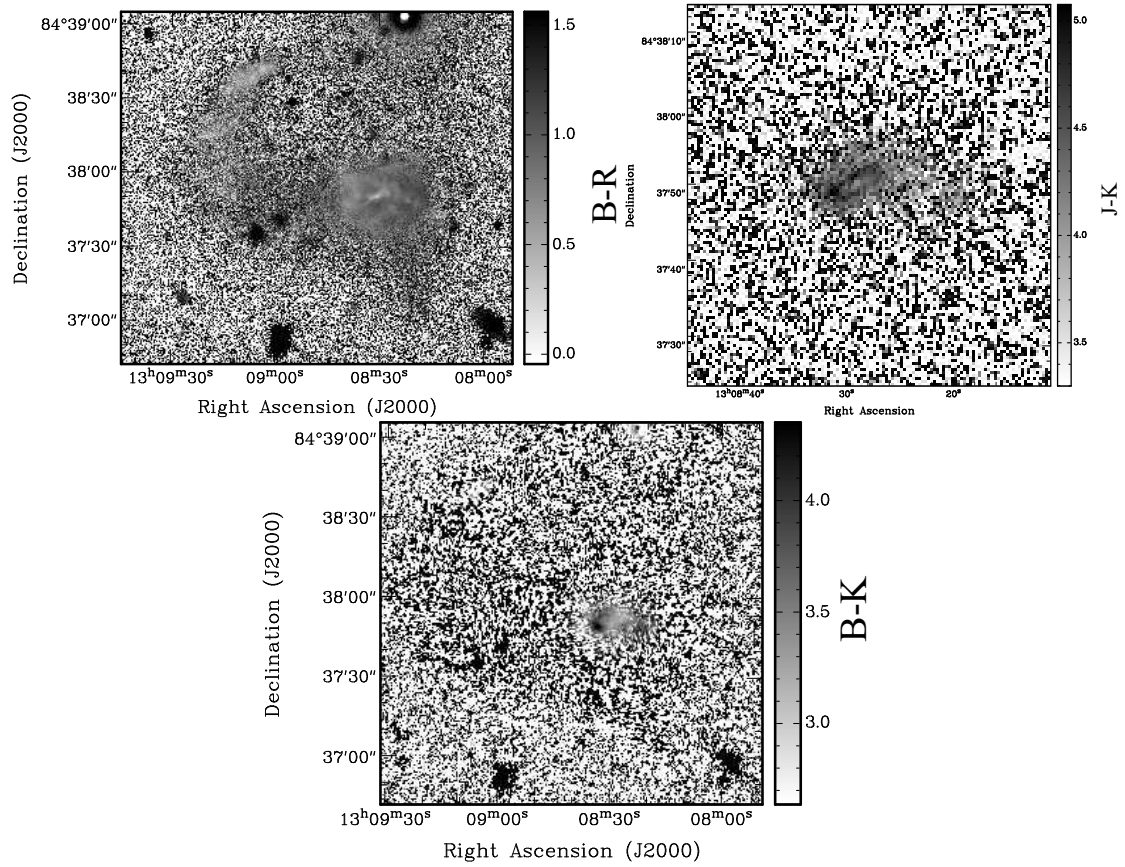


Figure 20: **UGC 8264**: (top left) B-R colour map, (top right) J-K colour map, (bottom) B-K colour map.

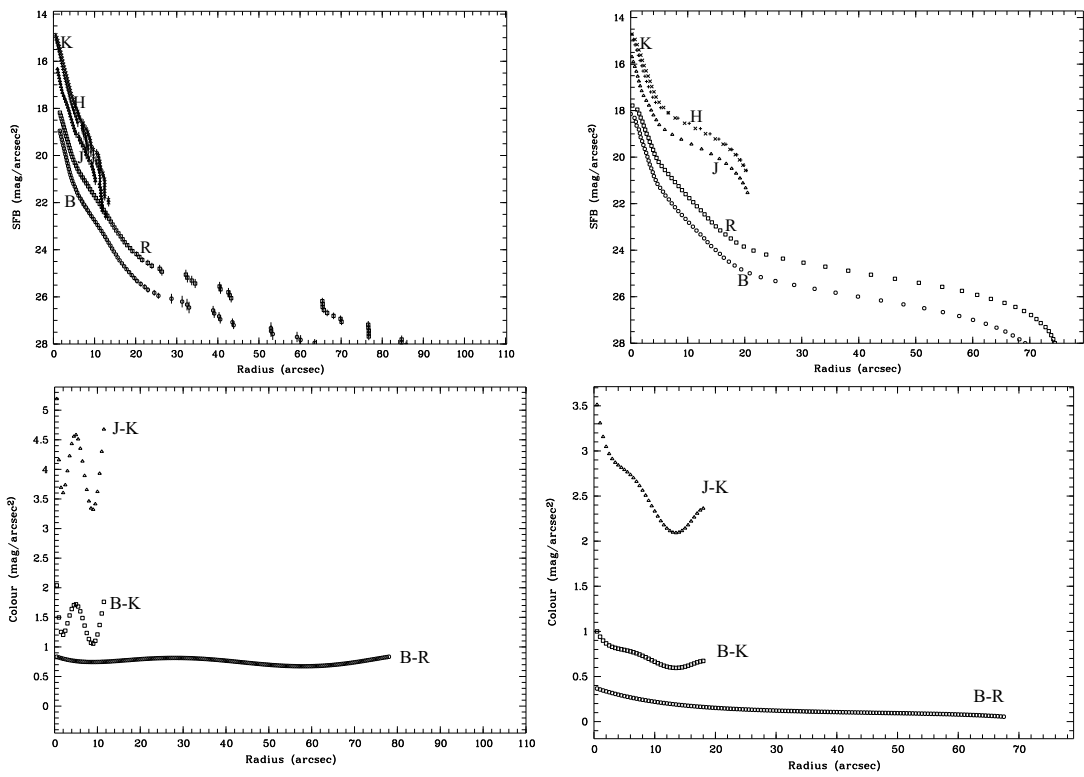


Figure 21: **UGC 8264**: (top left) radial profiles derived by ellipse fitting, (top right) radial profiles derived by pixel summation, (bottom left) colour profiles from the ellipse fitting, (bottom right) colour profiles from the pixel summation.

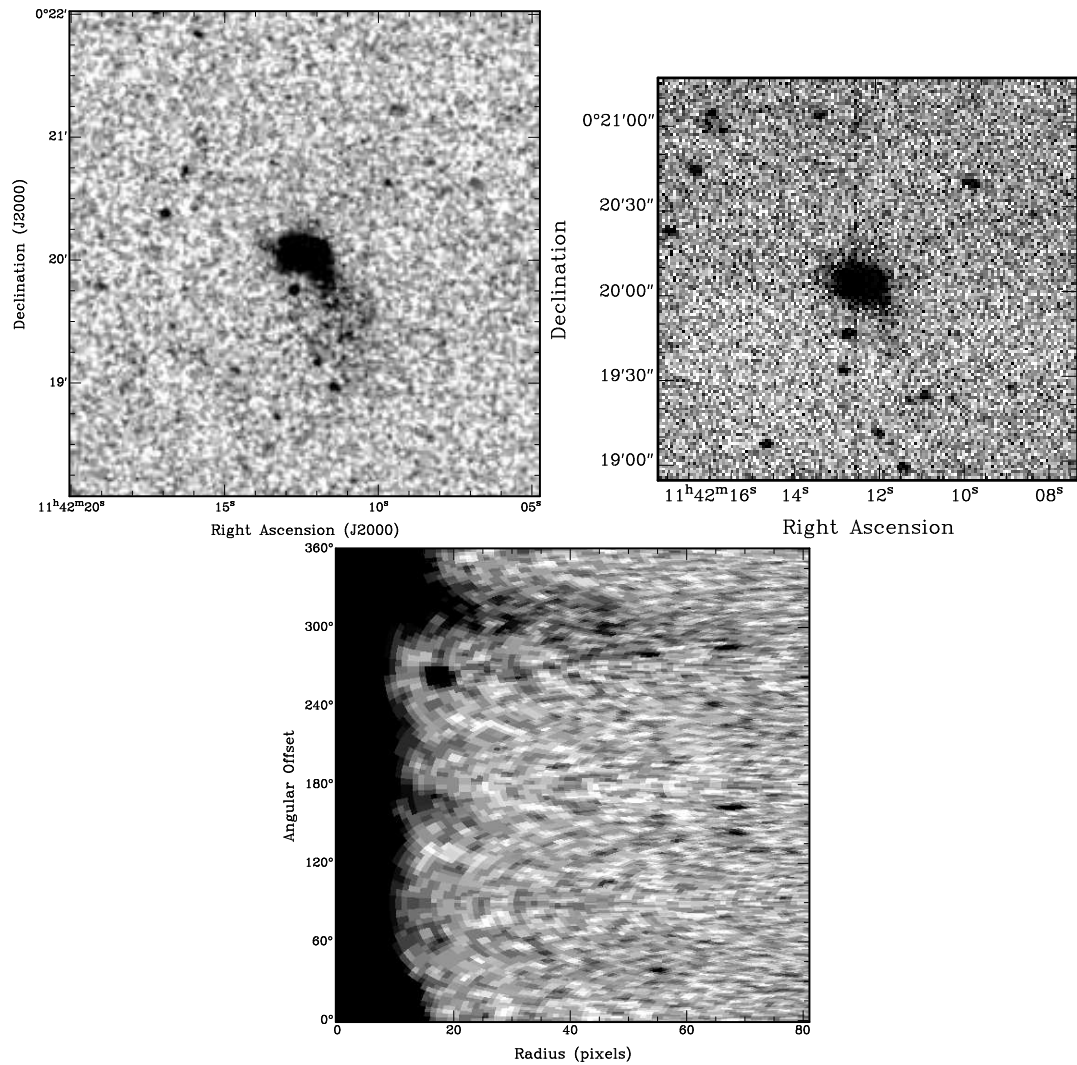


Figure 22: **Arp 161**: (top left) DSS2-red image, (top right) K-band image, (bottom) DSS2-red image in polar coordinates.

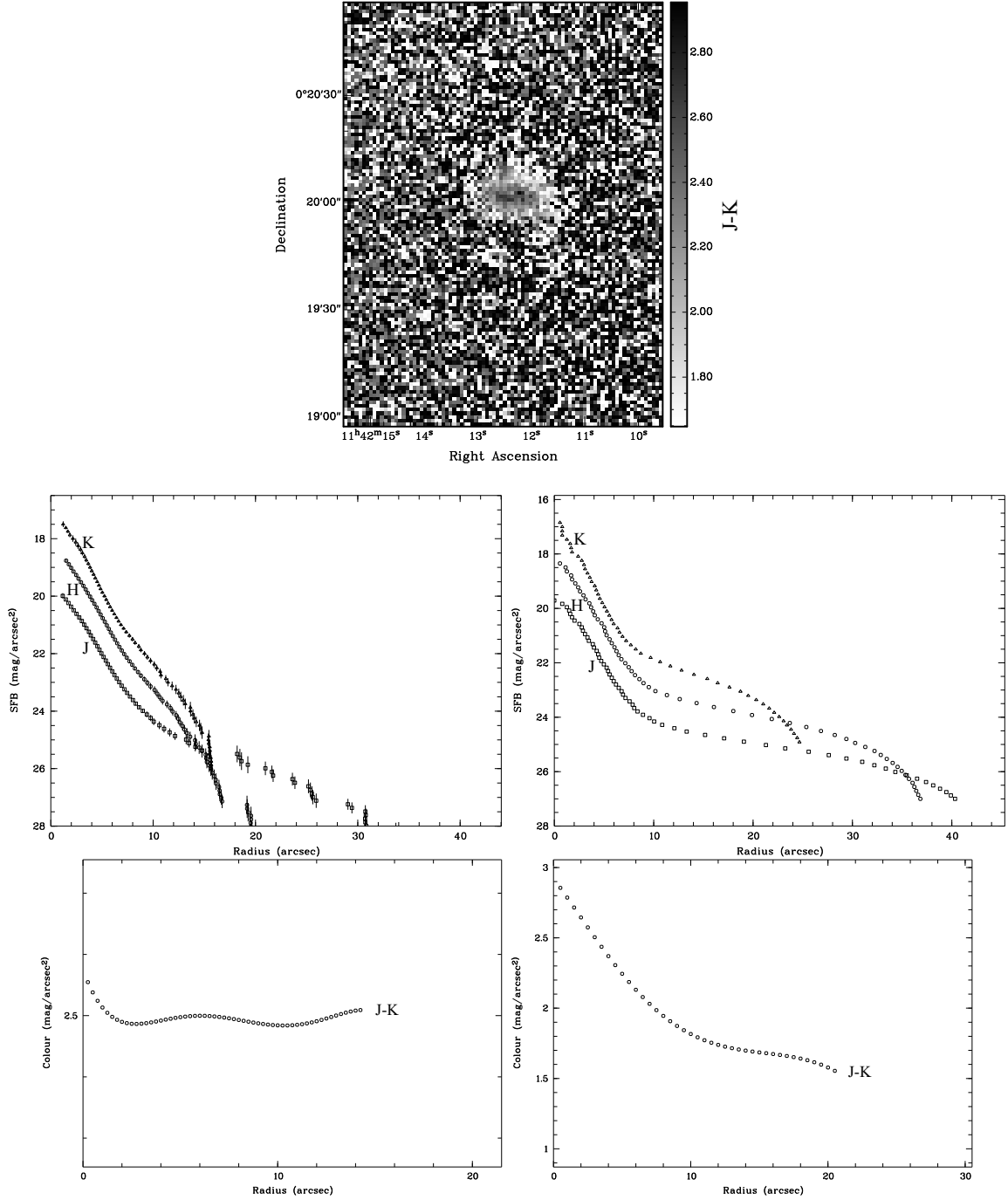


Figure 23: **Arp 161:** (top) J-K colour map, (middle left) radial profiles derived by ellipse fitting, (middle right) radial profiles derived by pixel summation, (bottom left) J-K colour profile from the ellipse fitting, (bottom right) J-K colour profile from the pixel summation.

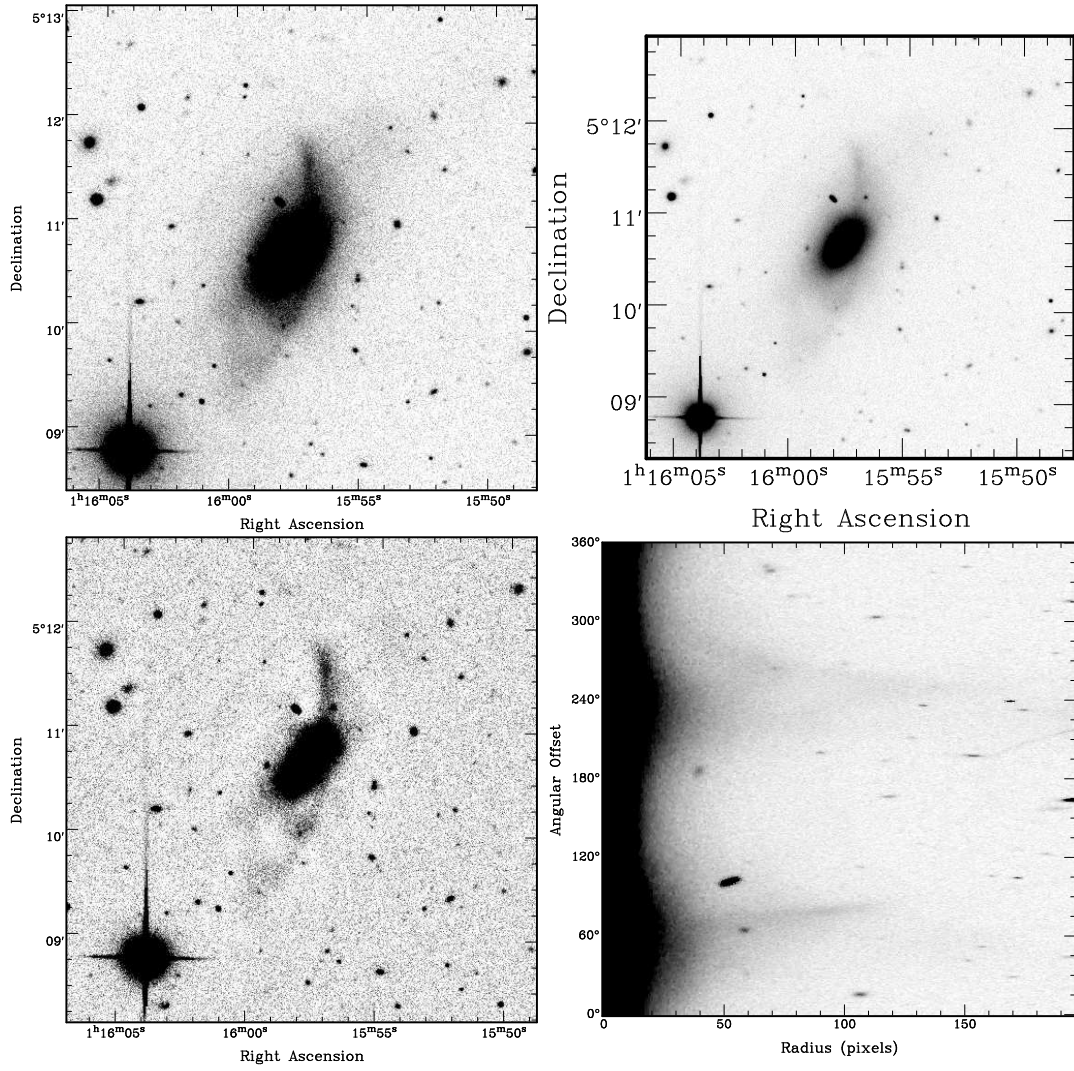


Figure 24: **Arp 164**: (top left) R-band image, (top right) R-band image of the center, (bottom left) R-band unsharp masking image, (bottom right) R-band image in polar coordinates. Data by courtesy of E. Wehner.

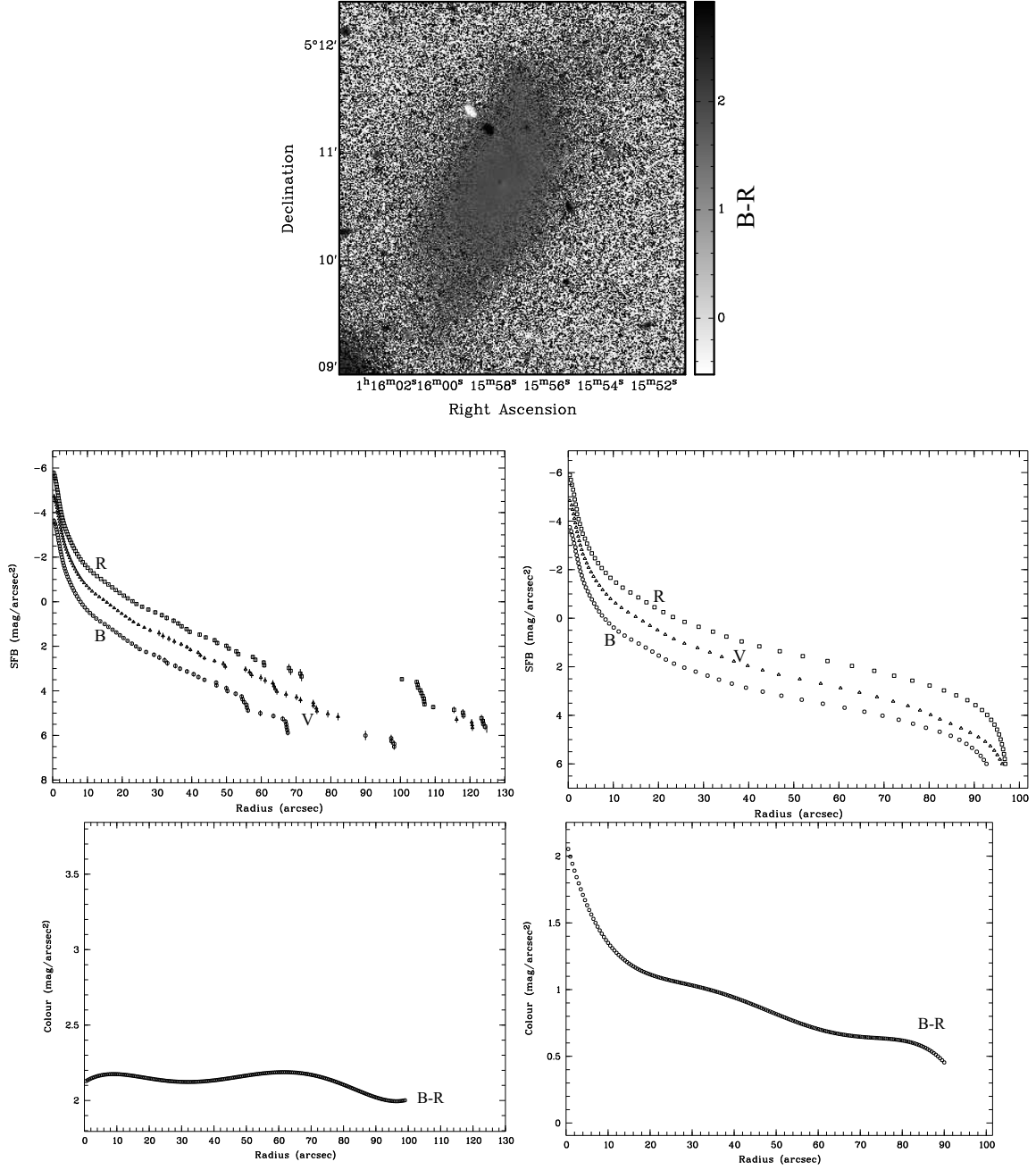


Figure 25: **Arp 164**: (top) B-R colour map, (middle left) radial profiles derived by ellipse fitting, (middle right) radial profiles derived by pixel summation, (bottom left) B-R colour profile from the ellipse fitting, (bottom right) B-R colour profile from the pixel summation.

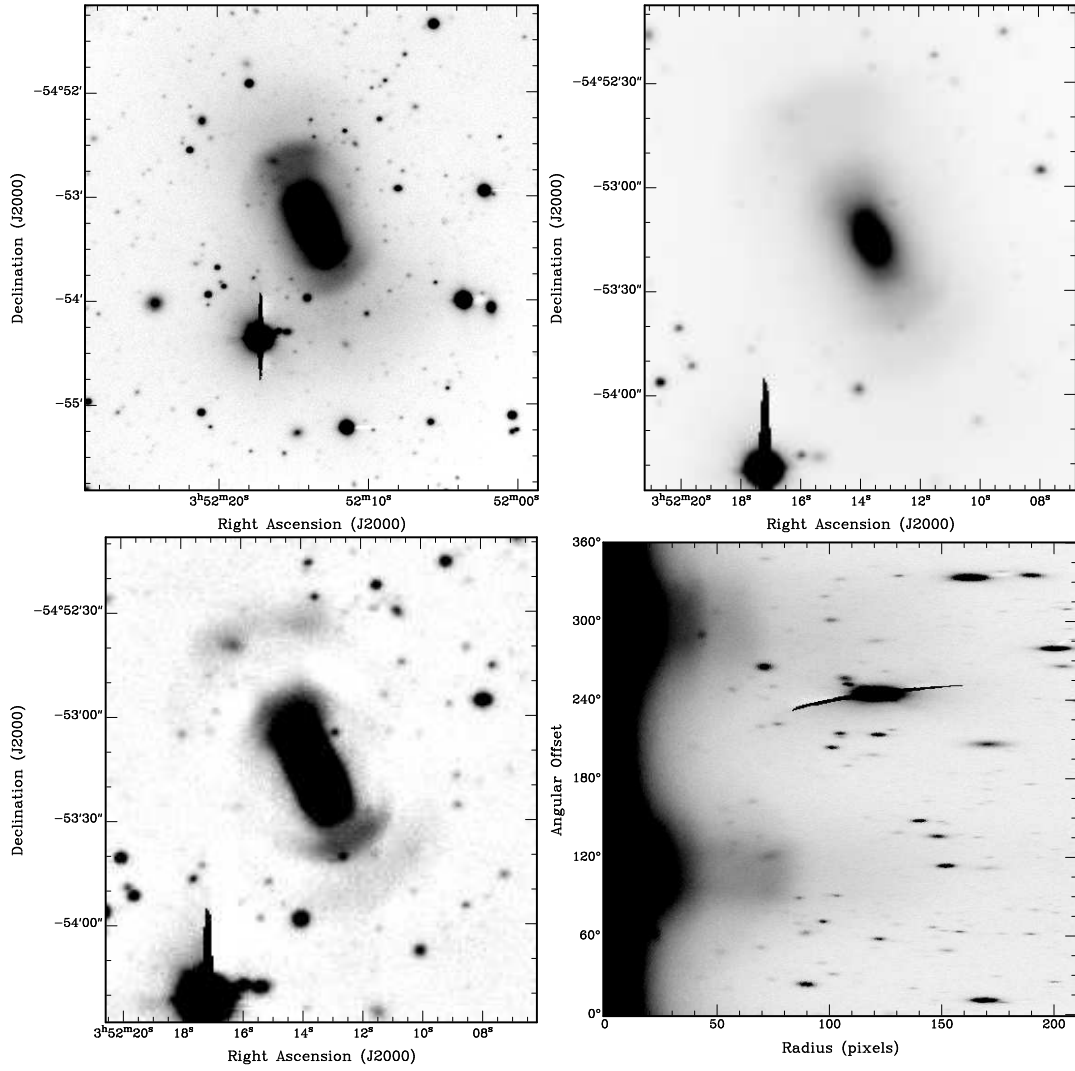


Figure 26: **ESO 156-18**: (top left) R-band image, (top right) R-band image of the center, (bottom left) R-band unsharp masking image ($r=28$ pix), (bottom right) R-band image in polar coordinates.

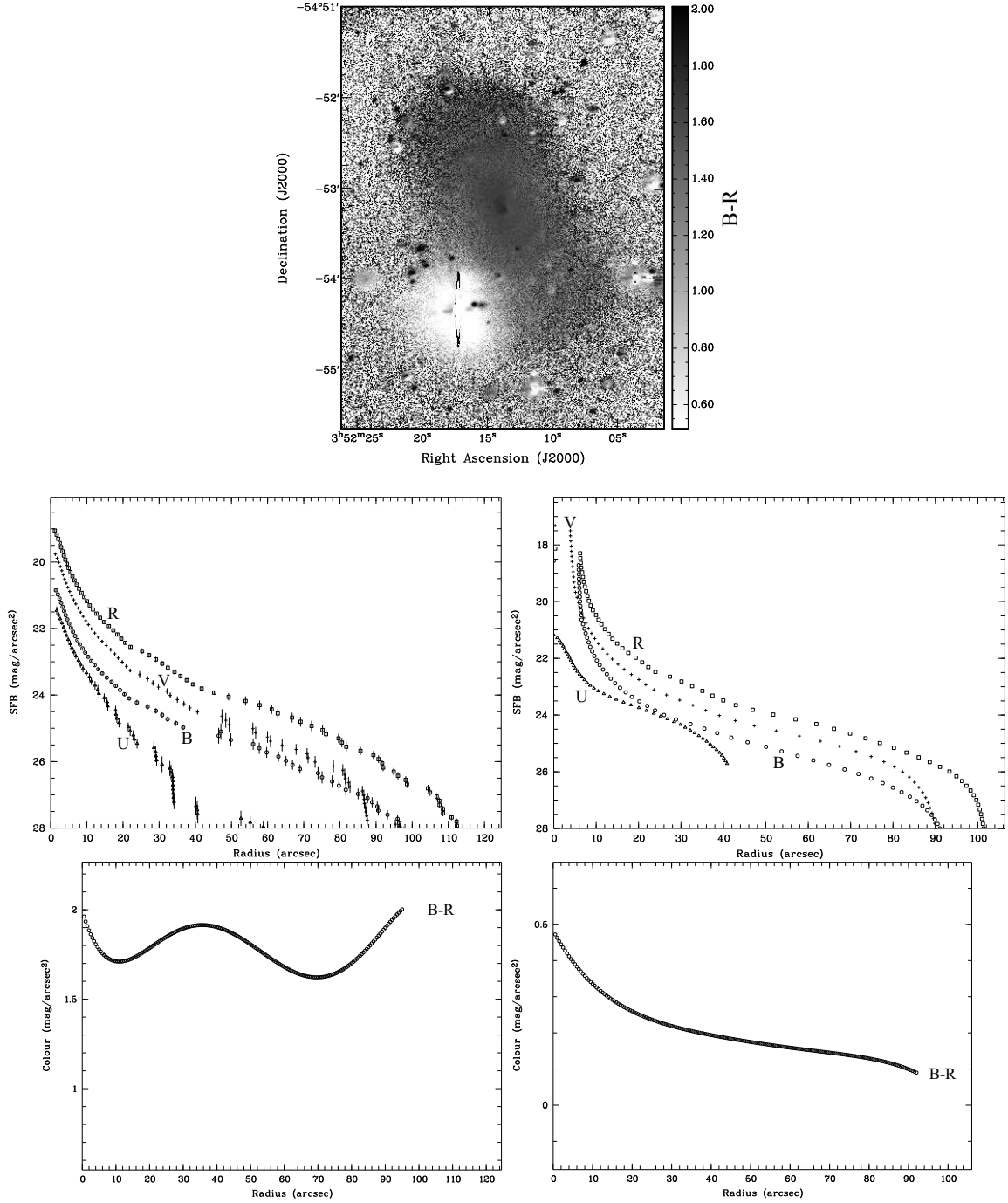


Figure 27: **ESO 156-18**: (top) B-R colour map, (middle left) radial profiles derived by ellipse fitting, (middle right) radial profiles derived by pixel summation, (bottom left) B-R colour profile from the ellipse fitting, (bottom right) B-R colour profile from the pixel summation.

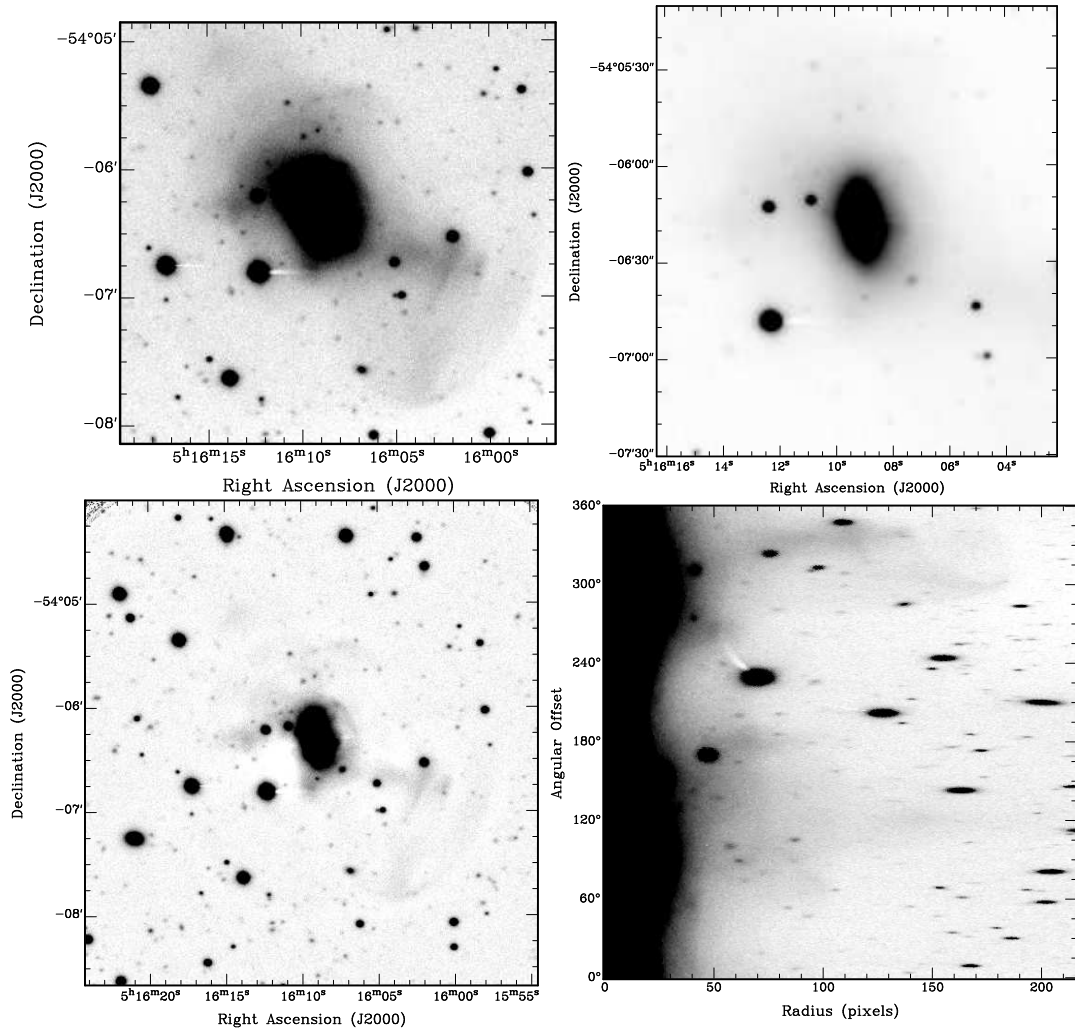


Figure 28: **ESO 159-03**: (top left) R-band image, (top right) R-band image of the center, (bottom left) R-band unsharp masking image ($r=33$ pix), (bottom right) R-band image in polar coordinates.

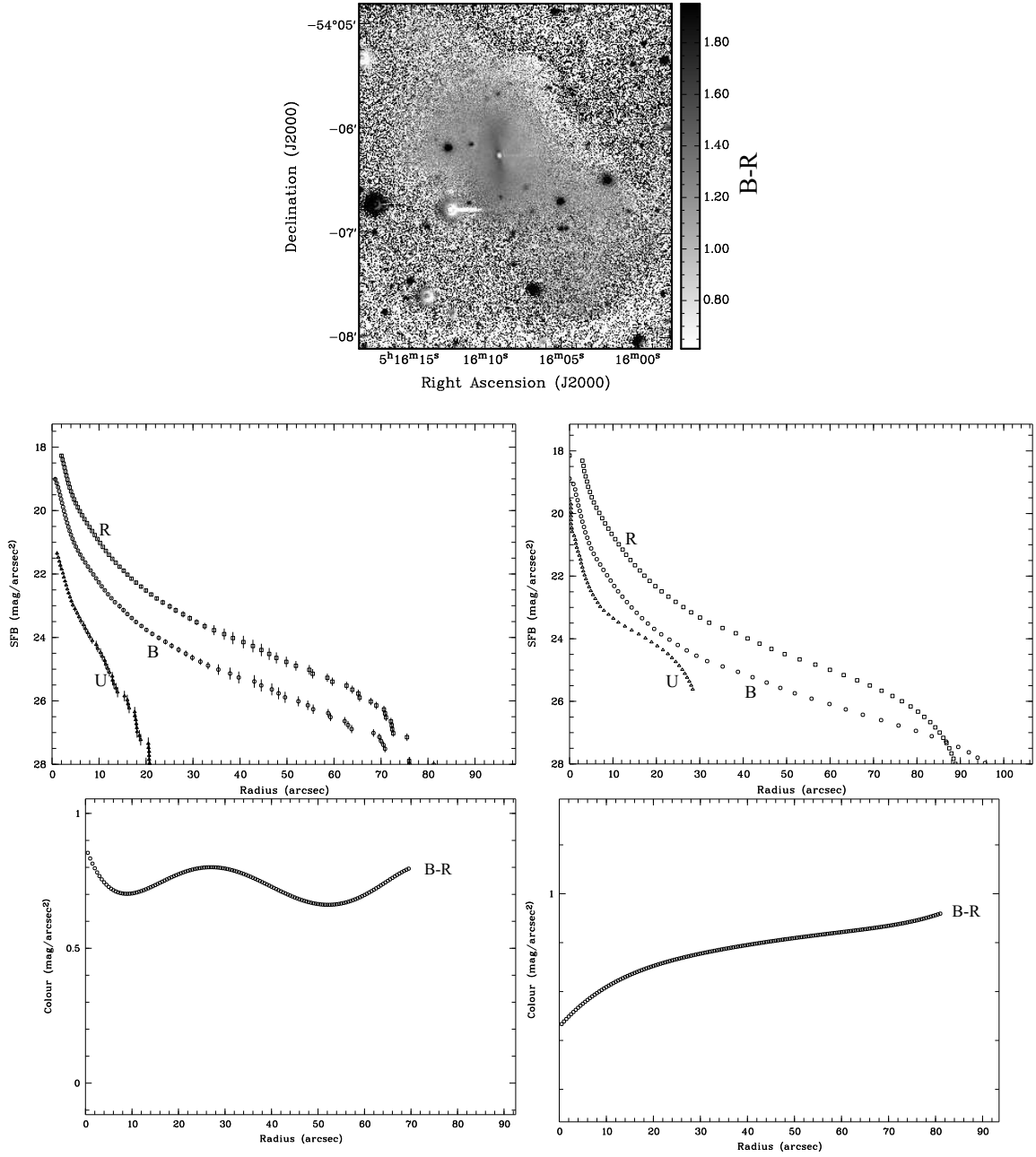


Figure 29: **ESO 159-03**: (top) B–R colour map, (middle left) radial profiles derived by ellipse fitting, (middle right) radial profiles derived by pixel summation, (bottom left) colour profiles from the ellipse fitting, (bottom right) colour profiles from the pixel summation.

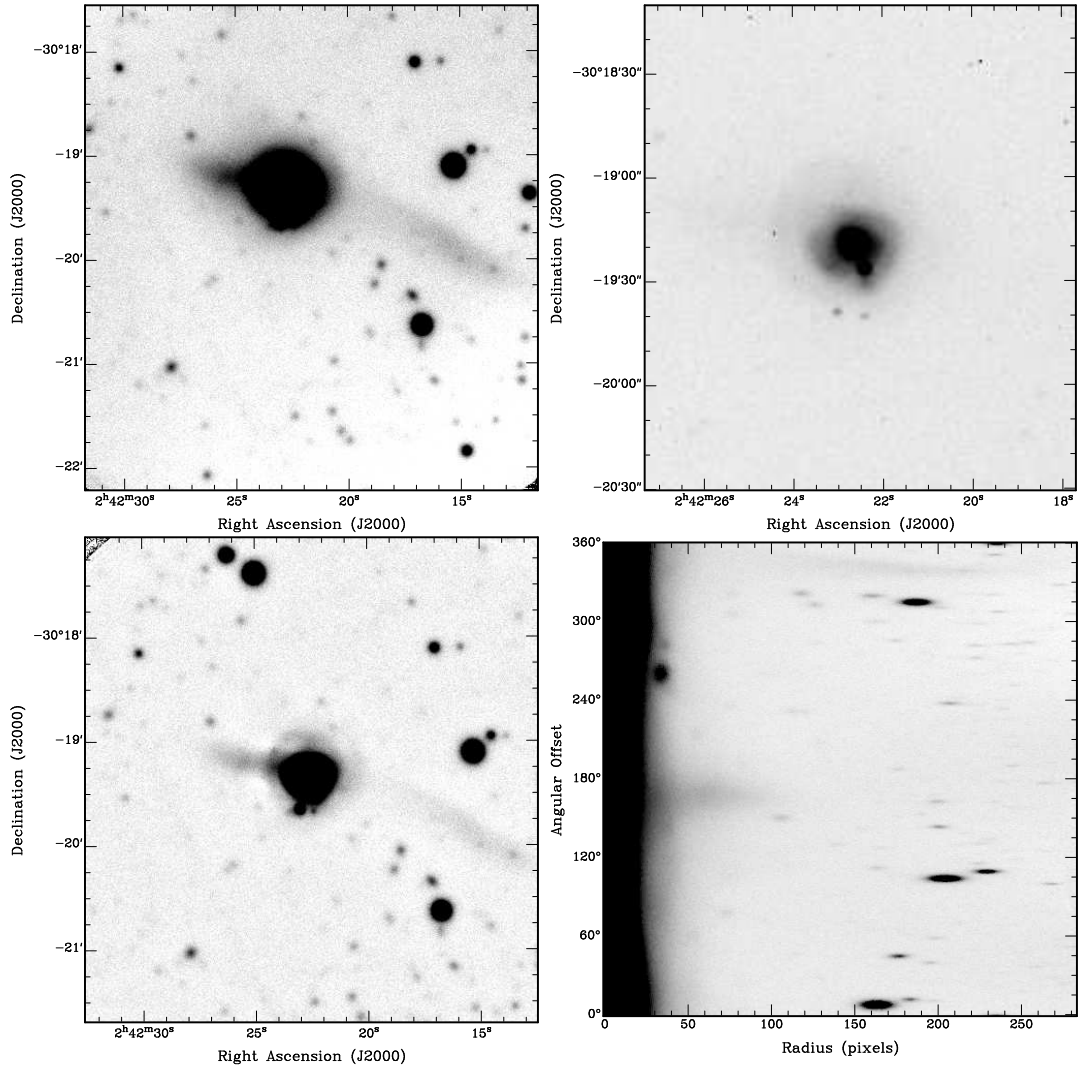


Figure 30: **ESO 416-09**: (top left) R-band image, (top right) R-band image of the center, (bottom left) R-band unsharp masking image ($r=33$ pix), (bottom right) R-band image in polar coordinates.

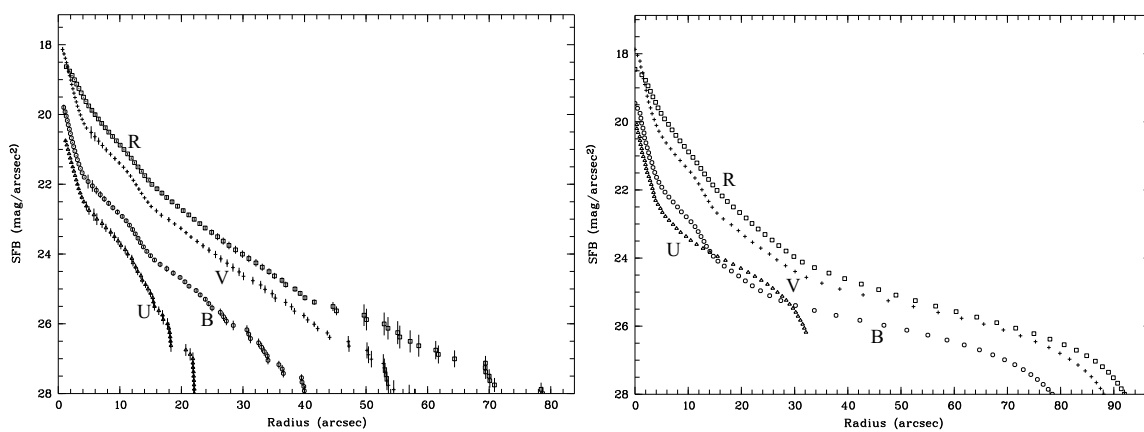


Figure 31: **ESO 416-09**: (left) radial profiles derived by ellipse fitting, (right) radial profiles derived by pixel summation,

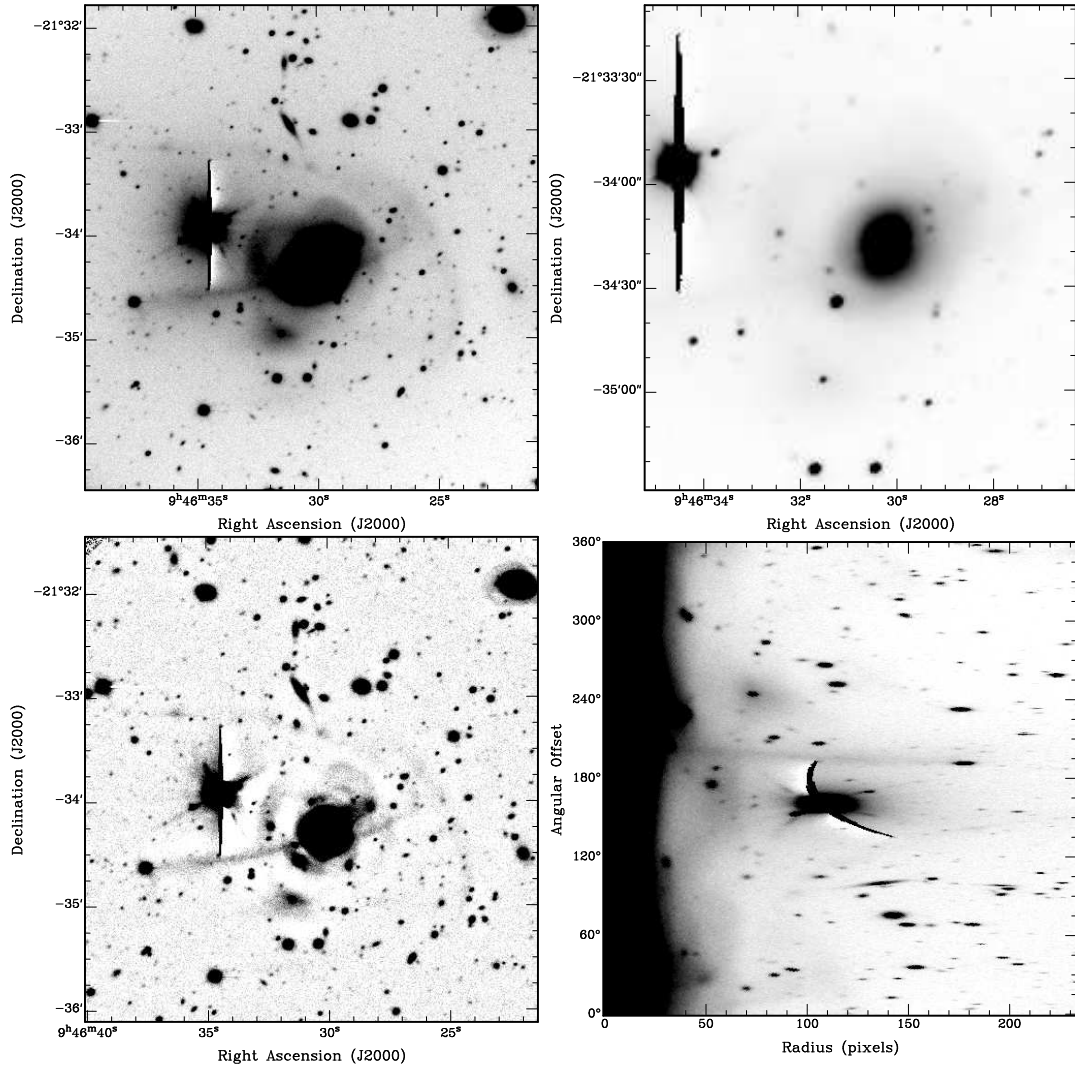


Figure 32: **NGC 2996**: (top left) R-band image, (top right) R-band image of the center, (bottom left) R-band unsharp masking image ($r=23$ pix), (bottom right) R-band image in polar coordinates.

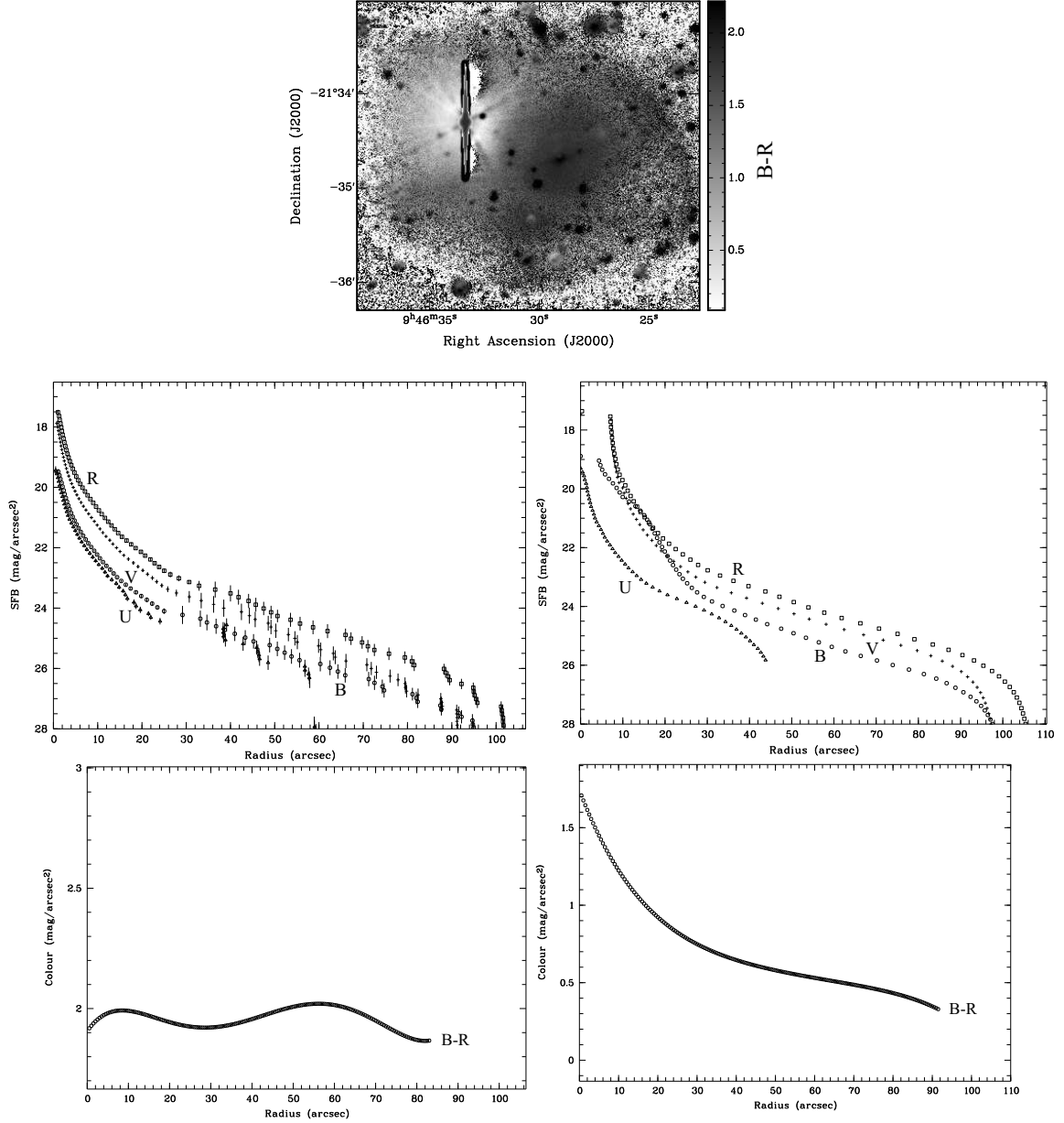


Figure 33: **NGC 2996**: (top) B-R colour map, (middle left) radial profiles derived by ellipse fitting, (middle right) radial profiles derived by pixel summation, (bottom left) colour profiles from the ellipse fitting, (bottom right) colour profiles from the pixel summation.

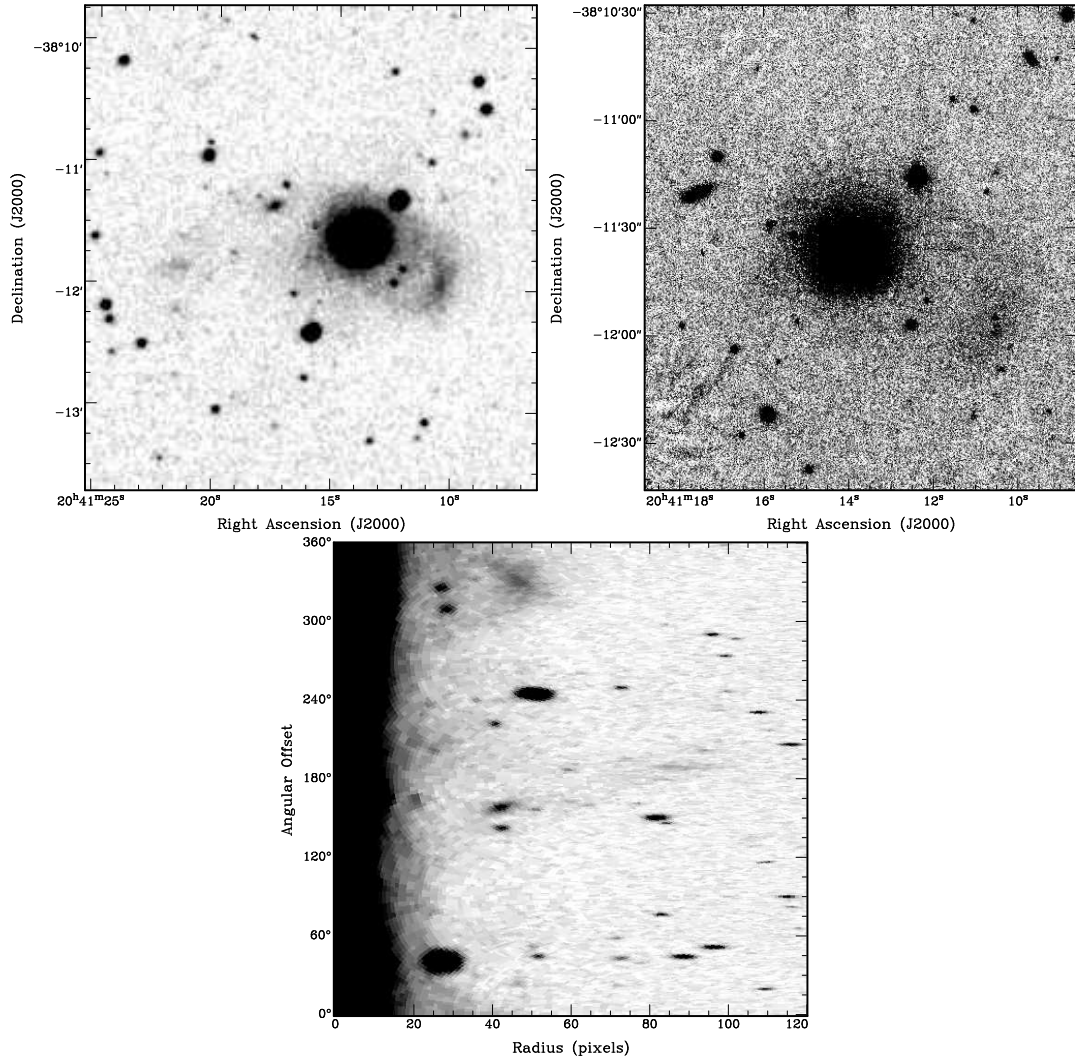


Figure 34: **ESO 341-04**: (top left) DSS2-red image, (top right) K-band image, (bottom) DSS2-red image in polar coordinates.

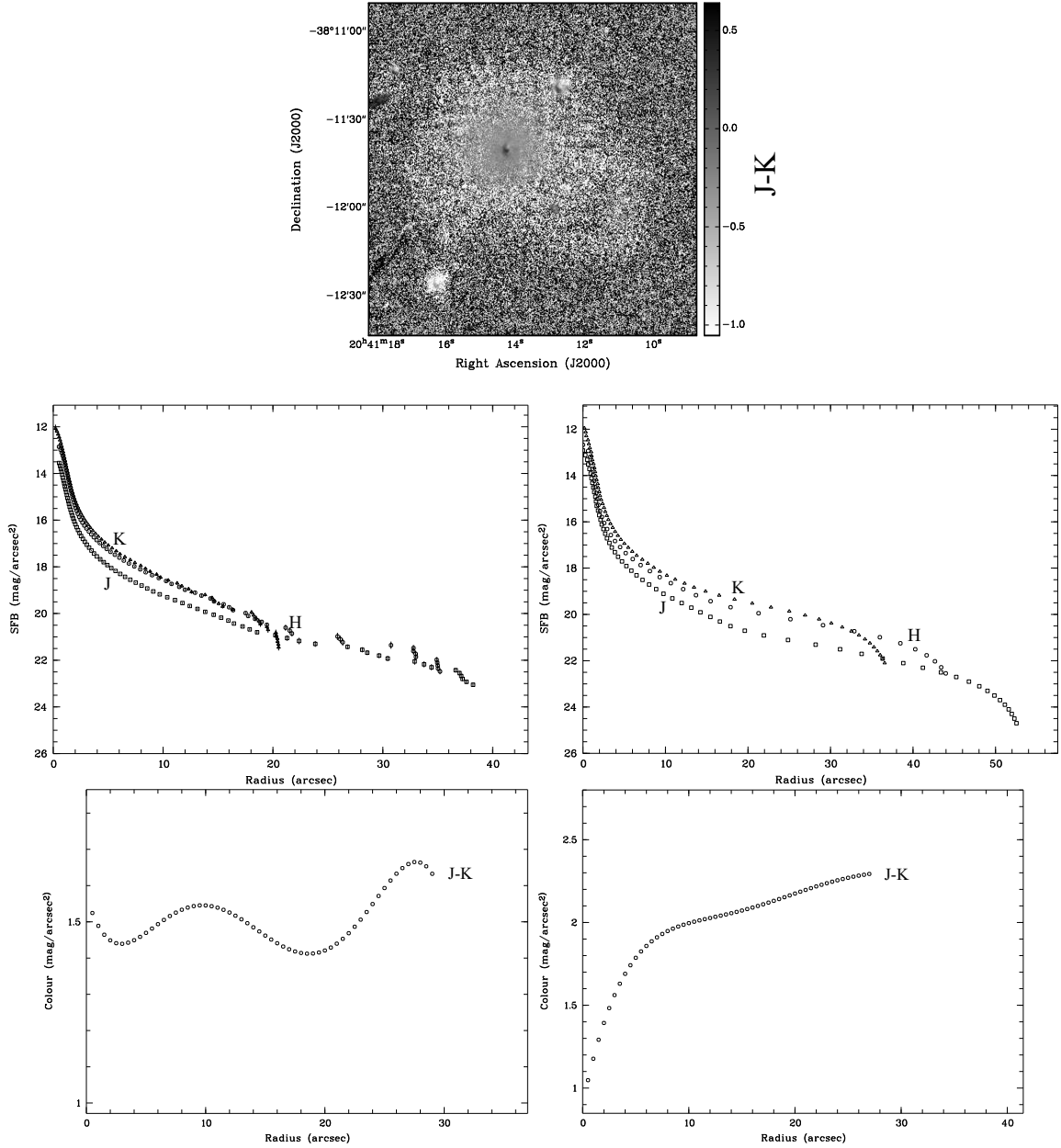


Figure 35: **ESO 341-04**: (top) J-K colour map, (middle left) radial profiles derived by ellipse fitting, (middle right) radial profiles derived by pixel summation, (bottom left) J-K colour profile from the ellipse fitting, (bottom right) J-K colour profile from the pixel summation.

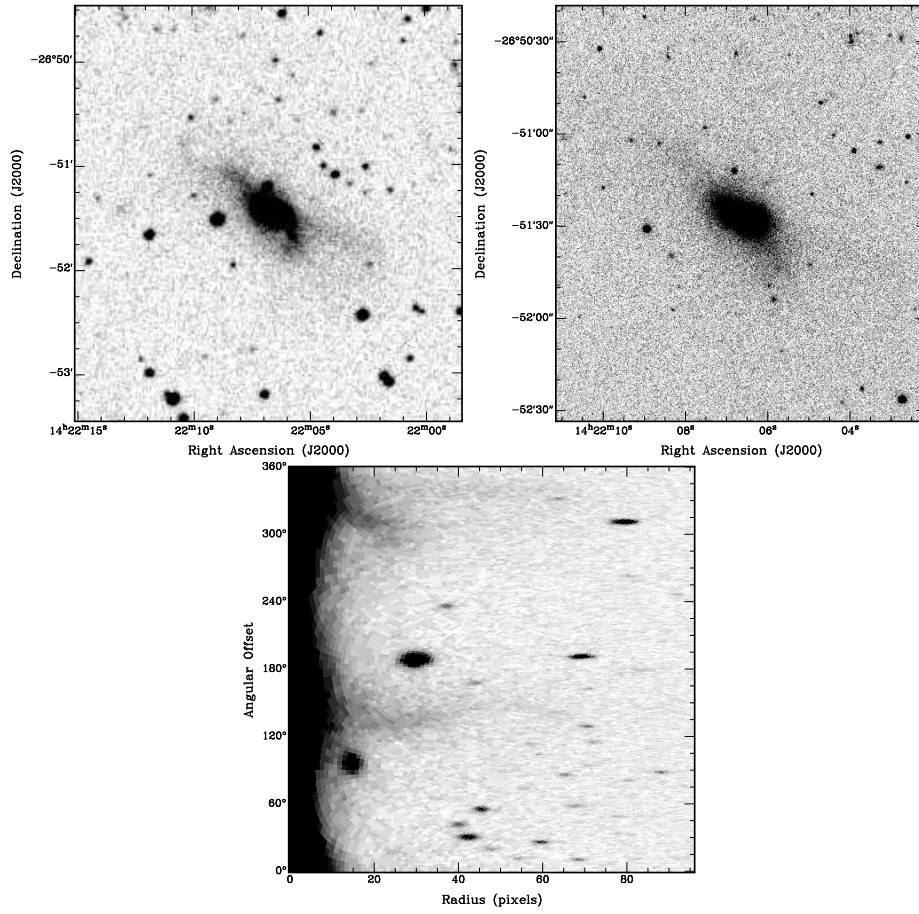


Figure 36: **ESO 511-35**: (top left) DSS2-red image, (top right) K-band image, (bottom) DSS2-red image in polar coordinates.

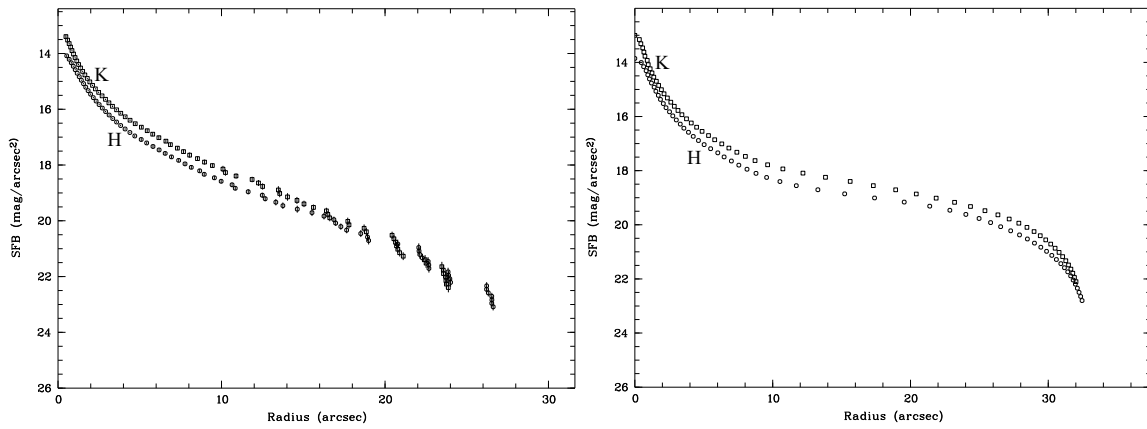


Figure 37: **ESO 511-35**: (left) radial profiles derived by ellipse fitting, (right) radial profiles derived by pixel summation.

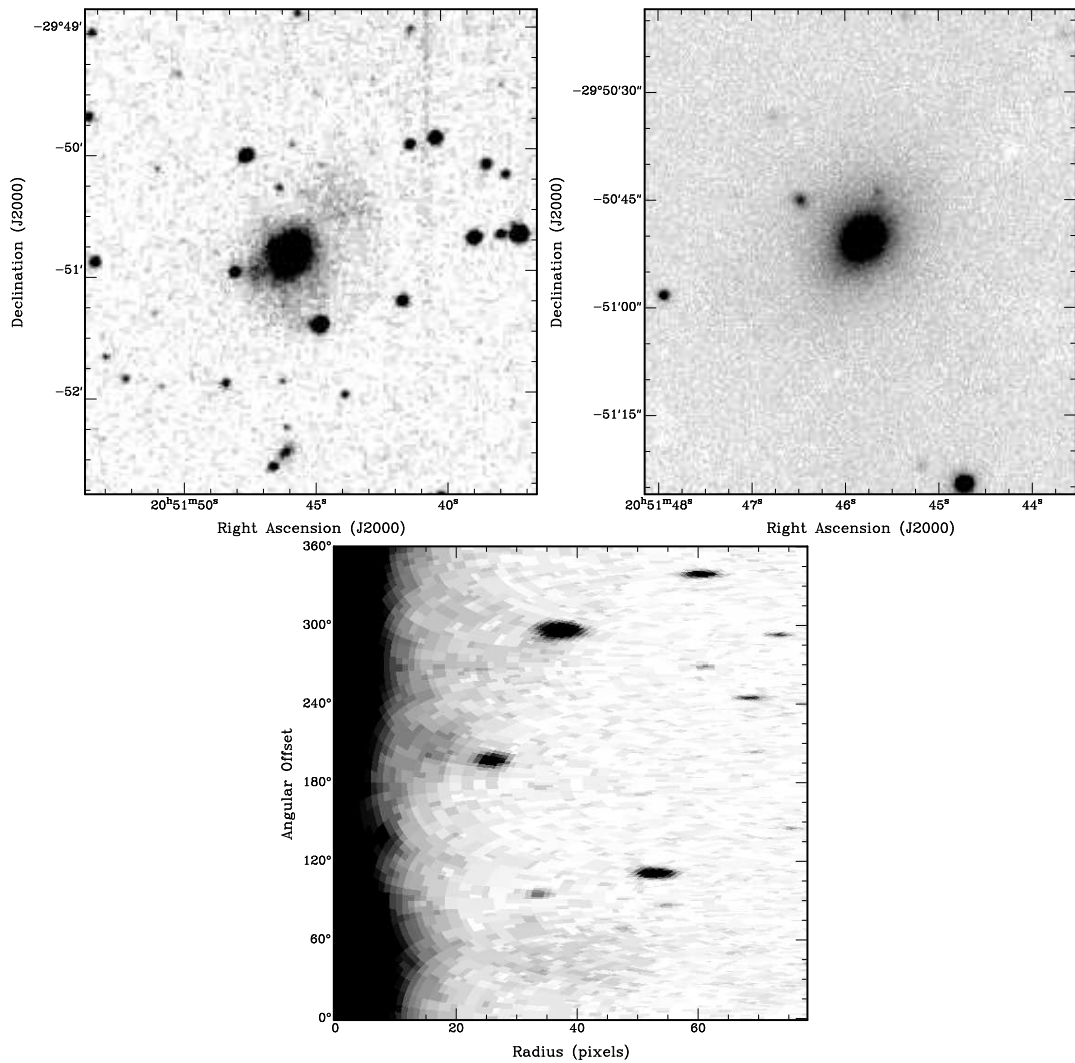


Figure 38: **IC 5065**: (top left) DSS2-red image, (top right) K-band image, (bottom) DSS2-red image in polar coordinates.

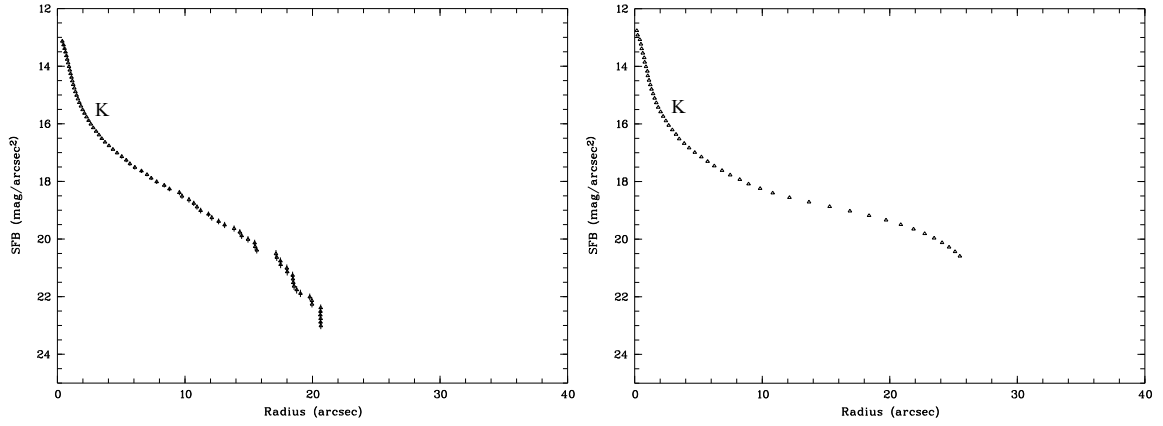


Figure 39: **IC 5065**: (left) K-band radial profile derived by ellipse fitting , (right) K-band radial profile derived by pixel summation.

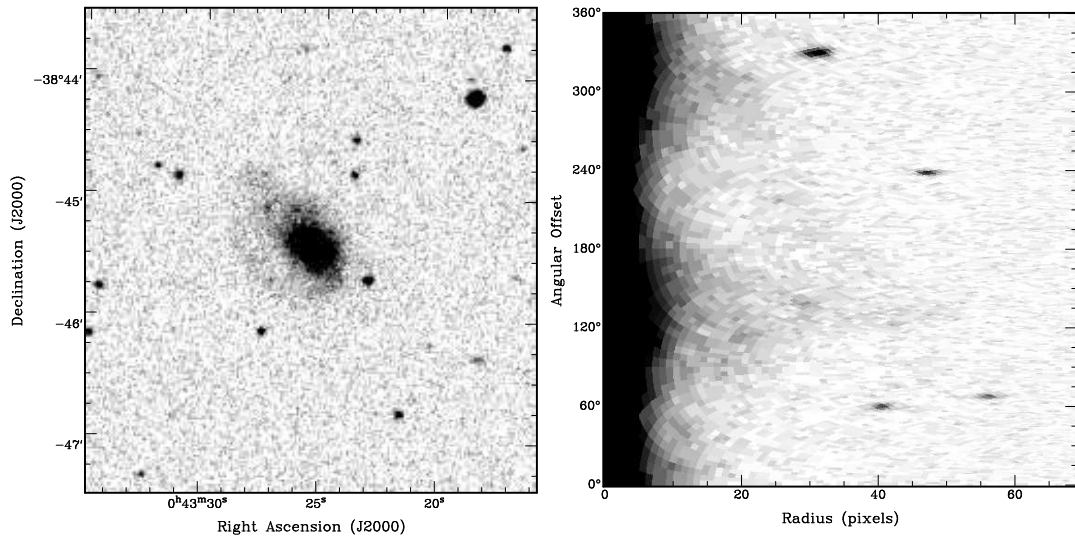


Figure 40: **ESO 295-02**: (left) DSS2-red image, (right) DSS2-red image in polar coordinates.

3.5.2 Optical spectroscopy

Six galaxies of the sample were spectroscopically observed in driftscan mode. Additional longslit spectra of the nuclei were taken to compare the central star formation activity with the global one. In Fig. 41 the extracted one-dimensional spectra are shown. For NGC 4004, which does not possess a distinct nucleus, the slit was aligned on the East and West part of the chain of knots in the main region. All spectra except for NGC 4441 are corrected for internal extinction using the Balmer decrement $c(\text{H}\beta)$. In NGC 4441, the $\text{H}\beta$ line could not be detected, thus no correction was applied.

The fluxes of the most important emission lines are given in Tab. 9 and Tab. 10.

The present star formation rate

Most galaxies show the typical spectral features of actively forming stars (compare with Kennicutt (1992), Liu & Kennicutt (1995)), like the increase of luminosity in the blue and the pronounced numerous emission lines. However, it is also obvious that there are differences in the stellar population mix and the ongoing star formation rate among the galaxies. This indicates that the assumption that the galaxies are in the same stage of the merger sequence has to be questioned. The clearest difference is found in NGC 4441, which has a spectrum typical for an evolved population with broad absorption lines and a red continuum, however is (still?) slightly forming stars, in particular in the center.

Comparing the nuclei spectra with the driftscan spectra, no significant differences in the shape can be seen, although slight variations in the relative intensity of some emission lines can appear. In the regions covered by the longslit, $\sim 30\text{-}40\%$ of the star formation rate estimated for the whole galaxies by the driftscan spectra are found.

The star formation rate can be estimated by measuring the $\text{H}\alpha$ line, because this emission comes from gas ionised by hot young stars with masses $> 10 M_{\odot}$. Because of the relatively short lifetime of those stars ($< 10 \text{ Myr}$), the $\text{H}\alpha$ emission is a good indicator of the *current* star formation. We used the relation of Kennicutt (1998b), assuming solar metallicities (which is reliable, see below, Tab. 10) and a Salpeter initial mass function (IMF):

$$\text{SFR}_{\text{H}\alpha} (M_{\odot}/\text{yr}) = 7.9 \cdot 10^{-42} L_{\text{H}\alpha} \quad (45)$$

with $L_{\text{H}\alpha}$ the $\text{H}\alpha$ luminosity in erg/s. The Salpeter IMF seems to be the most reliable relation confirmed by observations of starbursts, even though hints for a flattening at stellar masses below $1 M_{\odot}$ are found (Elmegreen (2005)). But the low-mass stars do not contribute to the ionising flux and thus this deviation can be neglected.

In Tab. 9 the star formation rates are given for all spectra. Note, that we can give only lower limits for NGC 4441, because due to the lack of the $\text{H}\beta$ line no extinction correction was possible. Thus, the $\text{H}\alpha$ line might be dimmed by dust and appears weaker.

The derived star formation rates lies within the range covered by the interacting starburst galaxy sample of Dopita et al. (2002). In most of our observed galaxies the star formation is enhanced, probably due to the merger. Only NGC 4441 seems to have a moderate star formation rate, even when considering the lower limit determination. Preliminary results of stellar population synthesis modelling of the star formation history of NGC 4441 in comparison with NGC 4194 let us suggest that the starburst phase in NGC 4441 is $\sim 1 \text{ Gyr}$ ago (Manthey et al. (2005)). This galaxy seems to be a more evolved merger compared to e.g., NGC 4194. This is also reflected in the optical morphology, because the more pronounced tidal features, in particular the shells, of NGC 4441 indicate a longer merging history than for NGC 4194.

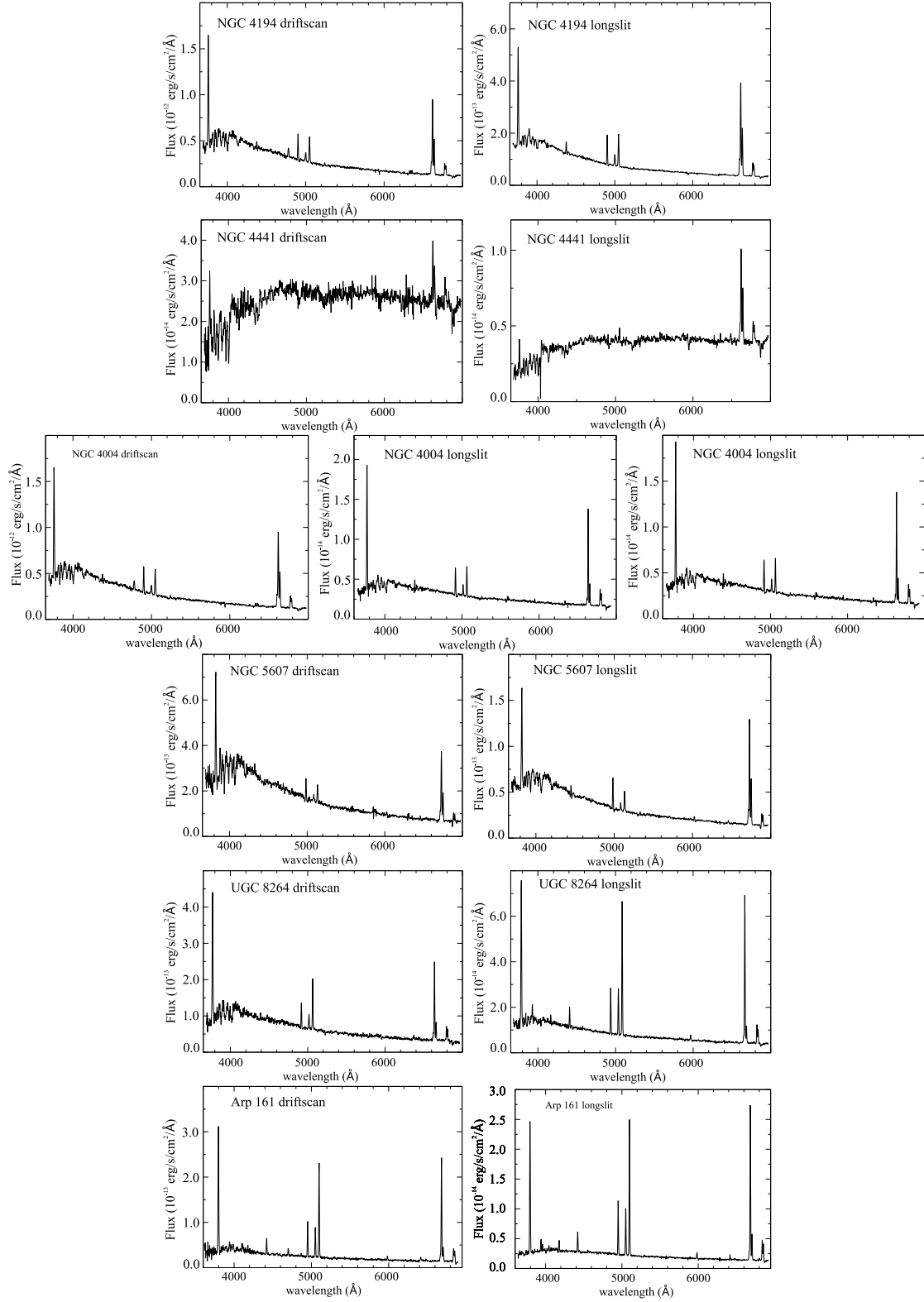


Figure 41: The optical driftscan spectra (left) and longslit spectra of the nuclei (right) of six sample galaxies. From top to bottom: NGC 4194, NGC 4441 (not corrected for extinction), NGC 4004 (two longslit spectra of the east and west part of the main region are shown), NGC 5607, UGC 8264, Arp 161. (Arp 161 driftscan and NGC 4004 driftscan by courtesy of J. Moustakas.)

Table 9: Results of the H α analysis. Given are the Balmer decrement $c(\text{H}\beta)$, the visual extinction A_V , the H α flux after correction for internal extinction (except for NGC 4441) and the resulting star formation rate.

| Galaxy | $c(\text{H}\beta)$ | A_V (mag) | H α flux (10^{-13} erg/s/cm 2 /Å) | SFR $_{\text{H}\alpha}$ (M_{\odot} yr) |
|--------------------|--------------------|----------------|---|--|
| NGC 4194 driftscan | 0.944 | 1.85 | 98.6 | 13.9 |
| NGC 4194 nucleus | 0.999 | 1.96 | 41.6 | 5.87 |
| NGC 4441 driftscan | – | – | 1.64 | >0.2 |
| NGC 4441 nucleus | – | – | 0.746 | >0.09 |
| NGC 4004 driftscan | 0.714 | 1.39 | 21.5 | 4.12 |
| NGC 4004 left | 0.552 | 1.07 | 1.08 | 0.2 |
| NGC 4004 right | 0.280 | 0.54 | 0.928 | 0.17 |
| NGC 5607 driftscan | 0.992 | 1.95 | 34.8 | 32.9 |
| NGC 5607 nucleus | 0.94 | 1.84 | 12.0 | 11.4 |
| UGC 8264 driftscan | 0.38 | 0.73 | 20.4 | 6.58 |
| UGC 8264 nucleus | 0.387 | 0.73 | 6.24 | 2.01 |
| Arp 161 driftscan | 0.436 | 0.84 | 23.4 | 7.7 |
| Arp 161 nucleus | 0.252 | 0.48 | 2.45 | 1.24 |

The properties of the ionised ISM

The emission lines can be used to analyse the properties of the ionised interstellar medium. For this purpose, typically ratios of strong lines are taken to derive the metallicity and the ionisation parameter q . However, two problems occur in such an approach: First, the commonly used ratios which trace the abundance highly depend on the ionisation parameter and vice versa. And second, the line ratios are double-valued and thus give no unique solutions. We followed a method described by Kewley & Dopita (2002), which is a combination of different calibrations of the R_{23} ratio introduced by Pagel et al. (1979) ($R_{23} = ([\text{OII}]\lambda 3727 + [\text{OIII}]\lambda\lambda 4959, 5007)/\text{H}\beta$). They examined the abundance-dependent reliability of the different calibrations (McGaugh (1991), Zaritsky et al. (1994), Charlot & Longhetti (2001) and their own). They provide an abundance determination method taking the best of all calibration in specific abundance ranges. They claim, that for an abundance $\log(\text{O}/\text{H}) + 12 > 8.6$, the best tracer is the line ratio $[\text{NII}]\lambda 6584/[\text{OII}]\lambda 3727$. In the upper part of Tab. 10, the abundances are determined with this method. For the galaxies in the lower part, this line ratio gives values smaller than 8.6. Following the guidance of Kewley & Dopita (2002), the abundances are derived with the R_{23} ratio calibrated by the authors. For four spectra, the parameterised fit of the abundance determination gave irregular results, therefore, the method of Charlot & Longhetti (2001), which considers the $[\text{NII}]\lambda 6584/[\text{SII}]\lambda\lambda 6717, 6731$ and $[\text{OII}]\lambda\lambda 3726, 3729/[\text{OIII}]\lambda 5007$ ratios, was used instead.

The galaxies span a range of metallicities from a third of what is measured in the sun (UGC 8264) to solar metallicities (NGC 4194, NGC 5607). Only marginal differences are found between the overall metallicities derived from the driftscan spectra and the metallicities in the nuclei.

The estimated ionisation parameter varies between 0.5 and $5.0 \cdot 10^7$ cm/s. These are typical values found in extragalactic HII regions, both in normal spirals (e.g., Dopita et al. (2000)) and starburst galaxies (Kewley et al. (2000)). As mentioned by Kewley et al. (2000), in star-

burst galaxies there is a trend of a smaller ionisation parameter. This is agreement with our measurements, which give the lowest values for NGC 4194 and NGC 5607, the galaxies with the highest star formation rate.

3.6 Summary

1. We selected a sample of 15 candidates for mergers between a Spiral and an Elliptical. All galaxies have a moderate far-infrared luminosity $> 10^{11} L_{\odot}$, and show the typical tidal features for such mergers like a tail and shells. Here, we presented the optical and near-infrared results of a multi-wavelength study of this sample. Optical and near-infrared observations are performed for most of the sample galaxies. In addition, spectroscopic observations are obtained for six galaxies to analyse the current star formation rate and the properties of the ISM.
2. A variety of tidal features is found in the observed galaxies. The colours of these features are generally bluer than the main body of the merger remnants. This indicates that the shells are younger, maybe formed during the merger induced starburst and is in agreement with what is found in other studies of shell galaxies.
3. In the near-infrared, the tidal features are barely visible. This fits to the suggestion that they are younger than the stellar populations in the main body, which consists of the populations from the progenitor galaxies.
4. From the optical spectra, we determined the current star formation rate using the H α emission. All but NGC 4441 show enhanced star formation (overall SFR = $2.32 M_{\odot}/\text{yr}$), likely induced by the merger. For NGC 4441, we could only derive lower limits, because not extinction correction could be obtained. The spectrum of this galaxy is nevertheless strikingly different to the others, showing the spectral features of an evolved population with broad absorption lines and a reddish continuum. This galaxy is apparently in a post-starburst phase with little ongoing star formation.
5. The metallicities derived for the galaxies range from a third to solar abundance. The ionisation parameter varies from 0.5 to $5.0 \cdot 10^7$ cm/s. These are typical values for HII regions in starbursts and normal galaxies.

Table 10: Fluxes of the emission lines used for oxygen abundance estimation of the ionised ISM, the derived abundance $\log(\text{O}/\text{H}) + 12$, the equivalent metallicity with respect to the sun Z_{\odot} and the ionisation parameter q . The fluxes are given in $10^{-13} \text{ erg/s/cm}^2/\text{\AA}$. In the upper part (above the line), the abundance is derived using the $[\text{NII}]/[\text{OII}]$ ratio, because the metallicity is high enough. In the lower part, the abundance is estimated based on the $[\text{OIII}]$ and $[\text{SII}]$ lines, following either the combined method in Kewley & Dopita (2002) (KD02) or Charlot & Longhetti (2001) (C01) alone.

| Galaxy | [NII] | [OII] | [OIII] | [SII] | H β | $\log(\text{O}/\text{H}) + 12$ | Z (Z_{\odot}) | q (10^7 cm/s) |
|--------------------|-------|-------|---------------|----------------|-----------|--------------------------------|-------------------|---------------------------|
| NGC 4194 driftscan | 44.5 | 138.0 | 13.0+32.2 | 16.9+15.3 | 27.2 | 8.87 | 1.0 | 0.6 |
| NGC 4194 nucleus | 20.6 | 42.6 | 5.1+14.0 | 5.9+5.1 | 12.0 | 8.98 | 1.1 | 5.0 |
| NGC 4441 driftscan | 2.15 | 0.973 | – | 0.74 | – | <9.23 | <2.0 | – |
| NGC 4441 nucleus | 0.434 | 0.223 | 0.077 | 0.20+0.16 | – | <9.21 | <2.0 | – |
| NGC 5607 driftscan | 14.3 | 50.9 | 0.96 | 3.2+8.9 | 3.6+2.4 | 8.82 | 1 | 0.5 |
| NGC 5607 nucleus | 5.22 | 12.4 | 0.86+2.5 | 1.4+1.1 | 3.3 | 8.95 | 1.1 | 0.6 |
| Arp 161 nucleus | 0.426 | 2.28 | 0.74+2.08 | 0.36+0.29 | 0.84 | 8.65 | 0.6 | 7.0 |
| Arp 161 driftscan | 3.85 | 29.9 | (6.85+20.7) | (3.54+3.30) | 7.55 | 8.47 (C01) | 0.4 | 5.0 |
| NGC 4004 driftscan | 4.61 | 39.2 | (4.20+13.1) | (3.93+3.23) | 6.38 | 8.6 (C01) | 0.5 | 2.7 |
| NGC 4004 left | 0.244 | 1.54 | (0.124+0.361) | (0.216+0.162) | 0.328 | 8.36 (KD02) | 0.4 | 1.9 |
| NGC 4004 right | 0.146 | 1.07 | (0.217+0.648) | (0.099+0.0764) | 0.313 | 8.18 (KD02) | 0.2 | 4.8 |
| UGC 8264 driftscan | 2.79 | 28.8 | (6.00+18.2) | (3.59+3.05) | 6.77 | 8.3 (C01) | 0.3 | 3.3 |
| UGC 8264 nucleus | 0.856 | 7.23 | (2.04+6.00) | (0.858+0.774) | 2.01 | 8.4 (C01) | 0.3 | 3.5 |

References

- Aalto, S. & Hüttemeister, S. 2000, *A&A*, 362, 42
- Aalto, S., Hüttemeister, S., & Polatidis, A. G. 2001, *A&A*, 372, L29
- Aronica, G. 2006, (PhD thesis)
- Barnes, J. E. 1994, in *The Formation and Evolution of Galaxies*, 399
- Barnes, J. E. & Hernquist, L. E. 1991, *ApJ*, 370, L65
- Bergvall, N. 1981, *A&A*, 97, 302
- Bergvall, N., Ronnback, J., & Johansson, L. 1989, *A&A*, 222, 49
- Carter, B. S. & Meadows, V. S. 1995, *MNRAS*, 276, 734
- Carter, D., Allen, D. A., & Malin, D. F. 1982, *Nature*, 295, 126
- Charlot, S. & Longhetti, M. 2001, *MNRAS*, 323, 887
- de Vaucouleurs, G., de Vaucouleurs, A., Corwin, H. G., Buta, R. J., Paturel, G., & Fouque, P. 1995, *VizieR Online Data Catalog*, 7155, 0
- Dopita, M. A., Kewley, L. J., Heisler, C. A., & Sutherland, R. S. 2000, *ApJ*, 542, 224
- Dopita, M. A., Pereira, M., Kewley, L. J., & Capaccioli, M. 2002, *ApJS*, 143, 47
- Dupraz, C. & Combes, F. 1985, *Lecture Notes in Physics*, Berlin Springer Verlag, 232, 151
- Elias, J. H., Frogel, J. A., Matthews, K., & Neugebauer, G. 1982, *AJ*, 87, 1029
- Elmegreen, B. G. 2005, in *ASSL Vol. 329: Starbursts: From 30 Doradus to Lyman Break Galaxies*, ed. R. de Grijs & R. M. González Delgado, 57
- Forbes, D. A., Thomson, R. C., Groom, W., & Williger, G. M. 1994, *AJ*, 107, 1713
- Fort, B. P., Prieur, J.-L., Carter, D., Meatheringham, S. J., & Vigroux, L. 1986, *ApJ*, 306, 110
- Gonzalez, R. C. & Woods, R. E. 1992, *Digital Image Processing* (Addison–Wesley Company, 1992)
- Hernquist, L. & Quinn, P. J. 1988, *ApJ*, 331, 682
- Hibbard, J. E. & Mihos, J. C. 1995, *AJ*, 110, 140
- Hibbard, J. E., Vacca, W. D., & Yun, M. S. 2000, *AJ*, 119, 1130
- Hibbard, J. E. & van Gorkom, J. H. 1996, *AJ*, 111, 655
- Hunt, L. K., Mannucci, F., Testi, L., Migliorini, S., Stanga, R. M., Baffa, C., Lisi, F., & Vanzi, L. 1998, *AJ*, 115, 2594

- Johansson, L. 1988, *A&AS*, 73, 335
- Kennicutt, R. C. 1992, *ApJS*, 79, 255
- Kennicutt, R. C. 1998a, in *Saas-Fee Advanced Course 26: Galaxies: Interactions and Induced Star Formation*, 1
- . 1998b, *ARA&A*, 36, 189
- Kewley, L. J. & Dopita, M. A. 2002, *ApJS*, 142, 35
- Kewley, L. J., Dopita, M. A., Heisler, C. A., Sutherland, R. S., Rocca-Volmerange, B., & Moy, E. 2000, in *Revista Mexicana de Astronomia y Astrofisica Conference Series*, ed. S. J. Arthur, N. S. Brickhouse, & J. Franco, 163–165
- Kewley, L. J., Heisler, C. A., Dopita, M. A., & Lumsden, S. 2001, *ApJS*, 132, 37
- Kojima, M. & Noguchi, M. 1997, *ApJ*, 481, 132
- Landolt, A. U. 1992, *AJ*, 104, 340
- Larson, R. B. & Tinsley, B. M. 1978, *ApJ*, 219, 46
- Liu, C. T. & Kennicutt, R. C. 1995, *ApJ*, 450, 547
- Maia, M. A. G., da Costa, L. N., Willmer, C., Pellegrini, P. S., & Rite, C. 1987, *AJ*, 93, 546
- Malin, D. F. & Carter, D. 1983, *ApJ*, 274, 534
- Manthey, E., Hüttemeister, S., Haberzettl, L., & Aalto, S. 2005, in *AIP Conf. Proc. 783: The Evolution of Starbursts*, ed. S. Hüttemeister, E. Manthey, D. Bomans, & K. Weis, 343–348
- McGaugh, S. S. 1991, *ApJ*, 380, 140
- McGaugh, S. S. & Bothun, G. D. 1990, *AJ*, 100, 1073
- Moustakas, J. & Kennicutt, R. C. 2005, *ArXiv Astrophysics e-prints*
- Oke, J. B. 1990, *AJ*, 99, 1621
- Pagel, B. E. J., Edmunds, M. G., Blackwell, D. E., Chun, M. S., & Smith, G. 1979, *MNRAS*, 189, 95
- Papaderos, P., Loose, H.-H., Thuan, T. X., & Fricke, K. J. 1996, *A&AS*, 120, 207
- Pence, W. D. 1986, *ApJ*, 310, 597
- Raimann, D., Bica, E., Storchi-Bergmann, T., Melnick, J., & Schmitt, H. 2000, *MNRAS*, 314, 295
- Sanders, D. B., Mazzarella, J. M., Kim, D.-C., Surace, J. A., & Soifer, B. T. 2003, *AJ*, 126, 1607
- Sanders, D. B. & Mirabel, I. F. 1996, *ARA&A*, 34, 749

-
- Schlegel, D. J., Finkbeiner, D. P., & Davis, M. 1998, *ApJ*, 500, 525
- Schweizer, F. 2005, in *ASSL Vol. 329: Starbursts: From 30 Doradus to Lyman Break Galaxies*, ed. R. de Grijs & R. M. González Delgado, 143–+
- Toomre, A. 1977, in *Evolution of Galaxies and Stellar Populations*, 401
- Toomre, A. & Toomre, J. 1972, *ApJ*, 178, 623
- Turnbull, A. J., Bridges, T. J., & Carter, D. 1999, *MNRAS*, 307, 967
- Weil, M. L. & Hernquist, L. 1993, *ApJ*, 405, 142
- Weistrop, D., Eggers, D., Hancock, M., Nelson, C. H., Bachilla, R., & Kaiser, M. E. 2004, *AJ*, 127, 1360
- Zaritsky, D., Kennicutt, R. C., & Huchra, J. P. 1994, *ApJ*, 420, 87

4 The atomic and molecular gas content of the advanced merger NGC 4441

Abstract

NGC 4441 is a candidate for a merger between a spiral and an elliptical galaxy (S+E merger), showing typical tidal structures like an optical tail and two shells, as well as two long HI tails. The galaxy possesses an extended molecular gas reservoir out to ~ 3.9 kpc. However, this galaxy is forming stars on a very moderate level. The maps presented here are obtained with the Westerbork Synthesis Radio Interferometer (HI), the Onsala Space Observatory 20 m and IRAM 30 m telescope (CO). By comparing the high resolution HI maps with deep optical images, differences between the stellar and gaseous tidal features are apparent. We calculate a total atomic gas mass of $1.5 \cdot 10^9 M_{\odot}$. The molecular gas has a gas mass of $\sim 6.0 \cdot 10^8 M_{\odot}$.

4.1 Introduction

Until now, extreme mergers between two large disk galaxies, leading to a super-starburst and to ULIRGs (Sanders & Mirabel (1996)) have been in the focus of research, but those galaxies are rare. Small spirals and ellipticals dominate the galaxy population in many environments, but mergers between them, so-called S+E mergers, are poorly studied so far. Models of S+E mergers are in strong disagreement concerning the prediction of enhanced star formation induced by the merger. Weil & Hernquist (1993) used a model in which the gas is treated as collisionless clouds. The stellar and gaseous components are quickly segregated. While the stars form features like shells, the gas congregates in the center of the remnant galaxy, leading to a strong gas concentration and thus resulting in a starburst, similar to ULIRGs. Simulations by Kojima & Noguchi (1997) however predict a scattering of gas which might not lead to a starburst at all, because the density of the gas is too low to collapse and form new stars. They model the gas component as a system of inelastic cloud particles dissipating kinetic energy in mutual collisions. The stellar component in this model appears to be similar to the gas distribution. While the contrast of the structures is somewhat higher for the stellar component, both show shell-like features, as were also found for the stars in the models of Weil & Hernquist (1993). Observations of possible S+E mergers are needed to narrow the parameter space and to improve the current models.

One 'prototypical' S+E merger candidate is NGC 4194, the Medusa. In the optical we see a diffuse tail going to the north and on the opposite side 2 shells are visible, as models predict it. Molecular gas is found in a continuous distribution out to 4.7 kpc away from the center, i.e. much more spread out than in the case of a ULIRG (Aalto & Hüttemeister (2000); Aalto et al. (2001)). However, this galaxy is clearly undergoing an intense starburst phase, albeit not as strong as in ULIRGs (Weistrop et al. (2004)).

Here we present high resolution interferometric HI data and CO maps of another S+E merger candidate, NGC 4441. This galaxy is morphologically very similar to the Medusa. It possesses one tidal tail and two bluish shells on the opposite side, which are, however, brighter, i.e. more evolved, than the shells in the Medusa. The main body has an elliptical shape (Bergvall (1981)) with a small dust layer through the center on the minor axis. Bergvall (1981) obtained spectroscopic observations and claims that this galaxy is a merger where most of the gas has been already used for star formation, which means only little ongoing star formation. However, there must have been a period of enhanced star formation, since the stellar population is younger than that of a normal elliptical galaxy.

Table 11: Basic properties of NGC 4441. The distance is based on $H_0 = 75$ km/s/Mpc.

| property | |
|-------------------------------------|------------|
| RA (2000) | 12:27:20.3 |
| DEC (2000) | +64:48:05 |
| $v_{\text{opt, hel}}$ (km/s) | 2674 |
| D (Mpc) | 36 |
| L_B ($10^9 L_\odot$) | 1.79 |
| L_{FIR} ($10^9 L_\odot$) | 5.4 |

The observations presented here were obtained with the Westerbork Synthesis Radio Telescope (WSRT), the Onsala Space Observatory (OSO) and IRAM 30 m, respectively. We refer to the analysis of optical longslit-spectra for metallicity estimations, but these data are presented in detail in Ch. 3.

In Tab.11 general information about NGC 4441 is given. Note that we calculate the distance using the redshift of NGC 4441 as 36 Mpc and do not use the distance based on results of Tonry et al. (2001) by using surface brightness fluctuations (SBF). There is a large disagreement between the results of both methods, which were not mentioned in the paper by Tonry et al. (2001) due to an old, wrong velocity measurement of NGC 4441, which lies close to their SBF based result (i.e., a distance of 19 Mpc). We do not see, however, any reason, why NGC 4441 should deviate that strongly from the Hubble flow, since this galaxy does not lie close to a center of a cluster. Besides, NGC 4441 is not a good target for surface brightness fluctuation measurements, since this is clearly not an Elliptical, for which this method works best, with a homogeneous distribution of stellar populations, esp. giants. Due to its merger nature, there is a mix of populations originating from the progenitor galaxies as well as newly formed stars. Furthermore, we find a dust layer in the inner region, which also complicates SBF measurements, as stated by Tonry et al. (2001).

In Section 2 we give basic informations about the observations obtained, in Section 3 we describe the data reduction for the interferometric and single-dish data. Results are presented in Section 4, including derived properties like HI and H₂ gas mass and the star formation rate based on the 20 cm continuum flux. In Section 5 we discuss the observations with particular emphasis on models of mergers between Elliptical and Spirals and we compare NGC 4441 with its 'younger sister', the Medusa. Finally, in Section 6 we summarise the observations and results.

4.2 Observations

4.2.1 WSRT

The HI observation with the Westerbork Synthesis Radio Telescope (WSRT⁹) were carried out in February 2003. Tab.12 summarises the most important observing parameters. We observed NGC 4441 in one 12h run in the maxi-short array configuration. This is best suitable for observations of an extended source within a single 12 hours track. The quality of the data is good, no interference problems occurred. For bandpass and flux calibration, the calibrator 3C48 was observed before the observations. Note that no secondary phase calibrator was observed. Instead, phase calibration at the WSRT is usually done using selfcalibration.

⁹<http://www.astron.nl/p/observing.htm>

Table 12: Parameters for the WSRT observations.

| observing parameters | |
|----------------------------|-----------|
| date | 28.2.2003 |
| center frequency | 1408.9 |
| total bandwidth | 20 MHz |
| number of channels | 512 |
| velocity resolution (km/s) | 4.12 |
| beamwidth (") | 20 x 19 |
| primary beam | 0.6° |
| primary calibrator | 3C48 |

The chosen setup with a total bandwidth of 20 MHz (corresponding to ~ 4000 km/s) and a velocity resolution of 4 km/s/channel was capable to detect both narrow features in velocity space and a broad total velocity dispersion due to tidal disruption. With the chosen setup, two polarisations were observed, with 512 channels available for each of them.

4.2.2 Onsala Space Observatory 20 m

First $^{12}\text{CO}(1-0)$ observations were carried out in March 2003 using the 20 m telescope of the Onsala Space Observatory (OSO), Sweden. This telescope is enclosed in a radome, which provides no restrictions of humidity, wind and sun avoidance. CO observations are done with a SIS-mixer and a correlator with a total bandwidth of 512 MHz. The main beam efficiency at 115 GHz is $\eta = 0.43$. To account for the highly variable sky background, the observations were done in the beam switching mode to correct for atmospheric background variations. We observed the center position as given in Tab.11 under moderate weather conditions. The pointing and focus was regularly checked during the observations with the calibration sources R Leo and R Cas. Tab.13 summarises the observations. The noise level is given for the smoothed velocity resolution of 33.8 km/s.

4.2.3 IRAM 30 m

Follow-up CO observations of NGC 4441 were done with the IRAM 30 m telescope¹⁰ on Pico Veleta, Spain in July 2004. The weather conditions were good. We mapped an extended CO distribution both in the $^{12}\text{CO}(1-0)$ and $^{12}\text{CO}(2-1)$ line. We used the A 100 and B 100 as well as the A 230 and B 230 receivers to observe the $^{12}\text{CO}(1-0)$ and $^{12}\text{CO}(2-1)$ lines simultaneously. The 1 MHz filterbank with 2×512 channels was chosen. The observations were done in the beam switching mode. Pointing and focus calibration were regularly checked by observing Saturn. As a second pointing source nearby NGC 4441, we observed the calibration source 0954+658. To get a proper spatial coverage (a fully sampled map) even in the $^{12}\text{CO}(2-1)$ line, we mapped the center using a 3×3 grid with a spacing of 6", i.e. the half beamwidth of $^{12}\text{CO}(2-1)$. For the outer position, we used offset steps of 22" (full beamwidth of $^{12}\text{CO}(1-0)$) to cover more efficiently a larger area, since we wanted to track the extension of the molecular gas. In total, we observed 17 positions out to 44". In the most distant pointings we do not find emission any more, thus, we covered the central molecular gas extension completely and

¹⁰<http://www.iram.es/IRAMES/>

Table 13: Parameters for the CO observations of NGC 4441 with the OSO 20 m and IRAM 30 m telescope.

| observing parameters | IRAM 30 m | OSO 20 m |
|-----------------------------|--|------------|
| system temperature (K) | 200-340 (^{12}CO) / \sim 145 (^{13}CO) | \sim 350 |
| beamwidth CO(1-0) | 22'' | 33'' |
| beamwidth CO(2-1) | 11'' | – |
| velocity resolution CO(1-0) | 21.0 km/s | 33.8 km/s |
| velocity resolution CO(2-1) | 21.0 km/s | – |
| beam efficiency | 0.75 (1-0) / 0.52 (2-1) | 0.43 |

are able to estimate the source size.

Furthermore, the center position was observed in $^{13}\text{CO}(1-0)$ and $^{13}\text{CO}(2-1)$.

4.2.4 Optical imaging

We present here an optical R band image which is taken with CAFOS at the 2.2 m telescope on Calar Alto, Spain (CAHA). The image was taken in April 2004. To study very faint morphological features, we obtained deep imaging with an integration time of 60 minutes. Standard reduction using IRAF was applied to the data. Here we use the optical image to compare the stellar and gaseous distribution. For further analysis of the optical data, we refer to Ch. 3.

4.3 Data Reduction

4.3.1 HI interferometry

The HI data were reduced using MIRIAD¹¹ with some additional tasks written by T. Oosterloo which are specific to the Westerbork interferometer¹². After inspecting and, if necessary, flagging the calibrators, the WSRT data have to be calibrated first for changes in the system temperature. Since no secondary calibrator was observed, after flux and bandpass calibration a continuum image was created to perform selfcalibration on continuum sources within the field. To achieve a proper calibration, it is inevitable to deeply CLEAN the continuum image. In an iterative process, first a mask was created which included only real emission to define the CLEANing components. Second, the image was CLEANed using the mask and subsequently a new, deeper mask could be generated for a better CLEANing. Once the image was finally CLEANed, selfcalibration was performed, and the loop started again with creating a mask, CLEANing and selfcalibration. The data quality was high enough that only 3 iterations were necessary for a proper calibration. The results were then applied to the target galaxy. CLEANing the HI cube was done in a similar way as CLEANing the continuum as described for the selfcalibration process. After continuum subtraction, we applied Hanning smoothing, since this was not done on-line. The datacube was then convolved with a Gaussian of roughly a double size of the original beam. With this smoothed image a mask was created including real emission only. This was checked for all channels using the KARMA movie option. This mask was used for CLEANing as described above. This CLEANing procedure was repeated

¹¹<http://www.atnf.csiro.au/computing/software/miriad/>

¹²<http://www.astron.nl/oosterlo/wsrtMiriad/>

Table 14: The optical velocity, HI velocity range, HI flux, HI mass and $M_{\text{HI-to-LB}}$ ratio of NGC 4441. Heliocentric velocities are given.

| HI properties | |
|---|-------------|
| $v_{\text{sys, hel}}$ (km/s) | 2674 |
| vel. range (km/s) | 2580 – 2900 |
| F_{HI} (Jy km/s) | 4.83 |
| $M_{\text{HI}}(10^9 M_{\odot})$ | 1.46 |
| $M_{\text{HI}}(10^8 M_{\odot})$ (central disk) | 4.2 |
| $M_{\text{HI}}(10^8 M_{\odot})$ (northern tail) | 2.1 |
| $M_{\text{HI}}(10^8 M_{\odot})$ (southern tail) | 3.4 |
| $M_{\text{HI}}/L_{\text{B}}$ | 0.82 |

3 times until no improvement could be reached. Integrated intensity and velocity maps were created using the MOMENT task in MIRIAD. Finally, primary beam correction was applied to the integrated intensity maps. We created maps which were naturally weighted, thus providing the highest sensitivity, as well as maps with a robust weighting of 0.5 to reach a higher spacial resolution. We reached an rms of 0.4 mJy/beam in the naturally weighted map and and rms of 0.5 mJy/beam in the robustly weighted map. Here we present only the robust map with the higher spatial resolution, because the naturally weighted maps, although more sensitive, do not show any significant flux contribution invisible in the robust map.

4.3.2 CO single-dish observations

The CLASS¹³ package was used for the data reduction of the CO spectra observed at Onsala, the IRAM CO data were reduced using XS¹⁴, a graphical reduction and analysis software for mm spectral line data written by P. Bergmann. After checking each single spectrum for any conspicuous feature, the spectra were averaged with a weighting based on the system temperature and integration time. A first-order baseline was fitted to the resulting spectrum and subtracted. The data were calibrated against efficiencies (given in Tab. 13). Finally, we smoothed the spectra to a velocity resolution of 20 km/s to achieve a better signal-to-noise ratio. For the different positions in the ¹²CO(1-0) map, we reached a noise level of 1.6 – 5.3 mK, in the ¹²CO(2-1) map the noise level lies between 2.1 and 9.6 mK T_{MB} . In the single spectra of the ¹³CO measurements the noise level is 0.7 mK (1–0) and 1.3 mK (2–1).

4.4 Results

4.4.1 Neutral hydrogen

The neutral hydrogen distribution in NGC 4441 shows two prominent tidal tails to the north and to the south (see Fig.42). The southern arm is blueshifted with respect to the system velocity, covering a range from 2580 km/s to 2640 km/s (for reference, see Fig.43). In contrast, the northern arm has a higher velocity, compared to the system velocity. It covers a range from 2700 km/s to 2820 km/s. Both tails have a similar extension: the northern tail is extended out to 4.6' (48 kpc), the southern tail out to 4' (42 kpc) from the nucleus and both form a

¹³Continuum and Line Analysis Single-dish Software, <http://www.iram.fr/IRAMFR/GILDAS/>

¹⁴<ftp://yggdrasil.oso.chalmers.se/pub/xs/>

relatively symmetric structure. The HI tails are clumpy, especially at the tip of both tails. Two large clumps are furthermore found $\sim 1.6'$ (17 kpc) from the center in both tails. It is noticeable that the symmetry in the HI distribution cannot be found when looking at the optical morphology. Here we see a tail to the North as well, which coincides nicely in position and extension with the large northern HI clump. In the southern direction, however, we see a misalignment of the HI distribution and the optical appearance. In the optical two shells are visible south-west of the main body. Since the HI tails goes nearly directly to the south, there is almost no overlap of the more western, outer shell with the HI tail. The tip of the inner shell corresponds to the southern closer HI clump. Three knots are visible in the optical at the position of the HI clump of which at least two do not look point-like, i.e., are probably not foreground stars. They might be star forming knots, probably to close to the galaxy to survive as tidal dwarf galaxies, but can also be background galaxies, because our deep R-band image shows an underlying background galaxy cluster. However, no HI is detected at higher velocities within our band, which may of course miss distant galaxies. Unfortunately, the distance of the background cluster is not known.

The northern tail starts from the north-east side of the central HI concentration and is only loosely connected to it. In projection, the tail seems to go east from the northern clump parallel to it and turns then to the west side, while the velocity is slightly increasing, esp. at the western edge of the tail. The tip and the eastern side have a lower velocity, which is, however, still higher than the system velocity. The southern tail emerges from the southern clump and turns to the east at the end. Here, the velocity structure is more complex with the lowest values at the western edge of the tail, whereas the velocity increases to the tip and in the direction of the main body. There is, however, a region of lowest velocity east of the southern clump, i.e. near to the center.

Fig.44 shows the central region of NGC 4441 and the HI distribution (robust=0.5) overlaid as contours. We find a distinct HI disk with a diameter of $\sim 1.04'$ (11 kpc) centered on the optical and CO nucleus. With a projected minor axis of $\sim 38''$ (6.7 kpc) and under the assumption of a uniform circular disk, we estimate an inclination $i = \arccos(\frac{b}{a}) \simeq 52^\circ$ (a is the major axis, b the minor axis). At the center of the disk there is a decline of HI, with a size of $\sim 20''$. Because this corresponds to the derived source size of the molecular gas distribution, it fits a typical behaviour of disk galaxies where atomic gas is found in the outer parts of the disk, whereas in the center the dominant gas phase is molecular. The highest concentration of HI is found in the east side of the disk, thus, east of the optical center. In the disk the gas appears to have a high dispersion (up to ~ 80 km/s) decreasing down to ~ 40 km/s at the edges of the HI associated with the galactic main body.

North-west of the center (~ 6.3 kpc), the dispersion map shows another region of increased velocity dispersion, compared to the surroundings. There is no obvious feature found either in HI or in the optical associated with this peak, but in the pv-diagram (Fig. 51) a second velocity component appears in this region.

The gas in the tails shows only little dispersion in general (< 15 km/s). The dispersion increases slightly in regions of gradients in the atomic gas distribution, e.g. around clumps. The northern HI tail is separated from the gas concentration associated with the optical tail by a region of high dispersion, up to 55 km/s at the eastern tip. In general, the east side of this gas concentration seems to be more disturbed than the west side of the optical tail.

Between the southern clump and the central gas concentration there is also a region of high dispersion (up to ~ 70 km/s). This region is not related to any optical feature, it is situated at the southern faint edge of the main body.

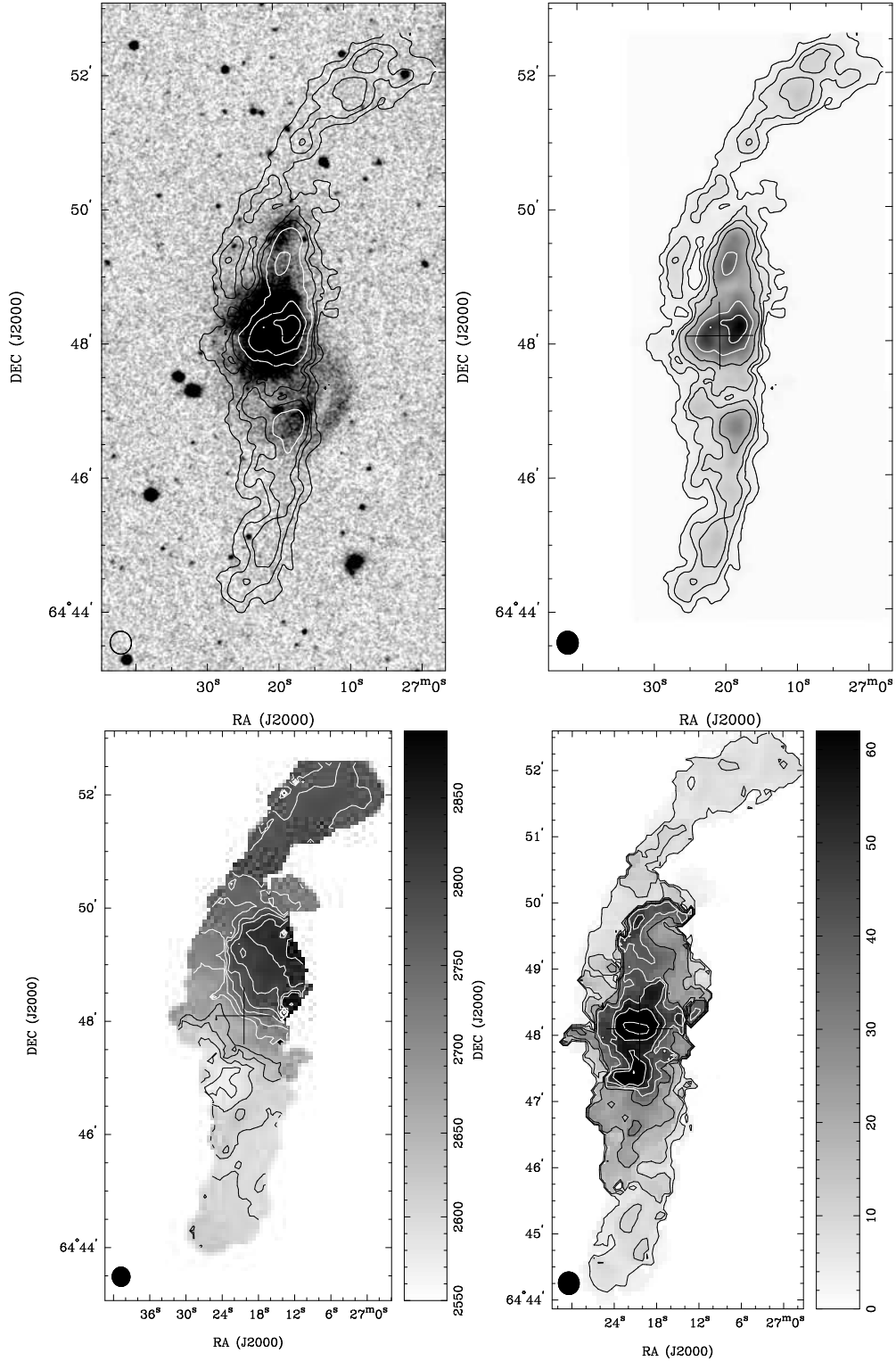


Figure 42: NGC 4441 – (**top left**) HI distribution overlaid on optical DSS image. Contour levels are 0.0001 0.01 0.03 0.05 0.1 0.2 0.3 Jy/beam km/s (0.0001 Jy/beam km/s corresponds to $2.8 \cdot 10^{17} \text{ cm}^{-2}$), (**top right**) HI distribution, contours same as above, (**bottom left**) velocity field, contour levels are 2575 to 2850 km/s, in steps of 25 km/s, (**bottom right**) HI velocity dispersion (2. moment), contour levels are 5, 10, 20, 30, 40, 50, 60, 75 km/s. The cross marks the optical center position.

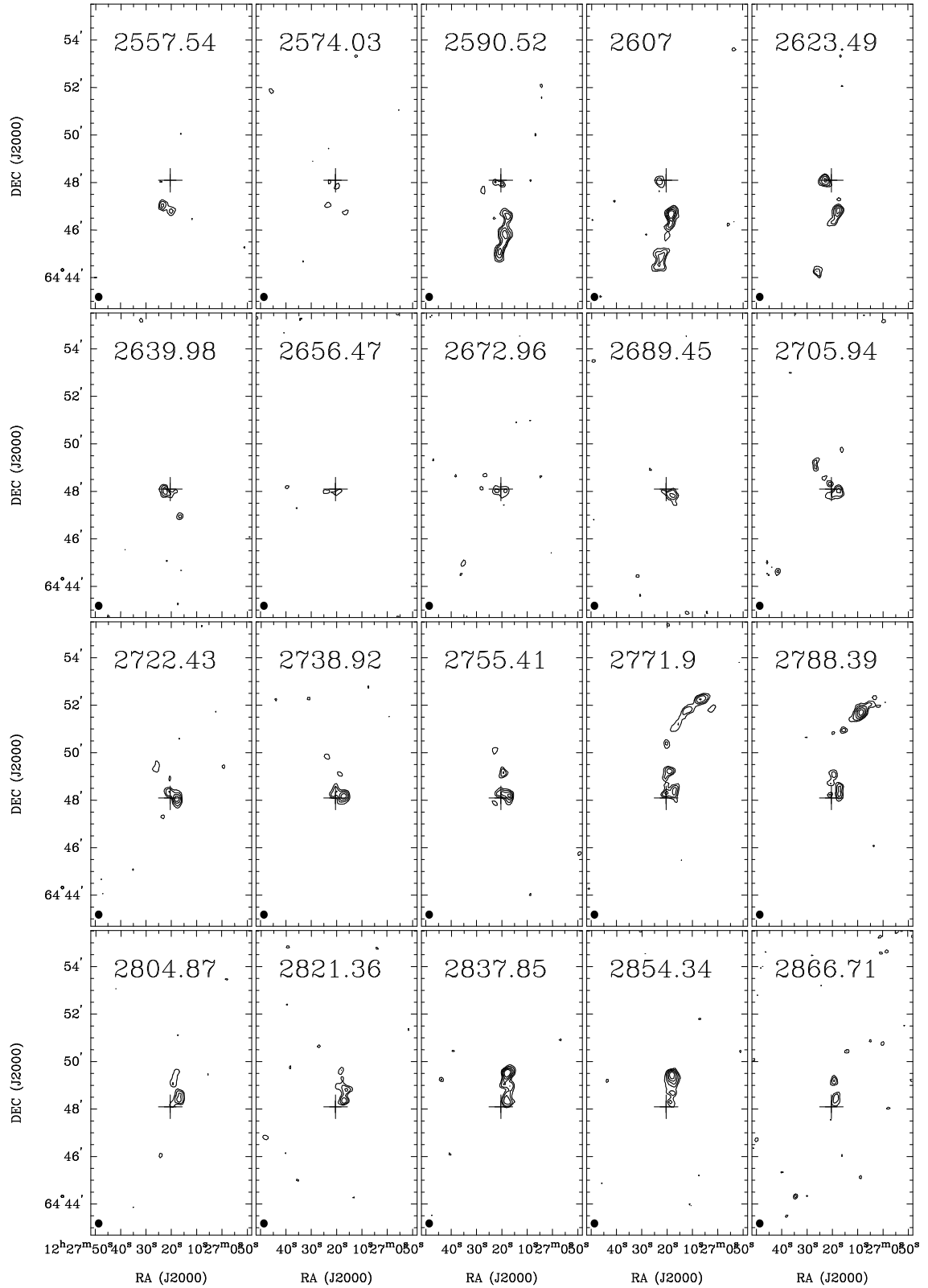


Figure 43: Channel maps (robust weighted) of NGC 4441. The optical center position is marked with a cross. The contour levels are 1.1, 1.3, 1.5, 1.7, 1.8, 2 mJy/beam. The heliocentric velocity is given at the top left, the beam at the bottom left corner.

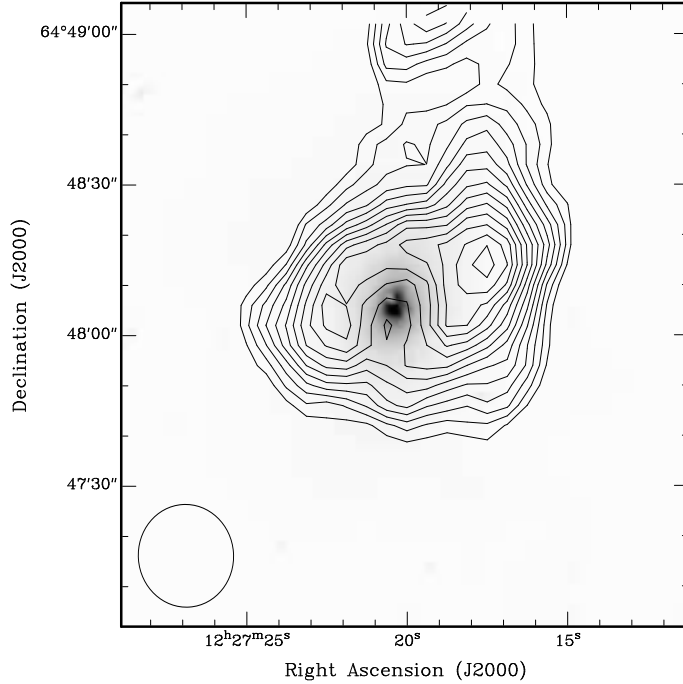


Figure 44: Deep R-band image (taken with the CAHA 2.2 m telescope) of the central region. HI is overlaid as contours, contour levels are from 0.1 to 0.36 Jy/beam km/s in steps of 0.02 Jy/beam km/s. The beamsize is shown in the lower left corner. The gas disk is centered on the optical nucleus, which exhibits a thin dust lane.

Note, that sharp regions of high velocity dispersion may also result from a low signal-to-noise ratio, which might esp. be the case for the border between the HI in the optical tail and the HI tail as well as the gap between the southern large clump and the main body, since in these regions only little HI is found.

4.4.2 20 cm Continuum

Fig.45 shows an optical image with the 20 cm radio continuum overlaid as contours. The continuum source in NGC 4441 is resolved (see below) and concentrated on the nucleus of the galaxy. To estimate the star formation rate (SFR) from the 20-cm radio continuum flux density we use

$$\text{SFR} (M_{\odot} \text{ yr}^{-1}) = 0.14 D^2 F_{20 \text{ cm}}$$

derived from Condon (1992) and Haarsma et al. (2000), where D is the distance in Mpc and $F_{20 \text{ cm}}$ is the 20-cm radio continuum flux density in Jy. In Tab.15 the results for NGC 4441 are given. Tab.15 also gives the SFR estimated from the FIR luminosity:

$$\text{SFR} (M_{\odot} \text{ yr}^{-1}) = 0.17 L_{\text{FIR}}$$

following Kennicutt (1998), with L_{FIR} in units of $10^9 L_{\odot}$. The IRAS 60 μm and 100 μm flux densities were taken from Moshir & et al. (1990). The SFR of 1–2 M_{\odot} /yr calculated with both methods is low for a merger and normal for typical spirals. This is remarkable,

Table 15: Continuum and FIR fluxes, SFR based on continuum and FIR emission, respectively, and q parameter.

| properties | |
|--|-------|
| 20 cm (Jy) | 0.013 |
| 60 μm (Jy) | 2.69 |
| 100 μm (Jy) | 3.88 |
| SFR _{20 cm} (M_{\odot}/yr) | 2.36 |
| SFR _{FIR} (M_{\odot}/yr) | 0.95 |
| q | 2.4 |

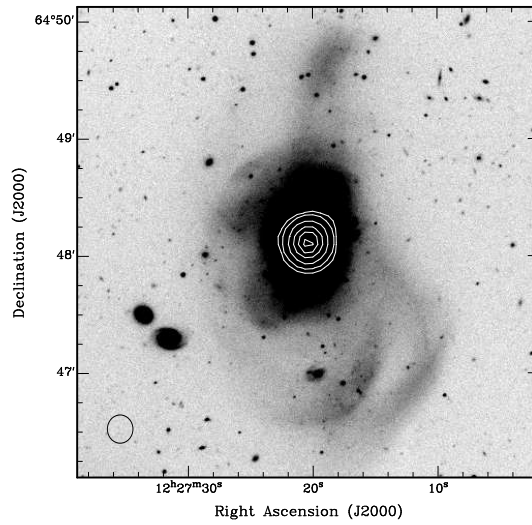


Figure 45: R-band image (NOT) and contours of the 20 cm continuum flux. The beam is shown in the lower left corner of the image. Contour levels are 5, 10, 20, 50, 75, 100 \times 0.0001 Jy.

because NGC 4441 is a merger with clear tidal features present in both the stellar and gaseous component. Thus, if this galaxy is already in a post-starburst phase, it still manages to retain a large amount of gas is available for star formation. We also calculated the logarithmic ratio of FIR to radio flux, the so-called q parameter (Helou et al. (1985)):

$$q = \log \frac{F(\text{FIR}) / (3.75 \cdot 10^{12} \text{ Hz})}{F(1.4 \text{ GHz})}$$

Note, that the continuum flux at 1.4 GHz $F(1.4 \text{ GHz})$ in this formula is in units of $\text{W}/\text{m}^2/\text{Hz} = 10^{-26} \text{ Jy}$. The FIR flux $F(\text{FIR})$ is a combination of the 60 μm and 100 μm flux densities, as used for determining L_{FIR} : $F(\text{FIR}) = 1.26 \cdot 10^{-14} \cdot (2.58 \cdot F(60 \mu\text{m}) + F(100 \mu\text{m}))$. To calculate q, $F(\text{FIR})$ is normalised by the mean frequency of 60 μm and 100 μm , which is $3.75 \cdot 10^{12} \text{ Hz}$. Helou et al. (1985) derived a mean value for q of 2.3. Although this parameter was determined for disk galaxies only (but independent of their star formation activity), NGC 4441 ($q = 2.4$) conforms to this value.

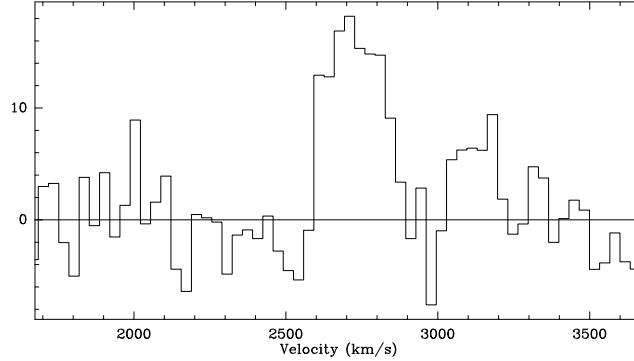


Figure 46: $^{12}\text{CO}(1-0)$ spectrum observed with the OSO 20 m telescope. The intensity is given in T_{MB} (mK).

4.4.3 Molecular gas

First OSO observations revealed a molecular gas content in the inner $33''$ of $\sim 4.7 \times 10^8 M_{\odot}$. Fig. 46 shows the observed CO spectrum.

Mapping NGC 4441 in CO with the IRAM 30 m telescope, we found a molecular gas distribution with a size of $22''$ (3.8 kpc), extending in particular to the south-east. Tab. 16 gives the pointings relative to the center position, the noise levels, the widths determined from Gaussians of both the $^{12}\text{CO}(1-0)$ and $^{12}\text{CO}(2-1)$ line and the integrated intensities. In Fig. 48 and Fig. 49 we present the spectra of the mapped positions for both the $^{12}\text{CO}(1-0)$ and $^{12}\text{CO}(2-1)$ line.

We found extended CO emission to the south-east visible in the beams $22''$ away from the center in both $^{12}\text{CO}(1-0)$ and $^{12}\text{CO}(2-1)$. In the outskirts to the north and west, we see only little CO. From the oversampled map of the center (Fig. 47), we see that the gas is concentrated to the center, because even in $^{12}\text{CO}(1-0)$ we find a clear decrease of intensity going away from the center only a quarter of beamsize. However, the spatial resolution and coverage are not sufficient to model the asymmetry, thus, we used a Gaussian as an approximation of the source, keeping in mind that derived parameters like the molecular gas mass are lower limits.

Under the assumption of a Gaussian distribution of the intensity, we plotted for both maps the intensity versus radial distance from the center and fitted a Gaussian to derive the source size. The real source size can be estimated from the observed source size and the known beam size as $\Theta_{\text{source}}^2 = \Theta_{\text{obs}}^2 - \Theta_{\text{beam}}^2$. We derive a size of $22''$ (3.9 kpc) for $^{12}\text{CO}(1-0)$. The estimated source size for $^{12}\text{CO}(2-1)$ is slightly larger, but this is probably an artefact due to the undersampling of the $^{12}\text{CO}(2-1)$ map and the clumpiness of the medium. Although we detected clear emission at the positions $22''$ away from the center, the gas does probably not fill the beam smoothly, but we may detect the edge of the source, which is not modeled by a Gaussian source size estimation. Thus, due to the smaller beamsize in $^{12}\text{CO}(2-1)$ the detection pretends a larger real source size. In our further discussion, we assume an identical extension

of $^{12}\text{CO}(2-1)$ and $^{12}\text{CO}(1-0)$. We determined a central H_2 column density of $1.8 \cdot 10^{21} \text{ cm}^{-2}$ based on a CO abundance of 10^{-4} and calculated a total molecular gas mass of $4.6 \cdot 10^8 M_\odot$. We used a 'standard' conversion factor of $X_{\text{CO}} = 2.3 \cdot 10^{20}$, referring to Strong et al. (1988). Since we found extended gas to the south-east (see Fig. 48 and Fig. 49), the assumption of a Gaussian distribution can give us only a lower limit, but the coverage of the currently available data is not sufficient for a more precise calculation.

The spectra in both maps clearly show two components, a fainter one (at the center) at 2690 km/s (2660 km/s in $^{12}\text{CO}(2-1)$) and the dominant one at 2790 km/s. Comparing the spectra at individual positions, the relative intensities of both line components change, esp. in the SE direction. Best visible in the $^{12}\text{CO}(2-1)$ map, the more blueshifted line is the brighter one at the offset position (+15.6", -15.6"). This component is centered at 2660 km/s in $^{12}\text{CO}(2-1)$ in each position, whereas in $^{12}\text{CO}(1-0)$ there seems to be a slight shift from 2690 km/s in the center to 2660 km/s in the outer region.

We also observed NGC 4441 in $^{13}\text{CO}(1-0)$ and $^{13}\text{CO}(2-1)$ at the center position. The $^{13}\text{CO}(1-0)$ line is clearly detected, the $^{13}\text{CO}(2-1)$ is only tentatively detected on a 2.8σ level, but a feature at the expected velocity of 2790 km/s is found (see Fig. 50). Tab. 17 gives the linewidths and integrated intensities of all four lines at the center position. We fitted only one single Gaussian to the ^{13}CO line. The fitted center velocity of $^{13}\text{CO}(1-0)$ (Tab. 17) lies between the derived values for the blue- and redshifted line using the ^{12}CO transitions. In contrast, in $^{13}\text{CO}(2-1)$ we see, if at all, the component with the higher velocity. The derived center velocity of 2785 km/s agrees with the fitted velocities based on the ^{12}CO data. This component is also the stronger one in ^{12}CO at the center. Thus, interestingly the shape of the $^{13}\text{CO}(1-0)$ spectrum is not in agreement with the $^{13}\text{CO}(2-1)$ and both ^{12}CO lines. However, the signal-to-noise ratio of $^{13}\text{CO}(2-1)$ is too low to draw firm conclusions from this behaviour.

4.5 Discussion

4.5.1 Size of the star forming region

We fitted a Gaussian to the continuum source using the MIRIAD task IMFIT and derived a deconvolved source size of $\text{FWHM} = 5'' \times 3''$, that is $875 \times 525 \text{ pc}$. If this emission comes from ongoing star formation only (and there are no hints for another origin, e.g. an AGN), the region of ongoing star formation is embedded into the reservoir of raw material for star formation, namely the molecular gas extension, but does not cover its full extent. Compared to the Medusa, where the region of ongoing star formation is extended on a scale of $\sim 2 \text{ kpc}$ (e.g., Armus et al. (1990)) and much more intense, the star forming activity seems to be shrunk in intensity and maybe also in spatial extent. Interestingly, the molecular gas mass of NGC 4441 is only a quarter of the Medusa ($4.6 \times 10^8 M_\odot$ for NGC 4441 versus $2 \times 10^9 M_\odot$ for the Medusa), whereas the amount of atomic hydrogen is comparable ($1.46 \times 10^9 M_\odot$ in NGC 4441 versus $2 \times 10^9 M_\odot$ in the Medusa). The question arises, why the starburst in NGC 4441 has already faded, while the Medusa is still intensely forming stars. Aalto & Hüttemeister (2000) estimate that the burst in the Medusa will continue only for $\sim 40 \cdot 10^6$ years, under the assumption that the current star formation rate will not change dramatically. If the star formation rate depends mainly on the duration of the burst and decreases with ongoing burst age, the phase of intense star formation in a merger event, which NGC 4441 and the Medusa both underwent, might be very short, and the Medusa will fade soon as well.

Table 16: CO line parameters of the map of NGC 4441. The reference coordinates are the center coordinates (J2000): RA: $12^{\text{h}}27^{\text{m}}20.36^{\text{s}}$, DEC: $+64^{\circ}48'06''$. Given are the offset positions, the total velocity range of the CO(1-0) and CO(2-1) line and the intensities of both lines. The temperatures are measured in T_{MB} .

| Δ RA ($''$) | Δ DEC ($''$) | $\text{rms}_{\text{CO}(1-0)}$ (mK) | $\Delta v_{\text{CO}(1-0)}$ (km/s) | $I_{\text{CO}(1-0)}$ (K km/s) | $\text{rms}_{\text{CO}(2-1)}$ (mK) | $\Delta v_{\text{CO}(2-1)}$ (km/s) | $I_{\text{CO}(2-1)}$ (K km/s) |
|-------------------------|--------------------------|---------------------------------------|---------------------------------------|----------------------------------|---------------------------------------|---------------------------------------|----------------------------------|
| 0 | 0 | 2.50 | 292 | 7.52 | 7.67 | 324 | 6.10 |
| 6 | 6 | 4.62 | 283 | 2.34 | 6.72 | 240 | 1.84 |
| 0 | 6 | 3.43 | 328 | 4.80 | 6.34 | 270 | 3.51 |
| -6 | 6 | 5.33 | 209 | 2.68 | 5.95 | 252 | 2.69 |
| 6 | 0 | 3.78 | 267 | 4.24 | 7.67 | 302 | 3.64 |
| -6 | 0 | 3.86 | 336 | 1.69 | 7.67 | 247 | 2.50 |
| 6 | -6 | 5.28 | 344 | 6.65 | 7.87 | 220 | 6.34 |
| 0 | -6 | 3.75 | 320 | 4.60 | 9.6 | 285 | 6.14 |
| -6 | -6 | 4.42 | 259 | 3.70 | 9.6 | 308 | 3.97 |
| 0 | 22 | 2.19 | 220 | 0.92 | 3.62 | – | – |
| -22 | 0 | 2.06 | – | 1.67 | 2.88 | – | – |
| 0 | -22 | 1.64 | 262 | 1.44 | 3.07 | – | – |
| 22 | 0 | 2.33 | 316 | 2.47 | 2.30 | 275 | 0.88 |
| 15.6 | -15.6 | 2.39 | 310 | 2.53 | 2.11 | 318 | 2.23 |
| 44 | 0 | 1.77 | – | – | 3.07 | – | – |
| 0 | -44 | 2.18 | – | – | 2.11 | – | – |
| 31 | -31 | 2.00 | – | – | 2.88 | – | – |

Table 17: Parameters of ^{12}CO and ^{13}CO at the central position. Gaussians were fitted to determine linewidths, peak intensity and center velocity. For ^{12}CO , we fitted two components to the measured line, in ^{13}CO only one component was visible. The given intensity is integrated over both components. Temperatures are given in T_{MB} .

| line | center velocity (km/s) | | linewidth (km/s) | | Peak (K) | | int. Intensity (K km/s) |
|-----------------------|---------------------------|------|---------------------|-----|-------------|-------|----------------------------|
| $^{12}\text{CO}(1-0)$ | 2698 | 2796 | 125 | 147 | 0.02 | 0.036 | 7.52 |
| $^{12}\text{CO}(2-1)$ | 2655 | 2802 | 93 | 114 | 0.016, | 0.039 | 6.10 |
| $^{13}\text{CO}(1-0)$ | 2725 | | 208 | | 0.0018 | | 0.37 |
| $^{13}\text{CO}(2-1)$ | 2785 | | 61 | | 0.0033 | | 0.25 |

Table 18: Molecular line ratios derived from the CO measurements at the central position.

| property | result |
|---|--------|
| M_{H_2} ($10^8 M_{\odot}$) | 4.6 |
| $^{12}\text{CO}(2-1)/^{12}\text{CO}(1-0)$ | 0.5 |
| $^{13}\text{CO}(2-1)/^{13}\text{CO}(1-0)$ | 0.42 |
| $^{12}\text{CO}(1-0)/^{13}\text{CO}(1-0)$ | 21 |
| $^{12}\text{CO}(2-1)/^{13}\text{CO}(2-1)$ | 25 |

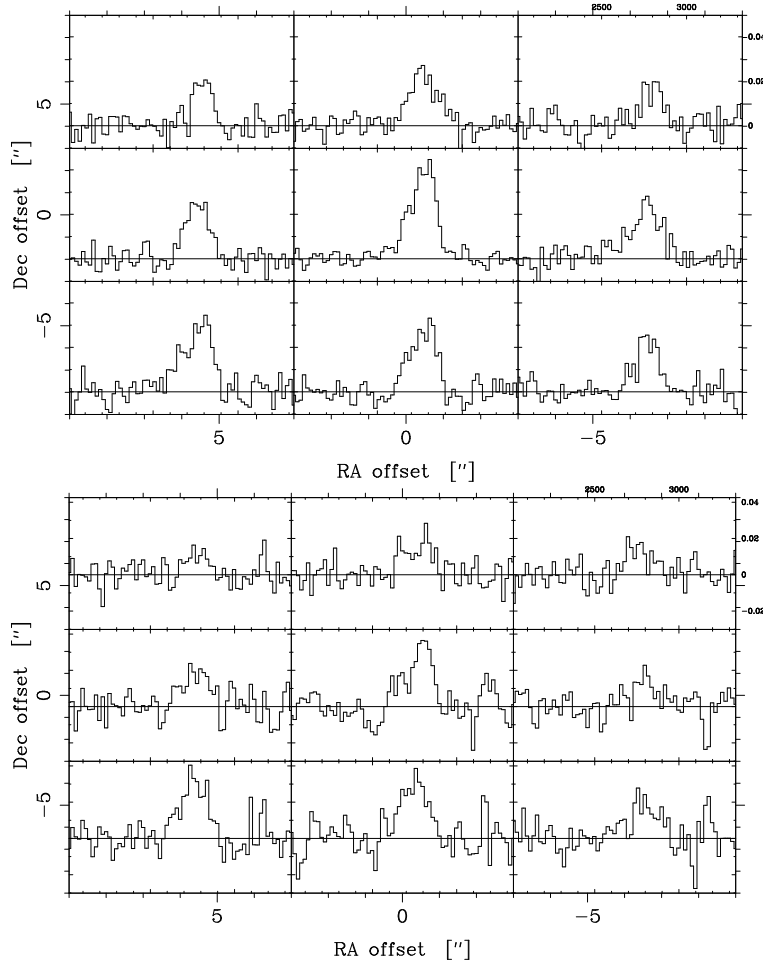


Figure 47: Inner $6'' \times 6''$ of the CO map observed with the IRAM 30 m telescope. The outer axes mark the spacing of the observing positions, the inner axes show the velocity (km/s) and T_{MB} (mK), respectively (labeled in the upper right spectrum). **(top)** $^{12}\text{CO}(1-0)$ map of the central region. Note that the data are highly oversampled (beamsize $22''$). **(bottom)** $^{12}\text{CO}(2-1)$ map of the central region. Note that the data are close to being fully sampled (beamsize $11''$).

4.5.2 Star formation efficiency

The relation between the ongoing star formation and the available resource for star formation (i.e., dense gas) can be expressed by the star formation efficiency: $\text{SFE}(\frac{1}{\text{yr}}) = \frac{\text{SFR}_{\text{FIR}}}{M_{\text{H}_2}}$. Thus, for NGC 4441 we derive a star formation efficiency of $\text{SFE} = 2.1 \cdot 10^{-9} \text{ yr}^{-1}$. The equivalent gas depletion time is $\tau = 1/\text{SFE} = 4.8 \cdot 10^8 \text{ yr}$. In comparison with the very effective star burst in the Medusa (up to an efficiency of $1.7 \cdot 10^{-8} \text{ yr}$ (Aalto & Hüttemeister (2000))), NGC 4441 has a moderate star formation efficiency: $\text{SFE}(\text{NGC 4194}) \sim 10 \times \text{SFE}(\text{NGC 4441})$. From radiative transfer models, we find that the molecular gas is thin and cold in NGC 4441 (see below), which makes it difficult to form new stars, whereas in the Medusa dense cores of ongoing star formation are found. It is, however, unclear, whether the difference in the gas phases are due to aging effects, e.g., NGC 4441 might have transformed all dense gas into

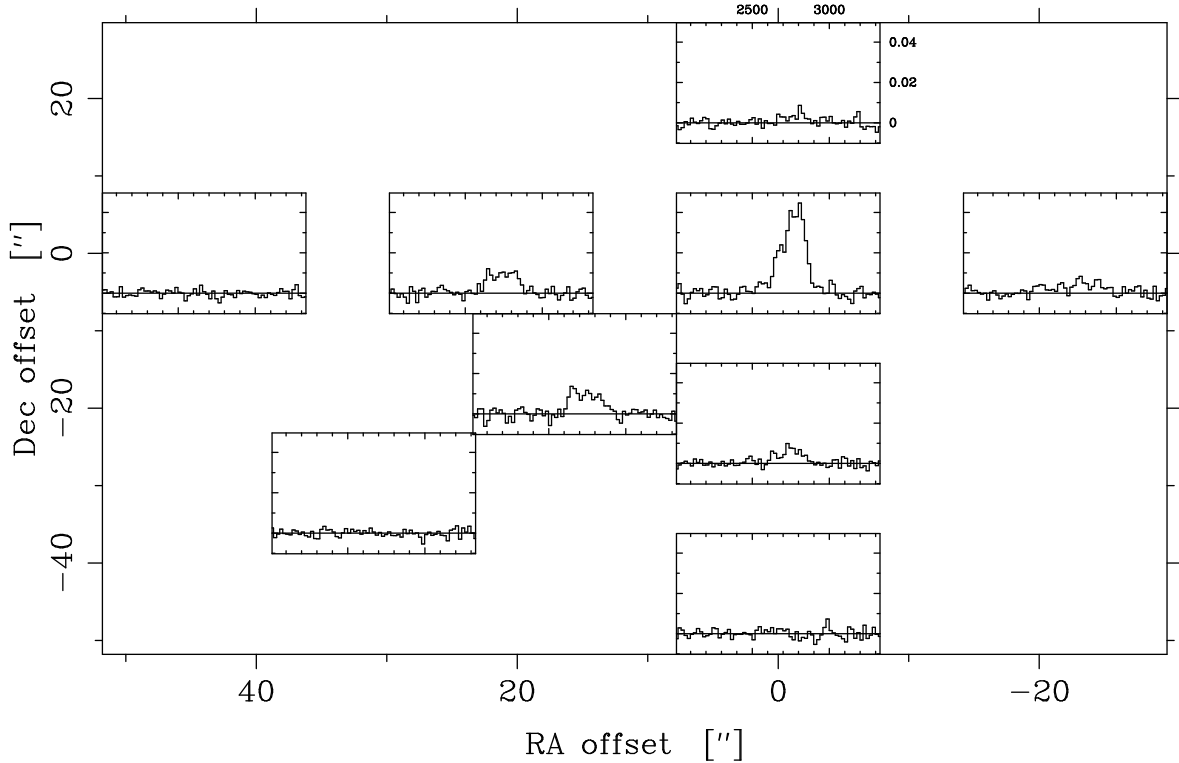


Figure 48: Large $^{12}\text{CO}(1-0)$ map of NGC 4441, observed with the IRAM 30 m telescope. The outer axes mark the spacing of the observing positions, the inner axes show the velocity (km/s) and T_{MB} (mK), respectively (labeled in the upper right spectrum). The positions the spectra were taken at have a spacing of one full beamsize.

stars, whereas in the Medusa this process is still ongoing. A second explanation is differences in the gas densities due to a different gas reservoir provided by the progenitors and/or different merger geometry.

4.5.3 Kinematics of the gas

In Fig. 51 we present position-velocity-diagrams (pv-diagrams) through the major axis of the HI disk (position angle (pa) = 323°), the minor axis (pa = 233°) and the major axis of the inner ring or disk (pa = 292°). The minor axis corresponds to the thin dust lane found in the central region (see Fig. 44). This is in agreement with what is found in the Medusa, where the dust lane follows the minor axis as well (Aalto & Hüttemeister (2000)). Thus, also from the dynamical point of view (when looking at the interplay between the gas and dust), these two galaxies seem to be very similar. From our observations, it remains unclear whether the dust lane is dynamically decoupled from the (inner) disk or is maybe feeding the inner disk which might lead to slightly enhanced star formation.

The pv-diagram of the major axis shows an extra velocity component north-west of the center. In the velocity dispersion map (Fig. 42) this position is seen as a region of high dispersion. In the HI distribution map, however, no obvious feature is found.

The pv-diagram of the inner ring or disk looks similar to a typical rotation curve, with the two bright blobs within the ring clearly separated in velocity space.

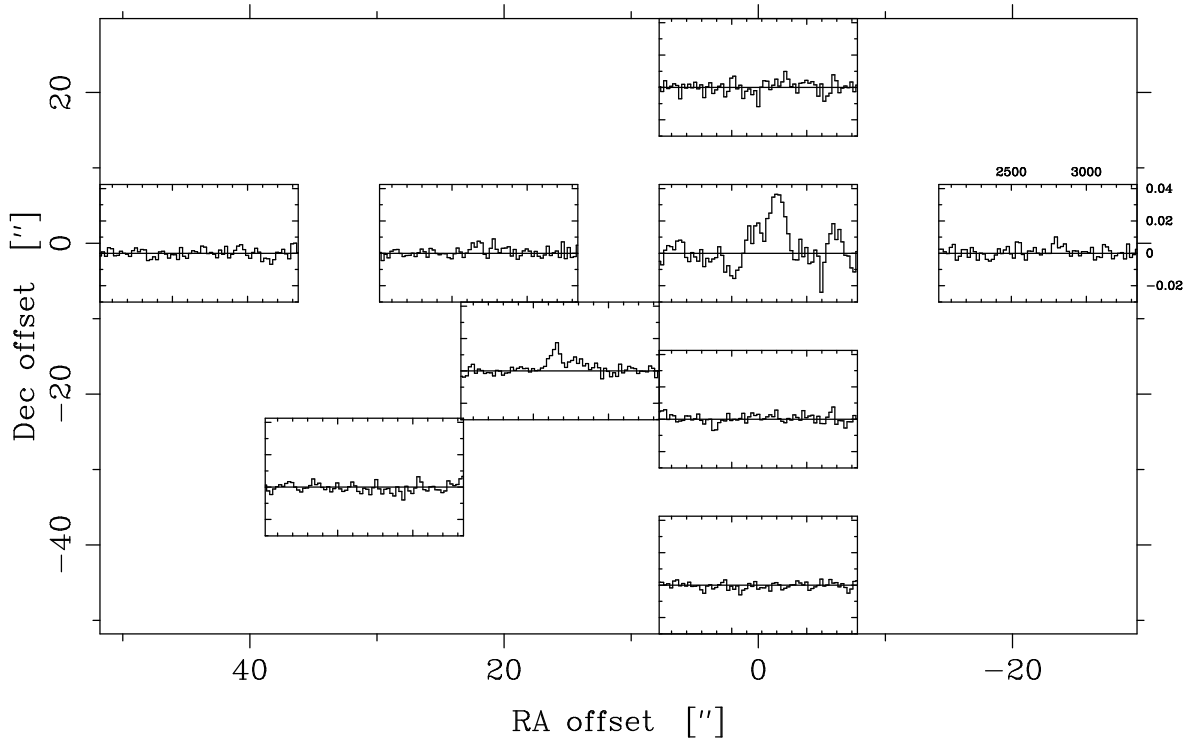


Figure 49: Large $^{12}\text{CO}(2-1)$ map of NGC 4441, observed with the IRAM 30 m telescope. The outer axes mark the spacing of the observing positions, the inner axes show the velocity (km/s) and T_{MB} (mK), respectively (labeled in the upper right spectrum). The positions were taken at have a spacing of two full beamsizes.

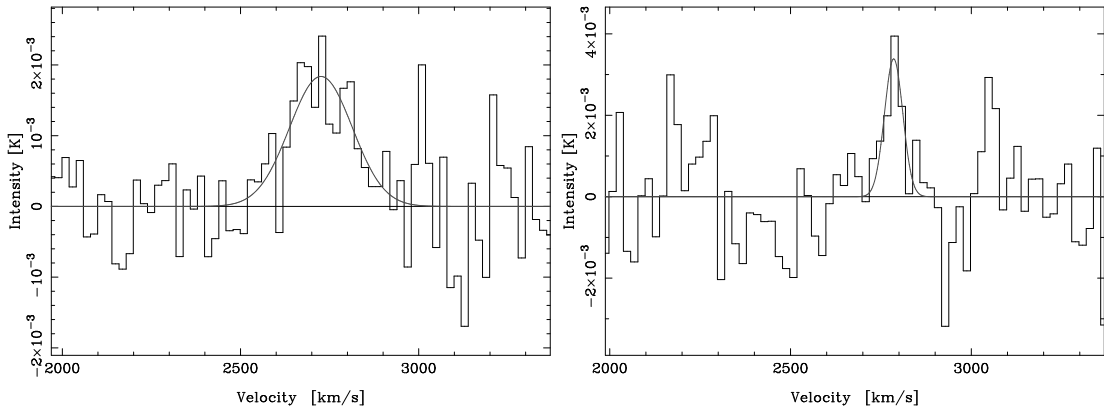


Figure 50: ^{13}CO observed at the center position of NGC 4441, measured with the IRAM 30 m telescope. The intensity is given in T_{MB} . (left): $J=1-0$, (right): $J=2-1$. Overlaid is a Gaussian fit to the lines. The parameters are given in Tab. 17.

Although we have only crude information about the CO velocity field, it is unlikely that the molecular gas has significantly different kinematics, decoupled from the HI. A comparison of the integrated spectra of the CO and the inner HI distribution (Fig. 52) show that both cover the same velocity range and does not show any particular discrepancies.

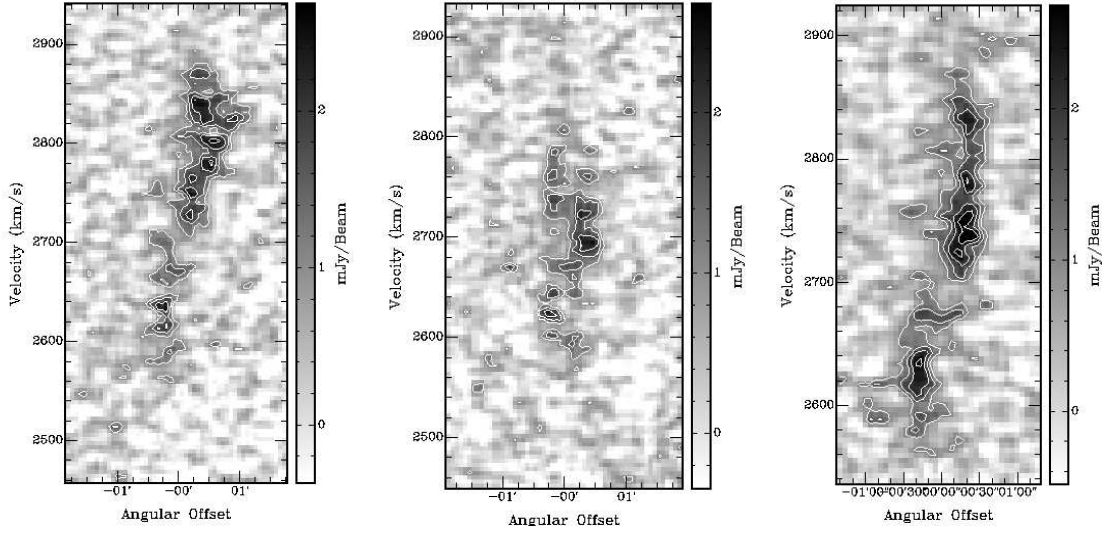


Figure 51: Position-velocity diagrams of three cuts through NGC 4441. **(left)** Slice through the major axis of the rotating disk, corresponding roughly to the major axis of the inner part of the elliptical stellar main body. The position angle is 320° . **(middle)** Slice through the minor axis of the rotation disk. The slice follows exactly the dust lane through the center. **(right)** Slice through the inner HI ring with the position angle of 290° .

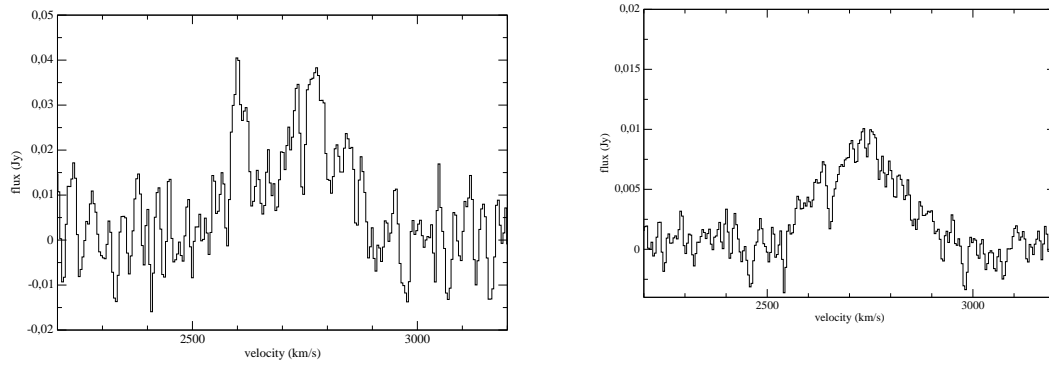


Figure 52: Integrated HI spectrum of **(left)** the total amount of HI in NGC 4441 and **(right)** the central disk.

4.5.4 Molecular gas properties

The extension of the molecular gas out to ~ 3.9 kpc is comparable to what is found in the Medusa (Aalto & Hüttemeister (2000); Aalto et al. (2001)), however, the geometry compared to the optical appearance is different in both galaxies. In the Medusa the CO follows roughly the direction of the optical tidal tail, whereas in NGC 4441 the molecular gas is more extended to the opposite side of the optical tail.

The $^{12}\text{CO}/^{13}\text{CO}$ line ratio in NGC 4441 is unusually high. Typical ratios of giant molecular clouds (GMCs) in the Galaxy are found to be 3 to 5, and more diffuse CO emission from

regions of moderate optical depth has an only slightly higher ratio of 6 – 7 (e.g., Polk et al. (1988)). Obviously, in NGC 4441 the molecular ISM is in a different stage than in normal galaxies, e.g. the Milky Way.

The high ratio cannot be explained by an underabundance of ^{13}CO , because this galaxy is not metal-poor (as derived from our optical spectrum, Ch. 3). In addition, the scenario for a ^{12}CO overabundance due to selective nucleosynthesis of ^{12}C as discussed by Casoli et al. (1992) for starbursts is not valid, because NGC 4441 is not in a starburst phase. The starburst occurred in the past, which additionally enriched the ISM with metals.

Aalto et al. (1995) compared the $^{12}\text{CO}(1-0)/^{13}\text{CO}(1-0)$ line ratio with the FIR flux ratio f_{60}/f_{100} at $60\ \mu\text{m}$ and $100\ \mu\text{m}$ and found a tendency of increasing CO ratio with increasing FIR flux ratio. They also differentiate between four FIR luminosity intervalls. Typically, galaxies with a lower FIR luminosity have also a lower CO ratio. With $^{12}\text{CO}(1-0)/^{13}\text{CO}(1-0) = 21$ and $f_{60}/f_{100} = 0.69$ NGC 4441 fits into the range covered by the sample galaxies of Aalto et al. (1995) in this diagram. However, its CO ratio is rather high, especially when considering that this galaxy has a FIR luminosity of less than $10^{10} L_{\odot}$.

In contrast to the Medusa, where the molecular gas is thermally excited due the ongoing starburst, the gas in NGC 4441 is subthermally excited.

To investigate the physical conditions of the ISM like the kinetic temperature, the H_2 number density and the column density, we used two different models for the analysis:

- RADEX¹⁵ is a one-dimensional non-LTE radiative transfer code available on-line (van Langevelde & van der Tak (2004), Schöier et al. (2005)). In this code, the mean escape probability method for an isothermal and homogeneous medium is used for the calculations. No information about the geometry or the velocity field of the source are needed.
- Second, we used a large velocity gradient (LVG) code based on the approach invented by Sobolev (1960). The code was originally written by Ch. Henkel and optimised by Hüttemeister (1993) and Dahmen (1995).

We assume that the ^{12}CO lines are optically thick ($\tau > 1$), so that the CO is selfshielded from the UV radiation field. The high $^{12}\text{CO}/^{13}\text{CO}$ line ratio on the other hand limits the optical depths to $\tau < 10$. As a second assumption, we treat the gas as being clumpy, thus not filling the beam smoothly. In Fig. 53 a comparison of the results from the LVG code and RADEX is shown for an H_2 column density of $10^{20}\ \text{cm}^{-2}$. Both codes give the same trend, i.e., the levels decrease from high temperatures at low densities to low temperatures at high densities. The measured line ratio of in NGC 4441 is in a fair agreement in both models, although the LVG code allows lower densities in the high temperature range. In general, at larger line ratios, the RADEX code however gives lower densities at a given temperature, but the shape of the levels is similar.

In Fig. 54 the results of both codes for column densities of $10^{20}\ \text{cm}^{-2}$ and $10^{21}\ \text{cm}^{-2}$. The best agreement of the $^{12}\text{CO}(2-1)/^{12}\text{CO}(1-0)$ and $^{13}\text{CO}(2-1)/^{13}\text{CO}(1-0)$ lines ratios is found for a column density of $10^{20}\ \text{cm}^{-2}$, for which in particular the LVG code matches very well. In all cases, the gas appears to be diffuse, with densities less than $10^4\ \text{cm}^{-3}$. From the ^{12}CO and ^{13}CO ratios alone it is not possible to determine the temperature more specific, but as seen in Fig. 54, for higher temperatures ($> 20\ \text{K}$) the density is well below $1000\ \text{cm}^{-3}$. No

¹⁵<http://www.strw.leidenuniv.nl/moldata/radex.html>

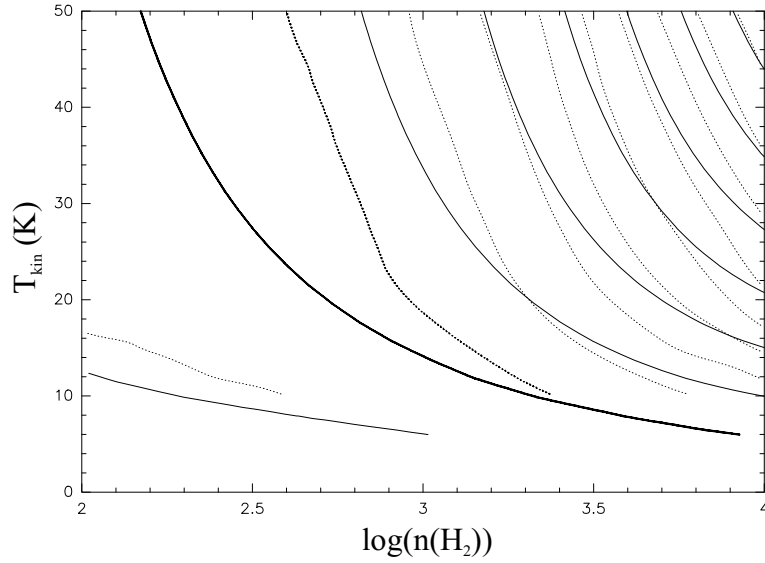


Figure 53: A comparison of the LVG (solid) and the RADEX (dotted) solutions for a given H_2 column density of 10^{20} cm^{-2} in ^{12}CO . The levels of the line ratios start at 0.25 and proceed in steps of 0.25. The bold lines mark the level for the derived line ratio of NGC 4441 (0.5)

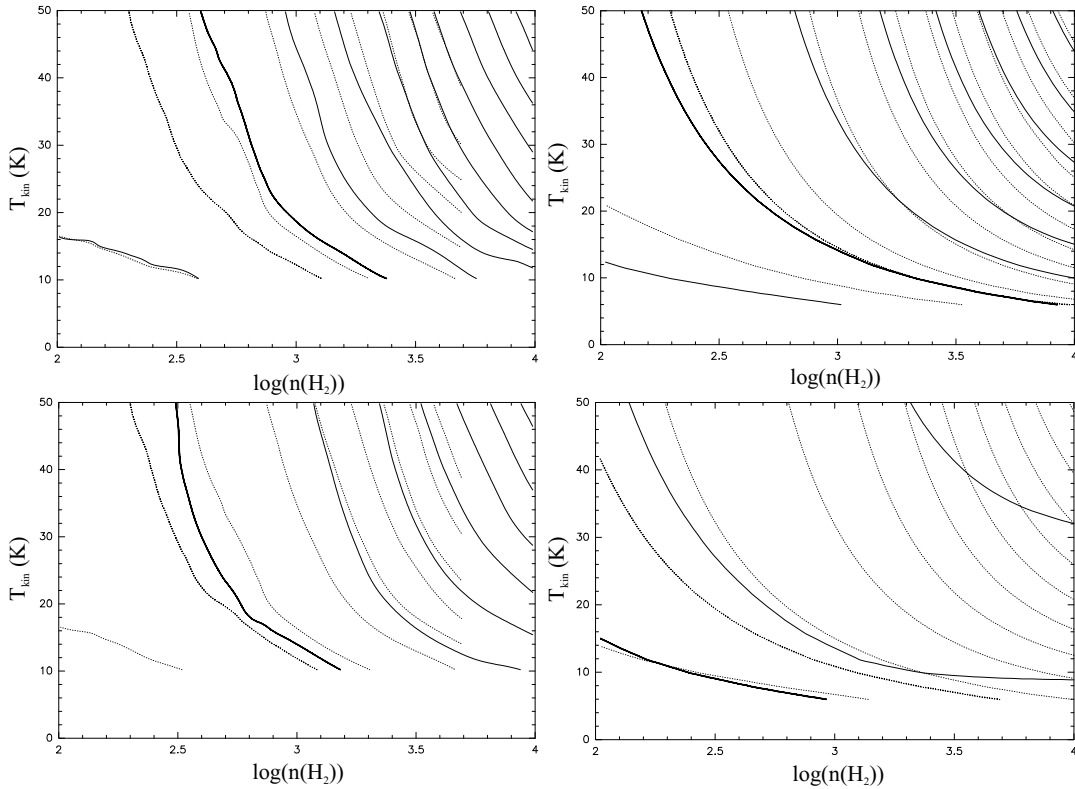


Figure 54: Results of the RADEX (left) and the LVG (right) analysis. In the upper panel, the H_2 column density is 10^{20} cm^{-2} , in the lower panel 10^{21} cm^{-2} . Shown are the line ratios of $^{12}\text{CO}(2-1)/^{12}\text{CO}(1-0)$ (solid) and $^{13}\text{CO}(2-1)/^{13}\text{CO}(1-0)$ (dotted). The bold lines mark the measured line ratios of NGC 4441. The levels of the line ratios start at 0.25 and proceed in steps of 0.25.

signs of cold or warm, dense cores, in which stars may be formed, could be found. This is in agreement with the moderate to low star formation rate derived for NGC 4441. Dense regions might have formed stars already, thus, only the diffuse component is left. It is, however also possible, that not much molecular gas was present from the beginning (due to the merger progenitors) and that it became too dispersed by the merger. In this case, the molecular gas never became concentrated enough to initiate a burst of the strengths found in the Medusa. Further work on the star formation history of NGC 4441 is needed to disentangle these two possibilities. Preliminary results of our stellar population synthesis analysis of the optical spectra of NGC 4441 indicate a burst ~ 1 Gyr ago, which let us favor the first scenario of the molecular gas left over after a period of enhanced star formation.

4.6 Summary and Conclusions

1. We observed the moderate luminosity merger NGC 4441 with the Westerbork radio interferometer and found a complex, extended HI structure affected by tidal forces. The total HI mass adds up to $1.46 \cdot 10^9 M_{\odot}$.
2. We detected two HI tails. Both tails have a similar extension out to 4' (42 kpc, southern tail) and 4.6' (48 kpc, northern tail) away from the center and they emerge from opposite sites of the main galactic body. The southern arm has a lower velocity compared to the system velocity, the northern arm is slightly redshifted.
3. The northern HI arm follows the optical tail closely, however the HI is more extended and shifted to the east. In contrast, the southern HI arm is not aligned with the shell structure found in the optical, but touches only the inner optical shell, whereas in the outer shell no neutral gas is found.
4. The velocity field shows a disk-like rotation pattern in the inner region, associated with the optical main body. The tidal tails differ from this rotation. The southern tail has a generally lower velocity as the system, the velocity of the northern tail is larger than the central velocity.
5. Furthermore, we mapped NGC 4441 with the single-dish IRAM 30 m telescope. We found extended molecular gas out to 22" (3.9 kpc). The total molecular gas mass is $4.6 \cdot 10^8 M_{\odot}$.
6. We derived $^{12}\text{CO}(2-1)/^{12}\text{CO}(1-0)$ and $^{13}\text{CO}(2-1)/^{13}\text{CO}(1-0)$ line ratios which are consistent with a diffuse ($n_{\text{H}_2} \leq 1000 \text{ cm}^{-3}$) molecular medium. However, the $^{12}\text{CO}(2-1)/^{13}\text{CO}(1-0)$ ratio is unusually high ($^{12}\text{CO}(2-1)/^{13}\text{CO}(1-0) = 21$), which is typical for the inner centers of luminous starbursts (Aalto et al. (1995)).
7. From the 20 cm continuum flux we calculated the star formation rate as $2.36 M_{\odot}/\text{yr}$. From the FIR fluxes we get a SFR of $0.95 M_{\odot}/\text{yr}$. The resulting ratio q is 2.4, which is in good agreement with the typical q value in the literature.
8. The estimated star formation rate is in good agreement with the results from the molecular gas analysis. Because no dense gas is present, no enhanced star formation can happen. It remains unclear, however, whether a starburst period has occurred in the past and the detected molecular gas is the left-over, or whether never a burst were possible because the gas was too dispersed from the beginning of the merger.

9. Because of the large differences in the stellar and gaseous distribution, it is unlikely that NGC 4441 is a merger between two large disk galaxies. If differences are found in those mergers, they are on much smaller scales and can be best explained by superwinds (see Hibbard et al. (2000)). In NGC 4441, no such strong galactic winds are expected, because the galaxy is in a phase of moderate star formation. A merger between two ellipticals can be also excluded, because we found a large amount of atomic and molecular gas and signs of a past strong star formation activity. This properties are not expected in E+E mergers. Thus, it is most likely, that NGC 4441 is the remnant of a S+E merger.

References

- Aalto, S., Booth, R. S., Black, J. H., & Johansson, L. E. B. 1995, *A&A*, 300, 369
- Aalto, S. & Hüttemeister, S. 2000, *A&A*, 362, 42
- Aalto, S., Hüttemeister, S., & Polatidis, A. G. 2001, *A&A*, 372, L29
- Armus, L., Heckman, T. M., & Miley, G. K. 1990, *ApJ*, 364, 471
- Bergvall, N. 1981, *A&A*, 97, 302
- Casoli, F., Dupraz, C., & Combes, F. 1992, *A&A*, 264, 55
- Condon, J. J. 1992, *ARA&A*, 30, 575
- Dahmen, G. 1995, *The Large Scale Distribution of Molecular Gas in the Galactic Center Region from C¹⁸O and the Nitrogen Isotope Abundance in the Galaxy* (PhD thesis)
- Haarsma, D. B., Partridge, R. B., Windhorst, R. A., & Richards, E. A. 2000, *ApJ*, 544, 641
- Helou, G., Soifer, B. T., & Rowan-Robinson, M. 1985, *ApJ*, 298, L7
- Hibbard, J. E., Vacca, W. D., & Yun, M. S. 2000, *AJ*, 119, 1130
- Hüttemeister, S. 1993, *Molecular Clouds in the Galactic Center and Selected External Galaxies* (PhD thesis)
- Kennicutt, R. C. 1998, *ARA&A*, 36, 189
- Kojima, M. & Noguchi, M. 1997, *ApJ*, 481, 132
- Moshir, M. & et al. 1990, in *IRAS Faint Source Catalogue, version 2.0* (1990), 0
- Polk, K. S., Knapp, G. R., Stark, A. A., & Wilson, R. W. 1988, *ApJ*, 332, 432
- Sanders, D. B. & Mirabel, I. F. 1996, *ARA&A*, 34, 749
- Schöier, F. L., van der Tak, F. F. S., van Dishoeck, E. F., & Black, J. H. 2005, *A&A*, 432, 369
- Sobolev, V. V. 1960, *Moving envelopes of stars* (Cambridge: Harvard University Press, 1960)

- Strong, A. W., Bloemen, J. B. G. M., Dame, T. M., Grenier, I. A., Hermsen, W., Lebrun, F., Nyman, L.-A., Pollock, A. M. T., & Thaddeus, P. 1988, *A&A*, 207, 1
- Tonry, J. L., Dressler, A., Blakeslee, J. P., Ajhar, E. A., Fletcher, A. B., Luppino, G. A., Metzger, M. R., & Moore, C. B. 2001, *ApJ*, 546, 681
- van Langevelde, H. J. & van der Tak, F. 2004, <http://www.strw.leidenuniv.nl/mol-data/radex.html>
- Weil, M. L. & Hernquist, L. 1993, *ApJ*, 405, 142
- Weistrop, D., Eggers, D., Hancock, M., Nelson, C. H., Bachilla, R., & Kaiser, M. E. 2004, *AJ*, 127, 1360

5 Large scale HI distribution in the Medusa merger

Abstract

We obtained HI synthesis observations of the Medusa merger, which is thought to be a proto-typical candidate for a merger between an elliptical and a spiral galaxy. To study the large scale atomic hydrogen distribution, we used the Westerbork Radio Synthesis Telescope. We found a single HI tail with a length of 56 kpc (4.95') and a mass of $7 \cdot 10^8 M_{\odot}$, thus harbouring $\sim 35\%$ of the total HI mass of $2 \cdot 10^9 M_{\odot}$. Interestingly, we observe a large discrepancy between the optical and gaseous tidal features. The optical tail and shells are not coincident with a high amount of neutral gas. In contrast, the HI tail is found opposite to the optical tail. We were also able to detect a small companion at a projected distance of 91 kpc (8.06'). It is, however, unlikely that this dwarf galaxy has a significant influence on the disturbed appearance of the Medusa.

5.1 Introduction

The Medusa galaxy, NCG 4194, is a nearby ($D=39$ Mpc) galaxy with the disturbed appearance typical for a merger. It has been interpreted as an excellent candidate for a merger between an elliptical and a spiral galaxy, a so-called S+E merger. The galaxy earned its nickname from the fuzzy and knotty optical tail to the North, reminiscent of hair or tentacles. A sharp shell-like structure is visible on the opposite side, confining the optical main body. A second, fainter shell further out is found on deep images (e.g., Manthey et al. (2006)).

In contrast to major mergers between two gas-rich disk galaxies, which often lead to Ultraluminous Infrared Galaxies (ULIRGs, $L_{\text{FIR}} > 10^{12} L_{\odot}$), S+E mergers should show a moderate far infrared (FIR) luminosity (less than $10^{11} L_{\odot}$) due to the lower gas content of at least one partner. At a distance of 39 Mpc, the Medusa has a L_{FIR} of $8.5 \times 10^{10} L_{\odot}$. A significant difference between ULIRGs and the Medusa and similar objects is found in the intensity and extent of the starburst induced by the merger. While the burst region is compact and typically concentrated to ≤ 1 kpc in ULIRGs (e.g., Sanders & Mirabel (1996)), the Medusa exhibits an extended region of ongoing star formation, which is, however, not as intense as in ULIRGs (Armus et al. (1990), Prestwich et al. (1994)).

Weistrop et al. (2004) obtained optical and ultraviolet HST images of the nucleus and found star-forming knots younger than 20 Myr in the center. They derived a star formation rate (SFR) of $\sim 6 M_{\odot}/\text{yr}$, but argue that the overall SFR in the Medusa might be up to $30 M_{\odot}/\text{yr}$ since the knots produce only 20% of the UV flux in the center.

Extended CO emission was detected by Aalto & Hüttemeister (2000). In their high resolution OVRO data, they found molecular gas out to 4.7 kpc aligned with a dust lane. Single-dish measurements revealed CO even in the optical tail (Aalto et al. (2001)), however, there is no sign of ongoing star formation within the tail (Armus et al. (1990)). The total molecular gas mass was estimated to be $2 \cdot 10^9 M_{\odot}$.

Recent investigations by Beswick et al. (2005) using sub-arcsecond MERLIN observations showed HI in absorption at the center. They found similar dynamics of the HI as for the molecular gas (Aalto & Hüttemeister (2000)), arguing, that the atomic and molecular component of the cold ISM are probably physically related. Furthermore, two compact radio sources were found in the central parsec, embedded in a region of diffuse radio continuum emission.

A single-dish HI spectrum was obtained by Thuan & Martin (1981) using the Greenbank 91 m telescope. They measured an integrated HI flux density of $1.45 M_{\odot}/\text{Mpc}^2$, corrected for

Table 19: Basic properties of NGC 4194. The distance is based on $H_0 = 75$ km/s/Mpc.

| | |
|---------------------------------|------------|
| RA (2000) | 12 14 09.5 |
| DEC (2000) | +54 31 37 |
| $v_{\text{hel,opt}}$ (km/s) | 2442 |
| D (Mpc) | 39 |
| L_B ($10^9 L_\odot$) | 15.7 |
| FIR flux 60 μm (Jy) | 25.66 |
| FIR flux 100 μm (Jy) | 26.21 |

beamsize. This corresponds to an HI mass of $1.7 \cdot 10^9 M_\odot$.

In this chapter, we present observations of the large scale HI distribution of the Medusa obtained with the Westerbork Radio Synthesis Telescope (WSRT). In section 2 we briefly present the observations and the data reduction. In section 3 we describe the results of our measurements. Finally, we discuss our results in section 4 and summarise the main points in section 5.

5.2 Observations & Data Reduction

5.2.1 HI observations

The observations with the WSRT were carried out in July 2003. We observed one full 12h track in the maxi–short array configuration under good conditions. As a flux calibrator, the standard source 3C147 was observed before and after the target. No phase calibrator was observed, since the standard procedure at WSRT for phase calibration is to obtain self-calibration. In Tab.20 we list the observing parameters and give information about the setup used. We chose a configuration which allowed us to both cover a large velocity range, because HI lines can typically be broader in mergers than in normal disk galaxies, and to reach a high resolution in velocity to be able to detect narrow features.

The WSRT data were reduced using MIRIAD together with additional, WSRT specific routines written by T. Oosterloo. The quality of the data was good, so that only little flagging of interferences was necessary. First, the data had to be calibrated to system temperature scale. Since no secondary calibrator was observed, after flux and bandpass calibration using the primary calibrator, a continuum image was created to perform self-calibration on continuum sources within the field. To achieve a deep CLEANing, we iteratively created a mask which includes emission only and which defines the regions to be CLEANed. After CLEANing and self-calibration a new mask was created and the process repeated until no improvement could be made. The results were then applied to the target galaxies.

CLEANing the HI cube was done in a similar way to CLEANing the continuum. After continuum subtraction, we applied Hanning smoothing, since this was not done during the observations. Again, we used as mask containing emission only to define CLEANing boxes. This procedure was repeated 3 times until the noise level was reached. Integrated intensity and velocity maps were created using the MOMENT task in MIRIAD. Finally, primary beam correction was applied to all data. A more detailed description of the reduction procedures will be given in Ch. 6.

In addition to naturally weighted maps we created maps using a robustness factor of 0.5, which gives a better resolution with slightly less sensitivity. Since the morphological features

Table 20: Observing parameters of the WSRT observations.

| observing parameters | |
|----------------------------|-----------|
| date | 12.7.2003 |
| center frequency (MHz) | 1408.6 |
| total bandwidth | 20 MHz |
| number of channels | 256 |
| velocity resolution (km/s) | 4.12 |
| synthesised beamwidth (") | 23 x 19 |
| primary beam (robust) | 36' |
| primary calibrator | 3C147 |

were the same in the natural and ROBUST 0.5 maps, we present here the latter maps only, because the structures in the HI tail are more obvious in these data. The reached rms noise level is 0.4 mJy/beam in the naturally weighted map and 0.6 mJy/beam in the ROBUST 0.5 weighted map, with a resolution of $23'' \times 19''$.

5.2.2 Optical imaging

We also present here optical Johnson V band images taken with ALFOSC mounted at the Nordic Optical Telescope (NOT) on La Palma, Canary Islands in January 2003. The field of view of ALFOSC is $6.4' \times 6.4'$, thus large enough to cover not only NGC 4194 completely but also a sufficient region of sky for a proper background subtraction. The integration time was 10 minutes. Standard reduction was applied to the data using the IRAF software. A further description of the observations and reduction as well as a detailed analysis of the optical data are given in Ch. 3.

5.3 Results

5.3.1 Continuum

Fig. 55 shows the NOT V band image of NGC 4194 with the 20 cm radio continuum overlaid with contours. The beamsize is shown in the lower left corner. The flux of the source is 0.108 Jy. We see continuum emission extending out to a deconvolved size of $6.6''$ (1.2 kpc) associated with the galactic main body. This is not surprising, since the 20 cm continuum flux is a tracer of star formation. As mentioned before, NGC 4194 exhibits an extended region of intense star formation. The continuum map shows a smooth distribution centered at the position of the nucleus seen in the optical.

5.3.2 Neutral hydrogen

The merger history is not only seen in the optical morphology, but is also reflected in the large scale HI distribution. Fig. 56 shows the integrated HI intensity map overlaid on an optical DSS image. Remarkable is the single long HI tail to the South.

HI in absorption is seen in the center, in accordance with Beswick et al. (2005).

We were also able to detect a dwarf galaxy at a distance of $8.06'$ (91 kpc) to the North-West ($\alpha = 12^{\text{h}}13^{\text{m}}26.38^{\text{s}}, \delta = +54^{\circ}36'31''$). Until now, it was not known that NGC 4194 has a companion, but our HI measurements show that this dwarf has a central velocity of

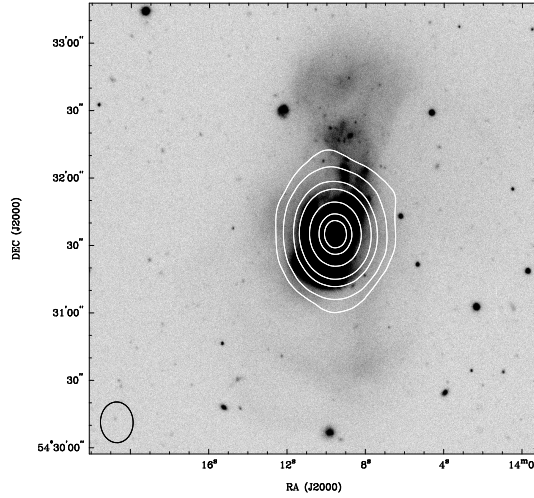


Figure 55: V-band image and contours of the 20 cm continuum flux. The synthesised beam is shown in the lower left corner of the image. Contour levels are 0.2, 0.5, 2, 5, 20, 50, 70 mJy.

Table 21: The optical velocity, HI velocity range, HI flux, HI mass and $M_{\text{HI-to-LB}}$ ratio of NGC 4194, its tail and the companion. The values for NGC 4194 include the tail.

| HI properties | NGC 4194 | tail | companion |
|--------------------------------------|-------------|-------------|-------------|
| v_{cent} (km/s) | 2500 | | 2370 |
| vel. range (km/s) | 2400 – 2580 | 2470 – 2520 | 2350 – 2390 |
| extension (kpc) | 81 | 56 | 14 |
| F_{HI} (Jy km/s) | 5.65 | 2.03 | 0.20 |
| M_{HI} ($10^9 M_{\odot}$) | 2.0 | 0.7 | 0.07 |
| $M_{\text{HI}}/L_{\text{B}}$ | 0.18 | – | – |

2380 km/s, which is only ~ 120 km/s lower than that of NGC 4194, thus probably indicating, that the two objects are physically connected. We carefully checked our HI channel maps for an HI bridge, but even in the naturally weighted maps no connection is visible. Fig. 57 shows the integrated HI spectra of NGC 4194 and the nearby galaxy derived from the data cube.

For a detailed analysis of the HI in NGC 4194, we show a close-up in Fig. 58. Here, we present the HI distribution, a map of the velocity field (first moment) and the velocity dispersion map. We show here the maps with a robustness weighting factor of 0.5 as a compromise of sensitivity and resolution. In Fig. 59 we show channel maps of the data cube to visualise the velocity field more completely.

The HI properties of NGC 4194, its tail and its companion are summarised in Tab. 21. We calculate a total HI mass of NGC 4194 of $2 \cdot 10^9 M_{\odot}$, in good agreement with the HI mass determination by Thuan & Martin (1981) of $1.7 \cdot 10^9 M_{\odot}$. This shows that we are not missing any significant diffuse emission with our interferometer observations.

HI in absorption

In the center, coincident with the optical nucleus, we found HI in absorption against the underlying continuum source of the star forming nucleus. Fig. 60 shows the measured spectrum. The multicomponent velocity structure clearly seen in the MERLIN data and discussed by

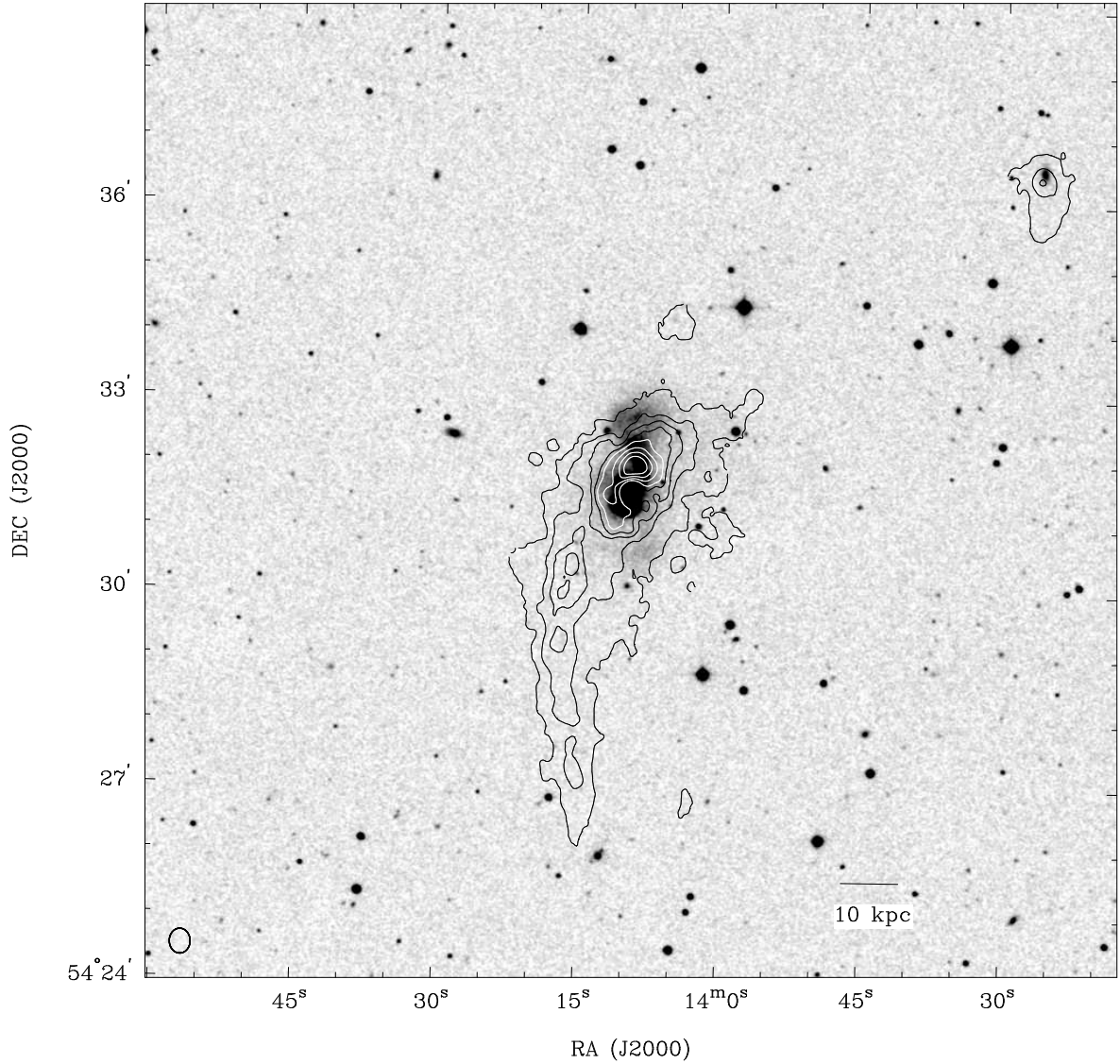


Figure 56: The HI distribution as contours overlaid onto a DSS image of NGC 4194 and its companion. Contour levels are 0.01,0.05,0.01,0.15,0.2,0.3,0.4,0.5 Jy/beam km/s. The bar in the lower right corner marks a projected distance of 10 kpc, assuming a distance of 39 Mpc. The lack of contours at the center of NGC 4194 is due to an absorption source. The beam is shown in the lower left corner.

Beswick et al. (2005) is tentatively seen here, too. Our spectrum shows at least two components, one at ~ 2500 km/s and one at ~ 2570 km/s.

The main body

Fig. 61 shows our optical V-band image, which is deeper than the DSS-2 image and thus shows more details of the optical morphology. The HI distribution is overlaid as contours. The HI emission peaks north of the absorption feature, aligned with the beginning of the optical tidal tail and some bright knots, which might be proto-star clusters. The HI embeds

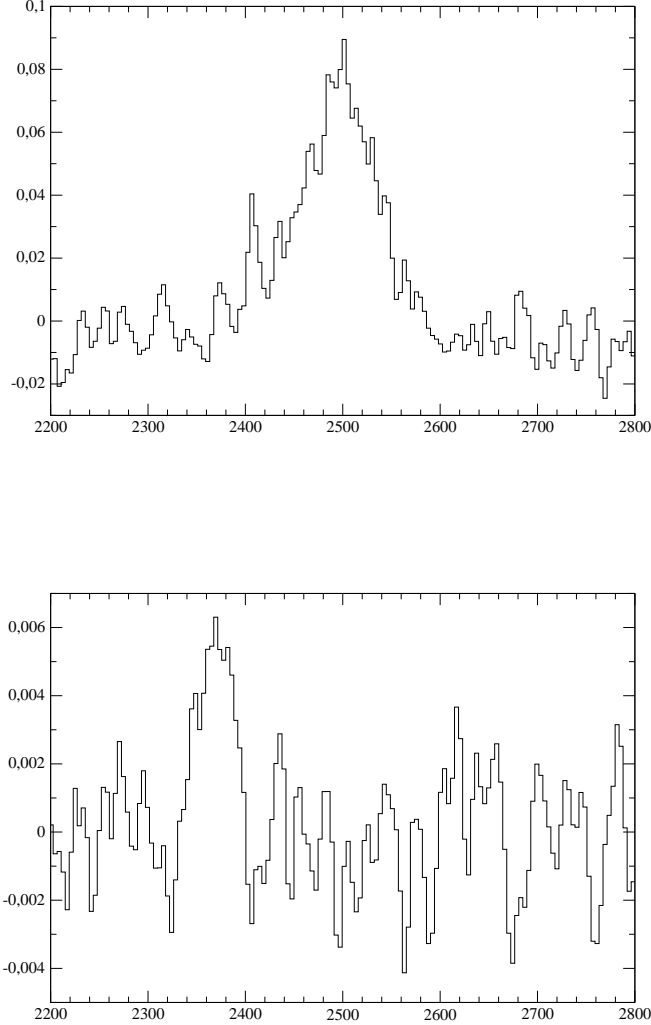


Figure 57: Integrated HI spectra of NGC 4194 (top) and the companion (bottom).

the optical tail completely, but is not considerably extended further out, i. e., no pronounced HI tail as a counterpart of the optical tail is found. The optical tail seems to be embedded in a smooth HI distribution somewhat extended towards the north-west, maybe coincidentally in the direction where the possible companion is found.

In the optical, we see two shells in the south, a bright one close to the center and a second, fainter one at a larger radius. We do not see any feature, neither in the HI distribution nor in the velocity and velocity dispersion maps which is related to these shells.

Looking at the velocity map, we find a slightly disturbed rotating disk, represented by a typical spider diagram, with regions of higher velocity on the eastern side and lower velocity on the western side.

The HI in the galactic body generally exhibits a larger dispersion than in the tail. The highest

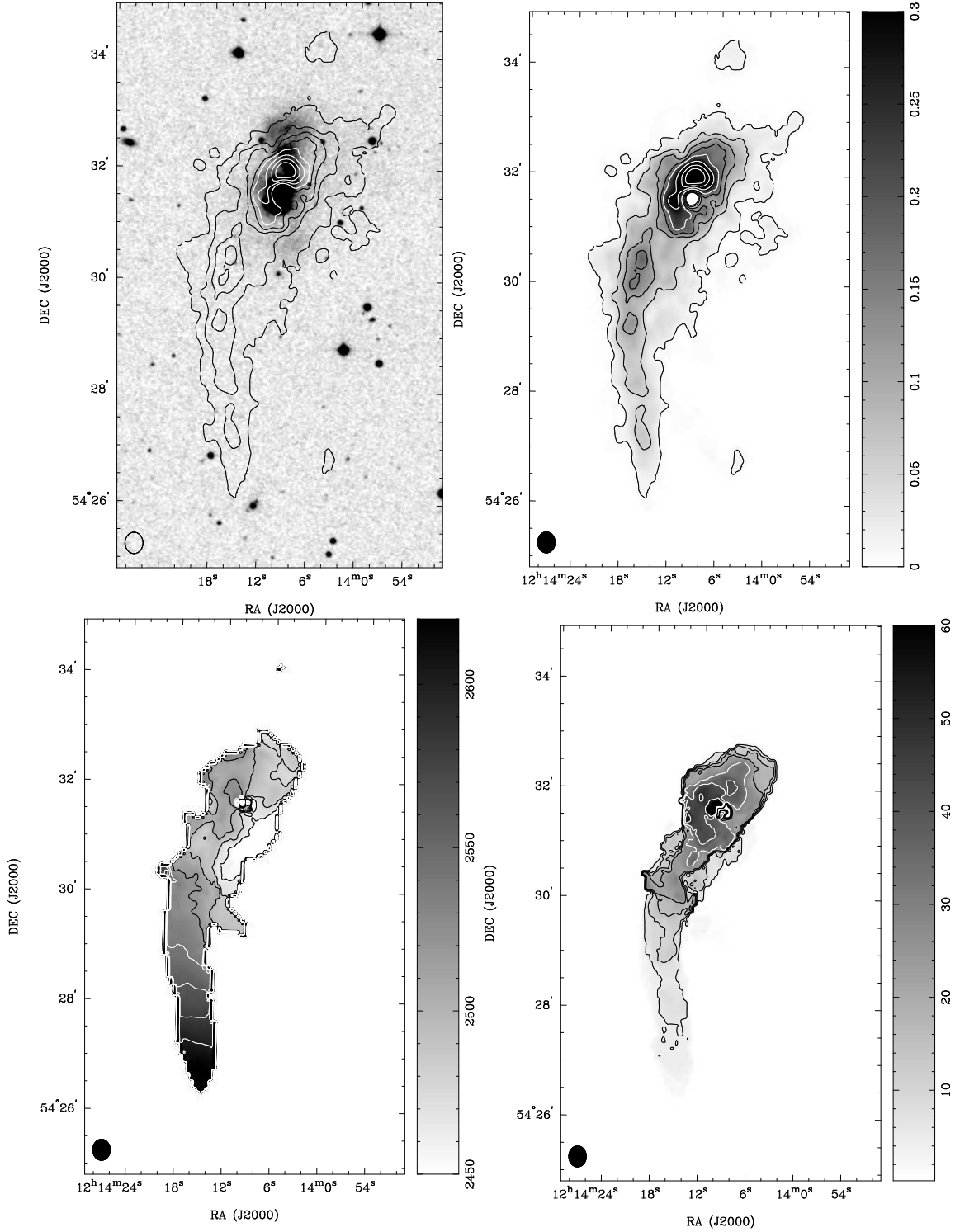


Figure 58: NGC 4194 – (top left) HI distribution overlaid on optical image (DSS). The contour levels are 0.01,0.05,0.01,0.15,0.2,0.3,0.4,0.5 Jy/beam km/s (0.01 Jy/beam km/s corresponds to $2.47 \cdot 10^{19} \text{ cm}^{-2}$), (top right) HI distribution as map and contours. Levels are the same. The white dot marks the region where HI absorption is found. (bottom left) Velocity field, contour levels are 2460 to 2600 km/s in steps of 20 km/s (bottom right) HI velocity dispersion (2. moment), contour levels are 5, 10, 15, 20, 30, 40, 50 km/s. The synthesised beam is marked in the bottom left corner.

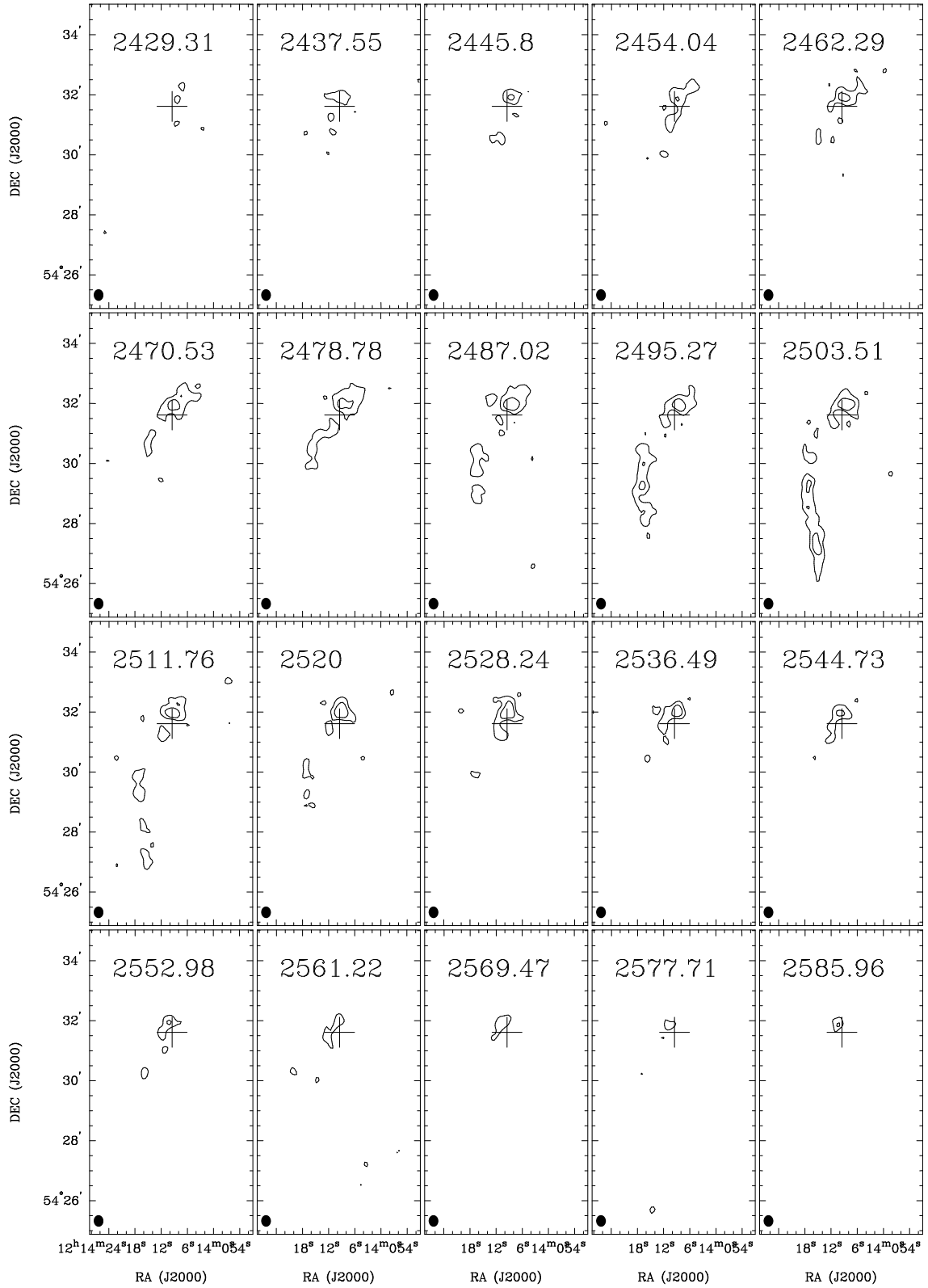


Figure 59: Channel maps (robust 0.5 weighted) of NGC 4194. The optical center position is marked with a cross. The contour levels are $1, 2, 5 \times 0.0016$ Jy/beam. The LSR velocity is given at the top left, the beam at the bottom left corner.

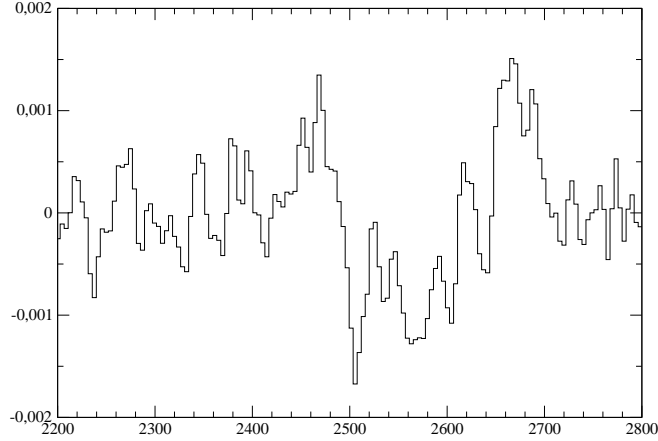


Figure 60: The HI absorption spectrum of NGC 4194 at the center.

values are measured north-east of the absorption region, where there is a slight dip in the HI distribution. This region is also roughly related to the dust lane and extended molecular gas found by Aalto & Hüttemeister (2000).

The HI tail

We detected a single remarkable HI tail going to the South out to ~ 56 kpc from the center. The HI tail contains several clumps embedded in smooth, diffuse HI emission. Unfortunately, our deep V-band image does not cover the whole tail. Neither in our V-band image, nor in the DSS image (for the outer part of the tail) did we find any optical counterpart of the HI clumps.

We determined the HI mass in the tail as $\sim 7 \cdot 10^8 M_{\odot}$, i.e. 35% of the total HI mass.

The velocity in the tail is smoothly increasing, with the highest velocity of ~ 2640 km/s at the tip. In the velocity dispersion map the smooth behaviour of the tail is found as a continuous but not disturbed increase of dispersion from the tip of the tail towards the galactic body. The dispersion is generally higher at positions of the clumps, especially in two large clumps close to the galaxy's main body.

The lowest velocity ($\sim 2455 - 2480$ km/s) is found in the region between the central HI concentration and these two bright clumps, marking the beginning of the tail. In this region, there is a gradient in velocity from north-east to south-west, ending in an area having the lowest velocity in the system southwards of the center. North-west of the two clumps the smooth decrease of velocity is intercepted by a 'ridge' of slightly increased velocity. In the velocity dispersion map we see enhanced dispersion there (~ 35 km/s² compared to ~ 10 km/s² left and right of this 'ridge'), whereas in the HI distribution map, if at all, there seems to be a slight dip in HI intensity associated with this 'ridge'.

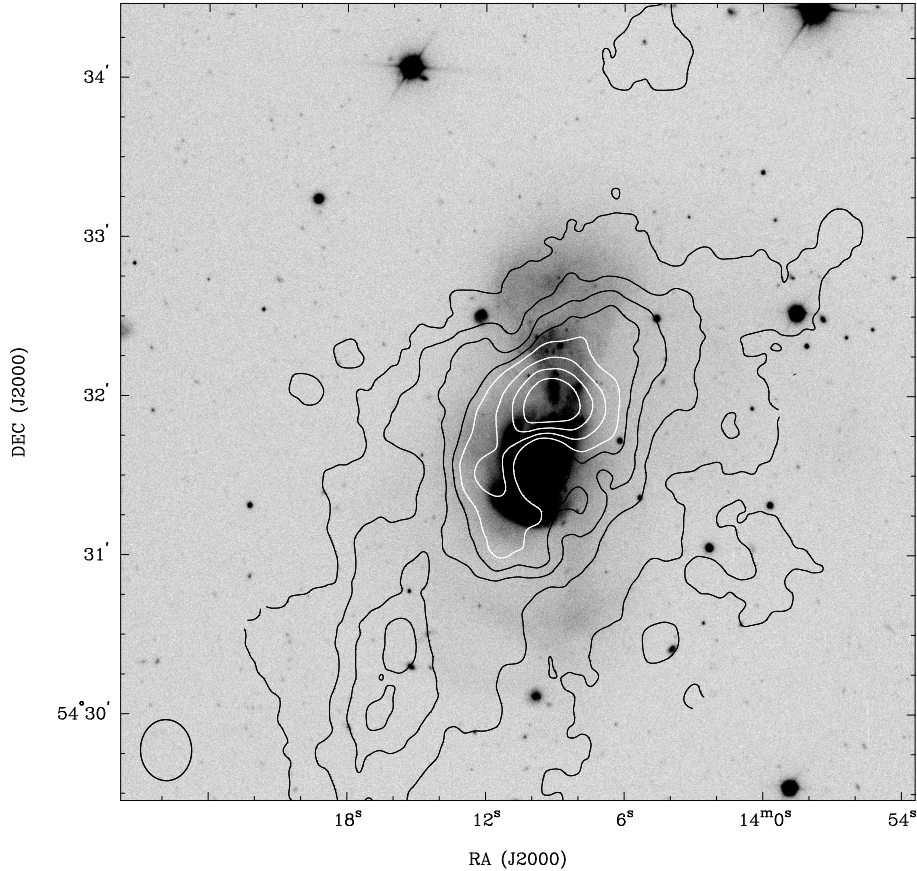


Figure 61: HI contours overlayed on our V band image taken with the Nordic Optical Telescope (La Palma). The field-of-view of the optical image covers only the upper part of the tail. Contour levels are 0.01, 0.05, 0.1, 0.15, 0.2, 0.3, 0.4, 0.5 Jy/beam km/s.

5.4 Discussion

5.4.1 Star Formation Rate

We followed Condon (1992) and Haarsma et al. (2000) and used the relation below to calculate the SFR from the 20 cm continuum flux:

$$\text{SFR} (M_{\odot} \text{ yr}^{-1}) = 0.14 D^2 F_{20\text{cm}}$$

where D is the distance in Mpc and $F_{20\text{cm}}$ is the 20-cm radio continuum flux density in Jy. In Tab.22 the results are given. We derived a SFR which is comparable to the results of Condon et al. (1990), who measured a flux of 122 mJy with the VLA and thus determined the SFR in the Medusa as $\sim 20 M_{\odot}/\text{yr}$.

Tab. 22 also gives the SFR estimated from the FIR luminosity:

$$\text{SFR} (M_{\odot} \text{ yr}^{-1}) = 0.17 L_{\text{FIR}}$$

following Kennicutt (1998), with L_{FIR} in units of $10^9 L_{\odot}$. As a reference for the IRAS $60\mu\text{m}$ and $100\mu\text{m}$ flux densities in Tab.19 we used the IRAS Faint Source Catalog (Moshir & et al. (1990)). The relation between the SFR estimated from the 20 cm flux and the FIR fluxes

Table 22: The measured continuum flux, star formation rates based on continuum and FIR emission, respectively, and q parameter.

| properties | |
|---|-------|
| 20 cm (Jy) | 0.108 |
| SFR _{20 cm} (M _⊙ /yr) | 22.8 |
| SFR _{FIR} (M _⊙ /yr) | 9.5 |
| q | 2.5 |

can be expressed by the q parameter defined by Helou et al. (1985), which is the logarithmic ratio of FIR to radio flux. Helou et al. (1985) derived a mean value of 2.3 for disk galaxies, but independent of their star formation activity. Although NGC 4194 is a merging galaxy, it conforms nicely to this value.

Helou et al. (1985) mention that even galaxies with a strong nuclear starburst, as Arp 220, are in agreement with this correlation of the FIR and radio flux, however within a higher scatter. Arp 220, e.g., has a q value of 2.65, whereas other prominent ULIRGs like Arp 299 and Mrk 231 have a value of 2.1.

Our results of NGC 4194 are in good agreement with the investigations of Weistrop et al. (2004), who used the UV flux of the central star forming knots to estimate the star formation rate. They estimates a SFR within the knots of 5 – 6 M_⊙/yr and suggest an overall SFR of up to 30 M_⊙/yr.

The continuum source was studied recently by Beswick et al. (2005) with sub-arcsecond resolution MERLIN data. They found a pair of continuum sources separated $\sim 0.35''$, thus unresolved in our image. They derived a SFR of 6 M_⊙/yr, which corresponds to the estimation based on the FIR fluxes and results of Weistrop et al. (2004), but they also pointed out that they only measured the star formation rate in the very center of NGC 4194.

Our measured continuum source size of 1.2 kpc is only slightly smaller than the star forming region of ~ 2 kpc, as determined by optical and CO observations (Armus et al. (1990), Aalto & Hüttemeister (2000)).

5.4.2 The merger remnant

Based on the optical morphology, NGC 4194 resembles strikingly the results of modelling a radial merger by Kojima & Noguchi (1997). We see shells in one direction and a tidal tail to the opposite direction. However, our HI measurements do not agree with the predictions of their models. Kojima & Noguchi (1997) used the so-called sticky particle method to model the interstellar gas as a system of inelastic cloud particles which dissipate their kinetic energies by collisions. Since the timescale for a cloud-cloud collision can be quite large, under favourable conditions, the stellar component behaves like the gas, resulting in a similar way of forming tidal tails and shells. These structures may last more than 1 Gyr. Kojima & Noguchi (1997) argue, that since the gas is scattered into the tidal debris, star formation will be suppressed when the tidal structures are formed. In the Medusa, however, an intense and extended burst is still going on, while simultaneously shells and a tail are formed by stars. The atomic hydrogen also formed a long tail, however not, as the models of Kojima & Noguchi (1997) prognoses, in correlation with the stellar tail, but on the opposite side. Thus, their models seems to describe the evolution of the stellar component quite nicely, there are however discrepancies between the observation and simulation of the gas.

Hibbard et al. (2000) studied some examples of disk-disk mergers which show anticorrelations between stellar and gaseous tidal features. They discuss various possibilities for these differences, including ram pressure stripping, photoionisation, dust obscuration and different origins in the progenitor galaxies. Although possibly at least several scenarios may play a role at some point, the lack of starlight associated with the large HI tail found in NGC 4194 can be easiest explained by the original position of the HI in the progenitor. Most likely, the atomic hydrogen forming the tail comes from the outer HI disk, which is typically optically faint. Considering the short lifetime of luminous stars and the large velocity dispersion of fainter stars, Hibbard et al. (2000) deduce that the HI-to-light ratio will even increase, thus this effect will become clearer with time.

The assumption of the original outer disk of the spiral progenitor being the origin of the HI in the tail is corroborated by the kinematics. Assuming a prograde rotation and a radial merger, the gas of the spiral outer disk formed one tail during the encounter.

5.5 Conclusions

1. We found one large HI tail in the S+E merger NGC 4194, extended out to $4.95'$, corresponding to a projected distance of 56 kpc. The tail contains $\sim 7 \cdot 10^8 M_{\odot}$ of HI, with no optical counterpart.
2. We found a large misalignment between optical and gaseous tidal features. The optical tail is situated at the opposite side of the HI tail, the optical shells do not seem to be connected to the HI tail. Although the shells are within the region of the HI tail, no connection is apparent neither in morphology nor in velocity distribution.
3. The tail is probably formed by material of the outer HI disk of the progenitor spiral galaxy. This would explain why we don't see an optical counterpart. The fact that the stars and the atomic gas developed a significantly different distribution shows, that these two components cannot be described with the same physical models, as it is done e.g. in simulations of Kojima & Noguchi (1997).
4. A possible dwarf companion was identified at a distance of 91 kpc North-West of NGC 4194. Its system velocity is with 2380 km/s only 120 km/s lower than that of the Medusa. This dwarf galaxy harbours $\sim 7 \cdot 10^7 M_{\odot}$ of HI. No connection, neither in the optical nor the HI could be found between the dwarf and NGC 4194.
5. Based on the 20 cm continuum flux, we calculated a star formation rate of $23 M_{\odot}/\text{yr}$. Using the FIR fluxes, we calculated a SFR of $10 M_{\odot}/\text{yr}$. This is in good agreement with the results of Weistrop et al. (2004) who found an intense ongoing burst in the Medusa. Taking the ratio of the SFR based on the FIR and 20 cm flux, the resulting q parameter is 2.4, which is in accordance to the mean value of 2.3 derived for disk galaxies by Helou et al. (1985).

References

- Aalto, S. & Hüttemeister, S. 2000, *A&A*, 362, 42
- Aalto, S., Hüttemeister, S., & Polatidis, A. G. 2001, *A&A*, 372, L29

- Armus, L., Heckman, T. M., & Miley, G. K. 1990, *ApJ*, 364, 471
- Beswick, R. J., Aalto, S., Pedlar, A., & Huttemeister, S. 2005, arXiv:astro-ph/0508637
- Condon, J. J. 1992, *ARA&A*, 30, 575
- Condon, J. J., Helou, G., Sanders, D. B., & Soifer, B. T. 1990, *ApJS*, 73, 359
- Haarsma, D. B., Partridge, R. B., Windhorst, R. A., & Richards, E. A. 2000, *ApJ*, 544, 641
- Helou, G., Soifer, B. T., & Rowan-Robinson, M. 1985, *ApJ*, 298, L7
- Hibbard, J. E., Vacca, W. D., & Yun, M. S. 2000, *AJ*, 119, 1130
- Kennicutt, R. C. 1998, *ARA&A*, 36, 189
- Kojima, M. & Noguchi, M. 1997, *ApJ*, 481, 132
- Manthey, E., Jütte, M., Hüttemeister, S., Aalto, S., & Haberbzettel, L. 2006, in prep.
- Moshir, M. & et al. 1990, in *IRAS Faint Source Catalogue, version 2.0 (1990)*, 0
- Prestwich, A. H., Joseph, R. D., & Wright, G. S. 1994, *ApJ*, 422, 73
- Sanders, D. B. & Mirabel, I. F. 1996, *ARA&A*, 34, 749
- Thuan, T. X. & Martin, G. E. 1981, *ApJ*, 247, 823
- Weistrop, D., Eggers, D., Hancock, M., Nelson, C. H., Bachilla, R., & Kaiser, M. E. 2004, *AJ*, 127, 1360

6 HI and CO properties of moderate luminosity mergers

Abstract

A powerful tool to study the interaction and merger history of galaxies is the investigation of the atomic hydrogen distribution and kinematics. Furthermore, observations of the molecular gas content give valuable clues on the star formation potential in a galaxy, which is particularly interesting in a merger. Here, we present interferometric HI and single-dish CO observations of a sample of *moderate luminosity merger* candidates. Some of the targets show an extended and very complex HI structure, which often shows large deviations from the optical tidal features, and also may host an extended region of enhanced star formation. Others are neither detected in HI nor CO, revealing the variety and complexity of merger events.

6.1 Introduction

Galaxy interaction and merging are the driving forces of ongoing galaxy evolution. Until now the main focus of research is put on the merger between two large disk galaxies, which lead to an object hosting a compact region of intense star formation. Thus, these galaxies are extremely bright in starburst tracers like the far-infrared (FIR) emission, giving them their name ultra-luminous infrared galaxies (ULIRGs) (Sanders & Mirabel (1996)). However, mergers between two large disk galaxies are rare objects, because the merging partners occur only with a low absolute frequency. More common are small spirals and elliptical galaxies, but the merger processes between these two species are poorly studied so far. Since less gas is involved in such mergers, one would expect to find less enhanced star formation there, leading to lower FIR luminosities compared to ULIRGs.

We have embarked a systematic multiwavelength investigation of a sample of mergers with a moderate FIR luminosity of $< 10^{11} L_{\odot}$, which are possible Spiral+Elliptical mergers (S+E mergers). The sample is introduced in Ch. 3. See that chapter for a detailed description of the sample selection as well as the optical properties of the galaxies.

In this chapter, we want to focus on the merging histories of our sample as revealed by the gaseous component. Enhanced star formation induced by the merger is fed by molecular gas. Thus, CO observations show us how much gas is available for the burst.

To study the overall dynamics in merging system, CO, however, is not well suited, since it is less common than HI, traces only dense, i.e., molecular, gas, and is normally only found in the central region. To study the interaction history of galaxies, neutral hydrogen is the best tracer, because in general HI is much more extended than the stellar component of a galaxy, hence the HI structure is more easily disturbed by a close encounter/merger. Additionally, when observing HI, not only the HI *distribution* is measured, but also information about the *velocity field* is obtained which allows to study the kinematics in the galaxy.

Here, we present radio- and millimeter observations of some of our *moderate luminosity mergers* sample galaxies. 7 galaxies were observed with radio interferometers to map the HI distribution. For 5 galaxies we obtained single-dish CO observations. Basic informations about the targets are given in Tab. 23. Two more galaxies, NGC 4441 and NGC 4194 are presented in separate chapters (Ch. 4 and Ch. 5).

6.2 Observations

Several telescopes were used for HI and CO observations. To study the HI distribution in detail, we obtained synthesis imaging of the 21 cm line of neutral hydrogen with radio interfer-

Table 23: Some basic parameters of the observed galaxies. The coordinates given in J2000, the distance D is based on $H_0 = 72 \text{ km/s/Mpc}$.

| Object | Coordinates (2000) | z | D (Mpc) | Type | observations |
|------------|----------------------|----------|---------|--------------|--------------|
| NGC 4004 | 11:58:05.2 +27:52:44 | 0.01126 | 47 | Pec | HI, CO |
| NGC 5607 | 14:19:26.7 +71:35:18 | 0.02533 | 105 | Pec | HI, CO |
| UCG 8264 | 13:08:29.4 +84:37:50 | 0.015481 | 59 | Pec | HI, CO |
| Arp 161 | 11:42:12.4 +00:20:03 | 0.018545 | 77 | Sb pec, HII | HI, CO |
| ARP 164 | 01:15:57.6 +05:10:43 | 0.01758 | 73 | S? | HI, CO |
| ESO 156-18 | 03:52:13.6 -54:53:15 | 0.04441 | 175 | SAB(s)0: pec | HI |
| ESO 159-03 | 05:16:09.1 -54:06:17 | 0.01302 | 49 | SB0: pec | HI |

ometers. Observations were carried out with the Australia Telescope Compact Array (ATCA), the Westerbork Synthesis Radio Telescope (WSRT) and the Very Large Array (VLA). For the CO observations we used single-dish telescopes, since we are interested in the total flux, i.e. the total molecular gas content. Also, before applying for time at mm-interferometers, first molecular gas has to be detected with a single-dish instrument. Where possible, we used our own deep R-band images to compare the HI structure with the stellar morphology. For a more detailed description of the optical observations, see Ch. 3. When no optical data of our own were available, we used DSS2-red images from the ESO database¹⁶. In the following the observation runs are summarised.

6.2.1 HI and 20 cm continuum observations

ATCA

Two galaxies from our southern sample were observed with the ATCA. The ATCA is situated in Narrabri, Australia. The array consists of six 22 m telescopes. Five of these antennas are movable on a three kilometer railway track oriented in east–west direction. The sixth antenna has a fixed position three kilometers away, thus allowing a maximum baseline of 6 km.

The observations were carried out in November 2002, using the 1.5 km configuration, including the 6 km antenna, and the 750 m configuration for a better uv-coverage. We obtained 12 hours of integration for each configuration, because of the east–west orientation of the array. Further observational information is listed in Tab. 24. For flux calibration, the primary calibrator 1934-638 was observed before and after the source observations. Phase calibration was done using a phase calibrator (secondary calibrator, here the source 0438-436), which was observed every 40 min.

To get a sufficient velocity resolution and a broad bandwidth we used the 'full_8_512-128' receiver configuration, which allows to measure two polarisations. Therefore, the total bandwidth was 8 MHz (corresponding to a velocity range of 1600 km/s), which allows covering a velocity range broad enough to include possible tidal features which might have a velocity of a few 100 km/s different from the system velocity. With 256 channels per baseline, the spectral resolution was 62.5 kHz, i.e., $\sim 12 \text{ km/s}$.

We created naturally weighted maps, which are most sensitive to faint emission. The noise level reached for both galaxies is 0.001 Jy/beam.

¹⁶<http://archive.eso.org/dss/dss>

Table 24: Observing parameters of the ATCA run. During this campaign, ESO 159-03 and ESO 156-18 were observed.

| ATCA configuration | 1.5A | 750A |
|----------------------|--|----------|
| date | Nov 2002 | Nov 2002 |
| center frequency | 1402.1 MHz (ESO 159-03), 1360.0 MHz (ESO 156-18) | |
| total bandwidth | 8 MHz | |
| number of channels | 512 | |
| velocity resolution | 12 km/s | |
| primary calibrator | 1934-638 | |
| secondary calibrator | 0438-436 | |

Table 25: Observing parameters of the WSRT run. NGC 4004, NGC 5607 and UGC 8264 were observed with the WSRT.

| | NGC 4004 | NGC 5607 | UGC 8246 |
|---------------------|-----------|-----------|-----------|
| date | 6.1.2003 | 28.4.03 | 3.3.03 |
| center frequency | 1404.6 | 1398.7 | 1385.3 |
| total bandwidth | 20 MHz | | |
| number of channels | 512 | | |
| velocity resolution | 4.2 km/s | | |
| beamwidth | 37" x 18" | 21" x 19" | 19" x 19" |
| primary calibrator | 3C48 | 3C147 | 3C48 |

WSRT

The WSRT is the Dutch radio interferometer situated in the northern part of the Netherlands. It consists of 14 antennae oriented in East–West direction. Each antenna has a diameter of 25 m. Ten of the antennae have a fixed position with a spacing of 144 m, whereas four are movable. The maximum baseline can be 2.7 km.

The HI observation with the WSRT were carried out in the first half of 2003. Five galaxies were observed with this interferometer, but two of them (NGC 4441 and NGC 4194) are presented separately in Ch. 4 and Ch. 5. Tab. 25 summarises the most important observing parameters. The DZB backend was used to observe two polarisations simultaneously. The bandwidth of 20 MHz, equivalent to ~ 4000 km/s, and a velocity resolution of ~ 4 km/s allows to detect tidal features at velocities, which are a few 100 km/s different from system velocities.

All galaxies were observed one 12 h run. The observations were done in the 'maxi–short–mode', which gives a good compromise between image quality in an extended object and a single–track observation. The quality of the data is good, no interference problems occurred. Note that no secondary phase calibrator was observed. Instead, phase calibration at the WSRT is usually done using selfcalibration.

Naturally and robust weighted maps were created, but here, only the robust maps with a robustness factor of 0.5 are presented. The noise level in the intensity maps is 0.0003 Jy/beam.

Table 26: Observing parameters of the VLA run. The targets of this observing campaign were Arp 161 and Arp 164.

| | Arp 161 | Arp 164 |
|------------------------|-----------|----------|
| date | 23.6.04 | 27.6.04 |
| center frequency (MHz) | 1394.5 | 1395.9 |
| total bandwidth | 6.25 MHz | |
| number of channels | 64 | |
| velocity resolution | 20.6 km/s | |
| beamwidth | 57 x 50 | 53 x 49 |
| primary calibrator | 1331+305 | 0542+498 |

VLA

The VLA is built on the Plains of San Augustin close to Socorro, New Mexico. The array consists of 27 antennas, each with a diameter of 25 m. The antennae are movable on a Y-shaped railway track, allowing a maximum antenna separation of 36 km in the largest configuration ('A array').

Arp 161 and Arp 164 were observed with the VLA in June 2004 during its D configuration (maximum separation 1 km) with the correlator mode 1A. Each galaxy was observed for 6 hours. Online Hanning-smoothing was applied. The bandwidth of 6.25 MHz corresponds to a covered velocity range of 1300 km/s. With 64 available channels, the velocity resolution was 20.6 km/s (97.7 kHz). As primary calibrators, the calibration sources 1331+305 (for Arp 161) and 0542+498 (for Arp 164) were observed. Phase calibration was done using the calibration sources 1150-003 (Arp 161) and 0119+084 (Arp 164).

Tab. 26 summarises the observations. The observations were done under good weather conditions. The velocity scale was heliocentric. Here, robust maps with a robustness factor of 0.5 are shown. The noise level of the maps is 0.0004 Jy/beam.

6.2.2 CO observations

Millimeter observations were carried out with the 20 m telescope of the Onsala Space Observatory (OSO), Sweden, and the IRAM 30 m telescope in Spain. All galaxies were observed at their center positions as given in Tab. 23. For UGC 8264, we also observed an offset position with the OSO telescope, where in the optical a knot at the tip of a tidal tail is visible, which thus might be a tidal dwarf galaxy.

OSO 20 m

Observations of the $^{12}\text{CO}(1-0)$ line were carried out in March 2003 under moderate weather conditions. The beamsize of the telescope is $33''$ for $^{12}\text{CO}(1-0)$. A characteristic of this mm-telescope is that it is enclosed in a radome, which leads to no restrictions concerning strong winds, humidity and sun-avoidance. CO observations are done with a SIS-mixer and a correlator with a total bandwidth of 512 MHz. The main beam efficiency at 115 GHz is $\eta = 0.43$. To account for the highly variable sky background, the observations were done in the beam switching mode, because this provides the flattest baselines. The pointing and focus of the telescope was regularly checked by observing several pointing sources (U Ori, R Leo,

Table 27: Observing parameters of the OSO and IRAM campaigns. NGC 4004, NGC 5607, UGC 8264 and Arp 164 were observed with the OSO telescope, Arp 161 and the tidal dwarf galaxy candidate in UGC 8264 (TDG) with the IRAM telescope.

| | NGC 4004 | NGC 5607 | UGC 8264 | Arp 164 | Arp 161 | TDG |
|--------------------|----------|----------|----------|---------|---------|---------|
| system temperature | 350–450 | 300–400 | 280–330 | 400–500 | 200–300 | 250–300 |
| rms (mK) | 2.3 | 5.3 | 3.5 | 3.2 | 1.5 | 1.9 |
| beamsize (") | 33 | 33 | 33 | 33 | 22 | 22 |
| beam efficiency | 0.43 | 0.43 | 0.43 | 0.43 | 0.75 | 0.75 |

R Cas). Tab. 27 summarises the observations. The given noise levels correspond to smoothed spectra with a velocity resolution of 33.8 km/s. The velocity scale is heliocentric.

IRAM 30 m

Observations of NGC 4441 (see Ch. 4) and Arp 161 were done with the IRAM 30 m telescope on Pico Veleta, Spain in July 2004. The weather conditions were good. Even though the main focus of this observing run lied on the mapping of the extended CO distribution in NGC 4441, we could obtain additionally a sensitive CO spectrum of Arp 161. The observations were done with the A 100 and B 100 receivers for the CO(1–0) line. The 1 MHz filterbank with 2×512 channels was chosen. Pointing and focus calibration were done by observing Jupiter. The observations were done in the beam switching mode. The system temperature was between 200 K and 300 K.

The velocity was measured with respect to the local standard of rest, in contrast to the heliocentric velocity measured in the other CO and HI observations. The main observing parameters are also given in Tab. 27. The rms level given in this table corresponds to a spectrum smoothed to a velocity resolution of 21 km/s.

6.3 Data Reduction

The radio data taken with the ATCA and WSRT were fully reduced with MIRIAD. Due to the different calibration strategies (see above), the reduction steps were slightly different. After inspecting and, if necessary, flagging the calibrators, for the ATCA data we followed the calibration scheme 12.3 given in the MIRIAD manual. The bandpass correction was done with the primary calibrator, the gain correction was determined using the secondary calibrator, and then corrected with the help of the primary calibrator. Thus, the secondary calibrator was mainly used for phase correction, only.

The WSRT data have to be corrected first for the system temperature. Since no secondary calibrator was observed, after flux and bandpass calibration a continuum images was created to perform selfcalibration on continuum sources within the field. To achieve a proper calibration, it is inevitable to deeply CLEAN the continuum image. In an iterative process, first a mask was created which included only real emission to define the CLEANing components. Second, the image was CLEANed using the mask and subsequently a new, deeper mask could be generated for a better CLEANing. Once the image was finally CLEANed, selfcalibration was performed, and the loop started again with creating a mask, CLEANing and selfcalibration. The data quality was high enough that only 2 – 3 iterations were necessary for a proper calibration. The results were then applied to the target galaxies.

For flagging and calibration of the VLA data AIPS was used. We followed the recommended way given in 'step-by-step guide to spectral-line data analysis'¹⁷. The procedure is similar to the calibration of the ATCA data, with the difference that one works with the so-called *channel 0* first and applies the calibration to the line data in the end. The *channel 0* dataset is created in the beginning and is basically a summation over all channels.

After the calibration, the ATCA, WSRT and VLA data could be treated in MIRIAD in the same way. For this, the VLA data were converted to fits format and re-read into MIRIAD. CLEANing the HI cube was done in a similar way as CLEANing the continuum as described for the selfcalibration process of the WSRT data. After continuum subtraction, we applied Hanning smoothing, since this was not done on-line (for the WSRT and ATCA data). The datacube was then convolved with a beamsize roughly double in size than the original beam size. With this smoothed image a mask created including real emission only. This was checked for all channels using the KARMA movie option. The mask was used for CLEANing as described above. This CLEANing procedure was repeated 2 – 3 times until no improvement could be reached. Integrated intensity and velocity maps were created using the MOMENT task in MIRIAD. Finally, primary beam correction was applied to the integrated intensity maps.

The CO data were reduced using the CLASS software. Baseline-fitting was done checking every spectrum to be able to delete bad data. In most cases baselines fitted by a first order polynomial were sufficient. The spectra were smoothed to a velocity resolution of 33.8 km/s (OSO) and 21.0 km/s (IRAM) to increase the signal-to-noise ratio. Finally, the spectra were converted from T_A^* to T_{MB} by multiplying with the beam efficiency η (see Tab. 27).

6.4 Results

6.4.1 Neutral hydrogen

Five out of nine galaxies were detected in HI and show prominent, extended HI structure. For the remaining four galaxies, we derived upper limits for their HI gas masses, assuming a typical linewidth of 200 km/s and flux-level of 5σ . Tab. 28 lists the total flux, gas mass, velocity range and the ratio M_{HI}/L_B of all galaxies. In the following, we present the HI data of the individual galaxies (NGC 4004, NGC 5607, UGC 8264 and Arp 161) in more detail. Two galaxies of the sample, NGC 4441 and NGC 4194, were already described in detail in Ch. 5 and Ch. 4, respectively. Thus, we refer to these chapters, but we use the results here in our discussion of mergers.

NGC 4004

In the Optical, NGC 4004 looks very disturbed and disrupted. No real main body can be found, the galaxy seems to consist only of a chain of star-forming HII regions. A long, knotty tail (~ 19 kpc) is found going to the south (see Fig. 62). The northern part seems to be even more disturbed and looks very fuzzy. An Elliptical (NGC 4004B) with a projected distance of $3.1'$ ($= 41$ kpc) to the west is its interacting partner, but most probably gravitational interactions with this galaxy alone cannot explain the optical morphology of NGC 4004.

¹⁷<http://www.aoc.nrao.edu/aips/CookHTML/CookBookap2.html>

Table 28: The optical velocity, HI velocity range, HI flux density, HI mass and M_{HI} -to- L_{B} ratio of the observed galaxies.

^a taken from Horellou & Booth (1997) for completeness, observed with the ATCA

| galaxy | $v_{\text{sys,opt}}$ (km/s) | vel. range (km/s) | F_{HI} (Jy km/s) | M_{HI} ($10^9 M_{\odot}$) | $M_{\text{HI}}/L_{\text{B}}$ |
|-------------------------|--------------------------------|----------------------|------------------------------|---|------------------------------|
| NGC 4004 | 3377 | 3140 – 3530 | 15.22 | 7.2 | 0.78 |
| NGC 5607 | 7595 | 7250 – 7540 | 5.97 | 14.2 | 0.73 |
| UGC 8264 | 4641 | 4490 – 4700 | 4.64 | 4.2 | 0.37 |
| Arp 161 | 5564 | 5210 – 5660 | 3.36 | 4.3 | 0.38 |
| Arp 164 | 5294 | – | < 0.4 | < 0.5 | < 0.02 |
| ESO 156-18 | 13315 | – | < 1.3 | < 9.4 | < 0.4 |
| ESO 159-03 | 3994 | – | < 1.3 | < 0.7 | < 0.07 |
| ESO 341-04 ^a | 6057 | 5800–6080 | 2.6 | 3.9 | 0.83 |

The neutral hydrogen follows roughly the optical appearance, is, however, slightly more extended. The HI is mainly north–south oriented (like the stellar component), but shows a warp-like signature in the south beginning at the end of the optical tail. Here, an HI tail turns to the south-east. At the tip of the tail an HI clump is situated. In the optical there is a faint stellar counterpart. Remarkable is the extension out to $\sim 2'$ (= 26 kpc) to the West in direction to its partner. The Elliptical itself, however, does not exhibit any HI at all.

The velocity increases quite smoothly from the South to the North, similar to a disk-like rotation (see also Fig. 63). Interestingly, the velocity field does not seem to be highly effected by the interaction, although the HI distribution and in particular the optical morphology show clear signs of the merger. This is also seen in the integrated HI spectrum (Fig 72), which shows a contiguous velocity pattern. The highest velocity is found in the northern edge of the western extension. This region is, however, of low intensity and has to be treated carefully. The velocity dispersion decreases from the nucleus to the outskirts. The HI associated with the optical tidal tail seems to have a slightly lower dispersion than the regions to the left and right, but this might be an effect due to the lower intensity and therefore higher noise level in these regions. This explanation is probably also valid for the spot of very high velocity dispersion at the northern edge of the western HI extension.

The total HI mass of NGC 4004 is determined as $7.2 \cdot 10^9 M_{\odot}$. This is in good agreement with the single-dish observations of Davis & Seaquist (1983) ($6.15 \cdot 10^9 M_{\odot}$), Gavazzi (1987) ($5.77 \cdot 10^9 M_{\odot}$) and Bottinelli et al. (1990) ($9.0 \cdot 10^9 M_{\odot}$) and is a good indicator that we do not miss any faint and extended flux. We estimate an HI mass of the southern tail of $2.6 \cdot 10^9 M_{\odot}$, which is 36% of the total HI mass.

The pair NGC 4016/17

South of NGC 4004 ($\sim 25'$, according to 327 kpc) we detected the strongly interacting pair NGC 4016/NGC 4017 in HI. This pair has a similar velocity as NGC 4004 ($v_{\text{opt,pair}} = 3448$ km/s), however is too far away for gravitational interactions. Likely, NGC 4004, NGC 4016 and NGC 4017 form a loose group. In Fig. 64 we show the integrated HI Flux overlayed onto a DSS image. Both galaxies look peculiar in the Optical: NGC 4016 is classified as SBdm and consists of an irregular body with diffuse, extended low surface brightness component. NGC 4017 is a barred spiral galaxy (classified as SABbc) with two asymmetric spiral arms.

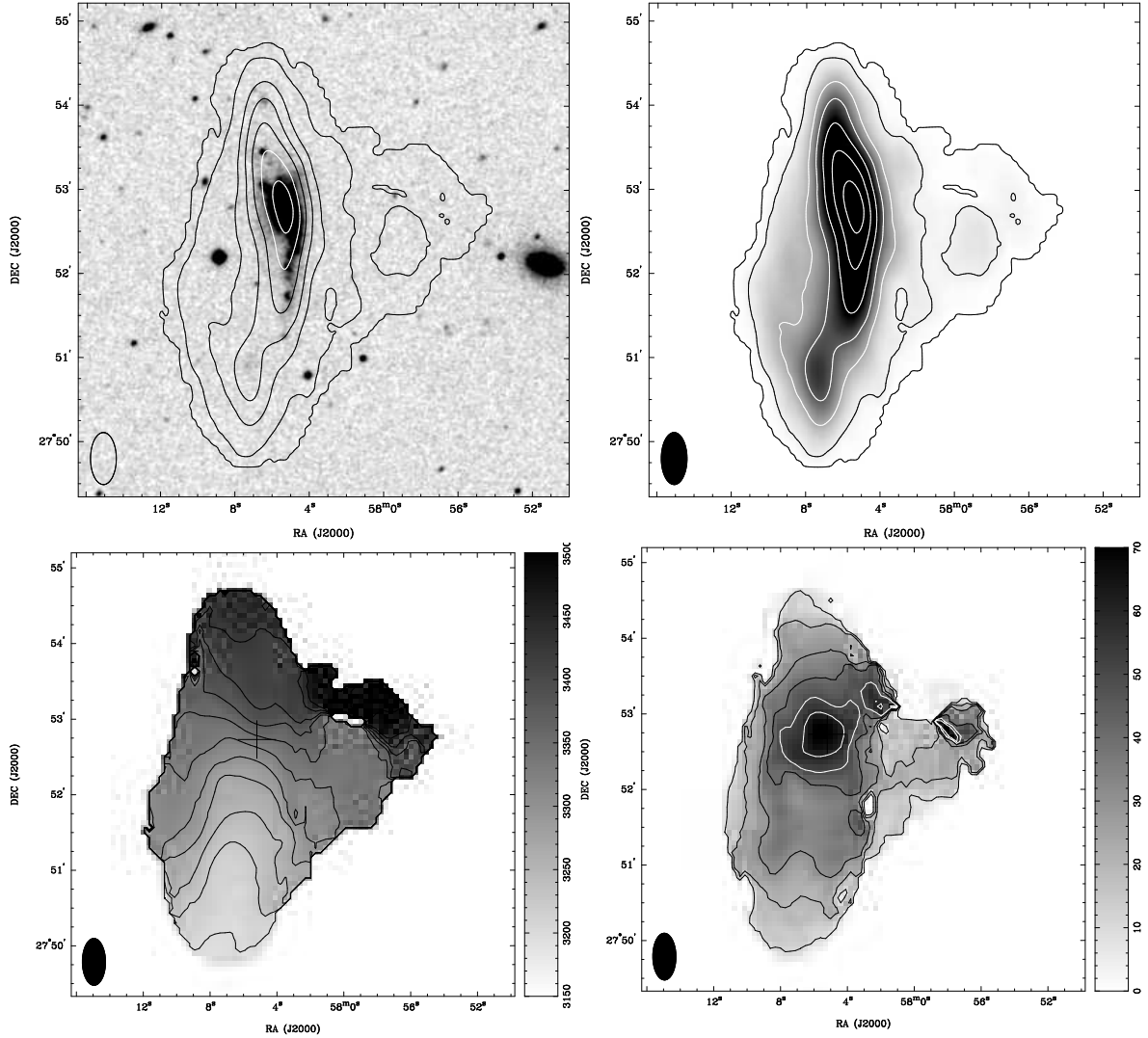


Figure 62: NGC 4004 – (top left) HI distribution, contour levels are 0.001, 0.05, 0.3, 0.6, 1, 1.5, 2 Jy/beam km/s ($0.001 \text{ Jy/beam km/s} = 1.6 \cdot 10^{18} \text{ cm}^{-2}$), (top right) HI distribution overlaid on optical image, contours same as before, (bottom left) velocity field, contour levels are 3200, 3225, 3250, 3275, 3300, 3325, 3350, 3375, 3400, 3425, 3450, 3500 km/s (bottom right) HI velocity dispersion (2. moment), contour levels are 10, 20, 30, 40, 50, 60 km/s The synthesised beam is marked in the bottom left corner. A cross marks the optical center position as given in Tab.23.

In particular the HI content of NGC 4017 reflects the interaction of these two galaxies. A curved tidal tail emanates to the South-East. To the opposite side the HI is spread out in the direction of NGC 4016, but no HI bridge could be measured. Within this HI extension there is an HI clump associated with a faint optical structure almost halfway to NGC 4016. This might be either consisting of stars and gas thrown out during a close encounter or newly formed stars within a tidal gas cloud. A further analysis of this pair will be done in later work.

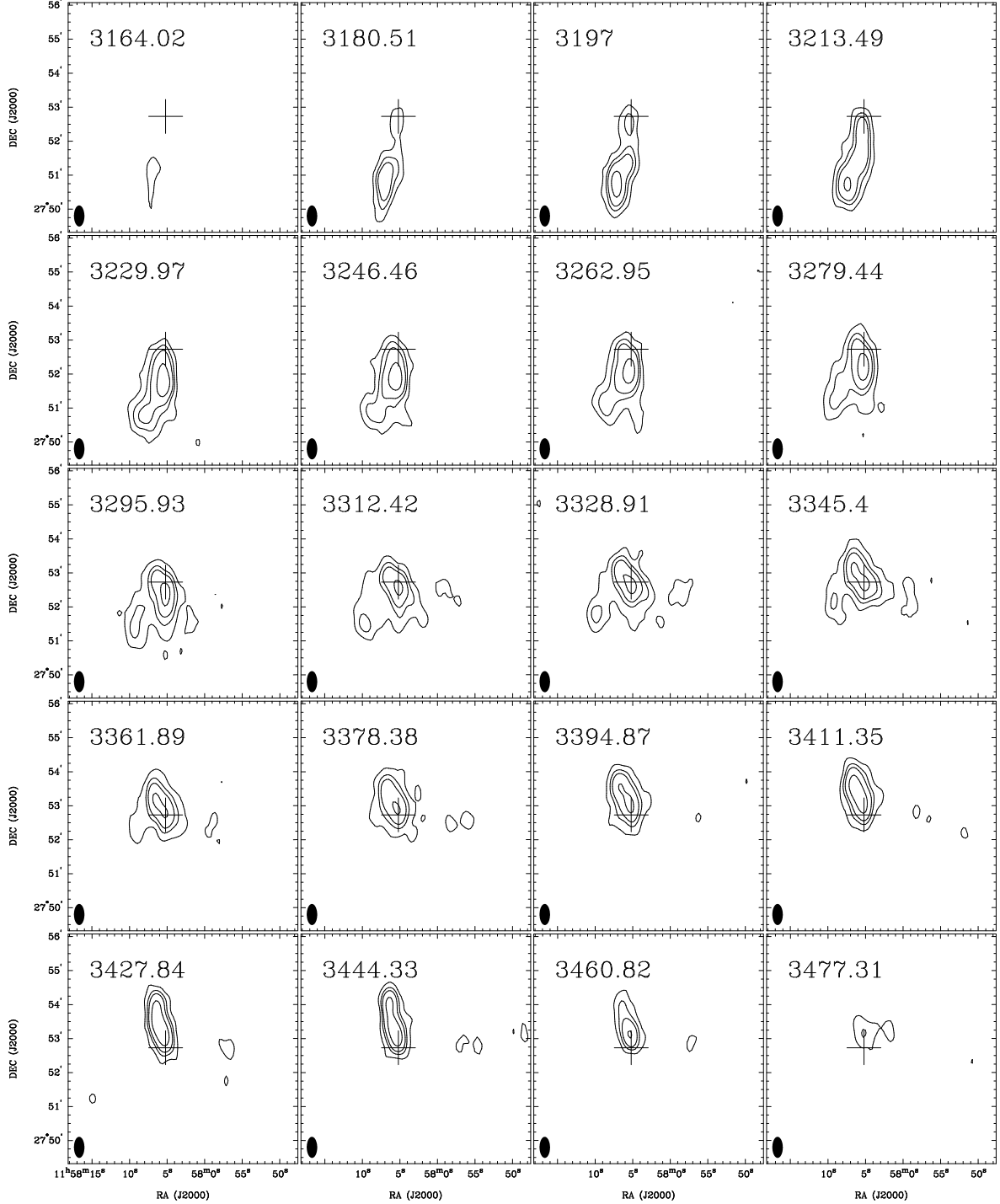


Figure 63: Channel maps (robust 0.5 weighted) of NGC 4004. The optical center position is marked with a cross. The contour levels are 1.1, 3, 5, 10 mJy/beam. The heliocentric velocity is given at the top left, the beam at the bottom left corner.

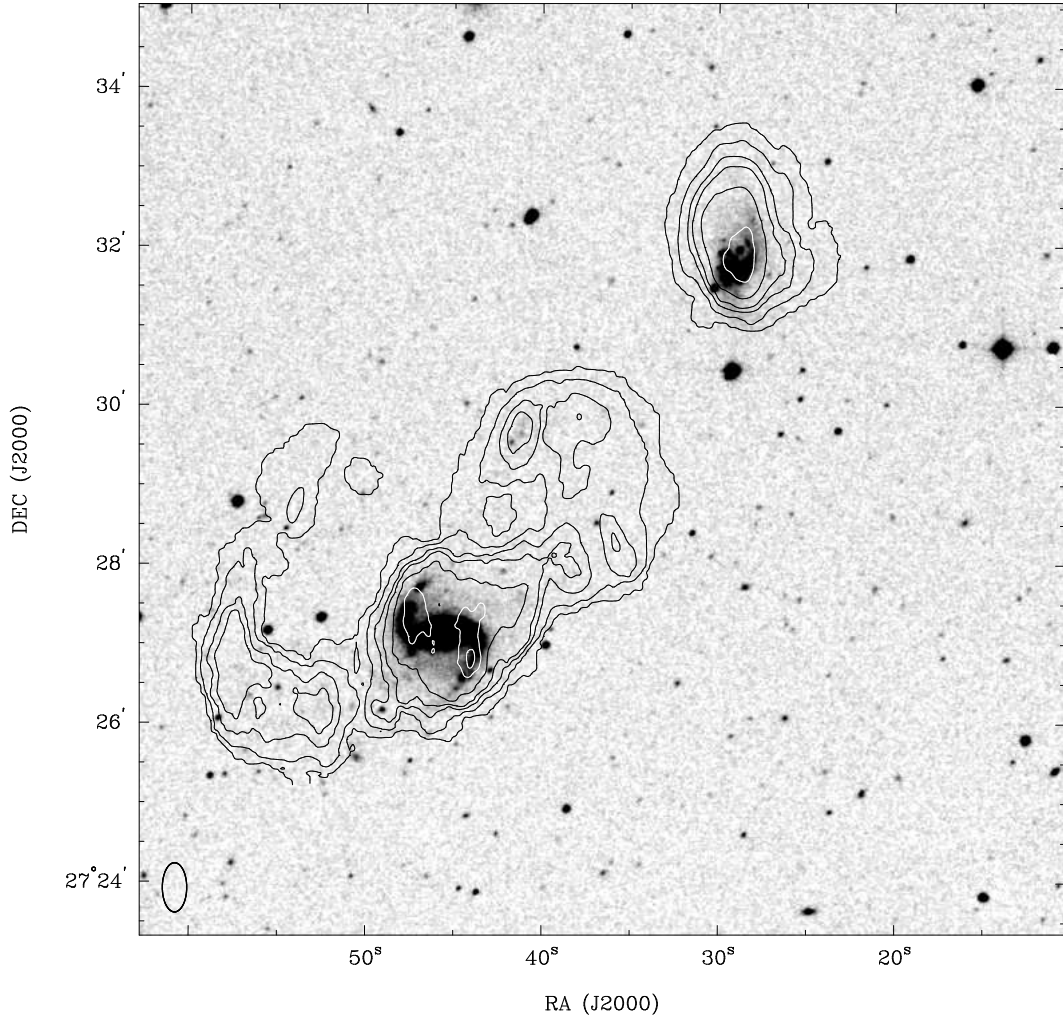


Figure 64: The interacting pair NGC 4016 (right) and NGC 4017 (left) – HI distribution (robustly weighted) as contours on a DSS2-blue image. Contour levels are 0.01, 0.08, 0.2, 0.3, 0.5, 0.8, 1 Jy/beam km/s. The synthesised beam is marked in the bottom left corner.

NGC 5607

NGC 5607 is a peculiar galaxy with a spiral arm-like feature to the West and a faint optical plume to the East. In HI, this galaxy shows a prominent tidal tail emanating from the West and turning southwards. The tail is knotty and shows three major HI clumps, one in the middle and two at the tip of the tail (Fig. 65). No optical counterparts could be identified. The projected distance from the center to the tip of the tail is $4.82' = 142$ kpc, the total length of the tail is even $\sim 6.9' = 203$ kpc. The HI is slightly elongated to the direction of eastern optical plume, however no disturbances in the velocity field are found. To the South we detected a very faint HI blob. Here we see in our optical image also a very faint spike-like structure going into the same direction (see Ch. 3). This extension shows the lowest velocity in the whole system, with almost no internal structure.

The velocity in the main body increases from east to west and even more in the tail, however, it decreases again after its turning point to the south (see also Fig. 66). In the integrated HI

spectrum (Fig. 72), the slightly higher velocity of the tail compared to the main galaxy is seen as a small asymmetry of the shape of the spectrum, with an excess to higher velocities.

The velocity dispersion of NGC 5607 has a maximum in the central region and decreases smoothly. The region north of the nucleus has a higher dispersion compared with the values in the other directions at the same distance. Neither in the optical nor in the HI map is there an obvious feature associated with the higher dispersion, but this might be the region where the HI tail is connected with the HI disk.

We calculate a total HI mass of $1.42 \cdot 10^{10} M_{\odot}$ for NGC 5607. Haynes & Giovanelli (1991) derived a mass of $1.74 \cdot 10^{10} M_{\odot}$, which is in good agreement with our measurements. For the HI tail, we estimate a gas mass of $1.6 \cdot 10^9 M_{\odot}$, which corresponds to 11% of the total mass.

UGC 8264

This galaxy appears to be very compact in the optical, with a small main body and an optical tail at the east side which turns around almost 180° and ends in a series of bright knots. This 'half circle' is 'completed' by the HI structure (Fig. 67), in which we found a feature emanating northwards and turning to the east, forming a clump which coincides with the optical knots. These knots might be tidal dwarf galaxies in formation. The projected distance of the HI clump is $1.24' = 22.4 \text{ kpc}$. In contrast to the optical, the HI forms a complete ring with an inner HI depression with a diameter of $35'' = 10.5 \text{ kpc}$. The largest extension from the center (eastwards) is $1.65' = 30 \text{ kpc}$. In addition, a weak extension to the north-west is found in HI with no optical counterpart, however on a very low level, thus it is not clear whether this feature is real.

Interestingly, the HI velocity field shows an almost disk-like rotation behaviour, not only within the galactic main body, but also in the overall HI distribution with its center in the HI depression. The northern part of the HI ring has the lowest velocity within the system, the HI in the southern half closes the ring at slightly higher velocity ($+70 \text{ km/s}$) (see Fig. 68). In general, the HI velocity range is rather narrow (see Fig. 72) compared to the other observed galaxies. This is in agreement with the relatively compact HI distribution. In comparison with the other galaxies, the HI in UGC 8264 almost does not extend the optical structure including the tidal tail.

As in the other galaxies, the velocity dispersion is highest in the center and decreases in the tidal features. In the middle of the ring-like HI distribution (where the HI has a local minimum), the dispersion is slightly higher than in the ring, but this might be due to a lower signal-to-noise ratio.

The HI mass of UGC 8264 was measured by Haynes & Giovanelli (1991) as $4.0 \cdot 10^9 M_{\odot}$, which agrees very well with our determination of $4.2 \cdot 10^9 M_{\odot}$. We derive a gas mass of the tidal structure of $1.8 \cdot 10^9 M_{\odot}$, which corresponds to 43% of the total gas mass. The tidal dwarf galaxy candidate has a gas mass of $\sim 2.5 \cdot 10^8 M_{\odot}$, which is 9% of the total gas mass.

In the vicinity of UGC 8264 we found a few more galaxies in the velocity range covered by the chosen bandwidth. Fig. 69 shows a DSS images with HI contours. UGC 8264 obviously belongs to a loose group, but no galaxy is close enough for tidal interactions creating the observed features.

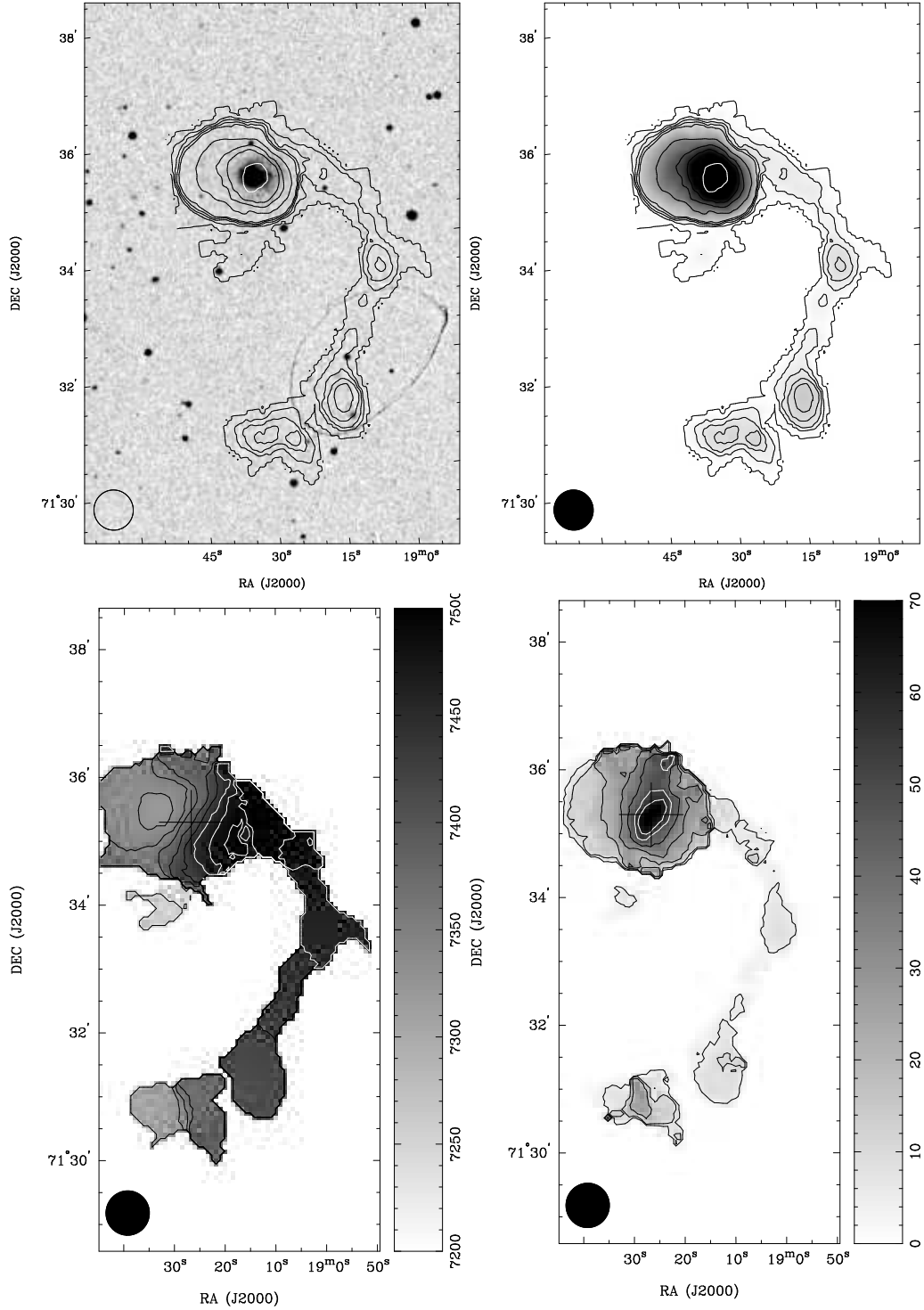


Figure 65: NGC 5607 – (top left) HI distribution, contour levels are 0.0001, 0.05, 0.1, 0.15, 0.2, 0.5, 0.8, 1, 1.5 Jy/beam km/s ($0.0001 \text{ Jy/beam km/s} = 6.3 \cdot 10^{16} \text{ cm}^{-2}$), (top right) HI distribution overlaid on optical image, contours same as before, (bottom left) velocity field, contour levels are 7250, 7330, 7350, 7370, 7400, 7425, 7450, 7475, 7490 km/s, (bottom right) HI velocity dispersion (2. moment), contour levels are 5, 10, 20, 30, 40, 50, 60 km/s The synthesised beam is marked in the bottom left corner. A cross marks the optical center position as given in Tab. 23.

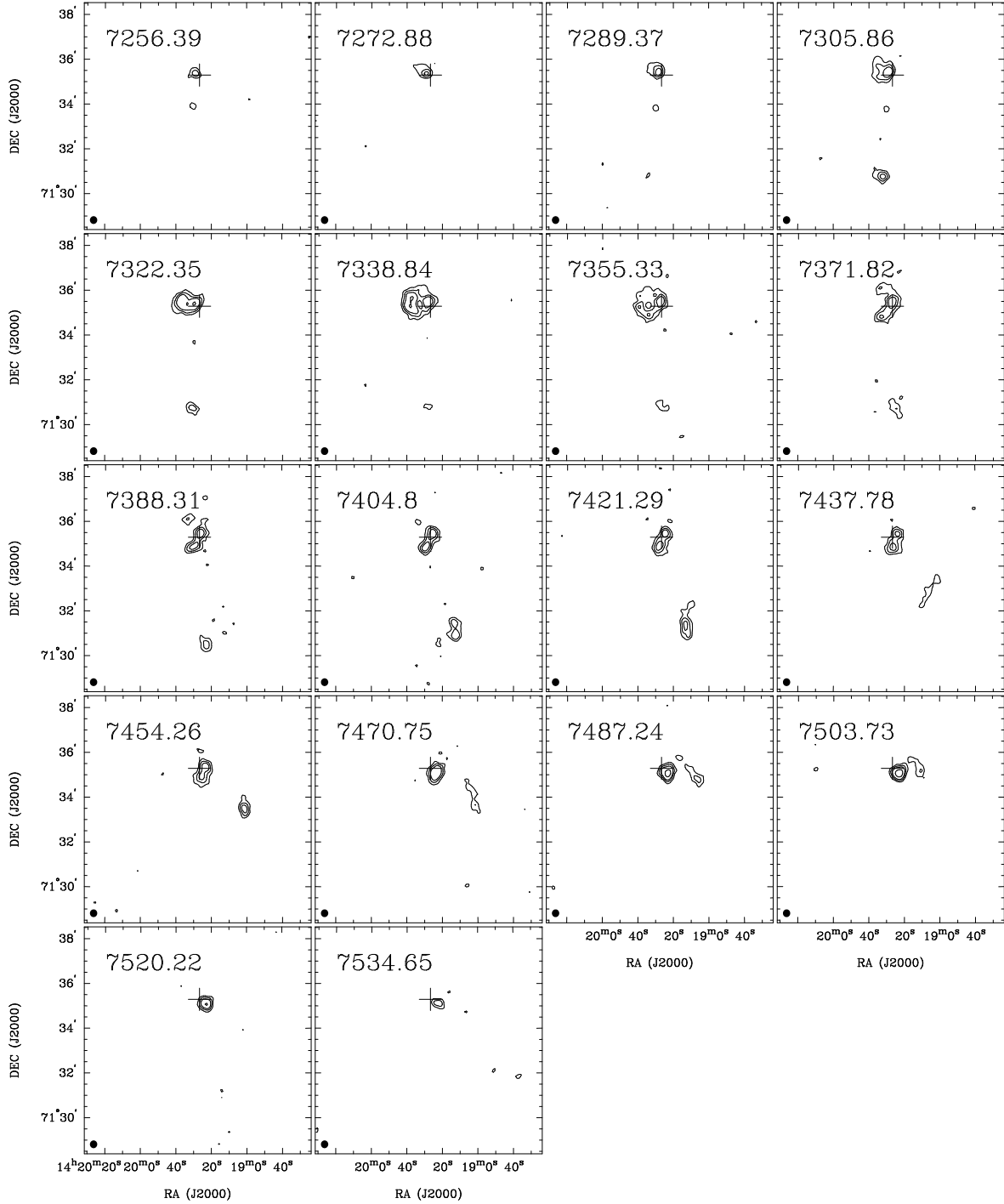


Figure 66: Channel maps (robust weighted) of NGC 5607. The optical center position is marked with a cross. The contour levels are 1.1, 2, 3, 5 mJy/beam. The heliocentric velocity is given at the top left, the beam at the bottom left corner.

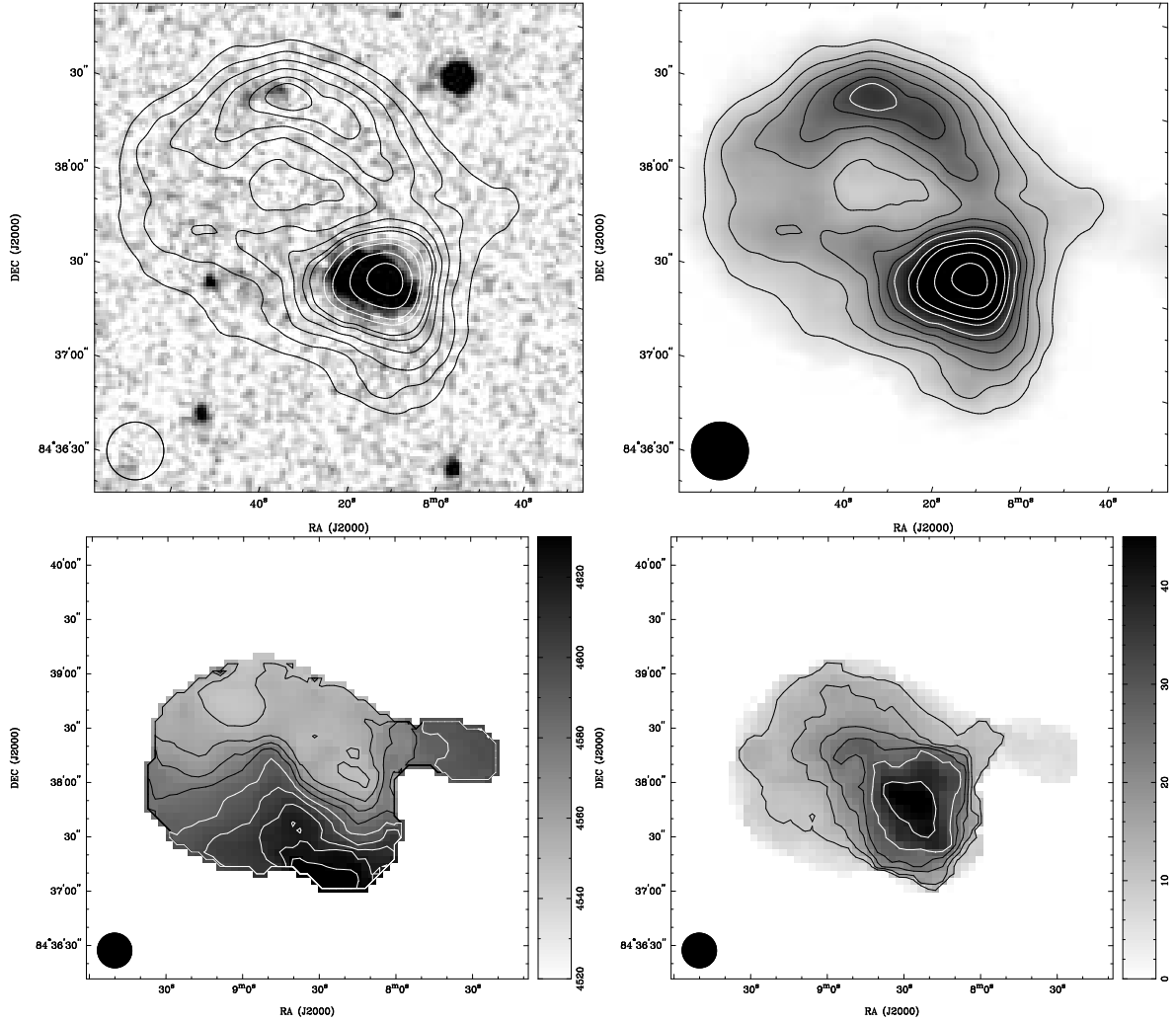


Figure 67: UGC 8264 – (top left) HI distribution, contour levels are 0.05, 0.1, 0.15, 0.2, 0.25, 0.28, 0.35, 0.4, 0.5, 0.6 Jy/beam km/s ($0.05 \text{ Jy/beam km/s} = 1.50 \cdot 10^{20} \text{ cm}^{-2}$), (top right) HI distribution overlaid on optical image, contours same as before, (bottom left) velocity field, contour levels are 4550, 4560, 4570, 4580, 4590, 4600, 4610, 4620, 4630 km/s, (bottom right) HI velocity dispersion (2. moment), contour levels are 10, 15, 20, 25, 30, 40 km/s. The synthesised beam is marked in the bottom left corner. A cross marks the optical center position as given in Tab.23.

Arp 161

Arp 161 is a compact, starbursting HII galaxy (Telles & Terlevich (1997)) with an optical plume to the south-western direction. The tail is embedded in the neutral hydrogen distribution, however, we found a more striking elongation to the north-west (see Fig. 70). The main HI disk is extended to the north, almost in perpendicular direction to the optical tidal tail. Westwards of the northern part of the HI disks is a broad HI plume with two distinct HI clumps. The maximum projected extension of the HI distribution is $3.55'$, equivalent to 76.3 kpc.

The velocity field is smooth, with a general trend of decreasing velocity from the south-east

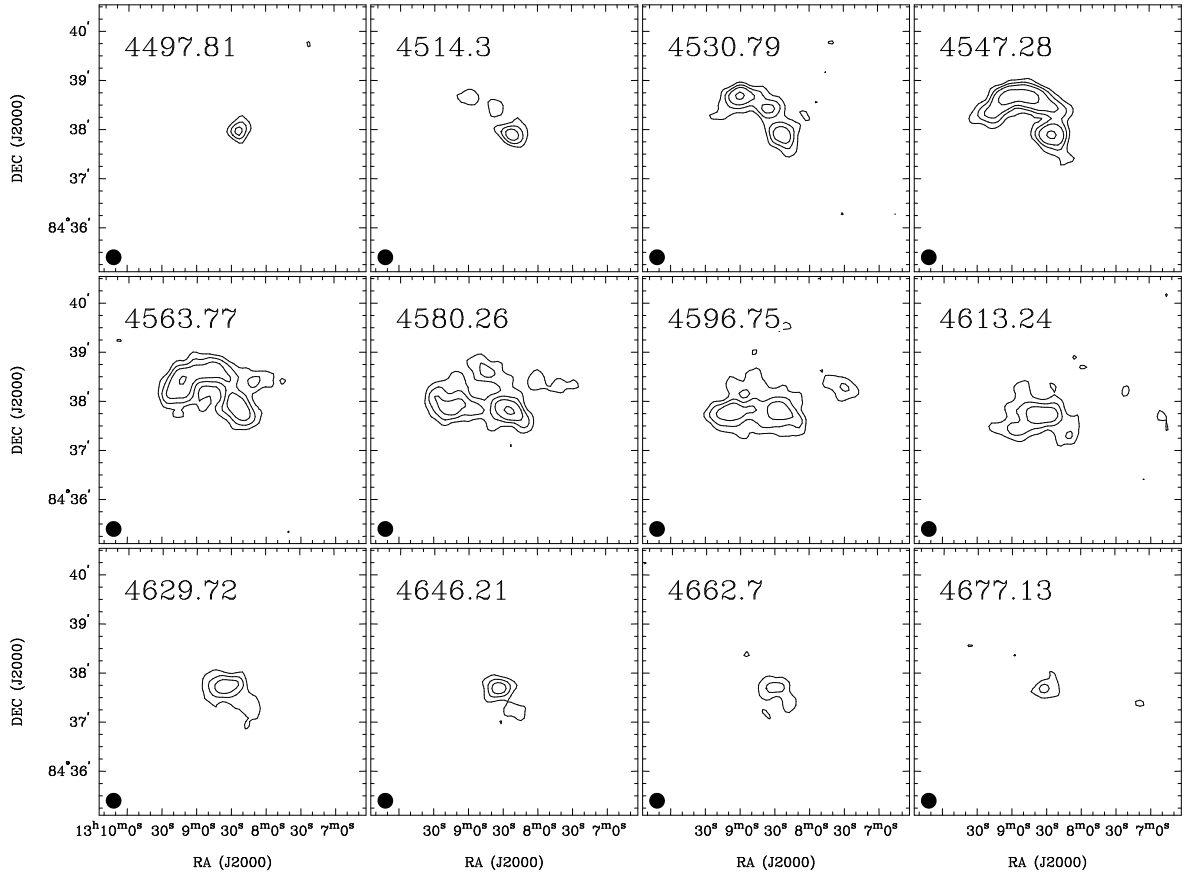


Figure 68: Channel maps (robustly weighted) of UGC 8264. The optical center position is marked with a cross. The contour levels are 1.1, 2, 3, 5 mJy/beam. The heliocentric velocity is given at the top left, the beam at the bottom left corner.

(galactic body) to the north-west (tidal extension) (Fig. 71). The only disturbance in the run of the velocity structure is found in the region between the main HI distribution and the tidal extension. Here, the iso-velocity contours (see Fig. 70) are slightly kinked towards the galactic center. In Fig. 72 the integrated HI spectrum is shown, which also shows a smooth, coherent velocity distribution.

A large fraction of HI has a rather large velocity dispersion values (> 40 km/s even in the tidal features) compared to what is found in the outskirts of the other sample galaxies. This might still reflect the disturbances due to the merger. But considering the starbursting nature of this galaxy, the high velocity dispersion might also be at least partly induced by turbulences within the ISM due to superwinds coming from supernova explosions.

Our derived HI mass of $4.3 \cdot 10^9 M_{\odot}$ is accordance with what is found by Bottinelli et al. (1990) ($5.57 \cdot 10^9 M_{\odot}$) and Mirabel & Sanders (1988) ($5.19 \cdot 10^9 M_{\odot}$). The tidal HI features to the north-west have an approximate mass of $\sim 1.4 \cdot 10^9 M_{\odot}$, which is 33% of the total HI gas mass.

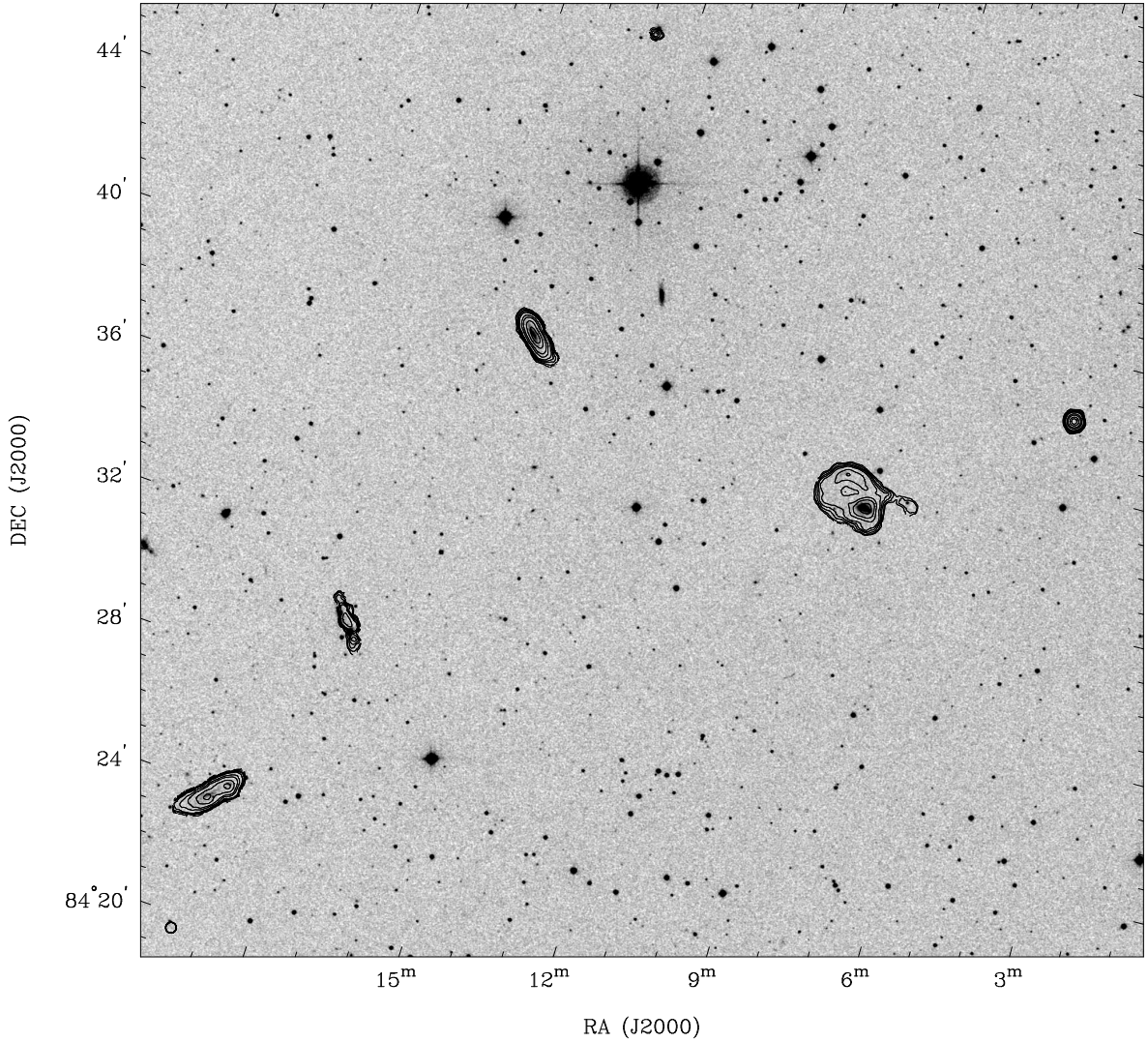


Figure 69: DSS2-red image of the surroundings of UGC 8264 with contours of the HI distribution. Contour levels are 0.02 ,0.03, 0.05, 0.07, 0.1, 0.2, 0.3, 0.5 ,0.7 Jy/beam km/s. Five other objects with HI emission are found within the field. The beam is shown in the the lower left corner.

Arp 164

Arp 164 has a disturbed stellar morphology with a tail to the north and a plume or arc to the south-east. With a noise level of 0.0004 Jy/beam, an assumed typical linewidth of 200 km/s and a 5σ significance level, we estimate an upper limit for the HI mass as $M_{\text{HI}} < 4.6 \cdot 10^8 M_{\odot}$ and an HI column density of $1.66 \cdot 10^{20} \text{ cm}^{-2}$. In the literature exist no other HI measurements of this galaxy. Compared to the HI masses found in the sample galaxies, this upper limit is at least one magnitude lower. Arp 164 has obviously a significantly different atomic gas content. A companion was found in HI ~ 66 kpc to the south-west. The HI distribution is shown in Fig. 73. It is unlikely, that the optical peculiarities found in Arp 164 result only from interaction with the companion, because neither the optical tidal features point towards the companion, nor shows the HI distribution any disturbance which might be related to Arp 164.

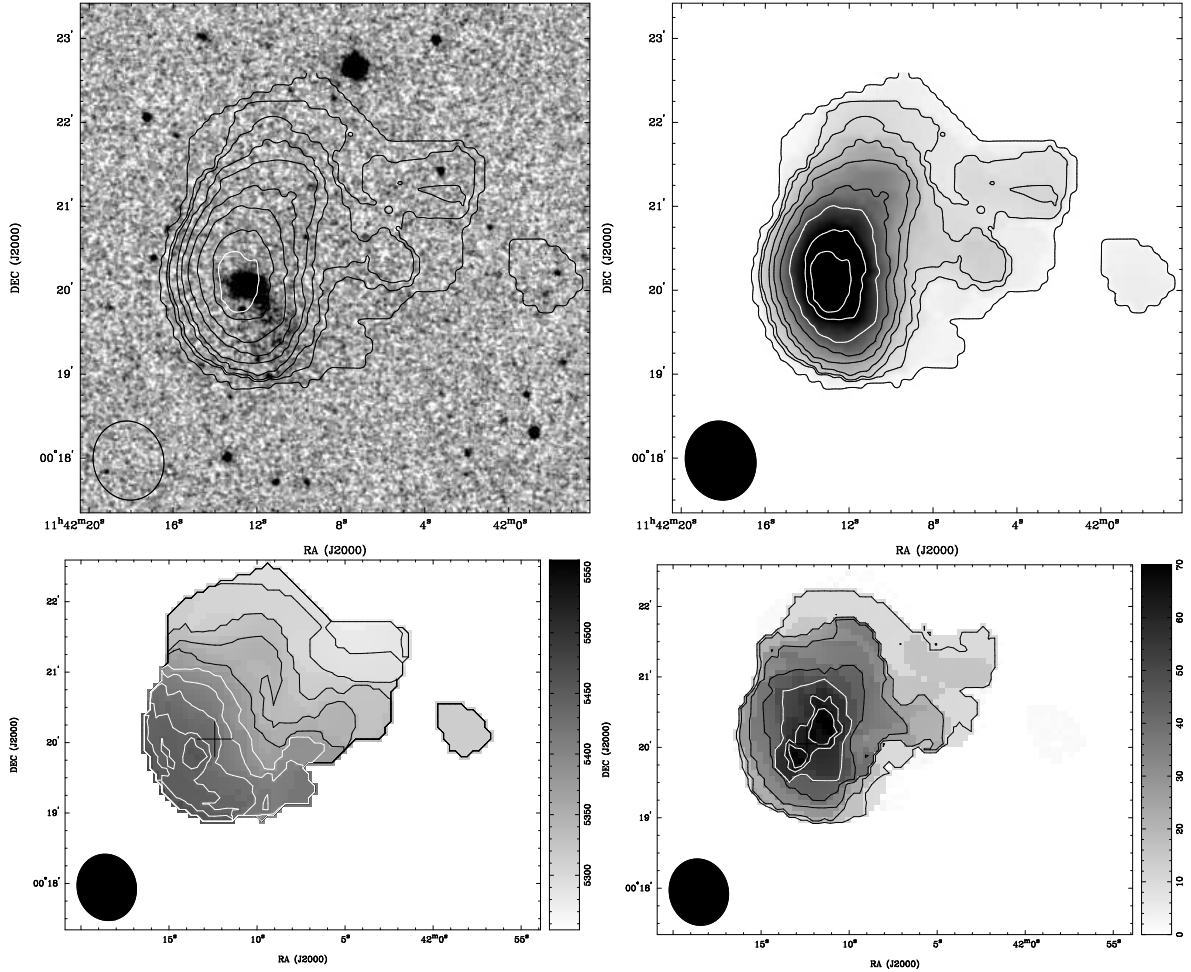


Figure 70: Arp 161 – (top left) HI distribution, contour levels are 0.01, 0.1, 0.15, 0.25, 0.35, 0.5, 0.7, 1, 1.2 Jy/beam km/s ($0.01 \text{ Jy/beam km/s} = 3.9 \cdot 10^{18} \text{ cm}^{-2}$), (top right) HI distribution overlaid on optical image, contours same as before, (bottom left) velocity field, contour levels are 5270, 5285, 5300, 5320, 5340, 5360, 5380, 5400, 5420, 5440, 5450 km/s, (bottom right) HI velocity dispersion (2. moment), contour levels are 10, 20, 30, 40, 50, 60, 65 km/s. The synthesised beam is marked in the bottom left corner. Crosses mark the optical center position as given in Tab.23.

ESO 156-18

ESO 156-18 is a peculiar SAB(s)0 galaxy with several shells seen in the Optical. We could not detect any HI with our ATCA measurements down to a noise level of 0.001 Jy/beam (Fig. 74). Due to its distance, we can only estimate a relatively high upper HI mass of $M_{\text{HI}} < 9.4 \cdot 10^9 M_{\odot}$ ($N(\text{HI}) = 4.16 \cdot 10^{20} \text{ cm}^{-2}$). In this case, the sensitivity of the ATCA was not high enough to reach a mass range which is significantly below to what is found in other sample galaxies. No HI observations are reported in the literature.

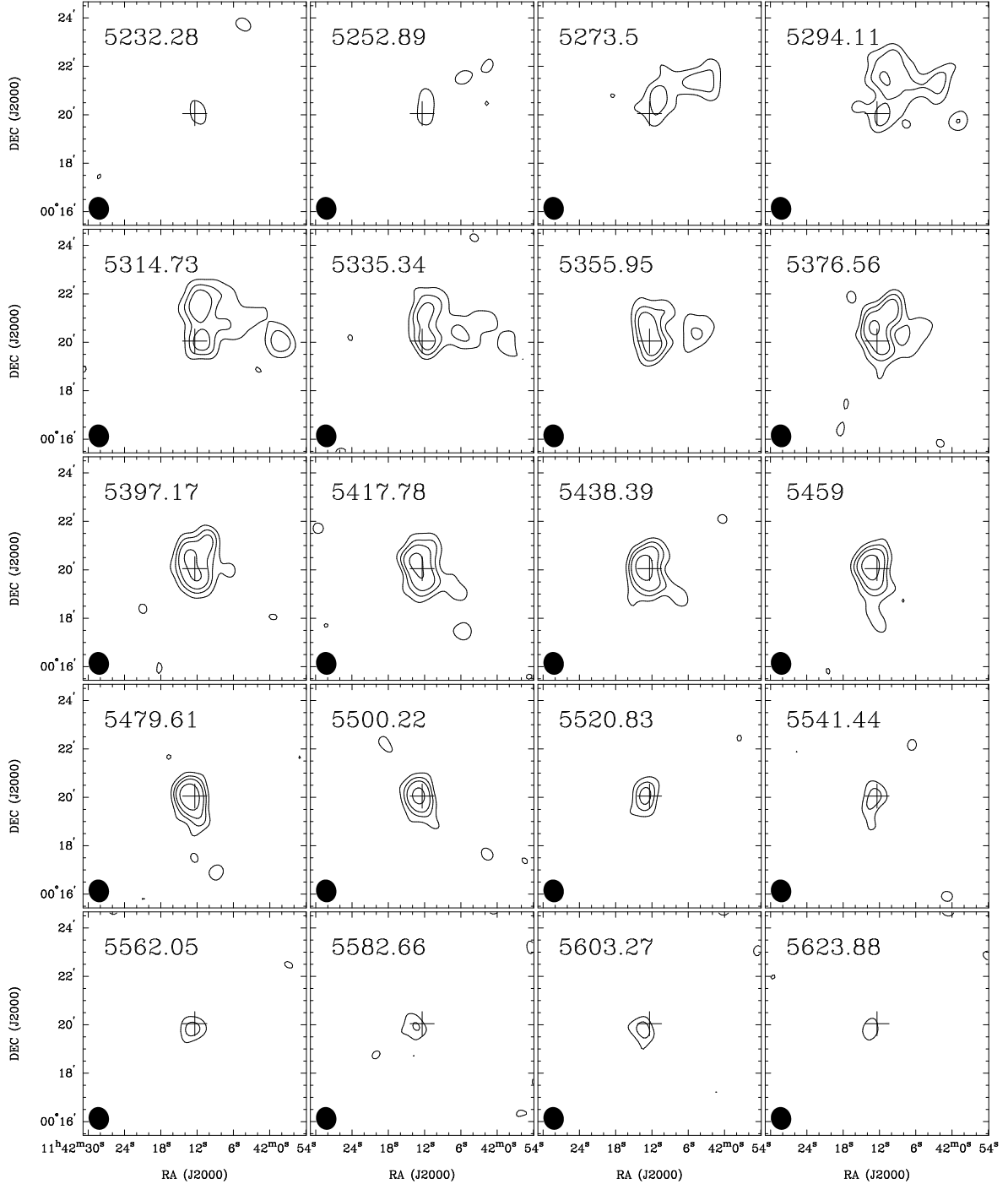


Figure 71: Channel maps (robust 0.5 weighted) of Arp 161. The optical center position is marked with a cross. The contour levels are 1.3, 2.4, 3.6, 6.0 mJy/beam. The heliocentric velocity is given at the top left, the beam at the bottom left corner.

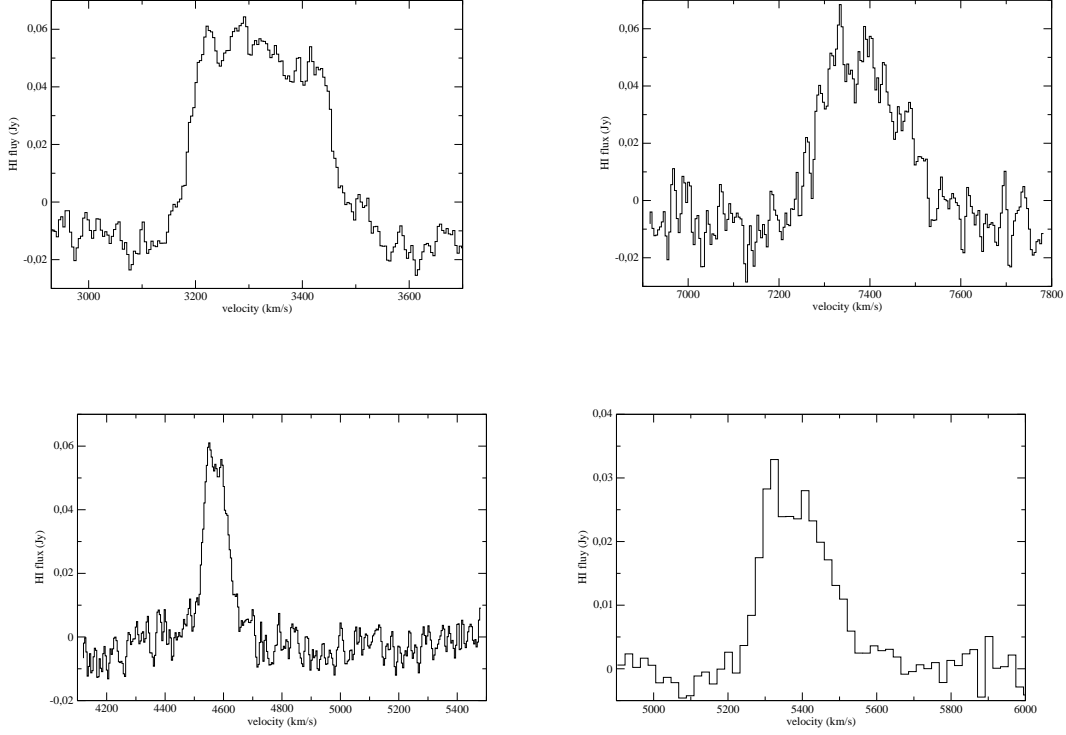


Figure 72: Integrated HI spectra of NGC 4004 (top left), NGC 5607 (top right), UGC 8264 (bottom left) and Arp 161 (bottom right).

ESO 159-03

This peculiar SB0 galaxy shows a few shell fragments and a faint tidal tail in the optical. We did not detect any HI down to a noise level of 0.0011 Jy/beam with the ATCA. With this value, we estimate an upper HI mass limit of $M_{\text{HI}} < 7 \cdot 10^8 M_{\odot}$, which is significantly lower than what is found in the other sample galaxies with HI detections. The limit for the HI column density is $4.16 \cdot 10^{20} \text{ cm}^{-2}$. Hawarden et al. (1981) observed ESO 159-03 with the Parkes telescope, but due to the lack of redshift information, they observed in the velocity range of 0–3700 km/s and therefore missed the correct range.

We detected a possible companion in HI $7.48'$ (106,6 kpc) to the west. In the optical, there is a small, edge-on disk galaxy, which is not classified in any catalog. Its HI velocity range is 3600–3720 km/s, thus ~ 250 km/s less than the optical system velocity of ESO 159-03. With a flux density of 1.09 Jy km/s and an assumed distance of 49 Mpc (same as ESO 159-3), we estimate an HI mass of $6.1 \cdot 10^8 M_{\odot}$.

6.4.2 Continuum

All four galaxies with detectable HI emission also show continuum emission. Fig.76 shows optical images with the 20 cm radio continuum overlaid with contours. In all four cases the continuum source is extended. The derived continuum source sizes are given in Tab.29 after beam deconvolution. Extended continuum emission is a sign of an extended star-forming

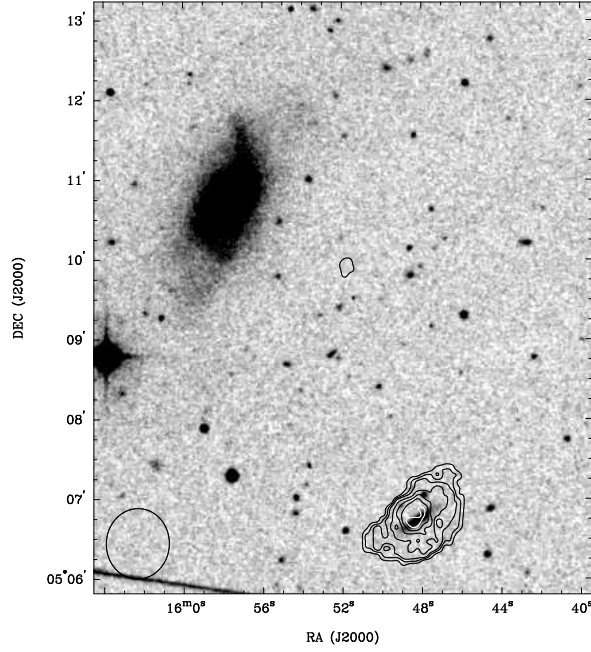


Figure 73: DSS image of Arp 164 and its surroundings. A companion is seen in HI ~ 66 kpc to the South-West. Contour levels are 0.05, 0.075, 0.1, 0.15, 0.2, 0.25, 0.3 Jy/beam km/s (0.05 Jy/beam km/s corresponds to $2.08 \cdot 10^{19} \text{ cm}^{-2}$). The synthesised beam is marked in the bottom left corner.

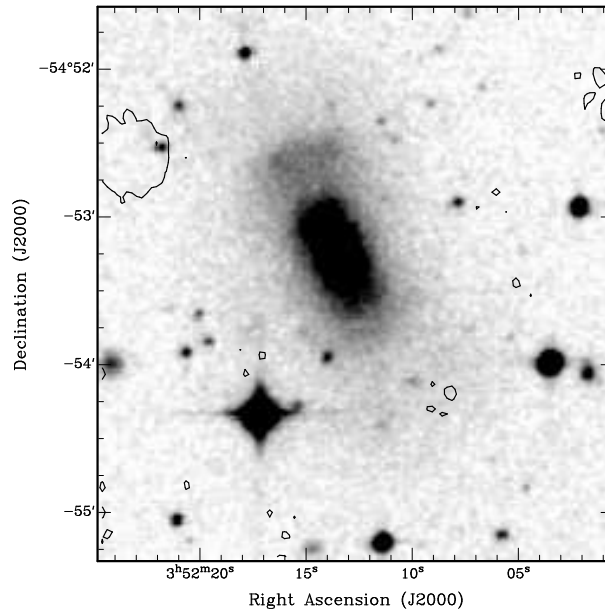


Figure 74: DSS image of ESO 156-18 and HI noise. The contour is the 3σ noise level 0.003 Jy/beam km/s, corresponding to $5.19 \cdot 10^{18} \text{ cm}^{-2}$.

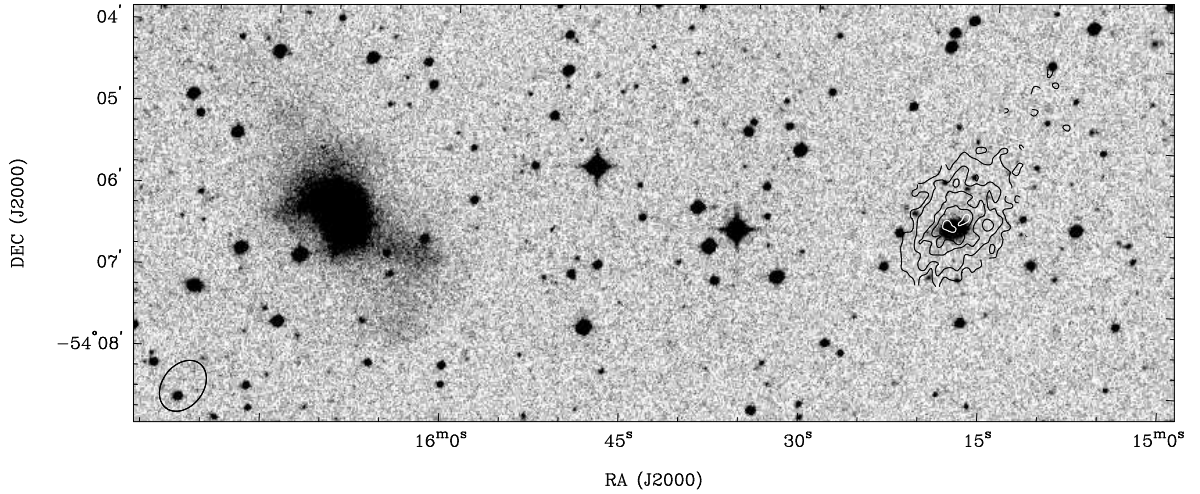


Figure 75: DSS image of ESO 159-3 and its surroundings. A companion is seen in HI ~ 107 kpc to the West. Contour levels are 0.1, 0.2, 0.3, 0.4, 0.5 Jy/beam km/s (0.1 Jy/beam km/s corresponds to $1.25 \cdot 10^{20} \text{ cm}^{-2}$). The synthesised beam is marked in the bottom left corner.

region. In NGC 4004 the source distribution is in accordance with the optical appearance, where a chain of bluish knots forms the main body as well as the tail of the galaxy. These knots are probably HII regions in which star formation is expected. However, with a source size of $6.6 \text{ kpc} \times 2.4 \text{ kpc}$ ($30.2'' \times 11.2''$) no continuum emission is detected from the knots and debris at the tip of the tail. Here, the star formation rate might be still too low. In NGC 5607 and UGC 8264 the continuum source sizes (and thus the possible star forming regions) are also several kiloparsec large, namely $4.9 \text{ kpc} \times 4.5 \text{ kpc}$ ($10.1'' \times 9.1''$) and $3.3 \text{ kpc} \times 2.4 \text{ kpc}$ ($10.8'' \times 7.9''$), respectively.

To estimate the star formation rate from the 20 cm radio continuum flux density we use

$$\text{SFR} (M_{\odot}/\text{yr}) = 0.14 \cdot D^2 \cdot F_{20 \text{ cm}} \quad (46)$$

derived from Condon et al. (1990) and Haarsma et al. (2000). Here, D is the distance in Mpc and $F_{20 \text{ cm}}$ the 20-cm radio continuum flux density in Jy. In Tab.29 the results for the objects are given. For the non-detections we give upper limits. Tab. 29 also gives the SFR estimated from the FIR luminosity:

$$\text{SFR} (M_{\odot}/\text{yr}) = 0.17 \cdot L_{\text{FIR}} \quad (47)$$

following Kennicutt (1998), with L_{FIR} in units of $10^9 L_{\odot}$. The IRAS $60\mu\text{m}$ and $100\mu\text{m}$ flux densities were taken from Sanders & Mirabel (1996). We also calculated the q parameter defined as the logarithmic ratio of FIR to radio flux (Helou et al. (1985)). The mean value for a broad range of different kinds of disk galaxies (including starbursting and dwarf galaxies) is found to be 2.3 (Helou et al. (1985)). With values between 2.1 and 2.3 our sample, though not consisting of real disk galaxies, conforms to this value.

Table 29: Continuum and FIR fluxes, SFR based on the 20 cm continuum and FIR emission, respectively and q parameter.

^a For the 20 cm continuum non-detections, the noise 1σ level is given. The upper limit for the star formation rate is calculated assuming 3σ .

| galaxy | 20 cm (Jy) | 60 μ m (Jy) | 100 μ m (Jy) | SFR _{20 cm} (M _⊙ /yr) | SFR _{FIR} (M _⊙ /yr) | q | 20 cm cont. source size kpc (") |
|-------------------------|---------------|--------------------|---------------------|--|--|-----|---|
| NGC 4004 | 0.030 | 3.4 | 6.7 | 8.5 | 2.1 | 2.2 | 6.6×2.4 (30.2×11.2) |
| NGC 5607 | 0.028 | 4.4 | 6.8 | 40.0 | 12.5 | 2.3 | 4.9×4.5 (10.1×9.1) |
| UGC 8264 | 0.027 | 3.0 | 3.4 | 14.5 | 3.0 | 2.1 | 3.3×2.4 (10.8×7.9) |
| Arp 161 | 0.029 | 4.2 | 4.3 | 22.2 | 5.6 | 2.2 | 5.9×2.1 (16.6×5.9) |
| Arp 164 ^a | 0.0004 | – | – | < 1.0 | – | – | – |
| ESO 159-03 ^a | 0.0001 | – | – | < 0.1 | – | – | – |
| ESO 156-18 ^a | 0.0001 | 0.040 | 0.310 | < 1.3 | 6.1 | – | – |

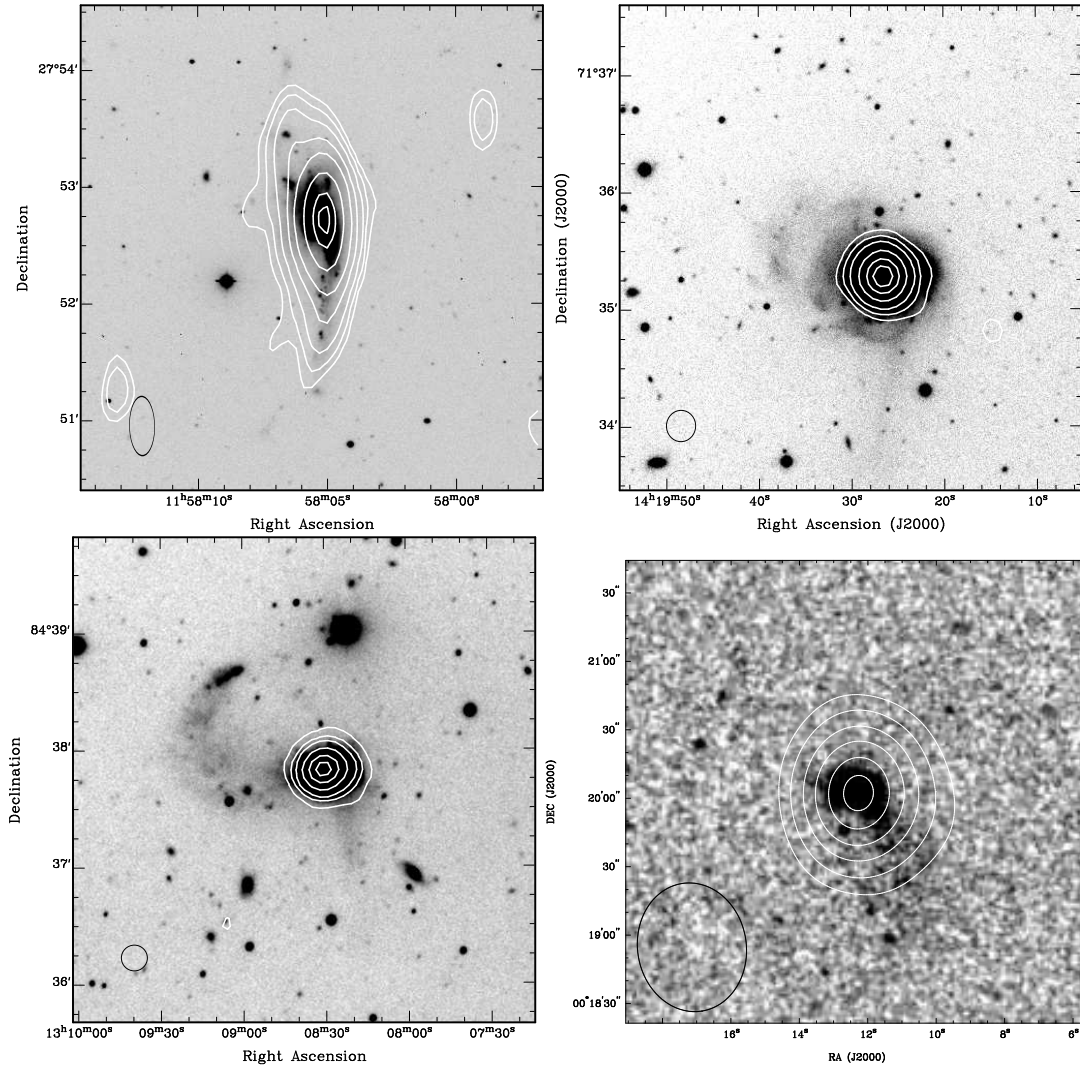


Figure 76: R-band images (taken with Calar Alto 2.2 m) and contours of the 20 cm continuum flux. (top left) NGC 4004, (top right) NGC 5607, (bottom left) UGC 8264 and (bottom right) Arp 161. The beam is shown in the lower left corner of each image.

6.4.3 Molecular gas

In three of the galaxies (NGC 4004, NGC 5607 and Arp 161) we were able to detect molecular gas, whereas in two (UGC 8264 and Arp 164) no CO emission could be measured. ESO 156-18 and ESO 159-03 could not be observed, because after the shutdown of the SEST no mm-telescope capable of sensitive extragalactic observations was available in the southern hemisphere. Tab.30 summarises the basic parameters of the CO observations. For the non-detections, we assumed a typical linewidth of 200 km/s and a 3sigma level to estimate an upper limit for the molecular gas mass. The integrated intensity can be calculated as $\int T_{\text{MB}} dv = 3 \cdot \text{rms} \cdot \sqrt{N} \cdot \Delta v_{\text{cw}}$, with v_{cw} the channel width in km/s, N the number of channels within the 200 km/s range ($= 5.9$ (OSO), $= 9.5$ (IRAM)) and the noise level rms is given in a T_{MB} scale in mK. In Arp,164, we tentatively see a signal with $\int T_{\text{MB}} dv = 3.2 \text{ K km/s}$. We treat this as an upper limit. In the observations of UGC 8264, the noise level is $T_{\text{MB}} = 3.5 \text{ mK}$ (see Tab. 27). For the observation of the tidal dwarf galaxy candidate (TDGC) in UGC 8264, we reached an rms of 1.9 mK when smoothing to a velocity resolution of 21 km/s.

While the CO spectra of NGC 4004 and NGC 5607 show a Gaussian shape, the spectrum of Arp 161 has a double-peak structure, with a lower peak centered at $\sim 5350 \text{ km/s}$ and a higher peak at $\sim 5500 \text{ km/s}$. In Tab. 30 the two components were not taken into account, thus, the linewidth is only approximately determined. In comparison with the HI spectrum of Arp 161, it is interesting that at velocities close to the higher CO peak, almost no HI is found any more, while the HI is peaked at a velocity similar to the centroid of the lower CO peak. This indication of a different molecular gas component has to be taken with care, however, because the HI spectrum covers a much larger spatial area than the CO spectrum, which only shows the gas in the central region.

Table 30: Width of the CO line, integrated flux, N_{H_2} , M_{H_2} and $M_{\text{H}_2} / M_{\text{HI}}$ of the sample. The spectra were smoothed to a velocity resolution of 33.8 km/s (OSO) and 21 km/s (IRAM). For the estimation of the upper limits, a linewidth of 200 km/s was assumed.

^a taken from Horellou & Booth (1997) for completeness, observed with the Swedish-ESO Submm Telescope (SEST)

| galaxy | $\Delta v_{\text{CO}(1-0)}$ (km/s) | $\int T_{\text{MB}} dv$ (K km/s) | N_{H_2} (10^{20} cm^{-2}) | M_{H_2} ($10^8 M_{\odot}$) | $M_{\text{H}_2} / M_{\text{HI}}$ |
|-------------------------|---------------------------------------|-------------------------------------|---|--|----------------------------------|
| NGC 4004 | 240 | 5.83 | 10.3 | 9.5 | 0.13 |
| NGC 5607 | 220 | 4.04 | 7.1 | 33.0 | 0.23 |
| UGC 8264 | – | <0.87 | <2.0 | <2.8 | <0.07 |
| UGC 8264 TDGC | – | <0.4 | <0.9 | <0.5 | – |
| Arp 161 | 220 | 2.74 | 6.3 | 5.3 | 0.12 |
| Arp 164 | – | <2.11 | <3.8 | <8.3 | <2.1 |
| ESO 341-04 ^a | 350 | 1.6 | 3.7 | 17.6 | 0.45 |

NGC 4004 was observed by Arnault et al. (1988), but was not detected. The authors give an upper limit for the CO luminosity of $L_{\text{CO}} < 49.6 \text{ K km/s kpc}^2$. Sage et al. (1992) obtained CO measurements of Arp 161 using the NRAO 12 m telescope and observed a CO Intensity for that galaxy of $I_{\text{CO}} = 1.8 \text{ K km/s}$. Considering a beamwidth of $55''$ for the NRAO 12 m telescope, their measurement corresponds to a molecular gas mass of $1.2 \cdot 10^9 M_{\odot}$, which is 2.3 times more than our value. This might be a hint that the molecular gas is much more extended than the area covered with the IRAM 30 m beam. But, as also mentioned by Sage

et al. (1992), the NRAO spectrum is not good, and CO only tentatively detected, thus, the discrepancies might also appear due to an overestimation by Sage et al. (1992). NGC 5607 was observed by Kandalyan (2003), who measured a molecular gas mass of $6.3 \cdot 10^9 M_{\odot}$. The higher gas mass compared to our results is again likely to be due to an extended source, which was not completely covered by our beam.

For the calculation of the molecular gas mass from the CO flux, we used the standard conversion factor $X_{\text{CO}} = 2.3 \cdot 10^{20}$, following Strong et al. (1988).

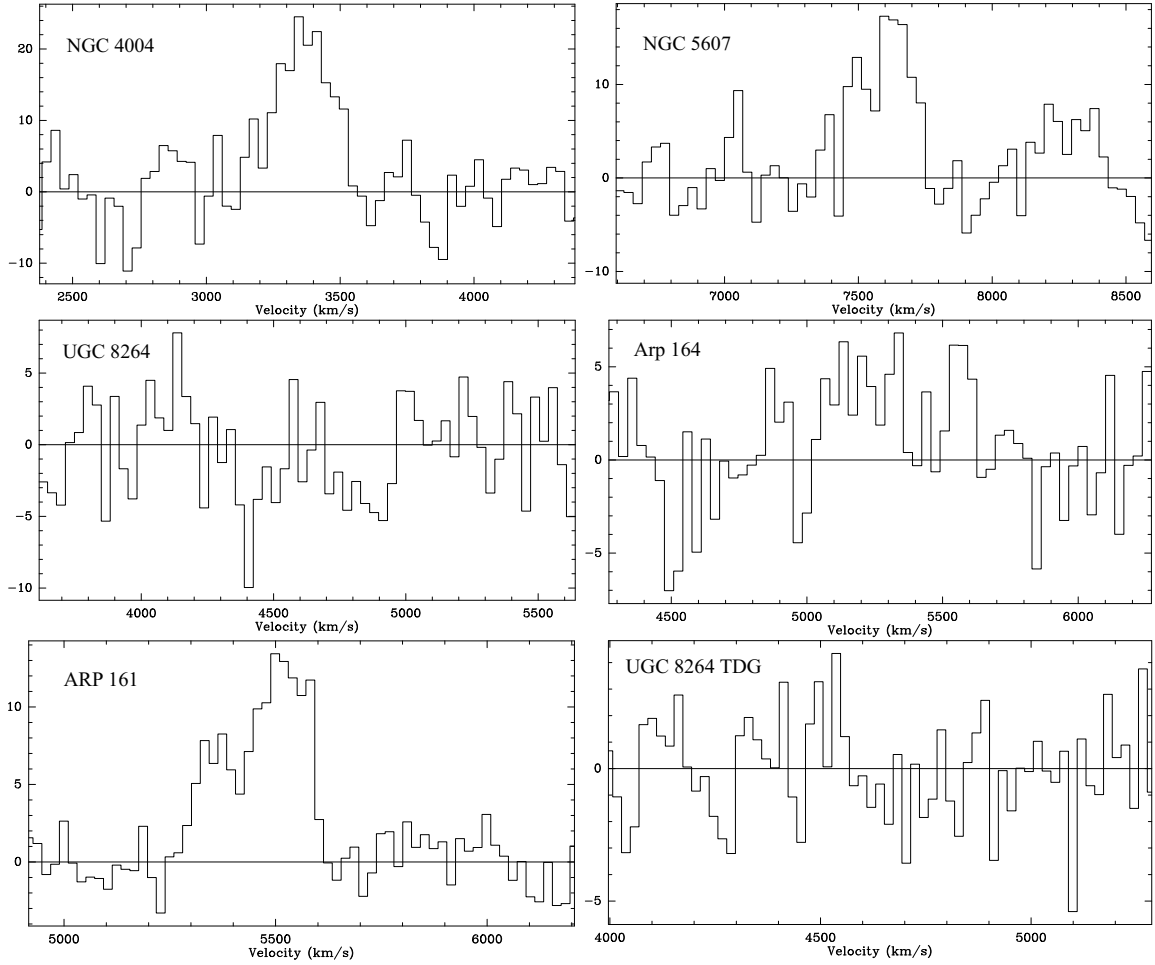


Figure 77: CO(1–0) spectra of NGC 4004 (upper left), NGC 5607 (upper right), UGC 8264 (middle left) and Arp 164 (middle right), observed with the OSO 20 m telescope. CO(1–0) observed with the IRAM 30 m telescope of Arp 161 (lower left) and the tidal dwarf galaxy candidate (TDGC) in UGC 8264 (lower right). The temperature T_{MB} is measured in mK.

6.5 Discussion

6.5.1 Stellar versus gaseous morphology

The six observed galaxies show a variety both in the HI content and the tidal features, covering a range from non-detections to enormous HI tidal tails. Although in all cases of HI detection the stellar components are embedded in HI, the tidal HI features do not always coincide with

the optical disturbances. In Arp 161, there is a faint optical fan to the south-west, however the HI is extended to the north with a tail-like structure to the north-west. UGC 8264 has a hooked optical tail with some knots at the tip, but the most prominent HI structure is found on the opposite side between the optical knots and the main galaxy. Most obvious are the differences in NGC 5607: this galaxy shows as a main morphological peculiarity a stellar loop to the east, whereas in HI there is a huge tail to the opposite side and no particular feature associated with the optical one. Hibbard et al. (2000) report differences between the stellar and gaseous tidal morphologies in three ULIRGs and conclude, that among several probable mechanisms the most important one are superwinds driven by the nuclear starbursts. Although the galaxies of the sample presented here also show star formation activity (on a lower level, though), the scenario of superwinds is probably not applicable here, because the differences are on another scale than what is found by Hibbard et al. (2000). They investigated offsets between the optical and gaseous tidal features or stellar structures with no HI at all. In contrast, the galaxies of our sample partly show gaseous and stellar tidal patterns with a completely different spatial orientation. The material of the tidal HI tails probably originates from the outer HI disks of the progenitor galaxies (Hibbard & van Gorkom (1996), Hibbard et al. (2000)). The huge tail of NGC 5607 indicates a long interaction history (compare with the tail found in Arp 299, Hibbard & Yun (1999)), although this galaxy is actively forming stars on a high level. Thus, the burst must have started much later than the gravitational interaction of the progenitors. This is also in agreement with what is found by Hibbard & Yun (1999) for Arp 299. In contrast to Arp 299, however, no optical tail associated with the HI is found.

Current numerical simulations of S+E mergers make contrary predictions concerning the correlation of the stellar and gaseous distribution. Weil & Hernquist (1993) predict a quick segregation of gas and stars accompanied (with the gas accumulating in the nuclear region) with no formation of extended gaseous tidal tail. In contrast, in simulations of Kojima & Noguchi (1997) the gas and the stars develop a very similar distribution, both forming long tails and shells. Obviously, from the morphological point of view, none of these two models can reproduce the galaxies presented here very well, if at all. Contradictory to Weil & Hernquist (1993), we found large HI tails and extended HI in all detected galaxies, though the optical structure is in nice accordance to their models. However, the gaseous tidal features of our observed galaxies are not aligned with the optical ones, which is what is suggested by Kojima & Noguchi (1997), though.

The misalignment of the stellar and gaseous tidal features might be an indication, that the observed galaxies are S+E merger remnants, despite the disagreement with the two (contradictory) models. In S+S mergers, the stellar and gaseous components develop similar tidal features, as they were similar distributed in the progenitor galaxies. In E+E mergers, no large gaseous tidal features are expected, because the progenitors host only little gas, if at all. In S+E mergers, however, only one of the merging partners has a gaseous disk aligned with the stellar disk. Thus, it is possible, that the tidal features differ, because the stellar component of the disk galaxy is mixed with the stars from the elliptical, which are not aligned with gas, and therefore form different features than the gas from the spiral.

Clearly, however, the merger process is not well understood so far and modifications have to be applied to the models to better reproduce the variety and complexity of the gaseous and stellar tidal features.

6.5.2 The star forming regions

The observed galaxies reveal their different characters not only in the HI distribution, but also in their star forming properties derived from the 20 cm continuum and far-infrared fluxes. For five of the seven galaxies IRAS observations were available and indicate enhanced star formation in the range of $3.0 M_{\odot}/\text{yr}$ (UGC 8264) to $12.5 M_{\odot}/\text{yr}$ (NGC 5607). Except for ESO 156-18, we could observe all of the IRAS-detected galaxies in HI and the 20 cm continuum. The fact that the star formation rate based in the far-infrared flux is higher than in normal galaxies ($6.1 M_{\odot}/\text{yr}$), we assume that ESO 156-18 has similar star forming and HI properties than the other observed galaxies, but could not be detected due to its distance. Interestingly, as the extensions of the star forming regions based on the 20 cm continuum source sizes are rather large, compared to other merging systems. We derived star forming regions of several kiloparsec in size, whereas e.g., ULIRGs have compact nuclear starbursts with sizes of a few 100's pc only (Sanders & Mirabel (1996)). Our observations of two other moderate luminosity mergers, however, NGC 4194 (Ch. 5) and NGC 4441 (Ch. 4), fit to these results. Both galaxies exhibit an extended 20 cm continuum source associated with extended star forming regions.

The differences in the star formation activity between the galaxies of our sample are also reflected in our molecular gas observations. Most of the galaxies showing star formation activity also possess a molecular gas reservoir to feed the star forming regions. In addition, no CO was detected in Arp 164, which also does not show any atomic gas or far-infrared emission (thus no signs of ongoing star formation). Most likely, the progenitors of this merger were different from those of the other observed objects, maybe two gas-poor galaxies (e.g., two Ellipticals). Puzzling is UGC 8264, because it hosts an extended region of enhanced star formation, it also contains HI with a mass comparable to what is found in the other sample galaxies, but no CO could be detected down to a reasonable limit. We derived an upper limit for the molecular-to-atomic gas ratio of $M_{\text{H}_2}/M_{\text{HI}} < 0.09$. The metallicity of this object is rather low ($0.3 Z_{\odot}$, see Tab. 10), but UGC 8264 is not metal poor enough to make CO detections impossible. Thus, metallicity is at most a partial explanation for the lack of a CO detection.

6.5.3 Star Formation Efficiency

With the molecular gas masses and the star formation rates it is possible to estimate the efficiency of a galaxy to convert the raw material (i.e., the molecular gas) into new stars. This so-called *star formation efficiency* is simply the ratio between the star formation rate and the available molecular gas mass: $\text{SFE} = \text{SFR}/M_{\text{H}_2}$. Because several estimators for the star formation rate give slightly different results, this approximation is of course dependent on which star formation rate tracer is used. When several tracers are available, it is possible to estimate a range of the star formation efficiency. We used the star formation rate derived from the 20 cm continuum flux, which gives the highest value of the used tracers, and from the far-infrared, which gives the lowest value (the star formation rate based on $\text{H}\alpha$ emission as given in Ch. 3 is typically slightly higher but of the same order of the far-infrared results). Furthermore, under the assumption that the star formation efficiency does not vary with time (but it probably *does!*), one can crudely approximate the time needed until the gas is depleted, which is $\tau = 1/\text{SFE}$. The results for the galaxies presented here are given in Tab. 31. We calculated the star formation efficiency for both the star formation rate estimated from the radio continuum and FIR observations, and the same for the gas depletion time. The

Table 31: Star formation efficiencies and gas depletion times of the sample. The values for NGC 4194 (Ch. 5), NGC 4441 (Ch. 5) and ESO 341-04 are included for completeness. For NGC 4194, Weistrop et al. (2004) derive a SFR of $\sim 30 M_{\odot}/\text{yr}$, based on HST H α imaging. The corresponding $\text{SFE} = 13.0 \cdot 10^{-9} \text{ yr}^{-1}$, $\tau = 0.77 \cdot 10^8 \text{ yr}$

| galaxy | $\text{SFE}_{20 \text{ cm}} (10^{-9} \text{ yr}^{-1})$ | $\text{SFE}_{\text{FIR}} (10^{-9} \text{ yr}^{-1})$ | $\tau_{20 \text{ cm}} (10^8 \text{ yr})$ | $\tau_{\text{FIR}} (10^8 \text{ yr})$ |
|------------|--|---|--|---------------------------------------|
| NGC 4004 | 8.9 | 2.2 | 1.1 | 4.5 |
| NGC 5607 | 12.1 | 3.8 | 0.8 | 2.6 |
| UGC 8264 | >38.2 | >7.9 | <0.26 | <1.3 |
| Arp 161 | 41.9 | 10.6 | 0.2 | 0.9 |
| NGC 4194 | 9.9 | 4.1 | 1.0 | 2.4 |
| NGC 4441 | 3.9 | 1.6 | 2.6 | 6.3 |
| ESO 341-04 | – | 1.3 | – | 7.8 |

star formation efficiencies and depletion times are of the same order of magnitude (a few 10^{-9} yr^{-1}) for all galaxies.

NGC 5607 seems to be slightly more efficient in forming stars and thus might have a shorter period of enhanced star formation. This galaxy has also the highest star formation rate.

In comparison with two other galaxies from our sample (NGC 4441, see Ch. 4 and NGC 4194, Aalto & Hüttemeister (2000)), the galaxies presented here fill the gap between their star formation efficiencies. NGC 4194 seems to have a very efficient burst (in particular when looking in H α), whereas the SFE in NGC 4441 is moderate and fitting nicely to the observations presented here.

The strange behaviour of UGC 8264, as seen in the molecular-to-atomic gas ratio, is also apparent in the star formation efficiency. Because there is enhanced star formation going on although no molecular gas could be detected, obviously the efficiency must be very high. In other words, the starburst phenomenon takes place on a short timescale compared with the other sample galaxies. Probably, most of the molecular gas is already used for star formation, hence we see the end of the starburst phase.

Arp 161 is the galaxy with the highest star formation efficiency. Sage et al. (1992) estimated the star formation efficiency for this galaxy and defined a lower limit of $\text{SFE} = \text{SFR}/M_{\text{H}_2}$ and an upper limit of $\text{SFE} = \text{SFR}/(M_{\text{HI}} + M_{\text{H}_2})$, claiming that the HI mass does not contribute much to the material used for star formation. They derive a star formation efficiency for Arp 161 of $\text{SFE} = 2.5 - 7.5 \cdot 10^{-9} \text{ yr}^{-1}$ and a gas depletion time $\tau = 1/\text{SFE} = 1.3 - 3.9 \cdot 10^8 \text{ yr}$. These values are rather low in comparison with our sample and in particular with our derived values. But as argued above, their CO detection were only very tentative, thus the value has to be taken with care.

6.5.4 Possible merger scenarios for the sample galaxies

The intention of the sample presented here was to obtain a systematic study of galaxies which are believed to be of the same kind of merger and in the same state. This assumption was based on optical morphology only, which is until now the only parameter for the classification of a merger, as it is done in classical merger sequences (e.g., Toomre (1977), Hibbard & van Gorkom (1996), see Ch. 1). However, when looking at other properties like the star formation rate, the gas content and the gas distribution, the galaxies of this moderate luminosity merger sample seem to be very different. They all have in common, that they are obviously

mergers, and that they have only a moderate far-infrared luminosity, indicating a moderate star formation rate. What merger scenarios are possible?

1. *I. Faded ULIRGs:* Of course it is possible that a moderate luminosity merger is simply an evolved ULIRG, in which the extreme starburst is fading, while the optical perturbances are still present. The progenitors in this case are two large disk galaxies. In this scenario, we expect to find little CO, because most of the molecular gas has already been used for new stars. And of course, the signature of an aged extreme burst would be seen when looking at optical spectra and investigating the star formation history.
2. *II. No gas:* In particular for galaxies, which show only little ongoing star formation and host only, if at all, a small fraction of gas (both atomic and molecular), a merger between two Ellipticals is probable. In this case, the progenitors were both gas-poor, thus, even a merger cannot induce enhanced star formation, because no raw material for star formation is present. In this case, an old dominating stellar population would be found.
3. *III. Scattered gas:* As already suggested in numerical models by Kojima & Noguchi (1997), the gas in S+E mergers can be scattered even in the outskirts. Thus, the gas might never come highly concentrated to initiate an extreme starburst like in ULIRGs. In this scenario, we may find signs of enhanced, maybe extended star formation (though not as strong as in ULIRGs). In addition, the molecular gas as well might be spread out over a few kiloparsec, and show an extended and complex distribution, forming tidal features like long tails.

Scenario III is that kind of merger that initiated our study, namely mergers between Ellipticals and Spirals.

Comparing these expectations with the properties of the mergers presented here (including NGC 4194, NGC 4441 and the data from the literature for ESO 341-04), it becomes clear that morphological appearance alone is not sufficient to classify a merger.

Six out of ten sample galaxies seem to fulfill the prospects of scenario three: NGC 4194 hosts an extended starburst accompanied with extended molecular gas and has a large HI tail (Ch. 5). NGC 4441 might be an evolved version of NGC 4194, possessing two large tails, extended CO but a weaker star formation rate than NGC 4194. Also, the optical morphological features are more evolved than those of NGC 4194. NGC 4004 shows star formation regions even out in the optical tidal tail, while its atomic gas is as well extended (although not showing such distinct tidal tails as other sample galaxies), and NGC 5607 exhibits a remarkable long HI tail and shows enhanced star formation, which is probably extended to a few kiloparsec, judging by the size of the 20 cm continuum source. Arp 161 is known to be a starbursting galaxy with a large tidal HI envelope. Based on the 20 cm continuum source size, enhanced star formation takes place almost in the whole galactic body. ESO 341-04 probably belongs to this third scenario, too, although we do not know the extension of the HI. But it hosts a large amount of atomic gas (which argues against scenario two) as well as molecular gas (which argues against scenario one).

Arp 164 might be a merger of type two, because neither HI nor CO is observed down to a reasonable upper limit for the gas masses. Also, no hints for ongoing enhanced star formation are found (no 20 cm continuum flux could be detected and no far-infrared fluxes are available). Thus, it is likely that two gas-poor galaxies (i.e., Ellipticals) were the progenitors. Also

ESO 159-03 might be a merger of this second class, because no HI could be measured down to an applicable limit, and although no CO observations were obtained, it is unlikely, that this galaxy has a significant amount of molecular gas while lacking atomic gas. Furthermore, no indicators of ongoing enhanced star formation were found.

UGC 8264 has some puzzling properties, since it shows the features of ongoing enhanced star formation in an extended region, but no molecular gas was detected. The question arises, how the star formation is fueled! As argued above, most of the CO has probably been already used, and since UGC 8264 has a high star formation efficiency, the period of enhanced star formation will be over soon. The HI in the system is rather compact, which means not showing any tails or plumes. The ring-like HI distribution has a diameter of only ~ 30 kpc. Thus, the gaseous properties are similar to what we expect to find for an object of the kind of scenario one, but the stellar remnant is too small for the result of a merger between two large disk galaxies.

Due to the high upper limit derived for the HI gas mass of ESO 156-18, it is not possible to exclude one of the scenarios. But since this galaxy is luminous in the far-infrared, a merger between two gas-poor Ellipticals is unlikely, because this would not lead to enhanced star formation. With our current data, both scenario one and three are possible (faded ULIRG and S+E merger).

The detailed analysis of the star formation history using stellar population synthesis models will clearly give more clues on the nature of the undergone merger event of our sample galaxies. This will be done in future work. Part of the relevant data, i.e., optical spectra, are already observed (see Ch. 3), and first test with the stellar population synthesis code PEGASE (Fioc & Rocca-Volmerange (1997)) are already done (Manthey et al. (2005)).

6.6 Conclusions

1. We observed nine galaxies of our *moderate luminosity mergers* sample with radio interferometers in HI. Six of them show a complex gas distribution with clear signs of interaction. Three galaxies could be not detected.
2. In NGC 4004 we found an extended HI disk with a warp at the southern end, associated with an HI clump at its tip. This clump has a weak optical counterpart. The highly disturbed character of the optical appearance is not that drastically reflected in the atomic gas, which has a rather smooth distribution along the optical galaxy and a smooth velocity field. We detected furthermore a faint HI extension to the west in direction of a nearby Elliptical. Based on our HI and CO observations, we calculate an HI mass of $7.2 \cdot 10^9 M_{\odot}$ and a molecular gas mass of $9.5 \cdot 10^8 M_{\odot}$. As expected from the optical, this galaxy undergoes a period of enhanced star formation ($\text{SFR}_{20\text{cm}} = 8.5 M_{\odot}/\text{yr}$, $\text{SFR}_{\text{FIR}} = 2.1 M_{\odot}/\text{yr}$).
3. NGC 5607 has a long tidal tail (≥ 200 kpc) with some clumps at the tip. No optical counterpart is found for this tail. The derived HI mass is $1.42 \cdot 10^{10} M_{\odot}$, for the molecular gas we calculate a gas mass of $3.3 \cdot 10^9 M_{\odot}$. From the radio continuum and far-infrared emission, we estimate an enhanced star formation rate of $40 M_{\odot}/\text{yr}$ and $12.5 M_{\odot}/\text{yr}$, respectively.
4. The optical tidal features of UGC 8264 are partly found in HI as well. The optical curved tail is continued and completed to a ring structure, with a larger amount of gas

found in the part of the ring, where no stars are present. At the tip of the optical tail, a bright knot is visible, which is aligned with an HI clump. Thus, this object is an ideal candidate for a tidal dwarf galaxy. From our observations, we calculate an HI mass of $4.2 \cdot 10^9 M_{\odot}$. Because we did not detect this galaxy in CO, we can only estimate an upper molecular gas mass of $< 3.8 \cdot 10^8 M_{\odot}$. The non-detection in CO is of particular interest, since this galaxy is star forming with rates between $14.5 M_{\odot}/\text{yr}$ (based on radio continuum) and $3.0 M_{\odot}/\text{yr}$ (based on the far-infrared emission).

5. Arp 161 with its faint optical tidal fan is embedded in an extended HI structure with a particularly prominent tidal plume to the north-west. This HI feature has no optical counterpart. The derived HI gas mass of this galaxy is $4.3 \cdot 10^9 M_{\odot}$, for the molecular gas mass, we find $5.3 \cdot 10^8 M_{\odot}$. In agreement with its classification as an HII-galaxy, Arp 161 shows an enhancement of star formation with rates of $22.2 M_{\odot}/\text{yr}$ (from the 20 cm continuum) and $5.6 M_{\odot}/\text{yr}$ (from the far-infrared).
6. No HI was found in Arp 164, ESO 156-18 and ESO 159-03. We derived upper mass limits of $0.4 \cdot 10^9 M_{\odot}$, $9.4 \cdot 10^9 M_{\odot}$ and $0.7 \cdot 10^9 M_{\odot}$, respectively. In the vicinity of Arp 164 and ESO 159-03 we detected small HI companions with compact optical counterparts. For Arp 164, we furthermore estimate an upper limit for the molecular gas mass as $8.4 \cdot 10^8 M_{\odot}$.
7. All in HI detected galaxies show a complex and extended gas structure and host an (extended) region of enhanced star formation. This does not fit in the common models for S+E mergers, neither from Kojima & Noguchi (1997) (predicting no enhanced star formation due to too dispersed gas), nor from Weil & Hernquist (1993) (claiming a very compact gas distribution). With the results of study, we cannot favour one of the models, but it seems obvious, that modifications have to be applied to the simulations. In particular the gaseous component and the developing of a burst is not well understood so far.
8. Often, the HI tidal features do not coincide with the optical ones, although the optical galaxy is in all cases completely embedded in the HI distribution. This is a strong hint, that the galaxies presented here are not remnants of disk–disk mergers, in which optical and gaseous features are often aligned or only slightly shifted due to superwinds, when strong starbursts are present.

References

- Aalto, S. & Hüttemeister, S. 2000, *A&A*, 362, 42
- Arnault, P., Kunth, D., Casoli, F., & Combes, F. 1988, *A&A*, 205, 41
- Bottinelli, L., Gougenheim, L., Fouque, P., & Paturel, G. 1990, *A&AS*, 82, 391
- Condon, J. J., Helou, G., Sanders, D. B., & Soifer, B. T. 1990, *ApJS*, 73, 359
- Davis, L. E. & Seaquist, E. R. 1983, *ApJS*, 53, 269
- Fioc, M. & Rocca-Volmerange, B. 1997, *A&A*, 326, 950

- Gavazzi, G. 1987, *ApJ*, 320, 96
- Haarsma, D. B., Partridge, R. B., Windhorst, R. A., & Richards, E. A. 2000, *ApJ*, 544, 641
- Hawarden, T. G., Longmore, A. J., Goss, W. M., Mebold, U., & Tritton, S. B. 1981, *MNRAS*, 196, 175
- Haynes, M. P. & Giovanelli, R. 1991, *ApJS*, 77, 331
- Helou, G., Soifer, B. T., & Rowan-Robinson, M. 1985, *ApJ*, 298, L7
- Hibbard, J. E., Vacca, W. D., & Yun, M. S. 2000, *AJ*, 119, 1130
- Hibbard, J. E. & van Gorkom, J. H. 1996, *AJ*, 111, 655
- Hibbard, J. E. & Yun, M. S. 1999, *AJ*, 118, 162
- Horellou, C. & Booth, R. 1997, *A&AS*, 126, 3
- Kandalyan, R. A. 2003, *A&A*, 398, 493
- Kennicutt, R. C. 1998, *ARA&A*, 36, 189
- Kojima, M. & Noguchi, M. 1997, *ApJ*, 481, 132
- Manthey, E., Hüttmeister, S., Haberzettl, L., & Aalto, S. 2005, in *AIP Conf. Proc. 783: The Evolution of Starbursts*, ed. S. Hüttmeister, E. Manthey, D. Bomans, & K. Weis, 343–348
- Mirabel, I. F. & Sanders, D. B. 1988, *ApJ*, 335, 104
- Sage, L. J., Salzer, J. J., Loose, H.-H., & Henkel, C. 1992, *A&A*, 265, 19
- Sanders, D. B. & Mirabel, I. F. 1996, *ARA&A*, 34, 749
- Strong, A. W., Bloemen, J. B. G. M., Dame, T. M., Grenier, I. A., Hermsen, W., Lebrun, F., Nyman, L.-A., Pollock, A. M. T., & Thaddeus, P. 1988, *A&A*, 207, 1
- Telles, E. & Terlevich, R. 1997, *MNRAS*, 286, 183
- Toomre, A. 1977, in *Evolution of Galaxies and Stellar Populations*, 401
- Weil, M. L. & Hernquist, L. 1993, *ApJ*, 405, 142
- Weistrop, D., Eggers, D., Hancock, M., Nelson, C. H., Bachilla, R., & Kaiser, M. E. 2004, *AJ*, 127, 1360

7 Summary

Abstract

In this thesis, a multiwavelength study of a sample of S+E mergers was presented. This is the first detailed and systematic study of this kind of mergers. Optical and near-infrared observations were obtained to study the morphology and the stellar population, and in particular the ongoing star formation rate. Interferometric HI observations were done to study the distribution and kinematics of the atomic gas, which nicely reflect the merger history. CO observations finally give clues about the present molecular gas reservoir, which might feed a starburst. Here, the main results from this survey are summarised.

In the study presented here, a sample of 15 galaxies were investigated, which initially were suspected to be in the same merger stage due to their similar optical morphology. This approach is different to other merger studies (e.g., Toomre (1977), Hibbard & van Gorkom (1996), Laine et al. (2003)), which deal with a merger sequence. However, these studies have to deal with the fact, that it is unsure whether the sequence of chosen galaxies really reflects an evolutionary sequence. In the study presented here, we compared the properties of galaxies, which from the position of the galaxies on a merger sequence, could be believed to be similar. In reality, we found large differences in particular in the gas content and the star formation rate. This exemplifies the difficulties of classifying mergers, and in particular selecting a merger sequence.

In the following, the major results are summarised, with special emphasis on the differences found between the galaxies. In Tab.32 the properties derived from the measurements presented here are given.

The observed variety of optical morphologies

Despite all being advanced mergers, the sample galaxies show a variety of tidal features, e.g. shells, tails and plumes. Besides the features clearly visible in DSS images, we found additional fainter disturbances of the galaxies. Among those, examples are fragments of the brighter features found, like the arclets around NGC 4441 and ESO 159-03, faint straight spikes like in UGC 8264 and NGC 5607 and diffuse and rather structureless distributions like in the northern part of NGC 4004.

The colours found in the tidal structures like the shells are slightly bluer (NGC 4441, NGC 4194, UGC 8264, NGC 4004, NGC 5607) or do not show a difference to the colour of the main galactic body (Arp 164, ESO 156-18, ESO 159-03). This is in agreement with other studies (e.g., Carter et al. (1982), Fort et al. (1986), Pence (1986) McGaugh & Bothun (1990), Turnbull et al. (1999)).

Most of the observed galaxies have a surface brightness distribution which can be described by an exponential disk in the outer parts and a bulge-like component in the center. Although it cannot be excluded that the targets will evolve into Ellipticals after a time of relaxation, this behaviour is in striking contrast to what is found in advanced disk-disk mergers (e.g., Stanford & Bushouse (1991), Hibbard & van Gorkom (1996), Schweizer (1996), Chitre & Jog (2002) and modelled by Barnes & Hernquist (1991)). These major mergers show an elliptical light distribution, when there is still enhanced star formation going on and the tidal features are clearly visible, i.e., in a similar stage as the galaxies in our sample. Chitre & Jog (2002) studied a sample of peculiar galaxies in the near-infrared K-band and claim, that mergers between galaxies of unequal masses (e.g., S+E mergers) keep a disk, while mergers between equal masses evolve into Ellipticals. They conclude, that the radial profiles can therefore be

used to distinguish between these two classes of mergers. This corroborates our observations and the assumption, that at least most of the galaxies in our sample are indeed S+E mergers with different masses of the progenitors.

The variety of star formation

Based on the optical spectra, the far-infrared emission and the 20 cm continuum emission, the star formation rates cover a broad range from no significant ongoing star formation (e.g., ESO 159-03), moderate star formation (NGC 4441) to enhanced star formation that can be described as an ongoing starburst (NGC 5607, NGC 4194). The regions of ongoing star formation are generally extended to typically a few kpc, based on the derived source sizes of the 20 cm continuum emission. This agrees with what is found in the 'prototype' of the sample, i.e., the Medusa and again confirms, that *moderate luminosity mergers* can indeed be seen as a distinct class not originating from a major merger event. Still, despite the similar optical morphology and generally extended region of star formation, the star formation activity can be very different. This shows, that the morphology alone is not suitable to make predictions about the evolutionary stage of the merger, because obviously the timescale of the star formation activity is extremely different to that of the dynamical evolution of the stellar distribution.

At present, it cannot clearly be disentangled whether a starburst occurred in all sample galaxies but has vanished in the more evolved ones, or whether in some galaxies no burst happened at all. A completion of the data set, esp. concerning optical spectroscopy, is necessary to bring light into this question (see below).

The variety of the present gas

The gas content (both atomic and molecular) in the observed galaxies ranges from non-detections (e.g., Arp 164) to galaxies which have a very extended and disturbed HI distribution and host a large molecular gas reservoir. Again, this reflects the different stages of the galaxies similar in the optical morphology. One has to keep in mind, that the differences in the gas content can originate either in evolutionary effects, i.e., the gas has already been consumed in a starburst, or in an initially different gas content because of different progenitors. The latter case would imply, that different progenitors can result in a (optically) similar remnant! Consequently, an optical classification of a merger would be questionable with respect to the merger *stage* and even the merger *kind*. Anyway, the determination of the gas content in a merger remnant is obviously more meaningful than the optical morphology alone.

The comparison of the optical and gaseous distribution revealed remarkable differences in all observed galaxies. For example, NGC 5607 has a huge HI tail with no optical counterpart, in Arp 161 and NGC 4194 the gaseous tidal features appear almost opposite to the stellar tails. These misalignments of the stellar and gaseous tidal features are much more significant than what is found by Hibbard et al. (2000). Until now, no satisfying explanation could be found, but it seems obvious, that once more a very important distinguishing feature of *moderate luminosity mergers* compared to large disk-disk mergers has been identified. Simulations of extreme cases like mergers between an elliptical and a very gas-rich small disk galaxy or even pure HI cloud may shed further light on this matter.

In the more detailed study of the gas content of NGC 4441 an unusually high $^{12}\text{CO}/^{13}\text{CO}$ ratio typical for starbursts was found, even though NGC 4441 is no starburst. In contrast, the results of the $^{12}\text{CO}(2-1)/^{12}\text{CO}(1-0)$ and $^{13}\text{CO}(2-1)/^{13}\text{CO}(1-0)$ line ratio analysis fit the low star formation rate found in NGC 4441. The molecular gas in NGC 4441 is diffuse with

no signs of cold (or hot), dense starforming cores. Whether this happened due to scattering during the merger (as predicted by Kojima & Noguchi (1997)) or the detected gas simply represents the left-over material cannot be distinguished so far, but further observations (see below) will be done to clarify this question. In any case, these results once more manifest the complexity of a merger event and its implications on the gas and the star formation activity, in particular when comparing NGC 4441 with the other sample galaxies.

Considering all results from the survey presented here, the conclusion must be, that it is not sufficient to classify (S+E) mergers from the optical morphology alone, but consider more properties, like the atomic and molecular gas content, the ongoing star formation rate and the star formation history (with particular emphasis on a past burst). This is in agreement with the statement of Laine et al. (2003), who obtained high resolution optical imaging of the Toomre sequence galaxies (Toomre (1977)) and found very different properties in the galaxies, not correlated to the assumed merger stage. They therefore note, that there 'is no one-to-one correspondence between the observed merger stage and nuclear morphology and activity'. Thus, the Toomre sequence is not a true evolutionary sequence.

The results presented here also have impact on the requirements of theoretical models. Recall the different predictions for the appearance of a starburst phase and the gas distribution when using different approaches to simulate the interstellar medium. In general, our study corroborates what was already indicated in the study of NGC 4194 (Aalto & Hüttemeister (2000)): Signs of enhanced star formation are found in most of the mergers, which is probably induced by the mergers, while clear optical and gaseous tidal features are present. In particular the analysis of the 20 cm continuum emission sources revealed that the star formation region is extended to > 1 kpc in all galaxies in which 20 cm continuum could be detected. This is neither predicted by the models of Weil & Hernquist (1993) (who suggest a compact starburst without extended HI structures), nor by Kojima & Noguchi (1997) (who suggest a dispersed gas distribution and no starburst, at least not when tidal features are visible).

The models furthermore have to deal with the variety of observed morphologies, both in the optical and the HI. In particular the often found misalignment of the gas and the stars has to be explained more quantitatively.

The timescales of the evolution of stellar and gaseous features and the duration of a burst are of further interest. When comparing in particular NGC 4441 and NGC 4194, the star formation rate is very different, whereas the morphology is very similar. Thus, if the star formation once was enhanced in NGC 4441, the burst must have been decreased significantly, while the optical features remain similar.

Table 32: Overview of the derived properties of the sample galaxies. (–) labels non-detections, whereas (*) labels no available measurements. The B–band luminosities are calculated from B–magnitudes taken from the UGC, assuming a solar apparent B–magnitude of 5.54. The K–luminosities are calculated from 2MASS K–band magnitudes, assuming a solar apparent K–magnitude of 3.28 (Binney & Merrifield (1998)). The far-infrared luminosities are calculated from the IRAS catalog (Moshir & et al. (1990)).

^a taken from Horellou & Booth (1997)

| galaxy | L_B ($10^{10} L_\odot$) | L_K ($10^{10} L_\odot$) | L_{FIR} ($10^{10} L_\odot$) | M_{HI} ($10^9 M_\odot$) | M_{H2} ($10^8 M_\odot$) | SFR_{20cm} (M_\odot/yr) | SFR_{FIR} (M_\odot/yr) | $SFR_{H\alpha,tot}$ (M_\odot/yr) | SFR_{nuc} (M_\odot/yr) | $\log \frac{O}{H} + 12$ total (nuc) |
|------------|--------------------------------|--------------------------------|------------------------------------|--------------------------------|--------------------------------|----------------------------------|---------------------------------|---|---------------------------------|--|
| NGC 4004 | 0.83 | 2.29 | 1.2 | 7.2 | 9.5 | 8.5 | 2.1 | 4.12 | 0.2 | 8.6 (8.4, 8.2) |
| NGC 5607 | 5.01 | 13.30 | 7.3 | 14.2 | 33.0 | 40.0 | 12.5 | 32.9 | 11.4 | 8.8 (9.0) |
| UGC 8264 | 1.39 | 2.03 | 1.7 | 4.2 | <2.8 | 14.5 | 3.0 | 6.58 | 2.01 | 8.3 (8.4) |
| NGC 4441 | 1.01 | 3.10 | 0.5 | 1.5 | 4.6 | 2.36 | 0.95 | >0.2 | >0.09 | 9.2 (9.2) |
| NGC 4194 | 1.57 | 3.73 | 8.5 | 2.0 | 20.0 | 22.8 | 9.5 | 13.9 | 5.87 | 8.9 (9.0) |
| Arp 161 | 1.29 | 3.53 | 3.2 | 4.3 | 5.3 | 22.2 | 5.6 | 7.7 | 1.24 | 8.5 (8.7) |
| Arp 164 | 1.67 | 13.68 | – | <0.5 | <8.4 | <1.0 | – | * | * | * |
| ESO 156-18 | 2.35 | 37.67 | 0.5 | < 9.4 | * | <1.3 | 6.1 | * | * | * |
| ESO 159-03 | 0.99 | 3.31 | – | <0.7 | * | <0.1 | – | * | * | * |
| ESO 416-09 | 2.63 | 8.17 | – | * | * | * | – | * | * | * |
| NGC 2996 | 8.17 | 23.77 | – | * | * | * | – | * | * | * |
| ESO 341-04 | 4.70 | 13.06 | 1.3 | 3.9 ^a | 1.7 ^a | * | 2.3 | * | * | * |
| ESO 511-35 | 5.65 | 17.86 | – | * | * | * | – | * | * | * |
| IC 5065 | 4.17 | 24.89 | – | * | * | * | – | * | * | * |
| ESO 295-02 | 2.54 | 23.33 | 1.4 | * | * | * | 2.4 | * | * | * |

Outlook

Clearly, this thesis can only be treated as a first step in understanding mergers which are different from ULIRGs. From the observational side, the next step will be to complete the data set for the whole sample both in the Optical/NIR and the mm-/radio regime (hoping that APEX is soon fully operational to get CO data for objects located in the southern hemisphere).

In addition to broadband imaging, we will obtain H α narrow-band imaging to map the star forming regions, in particular to determine the extent of the regions. These data will have much higher resolution than the 20 cm continuum maps.

Furthermore, a detailed analysis of the optical spectra to investigate the star formation history will be done using stellar population synthesis codes like PEGASE (Fioc & Rocca-Volmerange (1997)) and GALAXEV (Bruzual & Charlot (2003)). This will give a deep insight into the burst behaviour of the galaxies and thus will help to understand the merger history and the involved progenitors.

Interferometric CO observations are proposed for NGC 4441 to investigate the molecular gas mass distribution and kinematics at high resolution. This will allow us to study the gas surface density with respect to the distance from the center and the dynamics of the gas. In particular when comparing the observations with its 'younger sister' NGC 4194, conclusions can be drawn from these observations as to why NGC 4441 has a moderate star formation rate, while still a large amount of atomic and molecular gas is present and tidal features are well visible.

From the theoretical side, it is obvious that the current models are not sufficient. In collaboration with C. Horellou (OSO, Sweden), N-body simulations are being done to model the HI distribution of NGC 4194. The challenge in this galaxy is the presence of *one* dominant HI tail, which is in opposite direction of the optical tail. Beyond this one example, clearly simulations trying to reproduce the variety of misaligned HI and optical structures are needed.

In general, this thesis has shown, that *moderate luminosity mergers* are indeed not the result of (faded) major disk-disk mergers, but a class of their own, characterised by regions of extended star formation and (if HI is present) extreme misalignments between the gaseous and optical morphologies. However, within this class, the internal variety is large and striking, manifesting itself only once the observational evidence is taken beyond optical imaging. Thus, this newly established class warrants much deeper study to shed further light on galaxy evolution through merging in general.

References

- Aalto, S. & Hüttemeister, S. 2000, A&A, 362, 42
- Barnes, J. E. & Hernquist, L. E. 1991, ApJ, 370, L65
- Binney, J. & Merrifield, M. 1998, Galactic astronomy (Galactic astronomy / James Binney and Michael Merrifield. Princeton, NJ : Princeton University Press, 1998. (Princeton series in astrophysics) QB857 .B522 1998 (\$35.00))
- Bruzual, G. & Charlot, S. 2003, MNRAS, 344, 1000

- Carter, D., Allen, D. A., & Malin, D. F. 1982, *Nature*, 295, 126
- Chitre, A. & Jog, C. J. 2002, *A&A*, 388, 407
- Fioc, M. & Rocca-Volmerange, B. 1997, *A&A*, 326, 950
- Fort, B. P., Prieur, J.-L., Carter, D., Meatheringham, S. J., & Vigroux, L. 1986, *ApJ*, 306, 110
- Hibbard, J. E., Vacca, W. D., & Yun, M. S. 2000, *AJ*, 119, 1130
- Hibbard, J. E. & van Gorkom, J. H. 1996, *AJ*, 111, 655
- Horellou, C. & Booth, R. 1997, *A&AS*, 126, 3
- Kojima, M. & Noguchi, M. 1997, *ApJ*, 481, 132
- Laine, S., van der Marel, R. P., Rossa, J., Hibbard, J. E., Mihos, J. C., Böker, T., & Zabludoff, A. I. 2003, *AJ*, 126, 2717
- McGaugh, S. S. & Bothun, G. D. 1990, *AJ*, 100, 1073
- Moshir, M. & et al. 1990, in *IRAS Faint Source Catalogue*, version 2.0 (1990), 0
- Pence, W. D. 1986, *ApJ*, 310, 597
- Schweizer, F. 1996, *AJ*, 111, 109
- Stanford, S. A. & Bushouse, H. A. 1991, *ApJ*, 371, 92
- Toomre, A. 1977, in *Evolution of Galaxies and Stellar Populations*, 401
- Turnbull, A. J., Bridges, T. J., & Carter, D. 1999, *MNRAS*, 307, 967
- Weil, M. L. & Hernquist, L. 1993, *ApJ*, 405, 142

Acknowledgements

I thank the Deutsche Forschungsgemeinschaft for funding a scholarship of the Graduiertenkolleg 787 'Galaxy Groups as Laboratories for Baryonic and Dark Matter' during the PhD thesis project. Without this gradschool and in particular the generous travel money, this work would not have been possible. I would like to thank Ralf-Jürgen Dettmar as the head of the gradschool and chair of astronomy for his encouragement and support during my work. I am deeply indebted to Susanne Hüttemeister, who offered me the opportunity to work in one of the most exciting fields in astronomy, and greatly supervised my thesis with loads of discussions and suggestions. I would also like to thank her for giving me the opportunity to get first experiences in teaching and organising an international conference, where I got in contact with many interesting people. Furthermore, she introduced me to Susanne Aalto, whom I would like to express my gratitude for all the fruitful discussion, for giving me the opportunity to visit the Onsala Space Observatory several times, and for her enthusiasm and finally for being my second supervisor despite some organisational problems.

I very much appreciated the kind support at the NOT and the Roque de Los Muchachos Observatory on La Palma, the TCS on Tenerife, Calar Alto, ESO (particularly the NTT team), Siding Spring Observatory, the Bok telescope on Kitt Peak, IRAM and the ATCA. Furthermore, I thank the people of the VLA and WSRT for observing my targets in service mode. Special thanks to the people of the Onsala Space Observatory, not only for their assistance during my observations, but also for the nice and fruitful atmosphere during my visits.

A special thanks also to Tom Oosterloo, who helped me with the data reduction of the WSRT data. From this a fruitful collaboration developed, and I am looking forward to continue working with him together at Astron!

Furthermore, I thank Bärbel Koribalski very much for her patience introducing me to interferometric radio observations and data reduction and her interest in my thesis. Thanks to her and her family, I very much enjoyed my two visits at the ATNF in Sydney.

I am very grateful to Rob Kennicutt for his interest and his comments on my thesis. I very much appreciated the discussions with him about stellar populations, what we can learn and what *not*. Furthermore, he gave me the possibility to obtain spectra at the Bok telescope and to visit Steward Observatory in Tucson. A special thanks also to Christy Tremonti and John Moustakas, with whom I had a great time at Kitt Peak and Steward Observatory and who showed me how to obtain optical spectroscopy and the data reduction.

I would like to thank Elizabeth Wehner for her comments and in particular for the optical observations of Arp 164.

Special thanks to Eva Karlsson for joining me for the second NOT observing run. We had quite a lot of fun, hadn't we?

Tack så mycket to Evert Olsson for his help with AIPS and all the great time we had together in Onsala and Socorro. In particular, I enjoyed our boat trips and celebrating Swedish Midsummer!

Special thanks to Yuri Shchekinov for providing us with 'healthy' Russian liquids and chocolate and the discussions about science, politics and life in general.

I would like to thank all the members of the AIRUB very much, who attended me all the years while I was there, from an undergraduate student to the end of my PhD thesis. I very much enjoy the (working) atmosphere, which in my opinion is very special here. A special thanks to Dagmar Münstermann, who always took care of (by far not only) organisational and administrative things. Her special 'translations' are very much appreciated, too! Fur-

thermore, I would like to thank Jörn Rossa, Lutz Haberzettl and Marcus Albrecht for their fruitful discussions and comments concerning several aspects of this thesis and other stuff. Special thanks to Michael Pohlen for assisting me during my observations at the TCS, providing me his NIR reduction software for the TCS, lively discussions about MIDAS and IRAF and the fastest drive from the observatory to the airport. Special thanks also to Giuseppe Aronica for all the chats and constructive remarks, concerning astronomy, and life. I thank 'Doc Garlic' Sven Müller for always being so helpful and for his special catering service, in particular the hot stuff he is always carrying. Special thanks to Kai Polsterer, who crashed my computer during my absence, so that I got a very nice new and fast one! I would like to thank Giuseppe Aronica, Volker Knierim and Dominik Rosenbaum for helping me with some observations. Furthermore I thank Markus Nielbock, that he gave me the possibility to visit the SEST telescope and participate in an interesting project.

I would like to thank Andreas Schröer very much for his friendship and that he was able to convince me that theoretical physics is explainable!

This is the time to express my gratitude to my fellow students and friends Sandra, Thorsten and Jens, without whom studies would have been much harder and less amusing.

Last but not least, I want to express my deepest gratitude to my beloved family: my parents, my sister and my brother and my boyfriend Marcus Jütte. They always supported, helped and took care of me. Marcus, thank you so much for all the help, your patience and believe in me!

Curriculum vitae

Name: Eva Manthey
Address: Kemnader Str. 295
44797 Bochum
Date of birth: 2.9.1977
Family status: unmarried
Nationality: German

1983–1987: Theodor–Heuss elementary school in Essen
1987–1996: Helmholtz–Gymnasium in Essen, degree: Abitur (A-levels)
10/96: Begin study of physics at the Ruhr–Universität Bochum
09/98: Intermediate diploma in physics
04/00–04/01: Diploma thesis at the “Astronomisches Institut der Ruhr–Universität Bochum” (AIRUB)
Title: *Variable young stars in M17*
04/01: Diploma in physics, mark: 1 (“sehr gut”)
05/01–12/01: Research associate at the AIRUB
since 01/02: PhD thesis at the AIRUB
Title: *The structure and interaction history of moderate luminosity mergers*
04/02 –03/05: Member of the ”Graduiertenkolleg” *Galaxy Groups as Laboratories for Baryonic and dark Matter*
since 04/05: Research associate at the AIRUB

